

ABSTRACT

Title of Dissertation: HIGH WAVE VECTOR ACOUSTIC
METAMATERIALS: FUNDAMENTAL
STUDIES AND APPLICATIONS

Randy Tah Ganye, Doctor of Philosophy, 2020

Dissertation directed by: Professor Miao Yu
Department of Mechanical Engineering

Acoustic metamaterials are artificially engineered structures with subwavelength unit cells that hold extraordinary acoustic properties. Their ability to manipulate acoustic waves in ways that are not readily possible in naturally occurring materials have garnered much attention by researchers in recent years. In this dissertation work, acoustic metamaterials that enable wave propagation with high wave vector values are studied. These materials render several key properties, including energy confinement and transport, wave control enhancement, and enhancement of acoustic radiation, which are exploited for enhancing acoustic wave emission and reception.

The dissertation work is summarized as follows. First, to enable experimental studies of the deep subwavelength cavities in these metamaterials, a low dimensional fiber optic probe was developed, which allows direct characterization of the intrinsic properties of the metamaterials without seriously disrupting the acoustic fields.

Second, low dimensional acoustic metamaterials for enhancing acoustic reception were realized and studied. These metamaterials were demonstrated to achieve both passive and active functionalities, including passive signal amplification and frequency filtering, as well as active tuning for switching and pulse retardation control. Third, a metamaterial emitter was realized and studied, which is capable of enhancing the radiative properties of an embedded emitter. Parametric studies enhanced the understanding of the effects of different geometric parameters on the radiation performance of the structure. Finally, the metamaterial emitter and receiver were combined to form a metamaterial-based sonar system. For the first time, the superior performance of the metamaterial enhanced sonar system over conventional sonar systems was analytically and experimentally demonstrated. As a proof of concept, a robotic sonar platform equipped with the metamaterial system was shown to possess remarkably better tracking performance compared to the conventional system.

Through this dissertation work, an enhanced understanding of high- k acoustic metamaterials has been achieved, and their applications in acoustic sensing, emission enhancement, and sonar systems have been demonstrated.

HIGH WAVE VECTOR ACOUSTIC METAMATERIALS: FUNDAMENTAL
STUDIES AND APPLICATIONS

by

Randy Tah Ganye

Dissertation submitted to the Faculty of the Graduate School of the
University of Maryland, College Park, in partial fulfillment
of the requirements for the degree of
Doctor of Philosophy
2020

Advisory Committee:

Professor Miao Yu, Chair

Professor Amr Baz

Professor Balakumar Balachandran

Professor Sarah Bergbreiter

Professor Timothy Horiuchi, Dean's Representative

© Copyright by
Randy Tah Ganye
2020

Dedication

To my God, Jehovah.

Acknowledgments

My journey through this work was possible because of the help and support of many people, of whom I owe sincere gratitude.

First and foremost, I would like to express my deepest gratitude to my advisor, Professor Miao Yu. She took me under her wing and helped me grow academically in this six-year journey. I am deeply appreciative of her patience, encouragement, and support, especially during the times when things got complicated and frustrating. She challenged me academically, offering me opportunities such as co-teaching and giving key-note talks. Her pointed council and direction enhanced my strengths and provided vital help to improve on my weak areas. The intellectual conversations I was privileged to have with her were integral to my growth as a scientist and would continue to benefit me in my career in academia.

I am sincerely grateful to Professor Amr Baz for the help, advice, and personal interest he showed me. To have someone that would routinely offer me personalized advice and direction was indeed a blessing to me. His immense knowledge, coupled with his contagious passion for science and engineering and his excellent teaching abilities, have inspired me. He encouraged me to join the Future Faculty Program, from which I learned a lot. I cannot thank him enough for the signed copy of his book, and for the privilege of serving on my dissertation committee.

I want to thank all my dissertation committee members for their generous counsel and advice on my dissertation and defense. I was honored to defend my dissertation before a panel of distinguished Professors. Despite the lockdown due to

the pandemic, they generously gave of their time and advice and agreed to a remote defense. I am thankful to Professor Balachandran for his advice and for his help in furthering my career. I am also grateful to Professor Bergbreiter for all the pointers on my dissertation defense, and to Professor Horiuchi for his help on Bats research and for accepting to serve as the Dean's Representative on my dissertation committee.

I also want to thank all my friends and colleagues of the Sensors and Actuators Lab. I am especially grateful to Dr. Haijun Liu, who taught me a lot in experimentation, working with metamaterials, and fiber optic sensor manufacturing. I am indebted to Dr. Yongyao Chen for his great insight into research, theory, and simulations, as well as all the practical advice on how to navigate in academia. I also thank Dr. Hyungdae Bae for his insight in design and manufacturing. I am very grateful for the support of Dr. Hyun Tae Kim, Dr. Liuxian Zhao, Amirhossein Yazdkhasti, Keshav Rajasekaran, Zack Wong, and Jonathan Kordell.

I am privileged to be part of a very caring and supporting family that helped me at every step along the way. I am particularly grateful to my mother, Mrs. Magdalene Ntinglet, who did everything to support me through my journey. To know that I could always count on her when difficulties arose was an indispensable safety net of which I am forever grateful. I am also particularly grateful to my aunt, Dr. Emelda Fomanka, for her support and insight in academia; to my brother, Remy Ganye, for always checking on my progress and for the intellectual conversations; and to my cousin, Irvin Angu, for meticulously proofreading my dissertation. I also want to express sincere gratitude to each member of my spiritual family, who provided invaluable support throughout my journey.

Table of contents

Dedication	ii
Acknowledgments.....	iii
Table of contents.....	v
List of Figures	ix
List of Abbreviations	xxvi
 Chapter 1: Introduction and Background.....	 1
1.1 Problem statement.....	1
1.2 Background and Literature review.....	4
1.2.1 Acoustic wave propagation in material media.....	4
1.2.2 Acoustic wave propagation in metamaterials	5
1.2.3 Metamaterial classification	7
1.2.3.1 Helmholtz resonator-based metamaterials.....	8
1.2.3.2 Membrane-type acoustic metamaterials	13
1.2.3.3 Space-coiling acoustic metamaterials and metasurfaces	18
1.2.4 Metamaterial techniques and functionalities	27
1.2.4.1 Transformation acoustics and cloaking	27
1.2.4.2 Acoustic Superresolution	32
1.2.4.3 Sensing enhancement techniques.....	38
1.3 Motivation for this dissertation work.....	44
1.4 Overview and organization of the dissertation	47
1.4.1 Overview of dissertation	47
1.4.2 Organization of the dissertation	49
 Chapter 2: Understanding high wave vector acoustic metamaterials	 51
2.1 Motivation: Why High- k acoustic metamaterials?	52
2.2 Types and construction of high- k metamaterials	53
2.2.1 Types.....	53
2.2.2 Construction.....	55
2.3 Study methodology	58
2.3.1 Simulation studies.....	59
2.3.2 Experimental studies.....	60
2.3.3 Acoustic sensor development	61
2.3.3.1 Sensor fabrication process	63
2.3.3.2 Properties of the fiber optic microphone	65
2.3.3.3 Characterization of the fiber optic microphone	65
2.3.3.4 Sensor interrogation system:.....	68

2.4 Properties of high- k acoustic metamaterials	71
2.4.1 Energy confinement and transport	71
2.4.1.1 Analytical study of the energy confinement	72
2.4.1.2 Experimental demonstration of energy confinement and transport	75
2.4.1.3 Wave propagation mechanism	80
2.4.2 Enhancement of control	83
2.4.2 Radiation enhancement	87
2.5 Summary	89
Chapter 3: Low dimensional high-k acoustic metamaterials for reception.....	91
3.1 Motivation	92
3.2 Metamaterial design, fabrication, and experimental setup	95
3.2.1 Design and fabrication	95
3.2.2 Experimental setup	98
3.3 Metamaterial characterization studies	99
3.3.1 Role of vertical space above the on-chip metamaterial	106
3.4 Broadband filtering effects of the receiver metamaterial	112
3.5 Active tunable on-chip metamaterial	116
3.5 Metamaterial approximation of the mammalian cochlea	121
3.5.1 The mammalian cochlea	121
3.5.1.1 Analytical model of the basilar membrane of the mammalian cochlea	
.....	122
3.5.2 Metamaterial based artificial cochlea	127
3.6 Summary	137
Chapter 4: Bio-inspired High-k acoustic metamaterial for emission enhancement	139
4.1 Motivation	140
4.2 Metamaterial design	143
4.3 Parametric studies	144
4.3.1 Acoustic metamaterial cavity	144
4.3.1.1 Analytical studies on radiation enhancement	146
4.3.1.2 Accounting for radiation losses	154
4.3.2 Acoustic metamaterial coupler	158
4.3.2.1 Tapered structure without the metamaterial cavity	164
4.3.3 Gap thickness	166
4.3.4 Size of the emitter	170
4.3.5 Ambient temperature effects	174
4.4 Experimental and numerical studies on a 25.6 kHz metamaterial emitter	178
4.5 Summary	186

Chapter 5: Bio-inspired High-k acoustic metamaterial SONAR	188
5.1 Motivation.....	189
5.2 Analytical studies.....	192
5.2.1 Conventional sonar system	192
5.2.2 Metamaterial sonar system	194
5.3 Sonar experimental characterization.....	197
5.3.1 Echolocation range.....	199
5.3.2 Target size	201
5.3.3 Target separation.....	208
5.3.4 High-frequency metamaterial sonar.....	214
5.4 Metamaterial enhanced robotic tracking.....	220
5.4.1 Localization scheme.....	221
5.4.2 Tracking control scheme.....	224
5.4.3 Robotic tracking experiments	225
5.5 Summary	229
Chapter 6: Conclusion.....	231
6.1 Summary of the dissertation work	231
6.1.1 Research question responses.....	231
6.1.2 Research summary	232
6.1.3 Delineation of High- k properties in this study	238
6.2 Major contributions.....	239
6.3 Future work.....	241
Appendix A: MATLAB codes.....	244
A1: Metamaterial analytical model - frequency	244
A2: Metamaterial analytical model - spatial	247
A3: Cochlea analytical model- dispersion plotter.....	250
A4: Cochlea analytical model- spatial	251
A5: Sonar target size plotter	253
A6: Sonar echolocation range plotter	263
A7: Microphone calibration plotter	271
Appendix B: LabVIEW code	273
Pulse retardation analyzer	273
Appendix C: Calibration data	275
C1: Brüel & Kjær 4939 Ultrasonic microphone calibration datasheet	275
C2: Optical microphone sensitivity calculator.....	276
C3: SPU0410LR5H-QB Ultrasonic MEMS microphone frequency response	282

Appendix D: List of publications.....	283
Bibliography	284

List of Figures

Figure 1. 1 Schematic of dispersion curves for the free space (blue) and a high-k metamaterial medium (red). High-k metamaterials can sustain more waves per unit length x than the free space at the same frequency.....	3
Figure 1. 2 Schematic of a coupled mass-in-mass oscillator.	6
Figure 1. 3 (a) Schematic of the rainbow trapping metamaterial by Zhao et al. (b) Experimental setup. A loudspeaker is connected to the opening of the spiral tube to generate acoustic waves. Measurement is done using a point laser Doppler vibrometer at different locations. (c) Fourier transform of the particle velocity temporal plot of the 7 th cylinder. (d)-(i) A cylindrical space covered by the parity-time symmetric metasurface realized by Hao-xiang Li et al. (d) no cloak- strong backscattering and a shadow is observed. (e) camouflaging through complete absorption with a lossy semicircle metasurface only (f) cloaking via PT symmetry semicircle metasurface containing acoustic loss (gain) to fully absorb incoming (reemit outgoing) sound waves. (g)-(i) Experimental realization of the PT symmetric metasurface cloak made from two jointed semi shells (radius $a = 40$ cm).....	10
Figure 1. 4 (a) schematic and (b) photograph of a unit cell of the reconfigurable acoustic metamaterial realized by Bogdan-Ioan et al. (c) Metamaterial slab consisting of 10 cells. (d) Experimental results showing the lens' second harmonic response. (e) Comparison between the fields measured on the focal plane and an ideal lens imaging at the second harmonic (dotted curve) and the fundamental (solid curve). (f) Acoustic metamaterial with continuously tunable compressibility realized by Lee et al. (g) Theoretical plots and the experimental data for the effective compressibility β_r of the duct as a function of the tube length l	12
Figure 1. 5 (a) Schematic of a DMR with two coupled membranes realized by Yang et al. The rigid ring allows for extra tunability. (b) Displacement profiles of three low-frequency	

eigenmodes. The solid black lines show results from finite element simulations, while the red dots indicate the measured profiles using the laser vibrometer. (c) Transmission coefficient as a function of frequency. (d) Effective mass density (red) and bulk modulus (blue) plotted as a function of frequency. (e) The real part of the effective wave vector as a function of frequency. (f) A unit cell of the double membrane-type active acoustic metamaterial proposed by Langfeldt et al. (g) Isometric view of the unit cell illustrating the working principle.

Introducing pressurized air into the cavity causes the membranes to stretch, increasing the eigenfrequencies of the system. (h) Experimental and theoretical STL for the membrane-type acoustic metamaterial at three inflation pressure differences β 15

Figure 1. 6 (a) Schematic of the tunable acoustic metamaterial realized by Xiang Yu, comprising an array of DE resonators being attached to a duct. (b) Connecting four DE resonators to form a metamaterial array for realizing a much-broadened attenuation band. (c) Tunable acoustic metamaterial proposed by Wang et al. Each resonator consists of a metallic mass connected to the matrix through elastic beams. (c) The undeformed configuration. (d) Metamaterial with a compressive strain applied in the vertical direction. (e) Dispersion relations from Bloch-wave analysis for the infinite metamaterial under compressive strain. Shear dominated bands are colored in blue, pressure dominated bands in red and locally rotational bands in black. The grey region highlights the bandgap induced by local resonance. 17

Figure 1. 7 (a) The schematic diagram of an acoustic metasurface for the generalized Snell's law realized by Yong Li et al. It was made of two stiff corrugated beams with a channel coiling up the space. (b) The pressure strips of the reflected waves by the eight units. The phase shifts resulting from the corrugation lengths are evident. (c) Pressure field pattern showing the metasurface converting propagating waves to surface waves. (d) Spatial distribution and (e) transverse cross-section of the intensity profile of the acoustic axicon for the non-diffracting Bessel beam. 20

Figure 1. 8 (a) Schematic concept of wavefront modulating thin planar metasurface (solid line) and the generalized Snell's law (dashed line). (b) Photograph of the unit cell prototypes. (c) Six types of unit cells and the corresponding phase changes through the unit cells. (d) Simulations and (e) experimental results of field patterns at 45 degrees, demonstrating the negatively refracted transmission. The white arrows indicate the forward phase propagation directions. (f) Top: Measured near-field of the evanescent mode on the transmitted side at 25 degrees incidence. Bottom: Simulated and experimental results of the pressure field spatial Fourier transform across the surface. 22

Figure 1. 9 (a) Acoustic metasurface arrangement for a flat Fresnel lens by Boyang Xie et al. (b) and (c) shows the experimental intensity profile achieved at 4.53 kHz by the setup elemental arrangement in (a). (d) Transmission amplitude and (e) phase of the waves through elements “0” and “1”. (f) Quantized metamaterial bricks and grid setup reported by Gianluca et al. (g) Beam steering and focusing with the metasurface. (h) Experimentally obtained pressure field distribution and (i) acoustic levitation of a polystyrene bead using the pressure field distribution in (h). 24

Figure 1. 10 Acoustic hologram realized by Kai Melde et al. (a)-(e) Methodology steps for the acoustic hologram formation. The propagation medium used is water, and the acoustic hologram is formed in water. 2.06 MHz ultrasonic waves are used, and a hydrophone is used to obtain the pressure image in (e). (f) Schematic of the pressure field profile used for acoustic levitation. (g) Photograph of two water droplets levitated in the pressure field traps in (f). A 100 kHz transducer was used. The scale bar represents 5 mm. 26

Figure 1. 11 (a) Schematic of the pyramidal omnidirectional acoustic cloak proposed by Zigoneanu et al. (b) Instantaneous pressure field distribution showing the cloaking effectiveness of the device. The pressure field from the cloaked object mimics the empty ground. (c) Measured signals at locations a, b, and c in (a). The scattered acoustic pressure is

shown for the empty ground, the object placed on the ground, and the cloaked object in each case..... 30

Figure 1. 12 (a) Acoustic cavity scheme with a 3D object (blue colored) and the metamaterial cloak (grey layers) realized by Weiwei Kan et al. (b) Directivity plots of the calculated radiation profile in the x-z plane. The colored lines represent the profiles obtained for the empty cavity (black), the cavity with a mushroom-like object (red), the cavity with the object and the perfect cloak (green), and the expected profile when the reduced cloak is considered (blue). Results are obtained for $\lambda = 13$ cm (2.68 kHz). (c)-(f) Calculated total pressure field (real part) obtained from finite-element simulations for the different configurations of the cavity at $\lambda = 13$ cm (2.68 kHz): (c) empty, (d) with the object inside (thick white lines), (e) with the object and the ideal cloak on top (red lines), and (f) with the object and the reduced cloak (red lines). 31

Figure 1. 13 Superresolution achieved by Lemoult et al. (a), (b) Normalized intensities of the diffraction-limited pressure spots without the soda cans. (c), (d) Measured $\lambda/25$ pressure foci with iterative time reversal technique. 34

Figure 1. 14 Hyperbolic metamaterial developed by Chen et al. (a) schematic of the metamaterial and experimental setup. The thickness of the metamaterial corresponds to $0.9\lambda - 1.4\lambda$. (b) Normalized pressure magnitude distribution on the exiting surface of the metamaterial. Blue (solid), measurement with AHMM; blue (dashed), measurement without AHMM; red, simulation (real structure); black, simulation (effective medium). (c) Predicted effective density along the x and y directions. (d) The dispersion curves of the metamaterial showing a hyperbolic profile, and the equifrequency contours becoming flat at low frequencies. Solid line: lumped model. Circle mark: retrieved from numerical simulations. (e) Broadband performance of subwavelength imaging of the metamaterial. 36

Figure 1. 15 Acoustic magnifying hyperlens realized by Jensen Li et al. (a) Experimental pressure measurements in the propagation region. The object consists of the two sound

sources transmitting at 6.6 kHz and separated by 0.23λ at the input plane. (b) Simulation of the pressure field using the microstructure with the elastic fins (c) 2D simulation using the effective medium description of the lens. (d) The magnified image at the outer edge of the lens showing a $\lambda/4.3$ resolution (red), while the control experiment shows a single peak (blue). (e) The broadband performance of the acoustic hyperlens. The frequency ranges from 4.2 kHz–7 kHz. 38

Figure 1. 16 Graded-index acoustic metamaterial waveguide developed by Yongyao Chen et al. (a) Schematic of the acousto-optic sensing system. (b) Simulated and (c) experimentally obtained pressure gain spectra at different locations of the metamaterial. The locations Z_1 , Z_2 , and Z_3 , correspond to gaps 30, 45, and 66. (d) Measured directivity patterns of the maximum pressure gain at different frequencies. (e) Measured SNR in the metamaterial compared with that of the free space. 41

Figure 1. 17 (a) Schematic of the near-zero-index acoustic antenna (NZI-AA) proposed by Chengrong Ma et al. (b) Directivity patterns with/without the NZI-AA. (c)-(e) Acoustic pressure fields in a NZI-AA system under normal ((c) and (e)) and oblique ((d) and (f)) incidence. (e) and (f) shows the same configuration in (c) and (d) but without the NZI-AA. (g) and (h) Impedance matching acoustic metamaterial layer realized by Zheng Li et al. (g) Schematic showing the steps of fabrication of the metamaterial matching layer. Each pyramidal unit cell is 125 μm in diameter and 610 μm in length. (h) Distribution of the acoustic impedance (blue curve) and the longitudinal velocity (red curve) along the thickness direction. 43

Figure 2. 1 Wave vector distribution of (a) elliptical and (b) hyperbolic high-k metamaterials. 54

Figure 2. 2 Construction of different types of high-k acoustic metamaterials and some associated functionalities. 56

Figure 2. 3 Typical design format of the anisotropic metamaterials investigated in this work.	59
Figure 2. 4 (a) Diagram of the Fabry-Perot microphone tip showing key components. (b) Scanning electron microscopy (SEM) photograph of the Fabry-Perot microphone tip.....	62
Figure 2. 4 Fiber optic microphone fabrication.	64
Figure 2. 5 Schematic of the characterization of the fiber optic acoustic probe using a B&K reference microphone.....	66
Figure 2. 6 Schematic of the directivity measurement of the fiber optic probe.....	67
Figure 2. 7 Characterization of the fiber optic microphone probe. The frequency response reveals good sensitivity of up to 40 kHz. The directivity plots (inserts) reveal its omnidirectional response across the tested range.	68
Figure 2. 8 Schematic of acoustic wave amplitude and phase measurements by using a reference microphone and fiber interferometer system.	69
Figure 2. 9 Flow diagram of the data processing to obtain the complex acoustic fields (amplitude and phase) at the position (x, z) for each frequency f.....	70
Figure 2. 11 2D acoustic metamaterial waveguide.	73
Figure 2. 12 Pressure and refractive index distribution along the metamaterial at 7.5 kHz, illustrating the wave compression effect.....	75
Figure 2. 13 Schematic of a double tapered metamaterial waveguide with three sections. It is comprised of an array of stainless plates spaced by air gaps with thickness $t=1.4$ mm and an array periodicity of $p=3.3$ mm. The uniform section (Section 2) is constructed with 100 plates of a constant width $w=20$ mm. Sections 1 and 3 are identical tapered structures, and the plate width w increases from 2 to 20 mm with a step of 0.5 mm. For simplicity, the metamaterial waveguide can be considered as a 2D system where the wave propagation is assumed to be confined in the x - z plane.	76

Figure 2. 14 (a) and (b) 1D pressure field mapping at an input sound frequency of 5.5 kHz and 12 kHz, respectively.....	78
Figure 2. 15 (a) and (b) 2D field mapping at 5.5 kHz and 12 kHz for the specific region highlighted in Figure 2. 14 (a) and (b) ($z=165$ mm to 225 mm), respectively. The dashed line represents the metamaterial/air interface.	79
Figure 2. 16 Schematic of waveguiding mechanisms. (a), top: conventional acoustic waveguide and (bottom) metamaterial waveguide based on the microscopic perspective. (b) Measured pressure (colored map) and particle velocity fields (arrows) in the metamaterial waveguide. The length and direction of arrows indicate the magnitude and directions of air particle velocity. The gray bars represent the waveguide structure. (c) An optical analogy of the guided wave obtained by using finite-difference time-domain (FDTD) simulations. To establish an equivalence, the optical waveguide was chosen to have the same effective refractive index of $n=1.3$ as the acoustic metamaterial waveguide working at 5.5 kHz. Also, the normalized excitation frequency of the optical waveguide was chosen to be equal to that of the acoustic metamaterial waveguide, i.e. $f_{optic} = f_{acoustic} = w/\lambda = 0.32$, where $w=20$ mm is the width of the acoustic waveguide, and $\lambda=62.5$ mm is the sound wavelength at 5.5 kHz. The optical wavelength $\lambda = 1550$ nm and optical waveguide width of 500 nm were chosen to obtain the same normalized frequency. The length of the optical slab waveguide is 3.58 mm.	82
Figure 2. 22 Stimuli induced frequency change in high-k metamaterial versus low-k media. The frequency change $\Delta\omega$ brings about a larger momentum change in the high-k metamaterial Δk_{MM} than in the low-k medium Δk_a	84
Figure 2. 18 (a) Normalized pressure amplitude as a function of wavevector at different input sound frequencies. (b) Experimentally obtained dispersion curve for the uniform waveguide section compared with that in air and that from FEM simulations.	86
Figure 2. 19 Schematic of wave compression and energy density enhancement.	88

Figure 3. 1 (a) Schematic of the low-profile on-chip acoustic metamaterials with active capabilities. (b) Schematic showing the mechanical wave amplification and spatial frequency separation property of the mammalian cochlear (left), and equivalent pressure amplification and spatial separation of frequencies exhibited by the conical metamaterial receiver (right). (c) and (d) Illustration of the passive characteristics and active properties of the planar low dimensional “on-chip” acoustic metamaterial, respectively.	94
Figure 3. 2 (a) Photo of passive and active on-chip metamaterials. The passive device consists of 30 plates separated by 2 mm air gaps while the active device consists of 18 plates separated by 4 mm gaps. The active device is designed in a surrounding container to hold liquid, with arms for sensor attachment. Isopropanol (dyed blue in the picture) is used to actively tune the exposed plate heights of the metamaterial. (b) CAD rendering of the conical receiver metamaterial. The microphone used is a Sisonic ultrasonic microphone (SPU0410LR5H-QB). (c) The thickness of the plates and air gaps are $t = 2$ mm and $g = 1.5$ mm, respectively. The device consists of 24 plates, with widths w ranging from 2 mm to 8.95 mm.	97
Figure 3. 3 (a) Schematic of the experimental setup and the sensing system. The fiber optic detection system consists of a superluminescent diode (SLD) light source, tunable filter, coupler, and a photodetector connected to a computer through a data acquisition (DAQ) card. (b) Picture of the B&K reference microphone and the fiber optic microphone. The B&K has a diameter of 7 mm, while the fiber optic microphone is 323 μm in diameter.	99
Figure 3. 4 (a) Simulation of the frequency response characteristics of the last gap of the planar passive acoustic metamaterial. The inserts are simulations of the mode shapes of the fundamental mode (18 kHz) and a higher-order mode (34 kHz). (b) Normalized dispersion curve of the last gap of the metamaterial from the simulation. Normalization is with respect to the free space wave vector.	101

Figure 3. 5 Experimental scans of the last gap of the metamaterial to show the mode shapes of the first two modes. (a) shows outward scans (y-direction) from the center, while (b) shows upward scans (z-direction) from the center.....	102
Figure 3. 6 Simulation (a) and (b) and experimentally obtained (c) and (d)) spatial mapping of the acoustic field of the metamaterial to an 18 kHz incident plane wave. The red dotted lines in (c) and (d) highlight the confining effect of the metamaterial due to the gradual change in refractive index across the space.....	104
Figure 3. 7 3D plots of the experimentally obtained spatial field mapping of the acoustic field along the vertical plane (a) and the horizontal plane (b).....	106
Figure 3. 8 (a) Simulated unit cell of an uncovered metamaterial structure. The plate is 1 mm thick, 5 mm tall, and 15 mm wide. The unit cell comprises of the pate and a 2 mm air gap (1 mm on each side), with an imposed repeated boundary condition to simulate infinite plates. The red arrows indicate the velocity profile of the air media. (b) A simulated unit cell of a covered metamaterial structure. The dimensions of the unit cell are similar to that in (a), except for the added 1 mm thick cover. The turquoise arrows indicate the velocity profile of the air media.....	108
Figure 3. 9 (a) Metamaterials of different heights used to demonstrate the use of the space above the metamaterial structure. Each metamaterial shown has a periodicity of 2 mm with a gap size of 1 mm. The heights of the metamaterial plates are as shown. (b) Experimental setup of the showing MM1 covered with an acrylic plate.	110
Figure 3. 10 (a) Frequency response of the uncovered metamaterials. (b) The frequency response of the covered metamaterials.	111
Figure 3. 11 (a) Time-domain comparison of an 18 kHz pulse with a bandwidth of 1 kHz through the metamaterial versus without the metamaterial. Normalization is with respect to the peak of the pulse without metamaterial. (b) Comparison of the FFT of the pulses in (a).	113

Figure 3. 12 (a) Time-domain comparison of a 20 kHz pulse with a bandwidth of 4 kHz through the metamaterial versus without the metamaterial showing the pulse broadening and filtering effect of the metamaterial. Normalization is with respect to the peak of the pulse without metamaterial. (b) Frequency domain comparison of the pulses in (a).....	115
Figure 3. 13 Frequency response gain plots of different gaps of the metamaterial. Pure tone pulses at 200 Hz intervals were used. The gaps A-D correspond to locations 0, 9, 27, and 36 mm from the last gap.	116
Figure 3. 14 Experimentally obtained gain plots at different plate heights. The insert depicts a schematic of the exposed plate height h.....	117
Figure 3. 15 Dispersion curves of the metamaterial at different plate heights and of air (grey dotted line) from the simulation.....	118
Figure 3. 16 (a)-(d) Comparison of an 18 kHz pulse with a bandwidth of 5.4 kHz (a) through the metamaterial at different plate heights. (b) indicates the reference output for a pulse propagating in the free-space (no metamaterial). The time pulse delays Δt_1 and Δt_2 are between the reference pulse (b) and the pulses through the metamaterial at 3.5 mm and 4.5 mm heights, respectively.	120
Figure 3. 17 Schematic of the biological cochlea uncoiled for simplicity.	122
Figure 3. 18 Analytically obtained normalized wave vector as a function of distance (a) and frequency (b) of the basilar membrane of the biological cochlea for three frequencies.	124
Figure 3. 19 Analytically obtained normalized displacement as a function of distance (a) and frequency (b) of the basilar membrane of the biological cochlea for three frequencies.	126
Figure 3. 20 Analytically obtained normalized wave vector as a function of distance (a) and frequency (b) in the metamaterial. Normalization is with respect to the free-space wave vector.	129
Figure 3. 21 Analytically obtained normalized on-axis pressure as a function of distance (a) and frequency (b) in the metamaterial.	131

Figure 3. 22 (a) Photo of the metamaterial cochlea, 3D printed model of a human cochlea, and a coin for comparison. The coin is 19 mm in diameter. (b) FEM spatial pressure maps showing the spatial confinement and pressure amplification of waves propagating into the metamaterial. The distinct frequencies are spatially mapped to distinct locations in the metamaterial structure, which is similar in functionality to biological cochleae systems. ...	133
Figure 3. 23 Experimental (a) and simulated (b) pressure gain of the metamaterial as a function of frequency at three locations.....	134
Figure 3. 24 Experimentally obtained pressure fields in the gaps of the metamaterial for three frequencies.	135
Figure 4. 1 Sound enhancement mechanism in small insects such as the cicada [121] (a) and the cricket (b) using acoustic resonators. (c) Equivalent strong confinement and intensification of acoustic fields in acoustic metamaterial cavities for the enhancement of directional emission of sound.	141
Figure 4. 2 Schematic of the acoustic metamaterial emitter. It comprises two regions: the metamaterial cavity and the tapered coupling region. The parameters shown are the disk thickness t , gap thickness g , periodicity p , and the diameter of the uniform disks d	143
Figure 4. 3 (Top) Normalized pressure amplitude for the different metamaterial cavities (bottom). Normalization is with respect to the peak pressure of the data.	145
Figure 4. 4 Sound source radiation in free-space and metamaterial structure. (a) Schematic of acoustic radiation of a spherical monopole source placed in air. (b) Radiation of a spherical source in a metamaterial cavity comprised of four disks 8 mm in diameter and 2 mm thick, separated by 1 mm gaps. S_1 and S_2 represent the near-field (on the source surface) and far-field regions, respectively.	147

Figure 4. 5 Normalized radiation reaction force in the metamaterial cavity depicted in Figure 4. 4 (b). Normalization is with respect to the radiation force Fr_{air} in free-space, calculated using $Fr_{MM}Fr_{air}$, where Fr_{MM} is the radiation reaction force in the metamaterial.	149
Figure 4. 6 (a) Radiation resistances of a monopole source in the metamaterial cavity as compared with the same source placed in the free space. (b) The acoustic radiation power enhancement in the metamaterial cavity. A finite element method (COMSOL Multiphysics 5.4) is used to analyze pressure and velocity fields generated by a sound source, which are used in equations 4.11 - 4.14 to calculate reaction force, radiation resistance, and radiation enhancement factors.....	151
Figure 4. 7 (a) Comparison between a conventional acoustic cavity and a metamaterial cavity for sound radiation enhancement. The radiation enhancement spectrum in the metamaterial cavity as compared with that of a conventional acoustic cavity comprised of a unit cell of the metamaterial cavity. (b) The dispersion plot of the metamaterial cavity comprised of four disks (blue) compared with the free-space dispersion (black dashed line) from the simulation. The blue shading in (a) and (b) indicate the working frequency region.	153
Figure 4. 8 Far-field emission gain of metamaterial emitter. (a) The total radiation and far-field radiation enhancement of the metamaterial cavity with viscous-thermal dissipation. (b) Radiation loss in the metamaterial emitter. (c) Schematic for describing the emission enhancement, which is defined as the ratio of far-field radiation power measured on the metamaterial emitter's beam axis (right) to the power produced by the sound source without using metamaterial structures (left).....	155
Figure 4. 9 (a) Normalized pressure as a function of frequency for different taper angles. Normalization is with respect to the maximum pressure for the 4-cavity data (grey dashed line). The taper angles correspond to adding increments of four 1 mm spaced disks. (b) Schematic illustrating the taper angle. (c) Simulation pictures depicting some taper angles and their respective lengths.	159

Figure 4. 10 Maximum normalized pressure as a function of the taper angle. Normalization is with respect to the maximum cavity-only pressure.	161
Figure 4. 11 (a) FEM photos depicting the pressure field distribution of the metamaterial emitter. (b) The change of mode field distribution of the guided mode propagating along the z-axis in the regions identified in (a). \varnothing_1 to \varnothing_3 indicate the diameters of the corresponding air gaps in regions z_1 to z_3	162
Figure 4. 12 Comparison of the directivities of the metamaterials comprising of the cavity and tapered coupling region and a cavity-only metamaterial.	164
Figure 4. 13 Normalized pressure (to peak pressure in data) as a function of frequency for different taper angles for a metamaterial taper only. The inserts are simulation pictures of the metamaterial taper angle profiles for 19° , 3.9° , and 1.8° , respectively.	165
Figure 4. 14 (a) Normalized (to maximum pressure data) far-field pressure as a function of frequency for different metamaterial gap thicknesses. (b) Simulation photos of the different gap sizes.	167
Figure 4. 15 Dispersion plots for metamaterial unit cells with different gap sizes from numerical simulations.	169
Figure 4. 16 (a) Normalized (to maximum pressure data) far-field pressure as a function of frequency for different emitter sizes. (b) Normalized gain plots for the emitter sizes. The gain is obtained as the ratio between the settings with and without the metamaterials. Normalization is with respect to maximum gain data.	171
Figure 4. 17 Normalized gain as a function of emitter size.	173
Figure 4. 18 Analytically obtained metamaterial dispersion plots (solid lines) as a function of temperature for different temperature values. The corresponding free space dispersion curves are also shown (dotted lines).	176
Figure 4. 19 Normalized far-field pressure plots for the metamaterial as a function of frequency for different ambient air temperatures.	177

Figure 4. 20 (a) Exploded CAD model of metamaterial emitter assembly. The ultrasonic speaker is a commercially available unit with a center frequency of 25 kHz. (b) Photograph of metamaterial emitter realized studied in this work. The Transducer holder features a pinhole 1.2 mm in diameter to serve as a point source.	179
Figure 4. 21 (a) Emission spectrum of the emitter with and without the metamaterial (blue and red respectively) measured from 100 cm away. (b) Experimentally obtained and simulated emission gain of the metamaterial emitter, which is the ratio of the on-axis pressure amplitude of the emitter with and without metamaterial. The simulated data were equally obtained from 100 cm away.	181
Figure 4. 22 (a) Normalized directivity of the metamaterial emitter and the reference from the simulation. (b) The effective aperture of the metamaterial emitter obtained from the tip of the device.	183
Figure 4. 23 Experimentally obtained contour plot of normalized emission amplitude as a function of frequency and azimuth for the case with the metamaterial (top) and without the metamaterial (bottom).	185
Figure 5. 1 Schematic of biological sonar systems in the bat (a) and the dolphin (b). (c) CAD model of the metamaterial sonar system comprised of an emitter and receiver pair of metamaterials. (d) Schematic of the metamaterial sonar robot tracking and following a target robot with a mounted target.	191
Figure 5. 2 Schematic of the sonar system for use in deriving the metamaterial sonar equation.	193
Figure 5. 3 (a) Photo of the metamaterial sonar system. The alignment laser is used as a visual reference of the metamaterial axis. (b) Photo of the sonar system without metamaterials. (c)-(f) Flow chart for obtaining the echo energy. (c) The entire waveform obtained from the receiver. The echo is cropped from the signal (d), and a Fourier transform is carried out on	

the signal to expose all its frequency components. (e) The energy is then calculated from a cropped frequency spectrum (f).	198
Figure 5. 4 (a) Schematic of the target size and distance experiments. (b) Echo energy as a function of distance for a target with and without metamaterials. The target was 89 mm in diameter and 1.5 m tall.....	200
Figure 5. 5 Normalized echo energy for different target sizes with and without metamaterials. The targets were 40 cm tall and were placed 55 cm away from the sonar setup.	202
Figure 5. 6 Power spectrum of the 400 mm, 164 mm and 114 mm targets with metamaterial (top row) and without metamaterial (bottom row).....	203
Figure 5. 7 Power spectrum of the 89 mm, 60.6 mm, and 33.5 mm targets with metamaterial (top row) and without metamaterial (bottom row).....	203
Figure 5. 8 Power spectrum of the 27 mm, 19.1 mm, and 15.8 mm targets with metamaterial (top row) and without metamaterial (bottom row).....	204
Figure 5. 9 Power spectrum of the 12.5 mm, 9.5 mm, and 6.35 mm targets with metamaterial (top row) and without metamaterial (bottom row).....	204
Figure 5. 10 Power spectrum of the 2.4 mm and 1.3 mm targets with metamaterial (top row) and without metamaterial (bottom row).....	205
Figure 5. 11 Time domain data for the echoes of different targets with metamaterial (blue) and without metamaterial (red). Targets from 400 mm to 15.8 mm are shown.....	207
Figure 5. 12 Time domain data for the echoes of different targets with metamaterial (blue) and without metamaterial (red). Targets from 12.5 mm to 1.3 mm are shown.....	208
Figure 5. 13 Schematic of the target separation experiments. (a) Two pipes measure 89 mm and 60 mm in diameter and 40 cm tall, respectively (b) Gap experiments using two boards placed to form a gap in front of the sonar system.	209

Figure 5. 14 Experimental results of the target separation detection using the sonar setup with the metamaterials (a) and without the metamaterials (b). Normalization is with respect to the maximum energy value from the metamaterial sonar system.....	211
Figure 5. 15 Experimental results of the gap separation detection using the sonar setup with the metamaterials (a) and without the metamaterials (b). Normalization is with respect to the maximum energy value from the metamaterial sonar system.....	213
Figure 5. 16 Photographs of the emitter equipped with the metamaterial (a) and without the metamaterial (b). (c) The frequency response of the metamaterial emitter measured by a reference microphone placed in the far-field. The pressure gain plot is defined as the ratio of the signal amplitude measured with the metamaterial to that measured without the metamaterial. (d) Emission directivity at 40 kHz. (e) and (f) show contour plot of the normalized emission amplitude as a function of frequency and azimuth for the case without the metamaterial (e) and with the metamaterial (f). Normalization is with respect to the peak azimuthal pressure for each frequency.....	215
Figure 5. 17 Photographs of the receiver (MEMS microphone) equipped with the metamaterial (a) and without the metamaterial (b). (c) The frequency response of the metamaterial receiver measured by the ultrasonic MEMS microphone. The bottom plot is the gain plot obtained by normalizing the plot with metamaterial with the data without metamaterial. (d) Reception directivity at 40 kHz. (e) and (f) show contour plots of the normalized reception amplitude as a function of frequency and azimuth for the case without the metamaterial (e) and with the metamaterial (f). Normalization is with respect to the peak azimuthal pressure for each frequency.....	217
Figure 5. 18 (a) Photograph of the 40 kHz metamaterial sonar. (b) and (c) show echo signals (time and frequency domains respectively) detected by the metamaterial sonar as compared with the conventional sonar system (without using metamaterials). (d) The detection range enchantment. (e) and (f) show the directivity patterns of the active echolocation of pipes with	

different sizes for the cases without metamaterials and with metamaterials, respectively. (g)	
and (h) Experimental results of the target separation detection using the 40 kHz sonar setup	
without the metamaterials (g) and with the metamaterials (h).....	219
Figure 5. 19 Photograph of the four-wheeled sonar tracking robotic platform with the	
metamaterials.	221
Figure 5. 20 (a) Schematic of the tracking method showing the relationship between the target	
and the two emitted clicks. (b) Schematic of the directional cues used for robot tracking. The	
intensity difference is used to infer the target's position.	222
Figure 5. 21 Schematic of the control scheme used for target localization, tracking, and	
following.	225
Figure 5. 22 Sonar tracking of a target moving in a straight line. The “Actual” results (red)	
are from the target robot, while the “Measured” results are from the sonar robot. (a) Tracking	
results for the metamaterial sonar. The insert in (a) is a schematic of the experimental setup.	
(b) Tracking results for the sonar without the metamaterials.	227
Figure 5. 23 (a) Photo of the metamaterial sonar-equipped robot tracking and following the	
target robot. (b) Results of the metamaterial equipped tracking robot tracking and following	
the target robot on a circular path.	228

List of Abbreviations

B&K	Brüel & Kjær
BM	Basilar Membrane
CAD	Computer-Aided Design
DAQ	Data Acquisition
DOS	Density of States
EMM	Elliptical Metamaterial
FFT	Fast Fourier Transform
FP	Fabry-Perot
HMM	Hyperbolic Metamaterial
MM	Metamaterial
SEM	Scanning Electron Micrograph
SFT	Spatial Fourier Transform
SLD	Super Luminescent Diode
SNR	Signal to Noise Ratio
WKB	Wentzel-Kramer-Brillouin

Chapter 1: Introduction and Background

1.1 Problem statement

In many areas of physics, the ability to control wave propagation has always been a fundamental interest. When acoustic waves propagate through a medium, the characteristics that the waves take on are entirely dependent on the properties of the medium. For instance, the speed of the wave, attenuation over the medium, the directivity of the wave, group and phase velocity relations, and frequency dispersion treatment, are all characteristics that a medium would attribute to propagating waves due to the medium's intrinsic properties. If these properties can be altered of some sort, then it would be possible to control the propagation characteristics of waves through the medium. Most materials that occur in nature, however, do not provide a lot of latitude for controlling acoustic waves because their properties remain essentially fixed over a broad range of useful frequencies.

In order to obtain more control of the wave propagation, artificial materials would have to be engineered. When they are done in such a way that their unit cells are dimensionally smaller than the wavelength of the waves propagating through them, then the entire structure can be described in terms of effective parameters and can be consequently regarded as a new medium or "material" for the propagation of the waves. These artificially engineered structures with subwavelength unit cells are

called metamaterials (the prefix “meta” indicating characteristics beyond or higher than ordinary materials), and they can manipulate acoustic waves in ways that are not readily possible with naturally occurring materials.

Many wave phenomena were previously deemed unattainable in the realm of acoustic waves in natural media. The concept of the generalized Snell’s law, for example, is a feature common in electromagnetic waves such as light. Due to the relatively large wavelengths of acoustic waves, the abrupt phase shifts required to apply Snell’s law is generally not possible in natural materials [1], [2]. Also, the concept of negative refractive index, which, in the case of light, causes it to bend on the same side of the normal is another phenomenon which is strange in the field of acoustics when dealing with naturally occurring materials. Because of this, the rich physics and functional devices such as near field superlenses that can result from this phenomenon are alien. Another even stranger phenomenon is the idea of negative density that causes the response to a force to be in opposition to the direction of the force, or zero density, which implies no impedance. A medium that has this kind of characteristic can allow for such useful functionalities as perfect transmission or absorption devices, and supercoupling [3]–[6].

Thanks to acoustic metamaterials, these phenomena, and many more, have become not only theoretically plausible but also practically realizable, so that novel devices based on them have been developed. The past decade has witnessed a great interest in this field which has led to innovative ways of achieving perfect focusing, imaging, collimation, extraordinary transmission, sound insulation, enhanced sensing, acoustic filters, enhanced acoustic levitation, etc. in the field of acoustics [7]–[35].

There is a special class of metamaterials that can sustain acoustic waves with wave vectors much larger than what is allowable in the free space. As a result, there would be extra momenta in the system provided by the additional waves contained in the medium, as illustrated in the dispersion schematic in Figure 1. 1.

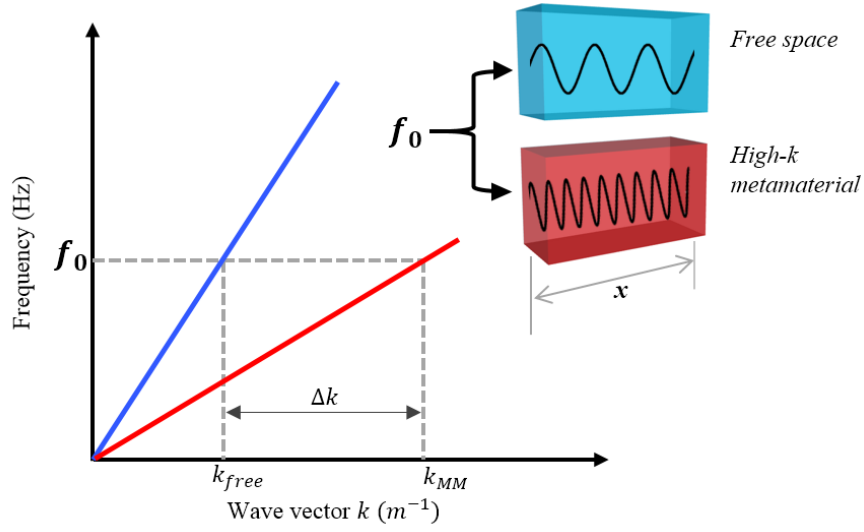


Figure 1. 1 Schematic of dispersion curves for the free space (blue) and a high-k metamaterial medium (red). High-k metamaterials can sustain more waves per unit length x than the free space at the same frequency.

Such metamaterials are known as called high wave vector (high- k) acoustic metamaterials, and they equip the propagating waves with unique and useful characteristics. For example, the extra momentum Δk (Figure 1. 1) can be used to achieve imaging beyond the diffraction limit, which is the property responsible for acoustic metamaterial superlenses and hyperlenses [31], [33], [34], [36]. Additionally,

a direct result of high- k metamaterials is that the speed of the wave through the metamaterial can be much slower than in the free space, giving a frequency-dependent refractive index that can be greater than one. This is a very useful property and is the key behind many functionalities that some metamaterials have, such as cloaking, sensing enhancement, and anomalous reflection [12], [13], [15], [27], [37]. The work presented in this doctoral dissertation focuses on these types of acoustic metamaterials.

This dissertation work aims at investigating the fundamental properties of high wave vector acoustic metamaterials and their applications. It would involve realizing new metamaterials and novel tools and methods to study them in order to unveil their unique high- k properties, as well as demonstrating applications in which they can be used. Particularly, it focusses on the interaction of airborne acoustic waves with high- k acoustic metamaterials.

1.2 Background and Literature review

1.2.1 Acoustic wave propagation in material media

Acoustic waves are mechanical, longitudinal, scalar waves, and so they require material media for their propagation. The medium must have an inertial property and a compressibility property so that acoustic energy propagates in the form of waves of compression and rarefaction. The physics behind acoustic wave propagation is well understood and can be described using three physical relations: the continuity

equation, which is a statement of conservation of mass; Newton's law for the conservation of momentum; and the ideal gas law, which is the equation of state. In elastic media, the acoustic wave equation can be written as

$$\nabla^2 P - \frac{\rho}{B} \frac{\partial^2 P}{\partial t^2} = 0$$

Here, P is pressure, ρ is the mass density, and B is the adiabatic bulk modulus. The mass density ρ and the bulk modulus B are constitutive parameters which are specific to the medium and define the speed of the wave through it by the Newton-Laplace relation $c = \sqrt{B/\rho}$. In naturally occurring media, these parameters are essentially constant across the acoustic spectrum, resulting in a constant behavior of acoustic waves propagating through them. For example, for air at room temperature and pressure, the density $\rho_{air} = 1.1839 \text{ kg/m}^3$ and the adiabatic bulk modulus $B_{air} = 141.838 \text{ kPa}$, giving $c_{air} = 346.13 \text{ m/s}$. It is noteworthy that the constitutive parameters B can be mapped to μ^{-1} and ρ to ϵ , where μ and ϵ represent the magnetic permeability and the dielectric constant for electromagnetic waves respectively. As a result, much underlying physics is shared between these two types of waves.

1.2.2 Acoustic wave propagation in metamaterials

Like naturally occurring materials, acoustic wave treatment by metamaterials is also valid for waves governed by Newton's law of motion, the thermodynamic state equation for adiabatic processes, and the continuity equation. However, unlike their natural counterparts, the constitutive physical parameters ρ and B in acoustic

metamaterials can assume unusual values from an effective viewpoint. As such, wave propagation through such structures inherits a dispersive phenomenon, where the speed is frequency-dependent across the acoustic spectrum. This is the key to the exotic characteristics that acoustic metamaterials can have.

There are many ways of realizing an artificial structure with subwavelength unit cells such that the effective bulk modulus or density assumes a dispersive phenomenon. A good example to illustrate this idea can be seen in a composite comprising of two materials that allow relative motion between the two materials, as illustrated in Figure 1. 2.

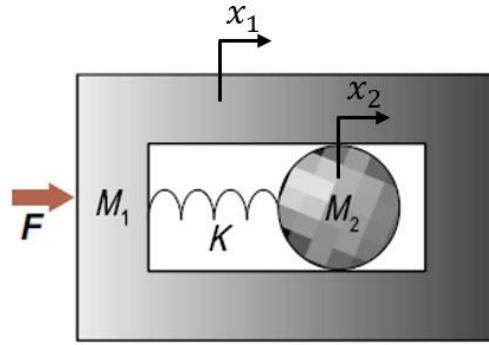


Figure 1. 2 Schematic of a coupled mass-in-mass oscillator.

Expressing the force in terms of the displacement x_1 yields

$$F = \left(M_1 + \frac{K}{(\omega_0^2 - \omega^2)} \right) \ddot{x}_1$$

Where $\omega_0 = \sqrt{K/M_2}$ is the resonant frequency of the internal system comprising of M_2 and K . As such the apparent inertia of the system is $M(\omega) = M_1 + \frac{K}{(\omega_0^2 - \omega^2)}$,

which is markedly different from a rigid material [11]. With the effective mass component having a frequency dependence, the effective density thus becomes a function of the excitation frequency, giving rise to a dispersive response.

Metamaterials that are based on this type of design can exhibit a phenomenon known as antiresonance, which tends to occur between the resonances of both mass-spring systems. When this occurs, both modes will be excited but with opposite phases, effectively canceling out the displacement.

The above is an example of realizing a metamaterial where the effective mass is responsible for the dispersive property. In what follows, a review of different classes of metamaterials is carried out. This would be followed by a discussion on some key functionalities exhibited by some acoustic metamaterials.

1.2.3 Metamaterial classification

Acoustic metamaterials can be classified in several ways. In this subsection, the classification will be based on the basic principles underlying their design and functionality. These basic principles usually result in special properties that the metamaterials in the said class enjoy. Three classes will be discussed: Helmholtz resonator-based metamaterials, membrane-type metamaterials, and space coiling metamaterials, along with their associated properties and examples. It should be noted

that some metamaterials may fall in more than one class, as well as may exhibit non-characteristic properties.

1.2.3.1 Helmholtz resonator-based metamaterials

Helmholtz resonators, which are the acoustic equivalents of electric LC resonators, make a good choice for designing metamaterial unit cells because the resonant wavelength of a Helmholtz cavity can be much larger than the size of the cavity. In these types of metamaterials, compressional and extensional motion is involved rather than a displacement of the center of mass. Therefore, the effective bulk modulus is the constitutive parameter responsible for the dispersive property of such metamaterials. A wide variety of novel properties and functionalities can be achieved using Helmholtz resonators as unit cells for the metamaterials because of the strong and well-established dependence of the local resonance characteristic on this resonant structure's geometric properties.

One such functionality is pressure enhancement by trapping them in the resonator. If judiciously designed, such a metamaterial could be broadband by having several unit cell structures tuned for specific frequencies, hence creating a passive spectral acoustic filter. This phenomenon is often referred to as acoustic rainbow trapping, and the effect is the creation of a space where frequency components of a wave are separated and trapped across the structure. Zhao et al. realized a compact acoustic rainbow trapping metamaterial comprising of Helmholtz resonators [38]. Their metamaterial consisted of 40 Helmholtz resonators of varying sizes (heights) linked by a tube through which sound waves enter the device. By coiling up their

structure in an Archimedean spiral manner reminiscent of a cochlea, they overcame the space penalty generally experienced by these types of metamaterials due to their bulky size; they report a 70 times reduction in size compared to other designs with the same bandwidth (Figure 1. 3 (a)-(c)).

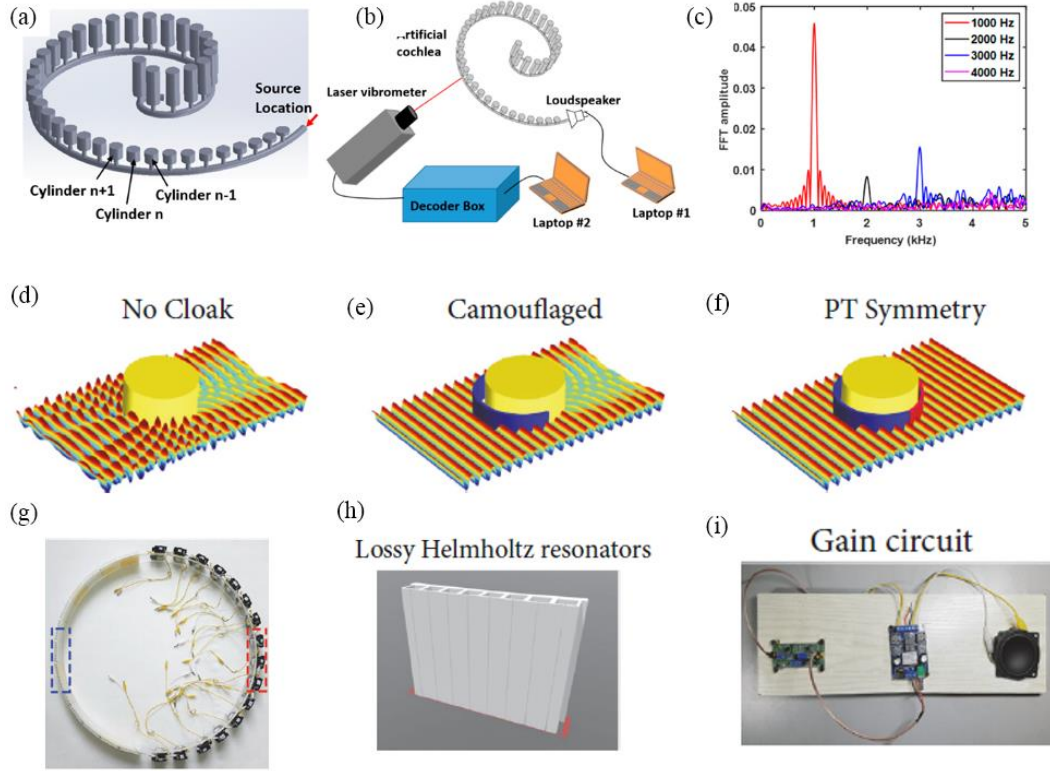


Figure 1. 3 (a) Schematic of the rainbow trapping metamaterial by Zhao et al. (b) Experimental setup. A loudspeaker is connected to the opening of the spiral tube to generate acoustic waves. Measurement is done using a point laser Doppler vibrometer at different locations. (c) Fourier transform of the particle velocity temporal plot of the 7th cylinder. (d)-(i) A cylindrical space covered by the parity-time symmetric metasurface realized by Hao-xiang Li et al. (d) no cloak- strong backscattering and a shadow is observed. (e) camouflaging through complete absorption with a lossy semicircle metasurface only (f) cloaking via PT symmetry semicircle metasurface containing acoustic loss (gain) to fully absorb incoming (reemit outgoing) sound waves. (g)-(i) Experimental realization of the PT symmetric metasurface cloak made from two jointed semi shells (radius $a = 40$ cm).

Helmholtz resonators can be employed in a metamaterial design to absorb incoming waves. If these absorbed waves can be re-radiated at another end in a manner consistent in amplitude and phase with the uninterrupted wavefronts, then cloaking can be achieved. This method was implemented by Hao-xiang Li et al. [39], where an array of Helmholtz resonators was employed to fully absorb the incoming sound waves as well as an array of speakers to reemit the outgoing sound waves. A Parity-time (PT) symmetric system was used to match the two systems for a seamless flow. In theory, this type of acoustic metasurface can be limitless in terms of working frequency, shape, or size. This method must consider the phase disparity that would emerge due to the shape of the cloaking surface. In their work, Hao-xiang et al. accounted for this by tuning the resonances of the Helmholtz resonators to have an angular dependence on their neck and depth. They demonstrated their apparatus to be capable of cloaking an object the size of a human from audible sound (Figure 1. 3 (d)-(i)).

In addition to their passive characteristics, Helmholtz resonator-based acoustic metamaterials can be constructed to have increased, modifiable capabilities by equipping them with active, reconfigurable properties. Bogdan *et al.* [40] reported an active acoustic metamaterial that is reconfigurable in real-time. Each of the ten unit cells of their device consists of an electronically controlled piezoelectric membrane mounted between two identical Helmholtz cavities. The three-terminal membranes serve both sensing and driving purposes, whereby incoming sound waves are detected, sent to a reconfigurable electronic control system for modification, and finally driven to emit the configured output (Figure 1. 4 (a)-(e)).

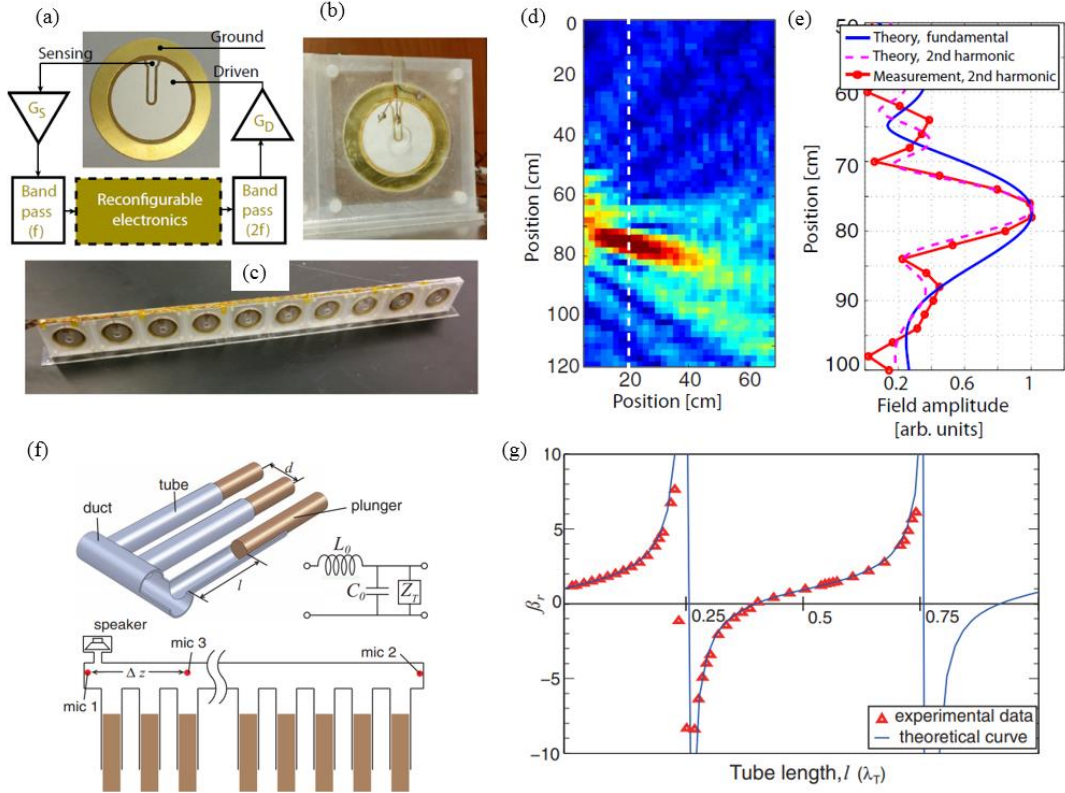


Figure 1. 4 (a) schematic and (b) photograph of a unit cell of the reconfigurable acoustic metamaterial realized by Bogdan-Ioan et al. (c) Metamaterial slab consisting of 10 cells. (d) Experimental results showing the lens' second harmonic response. (e) Comparison between the fields measured on the focal plane and an ideal lens imaging at the second harmonic (dotted curve) and the fundamental (solid curve). (f) Acoustic metamaterial with continuously tunable compressibility realized by Lee et al. (g) Theoretical plots and the experimental data for the effective compressibility β_r of the duct as a function of the tube length l .

Another resonant-type tunable metamaterial has been realized by Lee et al. [41], which consists of side tubes with plungers connected to the wall of the main duct (Figure 1. 4 (f) and (g)). This model solves the issues that plague traditional Helmholtz-type metamaterials due to the inherent narrow-band characteristic of

Helmholtz resonators. By operating the plungers through pushing them in and pulling them out, they were able to alter the effective compressibility of the air in the cavity hence changing the local resonances of the tubes.

1.2.3.2 Membrane-type acoustic metamaterials

A class of acoustic metamaterials called membrane-type acoustic metamaterials exist, which makes use of thin pre-stressed membranes with one or more small masses attached to the membrane material. The prestress applied on the membrane acts as the spring (restoring) force, while the mass can be chosen to set the desired resonant frequencies. Often called decorated membrane resonators (DMRs), these metamaterials can display dispersive properties due to both bulk modulus and mass densities. Bipolar symmetry in the frequency domain is typically a characteristic of these types of metamaterials due to the membrane's small thickness, usually in the low-frequency regime. As noted earlier, this can result in an antiresonance phenomenon when the excitation frequency falls between the two resonant peaks. The effective density in DMRs can vary widely, ranging from positive, near-zero, and negative values, and result in many desirable phenomena. A near-zero value indicates that the effective acoustic impedance of the arrangement can be matched to air's impedance, enabling optimal coupling of incident sound. This has been used to achieve a phenomenon known as supercoupling, wherein almost all the sound is transmitted through small channels under normal incidence [3], [17]. On the other hand, a negative effective density can occur, implying that the system's acceleration is in opposition to the external force.

It is noteworthy that the bipolar symmetry in DMRs exists in the low-frequency regime because the high-frequency components would couple into the vibrations in the membrane along its thickness. These high-frequency components, however, tend to be monopolar in nature, producing anomalous effects on the effective wave vector at these high frequencies. One idea to mitigate this phenomenon is to couple two membranes together. This was studied by Yang et al. using the metamaterial in Figure 1. 5 (a)-(e) where their DMR placed the monopole mode near the dipolar antiresonance. A near-zero effective density, B_{eff} , was attainable giving a characteristic impedance $Z = \sqrt{\rho_{eff} B_{eff}}$ that can match that of air while having large values for the effective density ρ_{eff} . They were also able to achieve a negative refractive index over a finite frequency range, as well as sustain wave vectors much larger than allowable in free space. The latter is a particularly useful feature that can be used to achieve such phenomena as focusing beyond the diffraction limit.

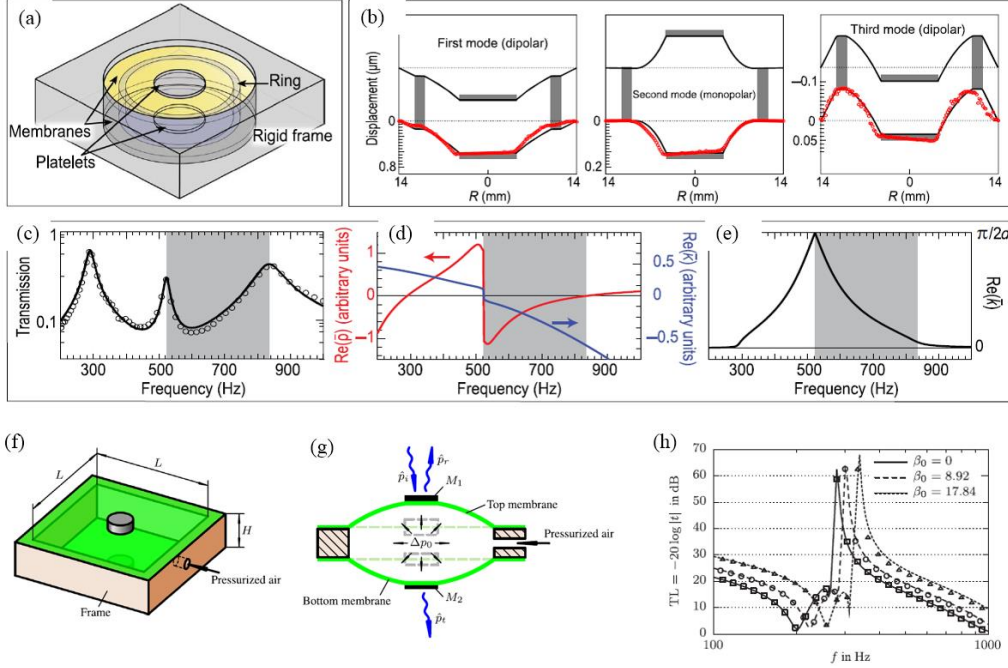


Figure 1. 5 (a) Schematic of a DMR with two coupled membranes realized by Yang et al. The rigid ring allows for extra tunability. (b) Displacement profiles of three low-frequency eigenmodes. The solid black lines show results from finite element simulations, while the red dots indicate the measured profiles using the laser vibrometer. (c) Transmission coefficient as a function of frequency. (d) Effective mass density (red) and bulk modulus (blue) plotted as a function of frequency. (e) The real part of the effective wave vector as a function of frequency. (f) A unit cell of the double membrane-type active acoustic metamaterial proposed by Langfeldt et al. (g) Isometric view of the unit cell illustrating the working principle. Introducing pressurized air into the cavity causes the membranes to stretch, increasing the eigenfrequencies of the system. (h) Experimental and theoretical STL for the membrane-type acoustic metamaterial at three inflation pressure differences β .

The narrow, low-frequency band characteristic of membrane-type acoustic metamaterials can be tuned by altering such parameters as the membrane pre-stress

and the size of the attached mass. Langfeldt et al. further achieved more tunability by pressurizing an air cavity in their proposed unit cell structure comprised of two masses attached to membranes that formed an enclosed cavity on a frame [42]. By altering the static air pressure in the unit cell cavity, the eigenmodes and transmission property are changed, shifting the sound transmission loss (STL) curve to accommodate higher frequencies (with increased pressure), as shown in Figure 1. 5 (f)-(h).

Another type of tunable membrane-type acoustic metamaterial was reported by Xiang Yu *et al.* [43] It comprised of an array of resonators attached to the sidewall of a rigid duct. Each resonator was constructed using a pre-stretched dielectric elastomer (DE) membrane whose thickness was configurable by the application of a voltage across electrodes coated on both sides of the membrane. An array of four resonators with different pre-stretched ratios increased the bandwidth of their structure (Figure 1. 6 (a), (b)).

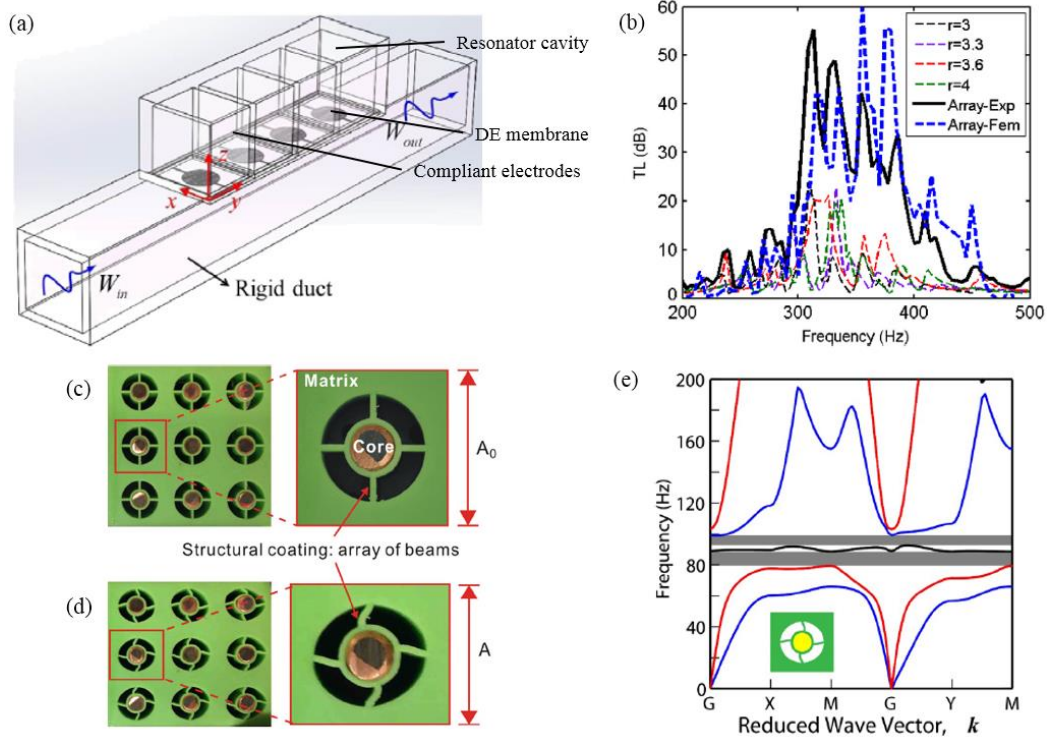


Figure 1. 6 (a) Schematic of the tunable acoustic metamaterial realized by Xiang Yu, comprising an array of DE resonators being attached to a duct. (b) Connecting four DE resonators to form a metamaterial array for realizing a much-broadened attenuation band. (c) Tunable acoustic metamaterial proposed by Wang et al. Each resonator consists of a metallic mass connected to the matrix through elastic beams. (c) The undeformed configuration. (d) Metamaterial with a compressive strain applied in the vertical direction. (e) Dispersion relations from Bloch-wave analysis for the infinite metamaterial under compressive strain. Shear dominated bands are colored in blue, pressure dominated bands in red and locally rotational bands in black. The grey region highlights the bandgap induced by local resonance.

The main idea around membrane-type metamaterials is to have a mass suspended in a matrix by spring-like elements. As noted earlier, the pre-stretched

membrane acts as the restoring spring force, while the mass is the inertial element. This idea can be modified to replace the membrane with easy-to-buckle elastic beams suspending the mass. In such a structure, applying a compressive force will cause the beams to buckle, changing the configuration of the array, and thus altering its acoustic properties. This idea was investigated by Wang et al., where they realized an adaptive acoustic metamaterial whose transmission properties could be adjusted by mechanical deformation [44]. In their structure, each unit cell comprises a mass suspended with four flexible beams (Figure 1. 6 (c)-(e)). When a compressive strain is applied to the structure, the beams deform, changing its resonant frequency. Additionally, this structure could be configured to completely switch off the transmission of sound with an applied strain.

1.2.3.3 Space-coiling acoustic metamaterials and metasurfaces

An advantageous characteristic that acoustic waves have over their electromagnetic counterparts is that they do not suffer from a cut-off frequency restriction. Generally, waveguides for electromagnetic waves would only propagate signals above a certain frequency known as the cut-off frequency which is given by $f_c = c/2a$, where c is the speed of the wave, and a is the internal waveguide dimension [45]. Because acoustic waves are longitudinal, they need not adhere to this physical constraint – a feat that can be further exploited by acoustic metamaterials. The idea in this design is to “coil up the space,” forcing the waves to propagate through passages that are longer than their physical dimension in the free space. If judiciously designed, it could induce large phase delays in the transmitted or reflected acoustic waves when

compared to the background waves. The induced delay $\Delta\Phi$ is related to the total acoustic path L by $\Delta\Phi = k_0 L$ where k_0 is the free-space wave vector [11]. It suffices, therefore, to adjust the total length of the passage to obtain any arbitrary phase values, and thus phase and group velocities of the acoustic waves. This simple but effective concept has been thoroughly exploited in the field in recent years due to their rich physics, and many novel effects such as negative refraction and near-zero index cloaking, and functionalities such as one-way transmission, focusing, etc. have been realized.

Because of its inherent nature, the space-coiling idea is a prime candidate for designing acoustic metasurfaces, which are low-profile metamaterials with subwavelength thickness capable of generating abrupt phase shifts across a single layer. This makes it possible for the generalized Snell's law to be applicable in acoustics since natural materials are generally incapable of providing the magnitude of phase shifts required for its application. Yong Li et al. showed that it is possible to apply the generalized Snell's law for acoustic reflected waves through ultrathin planar acoustic metamaterials [1] (Figure 1. 7). Their space-coiling metasurface was made up of eight units with phase shifts ranging from $0 \sim 2\pi$ in $\pi/4$ steps. Their device possessed anomalous reflection characteristics and could convert propagating waves into surface waves, produce a planar aberration-free lens, and form a non-diffracting Bessel beam.

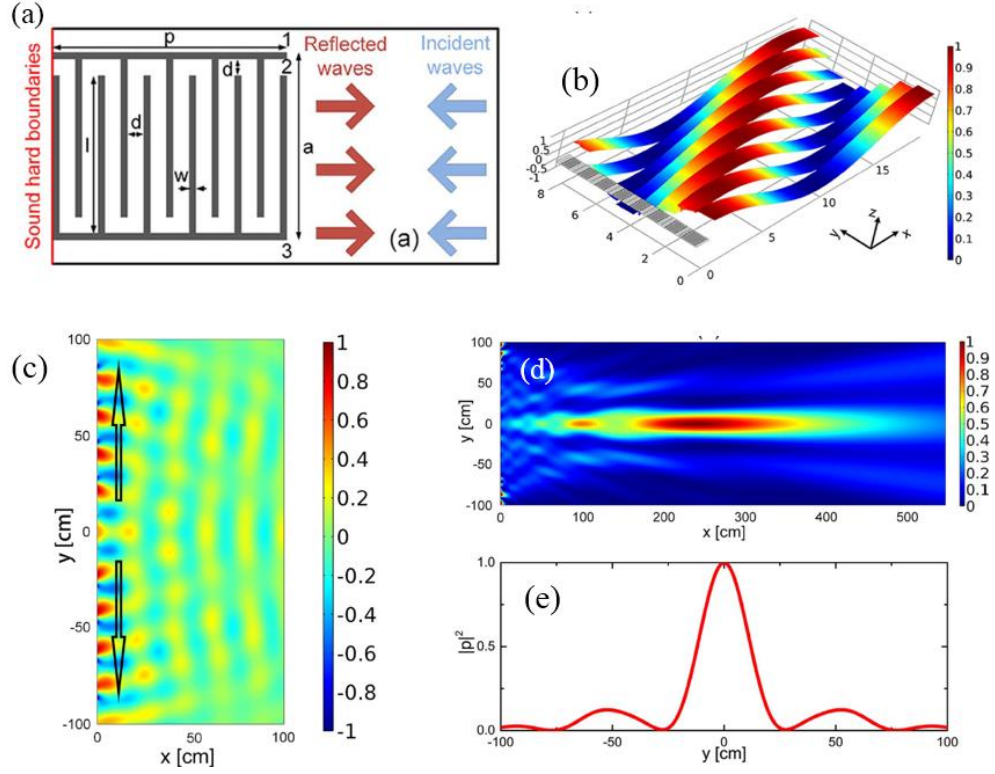


Figure 1. 7 (a) The schematic diagram of an acoustic metasurface for the generalized Snell's law realized by Yong Li *et al.* It was made of two stiff corrugated beams with a channel coiling up the space. (b) The pressure strips of the reflected waves by the eight units. The phase shifts resulting from the corrugation lengths are evident. (c) Pressure field pattern showing the metasurface converting propagating waves to surface waves. (d) Spatial distribution and (e) transverse cross-section of the intensity profile of the acoustic axicon for the non-diffracting Bessel beam.

The extra momentum Δk provided by the phase shift can cause the incident waves to undergo abnormal reflection or transmission. Yangbo Xie *et al.* realized a transmission-type acoustic metasurface with tapered labyrinthine unit cells that was capable of deviating from the generalized Snell's law. To accomplish that, their

metasurface introduced abrupt phase variations to the propagating waves, which deviates from the assumption in the generalized law that the accumulated phases are continuous across the interface. Their metasurface was also capable of extraordinary beam steering, negative effective refraction, and higher-order diffraction [46]. At a certain critical angle of incidence, the waves acquire an imaginary wave vector component and become evanescent. As a result, the metasurface was capable of sustaining waves with wave vectors higher than the free-space propagating waves, while converting propagating waves into surface waves. By combining metamaterial units consisting of coiled up pathways that produce different phase changes, frequency-dependent transmission characteristics were realized (Figure 1. 8).

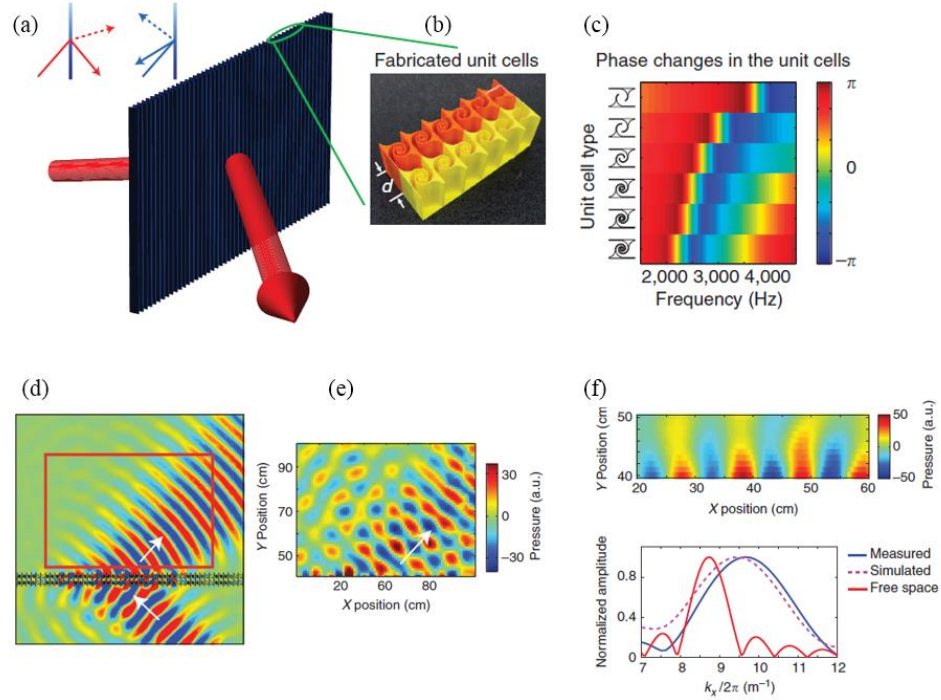


Figure 1. 8 (a) Schematic concept of wavefront modulating thin planar metasurface (solid line) and the generalized Snell's law (dashed line). (b) Photograph of the unit cell prototypes. (c) Six types of unit cells and the corresponding phase changes through the unit cells. (d) Simulations and (e) experimental results of field patterns at 45 degrees, demonstrating the negatively refracted transmission. The white arrows indicate the forward phase propagation directions. (f) Top: Measured near-field of the evanescent mode on the transmitted side at 25 degrees incidence. Bottom: Simulated and experimental results of the pressure field spatial Fourier transform across the surface.

An interesting application that space-coiling metamaterials can take advantage of is focusing. Careful placement of space-coiled pathways of different lengths can bring about interferences in the transmitted or reflected wavefronts. If prudently designed, focusing can be achieved. Boyang Xie et al. reported an acoustic

metasurface made up of interchangeable subunits that can be “coded” to achieve various transmitted beam patterns and branching wave effects [47]. Rather than having a set of unit cells corresponding to different phases, their elemental units constitute two types: “0” and “1”, corresponding to “off” and “on” states, respectively. These states represent the relative phases between their inlets and exits, where “0” represents a relative phase of π , while “1” represents a “0” relative phase. The phases are based on the local resonant modes of their cavities. With careful placement of the “0” and “1” unit cells, the transmitted waves would interact in constructive and destructive patterns that produced interesting pressure fields. One such field was a Fresnel lens-like zone effect, which produced a focused acoustic spot with a focal length of 50 cm. Interestingly their Fresnel lens metasurface was wider in frequency bandwidth compared to conventional Fresnel lens metasurfaces, which generally operate at a single frequency. (Figure 1. 9 (a)-(e)).

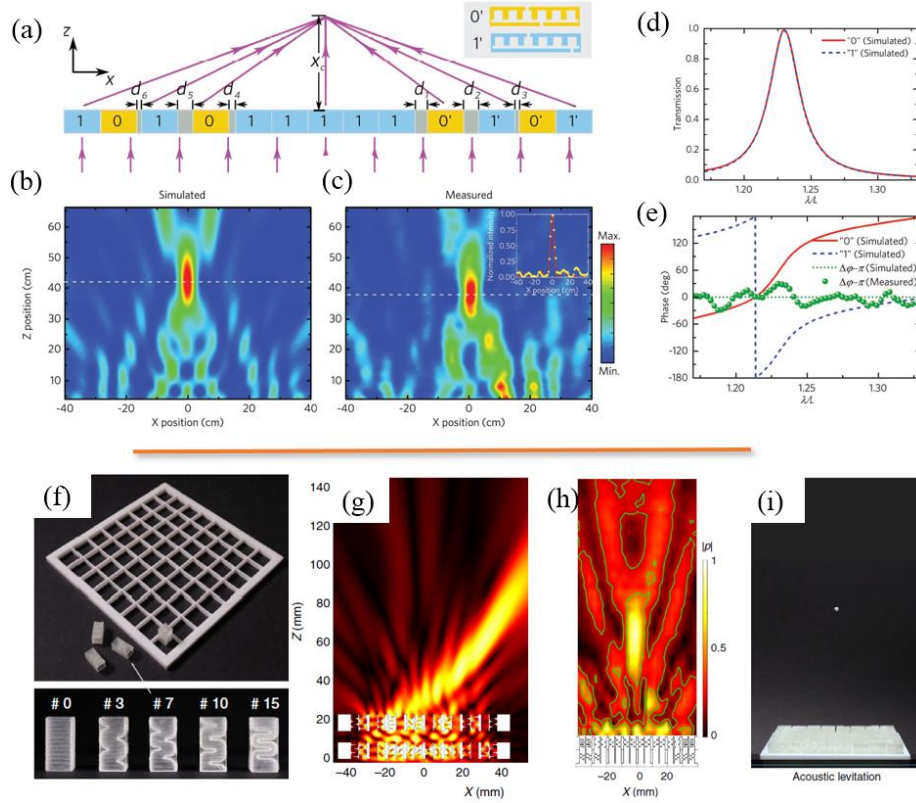


Figure 1. 9 (a) Acoustic metasurface arrangement for a flat Fresnel lens by Boyang Xie et al. (b) and (c) shows the experimental intensity profile achieved at 4.53 kHz by the setup elemental arrangement in (a). (d) Transmission amplitude and (e) phase of the waves through elements “0” and “1”. (f) Quantized metamaterial bricks and grid setup reported by Gianluca et al. (g) Beam steering and focusing with the metasurface. (h) Experimentally obtained pressure field distribution and (i) acoustic levitation of a polystyrene bead using the pressure field distribution in (h).

Another example of beam focusing and steering by acoustic metasurfaces was studied by Gianluca Memoli et al., where quantized metamaterial “bricks” were organized to form a surface that can generate a diffraction-limited acoustic field [20]. The bricks are designed in a transmission style configuration where phase changes are achieved by coiling up the propagation path, of which they were able to perform

focusing and steering. They were also able to generate a tractor beam by stacking a second layer of bricks to create a situation where a central layer is driven out of phase with the outer regions. This generated a “bottle-shaped” trap that could be used to levitate a small object, as shown in Figure 1. 9 (f)-(i). Although the bricks were designed to operate at 40 kHz, they could theoretically work at lower frequencies since the phase delay depends on the ratio between the effective path lengths in the bricks and the wavelength of the incident wave.

Holographic techniques have also been applied in the field of acoustics, where essentially 2-dimensional surfaces produce 3-dimensional images. Such techniques are greatly facilitated using metamaterials due to their ability to spatially control the amplitudes and phase components of traveling waves. One such example was published by Yangbo Xie et al. [48], in furtherance of their work on acoustic metasurfaces based on labyrinthine metamaterials. Here, they used the phase variations of the metamaterial unit cells, which constitutes of tapered labyrinthine structures, to produce an acoustic hologram. Another notable example of this was realized by Kai Melde et al. [49], where monolithic holograms, which are the acoustic analogs of optical kinoforms, are used to reconstruct diffraction-limited pressure fields. By placing the hologram in the path of an ultrasonic wave, a 2D phase profile is generated, which allows for the creation of 3D sound fields with diffraction-limited resolution (Figure 1. 10). They also demonstrated the manipulation of small objects (PDMS microparticles) using the phase gradient formed by the metasurface hologram. Additionally, using the hologram as a reflection-type metasurface, they

were able to perform acoustic levitation on two water droplets (Figure 1. 10 (f) and (g)).

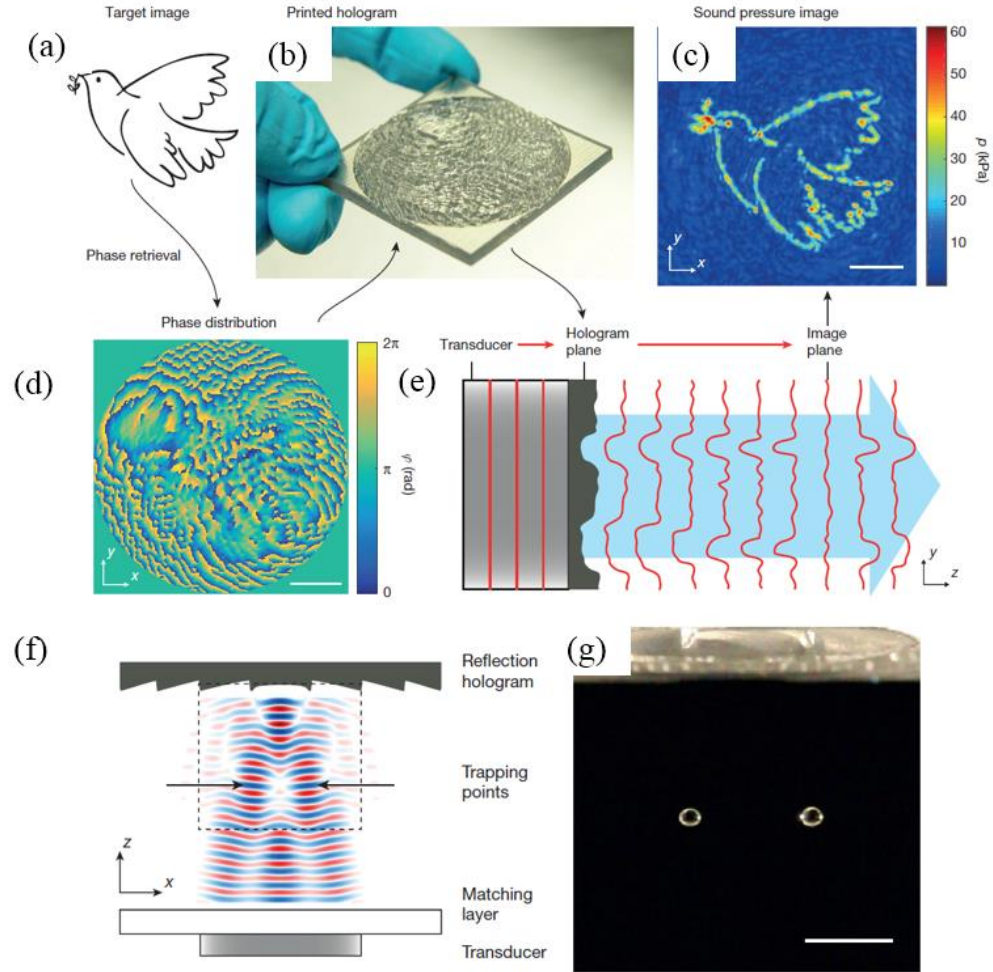


Figure 1. 10 Acoustic hologram realized by Kai Melde et al. (a)-(e) Methodology steps for the acoustic hologram formation. The propagation medium used is water, and the acoustic hologram is formed in water. 2.06 MHz ultrasonic waves are used, and a hydrophone is used to obtain the pressure image in (e). (f) Schematic of the pressure field profile used for acoustic levitation. (g) Photograph of two water droplets levitated in the pressure field traps in (f). A 100 kHz transducer was used. The scale bar represents 5 mm.

1.2.4 Metamaterial techniques and functionalities

There are a variety of techniques and functionalities that some acoustic metamaterials have been designed to exhibit that merit special attention. Many of these techniques can trace their origin from electromagnetic metamaterials, wherever a matching can be made between both kinds of waves. Some, on the other hand, take advantage of some unique properties possessed by acoustic waves that are not shared with their electromagnetic counterparts. In this subsection, a review will be made on three techniques: transformation acoustics, superresolution, and sensing enhancement, as well as a few examples from the literature.

1.2.4.1 Transformation acoustics and cloaking

In the study of electromagnetic waves, a technique was recently developed which established a correspondence between the material constitutive parameters and coordinate transformations. This technique is known as transformation optics and has been particularly useful in enabling the design of optical components that can control electromagnetic waves with unprecedented degrees of freedom, educing such functionality as invisibility cloaking. This transformation optics technique works due to the invariance of Maxwell's equations under coordinate transformations – a property that is not applicable in most wave equation systems [30], [50]. It turns out, however, that the acoustic wave equation is also invariant under coordinate transformations; thus, similar methods can be borrowed from the study of transformation optics in electromagnetics. Because of this, wave manipulation

reduces to a geometric problem of finding the proper coordinate transformation. If one considers the harmonic acoustic equation

$$\nabla \cdot [\vec{\rho}(\mathbf{x})^{-1} \nabla P(\mathbf{x})] = - \left[\frac{\omega^2}{B(\mathbf{x})} \right] P(\mathbf{x})$$

where $\vec{\rho}(\mathbf{x})$ is the mass density tensor, then under a coordinate transformation, each point \mathbf{x} is mapped to a corresponding point $\mathbf{x}'(\mathbf{x})$, so that the harmonic equation takes the form

$$\nabla' \cdot [\vec{\rho}'(\mathbf{x}')^{-1} \nabla' P(\mathbf{x}')] = - \left[\frac{\omega^2}{\overline{B}'(\mathbf{x}')} \right] P(\mathbf{x}')$$

Here, the transformed constitutive are $\overline{B}'(\mathbf{x}') = [\det J] B(\mathbf{x})$ and $\vec{\rho}'(\mathbf{x}') = J[\vec{\rho}(\mathbf{x})]J^T / \det J$ where J is the Jacobian matrix of the coordinate transformation. These would be the properties of the transformed acoustic media and are theoretically limitless in the values they can assume. It is discernible from these equations, however, that the new constitutive parameters transformed media are frequency dispersive, and so the transformation sustains a strong frequency dependence. A broader bandwidth transformed media would generally come with a sacrifice of a decrease in the performance.

The idea of acoustic cloaking is to achieve an acoustic concealing of objects in a fluid medium by bending impinged acoustic waves around the object such that the medium behaves as though the object is absent. Therefore, if within the vicinity of an object, the parameters are designed to cause traveling acoustic waves to interact

with the object in a manner that avoids scattering, an acoustic cloak is formed. A well-known example is the broadband omnidirectional ground cloaking metamaterial developed by Zigoneanu et al., which renders a region of space three wavelengths in diameter invisible to sound [51]. Their metamaterial was set up as a reflective type cloak, so that reflected waves behaved as though the cloaked space was absent. Their approach employs a unidirectional coordinate transformation technique applied to each section of the square pyramidal space to be cloaked. Their pyramidal acoustic metamaterial cloak was designed to have an effective bulk modulus 2.5 times higher than that of air, effectively creating a low refractive index medium for tailoring sound waves. This arrangement caused any object placed in the pyramid to become virtually invisible to sound waves from 3 kHz up to 6 kHz (Figure 1. 11).

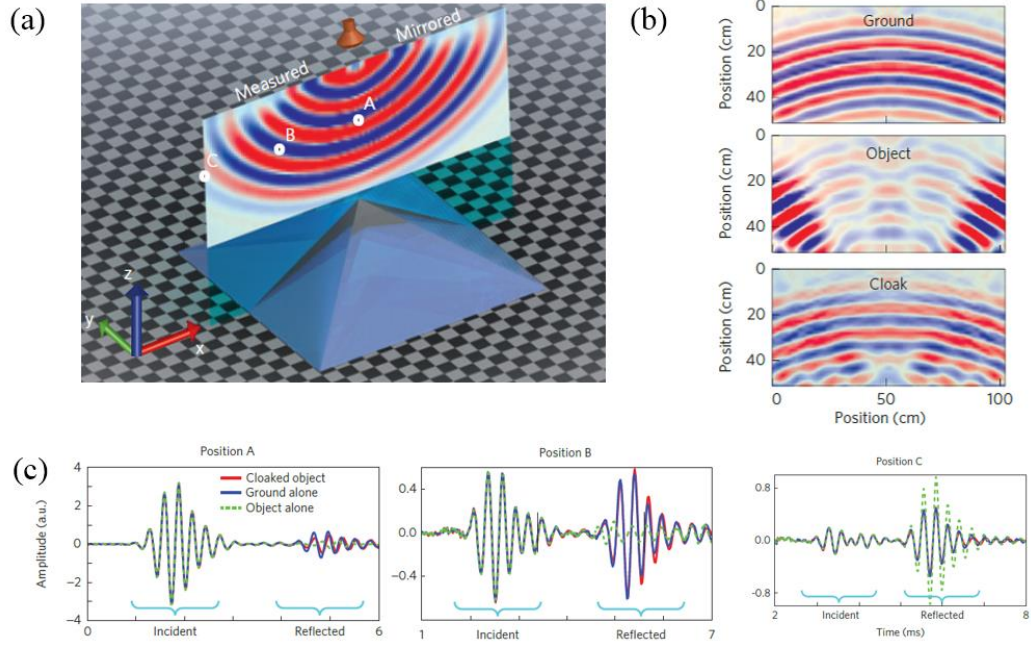


Figure 1. 11 (a) Schematic of the pyramidal omnidirectional acoustic cloak proposed by Zigoneanu et al. (b) Instantaneous pressure field distribution showing the cloaking effectiveness of the device. The pressure field from the cloaked object mimics the empty ground. (c) Measured signals at locations a, b, and c in (a). The scattered acoustic pressure is shown for the empty ground, the object placed on the ground, and the cloaked object in each case.

Another approach to acoustic cloaking focuses on solving the problem of rendering an arbitrary 3D object placed in an open cavity invisible to sound [29]. This was achieved by Weiwei Kan et al., where they applied transformation acoustics in designing an anisotropic structure with stacks of layers having subwavelength holey unit cells (Figure 1. 12). Because their design is devoid of resonant elements, it could operate over a wide bandwidth (in the domain of $10 \text{ cm} < \lambda < 17 \text{ cm}$) for a broad range of incident angles.

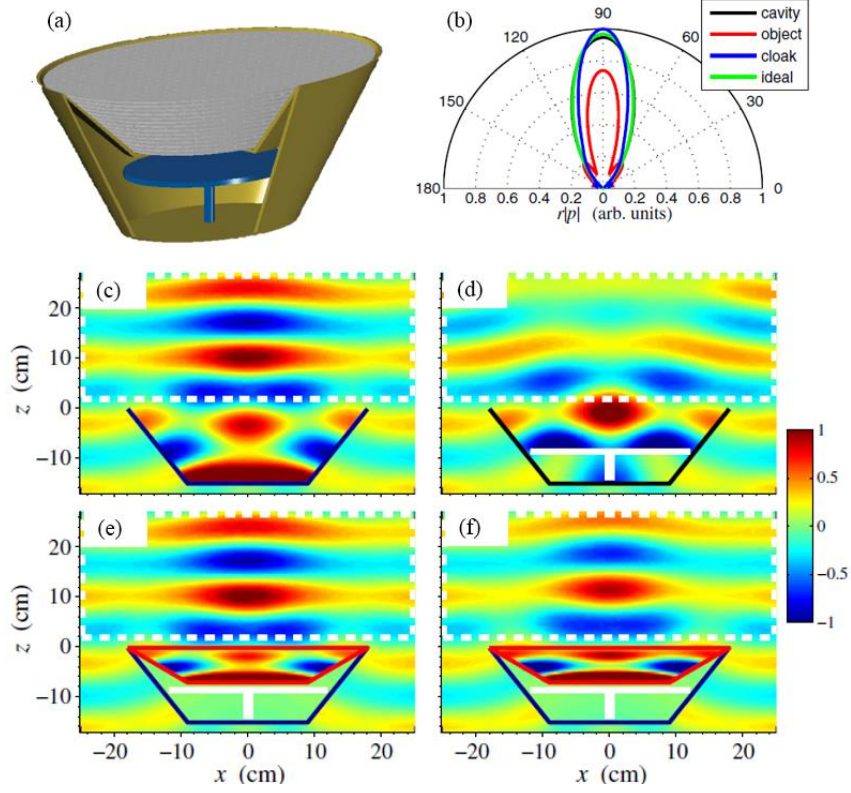


Figure 1. 12 (a) Acoustic cavity scheme with a 3D object (blue colored) and the metamaterial cloak (grey layers) realized by Weiwei Kan et al. (b) Directivity plots of the calculated radiation profile in the x - z plane. The colored lines represent the profiles obtained for the empty cavity (black), the cavity with a mushroom-like object (red), the cavity with the object and the perfect cloak (green), and the expected profile when the reduced cloak is considered (blue). Results are obtained for $\lambda = 13$ cm (2.68 kHz). (c)-(f) Calculated total pressure field (real part) obtained from finite-element simulations for the different configurations of the cavity at $\lambda = 13$ cm (2.68 kHz): (c) empty, (d) with the object inside (thick white lines), (e) with the object and the ideal cloak on top (red lines), and (f) with the object and the reduced cloak (red lines).

1.2.4.2 Acoustic Superresolution

Focusing and imaging have always been a prominent area of interest in the study of wave physics, with strides made towards approaching the diffraction limit, known as diffraction-limited resolution. This limit comes as a result of a physical constraint that is imposed on traveling waves by the dispersion relation $k^2 = (2\pi/\lambda)^2 = (\omega/c)^2$. As such, an object to be imaged would be only fully resolvable if its smallest feature is on the order of one wavelength or more. The advent of metamaterials, however, has extended the boundaries of what is possible in imaging, so that it is now possible to achieve a resolution beyond the limit of diffraction- a feat known as superresolution.

It is possible to split the wave vector k into two components: $k_{||}$ which is parallel to the image plane, and k_{\perp} which denotes the wave vector component perpendicular to the image plane. $k_{||}$ is the wave vector component responsible for imaging, and its magnitude is bounded by ω/c . k_{\perp} represents the propagating modes, which would carry the waves into the far-field. This is the component responsible for transmission or reflection of the acoustic energy. Because both components must satisfy the dispersion relation $k_{||}^2 + k_{\perp}^2 = (2\pi/\lambda)^2$, by allowing k_{\perp} to be purely imaginary, it is possible to increase the magnitude of $k_{||}$ to values larger than ω/c while still satisfying the dispersion relation. This will allow for imaging beyond the diffraction limit. It is important to note, however, that purely imaginary k_{\perp} are evanescent in nature, and so their magnitude decays exponentially with distance. These evanescent waves are responsible for carrying details of the image smaller than $\lambda/2$, and generally stay close to the source such that their amplitude is negligible at

about one wavelength from it. As such, the quality of the superresolution would decrease with distance as the magnitude of k^2 gradually returns to its diffraction-limited boundary of $k^2 = (2\pi/\lambda)^2$. Any details on the scale of $\delta < 2\pi/k_{max}$ do not contribute to the image and are lost in the far-field.

Fabrice Lemoult et al. experimentally demonstrated this concept of superresolution in the audible range using an array of Helmholtz resonators (soda cans) [52]. Their device demonstrated incredible enhancement of control of acoustic waves in the audible range – an attendant functionality of its high wave vector property. Focal spots as thin as $\lambda/25$ were attained using a technique called time reversal (TR), which entails measuring a time response of the system, flipping it in time, and sending it back to the medium with the same sensors. (Figure 1. 13)

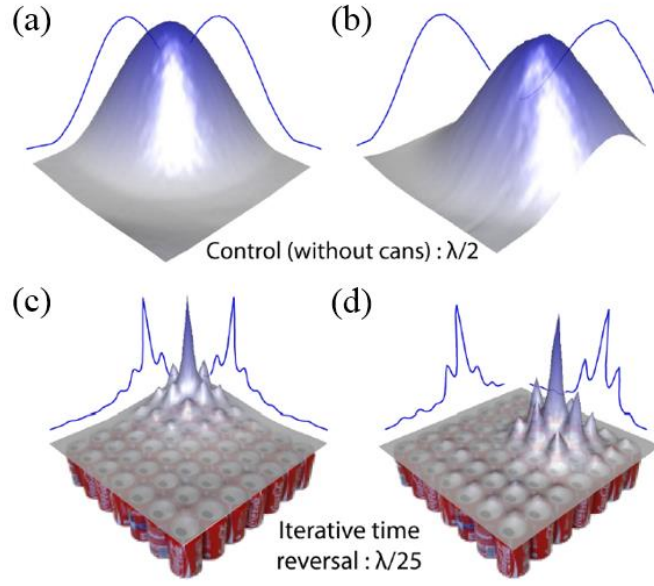


Figure 1.13 Superresolution achieved by Lemoult et al. (a), (b) Normalized intensities of the diffraction-limited pressure spots without the soda cans. (c), (d) Measured $\lambda/25$ pressure foci with iterative time reversal technique.

This concept of superresolution has led to the development of devices such as the acoustic superlens and the hyperlens. The idea behind the superlens is to create a medium with an effective negative refractive index, which can cause diverging waves to re-converge, thus capturing the information carried by the evanescent component of the waves before they vanish [18], [53]–[55]. In order to measure evanescent waves in the far-field, they must be converted into propagating modes. This is the realm of the hyperlens, and there are a few ways of achieving this. One way is to cause one of the effective parameters to have a hyperbolic dispersion relation. For example, using effective density $\bar{\rho}$, it can be made positive along the radial direction

but negative along the azimuthal direction, so that the hyperbolic dispersion relation is $\frac{k_r^2}{\bar{\rho}_r} + \frac{k_\theta^2}{\bar{\rho}_\theta} = \frac{\omega^2}{B}$. Because of this hyperbolic shape of the dispersion, the wave vector components are no longer bounded and can, in principle, assume arbitrarily large values while still satisfying the dispersion relation. An example of such a metamaterial can be seen in the work of Chen Shen et al., where they realized a broadband hyperbolic metamaterial resulting from a negative effective density (Figure 1. 14). Their device was capable of a subwavelength resolution of about $\lambda/4.7$ [56]

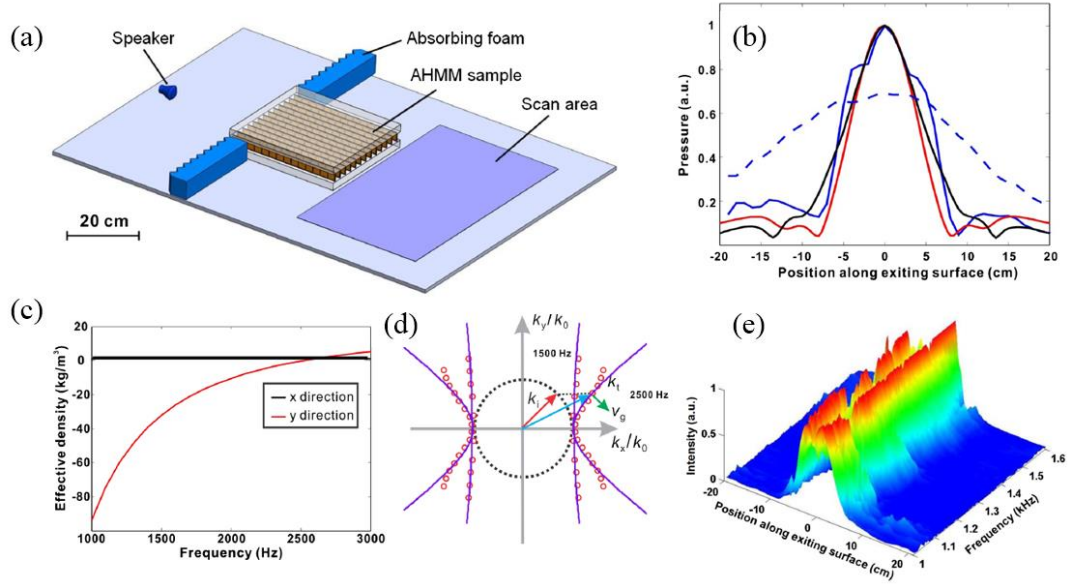


Figure 1. 14 Hyperbolic metamaterial developed by Chen et al. (a) schematic of the metamaterial and experimental setup. The thickness of the metamaterial corresponds to $0.9\lambda - 1.4\lambda$. (b) Normalized pressure magnitude distribution on the exiting surface of the metamaterial. Blue (solid), measurement with AHMM; blue (dashed), measurement without AHMM; red, simulation (real structure); black, simulation (effective medium). (c) Predicted effective density along the x and y directions. (d) The dispersion curves of the metamaterial showing a hyperbolic profile, and the equifrequency contours becoming flat at low frequencies. Solid line: lumped model. Circle mark: retrieved from numerical simulations. (e) Broadband performance of subwavelength imaging of the metamaterial.

It is noteworthy that if the negative parameter values of the wave vectors are as a result of local resonances, they can only be narrow band. If, however, the equifrequency contours assumed an elliptical shape, large wave vector components can be achievable with a broad-band capability. In principle, this also allows for very

large propagation distances, hence large magnification ratios. This was achieved by Jensen Li et al. using a fan-shaped metamaterial with alternating brass and air strips in the θ direction [33]. The vast difference in the mass densities and bulk moduli of both the constitutive components of their structure (air and brass) resulted in a metamaterial in which the effective densities $\bar{\rho}_r$ and $\bar{\rho}_\theta$ have the same sign but differ by a large ratio. This resulted in an elliptical equifrequency contour with a large eccentricity, allowing access to large wave vector components. The large ratio between the outer and inner radii of their hyperlens resulted in the retaining and compressing of significant portions for the evanescent components of the wave into the band of propagating waves. This resulted in up to an eight times magnification of the image (Figure 1. 15).

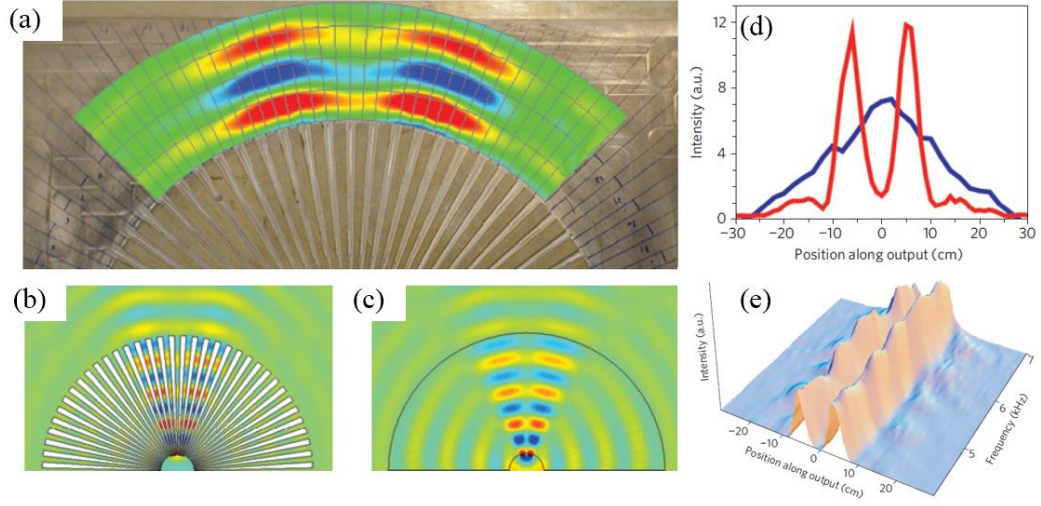


Figure 1.15 Acoustic magnifying hyperlens realized by Jensen Li et al. (a) Experimental pressure measurements in the propagation region. The object consists of the two sound sources transmitting at 6.6 kHz and separated by 0.23λ at the input plane. (b) Simulation of the pressure field using the microstructure with the elastic fins (c) 2D simulation using the effective medium description of the lens. (d) The magnified image at the outer edge of the lens showing a $\lambda/4.3$ resolution (red), while the control experiment shows a single peak (blue). (e) The broadband performance of the acoustic hyperlens. The frequency ranges from 4.2 kHz–7 kHz.

1.2.4.3 Sensing enhancement techniques

Of special interest in this dissertation work is the idea of sensing enhancement by high- k anisotropic acoustic metamaterials. It is often desirable for acoustic systems to be highly sensitive, noise redundant, and highly directive in some applications. Such characteristics can enable the acoustic energy to be more efficiently transferred into

the medium where it is desired. However, achieving these feats at the same time usually poses a problem with conventional methods such as microphone array systems. Acoustic metamaterials present a viable solution to addressing these issues due to the exotic properties they have been observed to possess. An obvious useful effect that the many advantageous properties that acoustic metamaterials have been shown to exhibit can have is the enabling of some signal processing processes to be accomplished directly in the physical layer, as opposed to the electronic layer. This adds an extra degree of adjustability to the system.

There are a variety of methods to go about designing an acoustic metamaterial for sensing enhancement. One method involves the use of the wave compressive properties of anisotropic graded-index metamaterials. This has been investigated by Yongyao Chen et al. in our research group [14], where a high refractive index waveguide was created. The graded-index anisotropic metamaterial waveguide consisted of thin slabs of stainless-steel plates interspaced by air gaps. The novelty of this feat is that the design solved a seemingly insurmountable obstacle faced by acoustic systems in creating high refractive index media: sound is generally slowest in air. Therefore, by creating a propagation medium that has a higher refractive index than air, acoustic waves could be guided within the medium. Also, sensing enhancement was achieved by compressing the acoustic waves and thus increasing the energy. This occurs because the increasing refractive index nature of the medium result in spatial compression of the acoustic waves, increasing their energy density. In addition to its highly directional response and high SNR, this metamaterial was also

highly dispersive, capable of amplifying signals up to its cut-off frequency while attenuating signals beyond that frequency (Figure 1. 16).

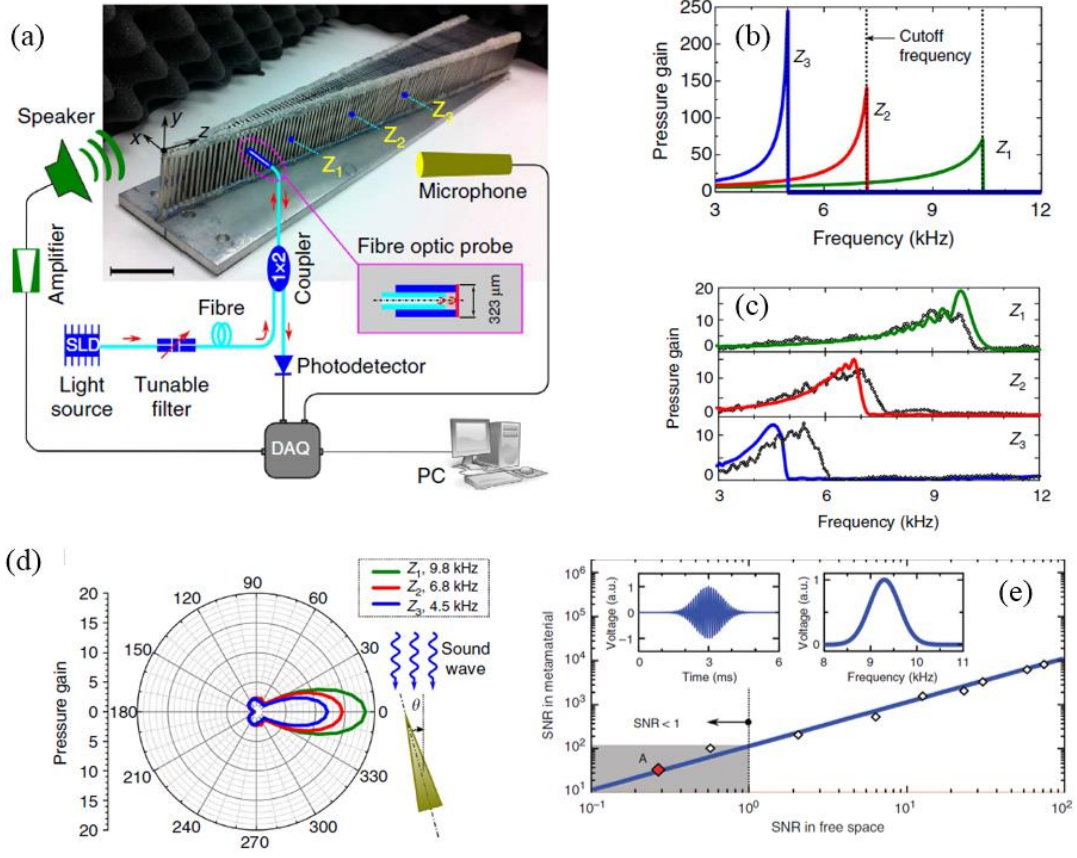


Figure 1.16 Graded-index acoustic metamaterial waveguide developed by Yongyao Chen et al. (a) Schematic of the acousto-optic sensing system. (b) Simulated and (c) experimentally obtained pressure gain spectra at different locations of the metamaterial. The locations Z_1 , Z_2 , and Z_3 , correspond to gaps 30, 45, and 66. (d) Measured directivity patterns of the maximum pressure gain at different frequencies. (e) Measured SNR in the metamaterial compared with that of the free space.

Metamaterials that can achieve a highly directional and amplified acoustic beam are also very desirable because they possess a wide range of possible applications, such as fault detection, noise source identification, sonar navigation, acoustic communication. An example of this was realized by Chengrong Ma et al.

using a honeycomb lattice of locally resonant phononic crystals boasting a near-zero refractive index [23]. This hyperbolic metamaterial (in terms of the 3D dispersion relation) was able to achieve more than 18 dB of amplification and a half-power beamwidth of fewer than 5 degrees. Interestingly, weak acoustic signals were resolvable even in the presence of strong interfering white noise with their metamaterial, as well as a 24 dB SNR at normal incidence (Figure 1. 17 (a) – (f)).

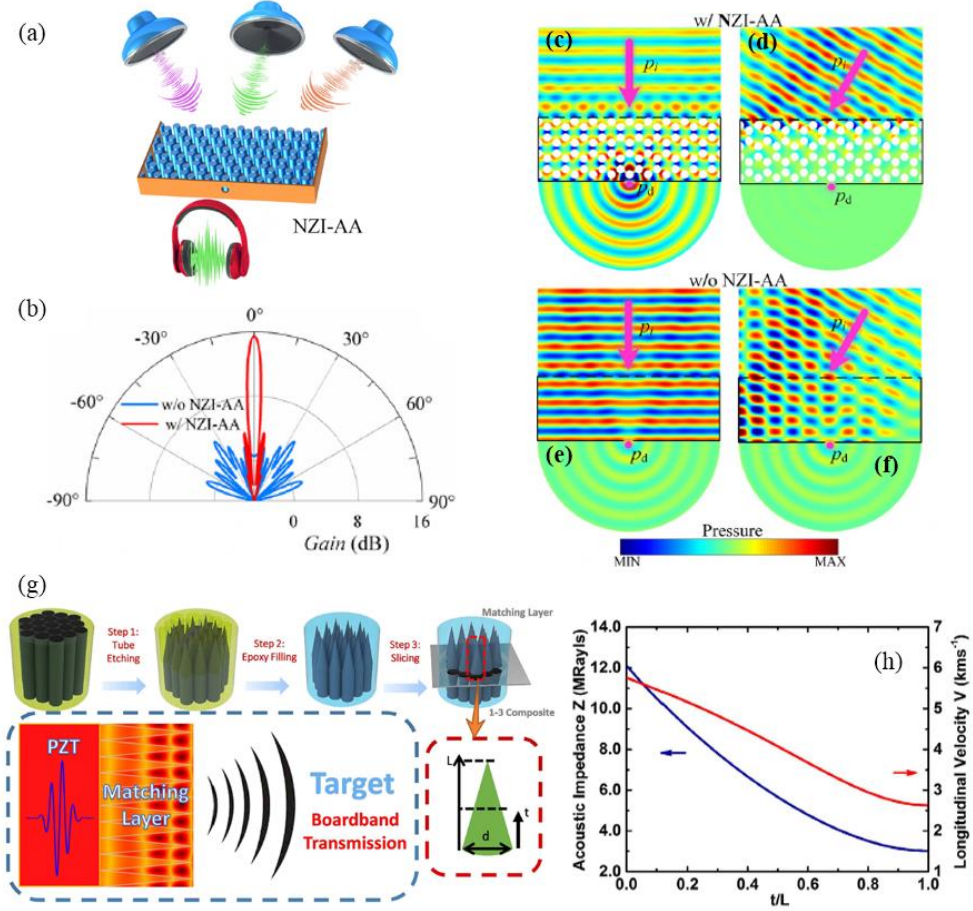


Figure 1. 17 (a) Schematic of the near-zero-index acoustic antenna (NZI-AA) proposed by Chengrong Ma et al. (b) Directivity patterns with/without the NZI-AA. (c)-(e) Acoustic pressure fields in a NZI-AA system under normal ((c) and (e)) and oblique ((d) and (f)) incidence. (e) and (f) shows the same configuration in (c) and (d) but without the NZI-AA. (g) and (h) Impedance matching acoustic metamaterial layer realized by Zheng Li et al. (g) Schematic showing the steps of fabrication of the metamaterial matching layer. Each pyramidal unit cell is $125\ \mu\text{m}$ in diameter and $610\ \mu\text{m}$ in length. (h) Distribution of the acoustic impedance (blue curve) and the longitudinal velocity (red curve) along the thickness direction.

Some metamaterials have been realized that enhance the capabilities of ultrasonic transducers. For example, a broadband gradient acoustic metamaterial was realized by Zheng Li et al. [28] that aims at improving the capabilities of ultrasonic transducers used in ultrasonography. The idea is to reduce the acoustic impedance mismatch that usually exists between the piezoelectric materials and the substrate, such as human tissue, which can be one to two orders of magnitude. This was accomplished by creating a gradient impedance matching layer which comprises periodically arranged unit cells of silica-epoxy composites (Figure 1. 17 (g) and (h)). They proved that a transducer equipped with their metamaterial matching layer provided a much better electromechanical coupling coefficient compared with conventional quarter-wavelength techniques.

1.3 Motivation for this dissertation work

Since the study of acoustic metamaterials is a relatively new field, it is bursting with unexplored knowledge, physics, classifications, understanding, and realization of new metamaterials that would stretch the boundaries of what is accomplishable in the field of acoustics. This work focuses on a subset of this new field of acoustic metamaterials – high- k acoustic metamaterials – and seeks to answer the following important but largely unexplored questions:

- i. Can the fundamental properties that electromagnetic high- k metamaterials possess be identified in the realm of acoustic metamaterials?

- ii. Is it possible to develop a tool or method that would enable accurate experimental studies of the intrinsic properties of high- k acoustic metamaterials?
- iii. Can these properties be leveraged to realize acoustic metamaterials with practical applications that would enhance acoustic sensing and emission?

The field of electromagnetic waves and their advanced control using metamaterials is much advanced compared to their acoustic counterparts. Although there are some fundamental differences in the types of waves these metamaterials control, some acoustic metamaterials have been constructed that establishes a mapping between acoustic waves and their electromagnetic counterparts. This has opened the path to creating novel acoustic metamaterials with ideas extracted from the field of electromagnetics. However, the well-known fundamental characteristics that high wave vector metamaterials exhibit has not yet been delineated in the field of acoustic metamaterials.

One of the key difficulties that experimental studies are faced with is the issue of measuring pressure fields in the deep subwavelength cavities of acoustic metamaterials. Generally, the higher the working frequencies of these artificial structures, the smaller the unit cells need to be. It, therefore, becomes a challenge to physically measure the pressure fields in such small devices without compromising them. As a result, experimental studies on acoustic metamaterials with deep subwavelength unit cells in the millimeters usually omit intrinsic characterization of their structures and rather employ input-output type measurements of the pressure fields around them. There are some cases where the metamaterial design allows for

measurements or visualization of the pressure fields inside the structure using devices such as scanning laser Doppler vibrometers. Still, such methods only allow for 2D topographical measurements and thus are not always ideal for measurements requiring probing of a 3D space. Additionally, only a few metamaterials or metasurfaces allow for such methods to be used due to their flat and open-ended topology. In order to experimentally unearth the intrinsic characteristics of acoustic metamaterials, there remains a need for a tool capable of probing the deep subwavelength space of these devices without compromising the acoustic field.

A complete story of studying acoustic metamaterials would necessitate the design, realization, and study of some metamaterial structures. In the literature, there has been work published on metamaterials with different capabilities. However, there is still a lot of room for the development of metamaterials aimed at enhancing the emissive and receptive properties of acoustic transducers. Additionally, to date, there have not been any strides towards acoustic metamaterials for enhancing sonar applications. This very practical field can yield obvious benefits in the field of science, such as furthering the research in sonar-based autonomous robotic navigation. In this work, one of the fundamental properties of high- k acoustic metamaterials will be leveraged to provide metamaterial enhancements to active echolocation. A comparison between the functionalities of these metamaterials and biological systems will be done, which would show that such relatively simple structures can be functionally comparable to much complex biological systems. Moreover, for the first time, it would be demonstrated that high- k acoustic

metamaterials can be used to enhance the autonomous tracking of a sonar robot greatly.

Furthermore, a low-dimensional acoustic metamaterial that has active tunable properties will be developed and studied. The novelty of this metamaterial and its potential uses would be outlined therein. This work would prove that the study of acoustic metamaterials can rise beyond academic curiosity and can produce useful technologies and devices to solve real-world problems.

1.4 Overview and organization of the dissertation

1.4.1 Overview of dissertation

The overall goal of this dissertation is to achieve an enhanced understanding of the properties of high- k acoustic metamaterials and use this understanding to investigate novel devices and applications based on the properties of the metamaterials. This work includes the following four research thrusts:

Research thrust 1: Achieve an enhanced understanding of the requirements and fundamental properties of high wave vector acoustic metamaterials

The unique criteria required to realize an acoustic metamaterial capable of sustaining high wave vectors are investigated in this thrust. These are the criteria that would be employed in realizing and studying the high wave vector metamaterials in this dissertation work. An enhanced understanding of the fundamental properties that high wave vector metamaterials exhibit will be outlined and investigated as pertaining to

acoustic metamaterials. A framework for realizing and investigating the metamaterials would be outlined, which includes the development of specific tools and methods for use in studying the metamaterials.

Research thrust 2: Develop and study the receptive properties of low dimensional high- k acoustic metamaterials

This thrust would involve investigating two sub-cases of high- k metamaterial structures to achieve an enhanced understanding of their receptive properties. One of the sub-cases will involve leveraging one of the fundamental properties of high- k acoustic metamaterials to realize a low-profile acoustic metamaterial device with active tunable properties. In another sub-case, similarities are established between the functionalities of the high- k structure and a mammalian cochlea in terms of their signal processing features. In both sub-cases, simulation and experimental studies will be employed to study and demonstrate the capabilities of high- k graded-index acoustic metamaterials to arbitrarily control the propagation of acoustic waves through them over a broad bandwidth.

Research thrust 3: Realize and study the emissive properties of a high- k bio-inspired acoustic metamaterial emitter

In this thrust, theoretical and experimental studies are carried out to achieve a fundamental understanding of the enhancement of sound generation in high- k metamaterial structures. This understanding is then used to develop an acoustic metamaterial that has enhanced emissive properties functioning in the ultrasound

region. Parametric studies would be carried out to gain an understanding of the various intrinsic and extrinsic factors that affect the performance of the metamaterial emitter.

Research thrust 4: Investigate the applications of high- k acoustic metamaterials for sonar and robotic tracking applications

Combining the emissive and receptive properties of the high- k metamaterials studied in the previous thrusts, this thrust will investigate the metamaterial enhancements to a conventional sonar system. The vast advantages afforded by the metamaterials are exposed, employing analytical studies and experiments. A mobile tracking robot equipped with the metamaterial sonar system will be employed to demonstrate the metamaterial enhancement to robotic tracking applications.

1.4.2 Organization of the dissertation

The rest of this dissertation is organized as follows: Chapter 2 describes the fundamental studies of high wave vector acoustic metamaterials. Their construction, properties, and study methodology are discussed therein. A miniature sensor for studying the metamaterials will be realized and characterized.

Chapter 3 will address the receptive properties of low dimensional acoustic metamaterials. Two low dimensional metamaterials are studied herein. One of them is a planar high- k acoustic metamaterial with active tunable properties. First, its passive properties are studied via simulations and experiments followed its active properties. The other device is a conical metamaterial, of which it is proven analytically and

through simulations and experiments that it functionally mimics the mammalian cochlea.

In Chapter 4, an investigation into a bio-inspired acoustic metamaterial emitter is carried out. Use is made of analytical, simulation, and experimental studies to investigate the intrinsic high- k properties of the metamaterial. Parametric studies of the design factors are also considered therein.

In Chapter 5, applications of these metamaterials would be addressed. The metamaterial emitter and receiver would be combined with acoustic transducers to create a metamaterial enhanced sonar system, which would be studied to showcase their advantages over conventional sonar systems. A robotic platform with a sonar tracking algorithm is employed to demonstrate the advantages of the metamaterial enhanced sonar system.

Finally, in Chapter 6, a summary of the dissertation work will be provided, along with the key contributions and an outline for future work.

Chapter 2: Understanding high wave vector acoustic metamaterials

The term “high wave vector” is commonly used describing some electromagnetic metamaterials that exhibit a set of unique and useful properties. These types of metamaterials can sustain waves with extraordinarily high wave vector (k) values and unusually high density of states (DOS), which enable them to exhibit such unique properties as energy confinement, wave radiation enhancement, energy transport, and enhanced dynamic control. These artificial structures can exist as one-dimensional (1D) wires, two-dimensional (2D) thin films, or bulk materials (assemblies of 1D and 2D materials) and are designed to enable passive or active modification of their constitutive properties such as the magnetic permeability and the dielectric constant. In this chapter, it is proven that some acoustic metamaterials could properly be identified as high wave vector metamaterials, and they can equally exhibit similar characteristic properties of energy confinement and transport, acoustic wave radiation enhancement, and enhancement of control. Furthermore, a miniature acoustic probe is realized, which would be used to study the intrinsic properties of the high- k acoustic metamaterials presented in the rest of this dissertation work.

2.1 Motivation: Why High- k acoustic metamaterials?

High- k electromagnetic metamaterials have recently garnered much attention because they can manipulate the electromagnetic density of states at broadband frequencies. This is mainly as a result of their ability to excite electromagnetic states with high momentum (high- k modes). A useful application that results from this is the ability of these high states to couple into emitting modes, leading to enhanced spontaneous emission effects and control [57]–[61]. The additional wave vectors sustainable in these structures are at the heart of such functionalities as sub-diffraction imaging and sub-diffraction mode confinement, as well as devices such as hyperlenses, negative index waveguides, etc.

Interestingly, there is strong evidence that acoustic metamaterials can propagate waves with high wave vectors and equally exhibit the high- k characteristics found in electromagnetic metamaterials in the acoustic domain [62]. Furthermore, many of these qualities come as a direct result of similar phenomena in electromagnetic metamaterials. For example, it has been discussed that the superlensing and hyperlensing capabilities that some acoustic metamaterials have are as a result of the extra wave vectors they can contain. Similar to their electromagnetic counterparts, the sub-diffraction imaging capability in these artificial structures is due to a portion of the acoustic wave energy coupling into evanescent modes, which are responsible for resolving objects beyond the diffraction limit [9], [16], [33], [52], [63]–[66]. High- k metamaterials have also been developed that enhance the emissive properties of an embedded emitter – an analogy to the Purcell effect common in

electromagnetic metamaterials [67], as well as high refractive index waveguides analogous to optical waveguides [27], [68]. Despite these similarities, however, high- k acoustic metamaterials have not been systematically studied in the literature to establish the equivalences of the characteristics exhibited by high- k electromagnetic metamaterials in the acoustic domain. Such a systematic study can be of great benefit to the field of acoustics by, for example, establishing a reference point through which acoustic metamaterials can be studied, as well as using the advanced work on high- k electromagnetic metamaterials as a framework to advance the research high- k acoustic metamaterials. This underlines the motivation to realize and study the characteristics of high- k metamaterials, as well as demonstrate their applications.

2.2 Types and construction of high- k metamaterials

2.2.1 Types

High- k metamaterials can exist either as *elliptical metamaterials* (EMMs) and *hyperbolic metamaterials* (HMMs) through their dispersion relation

$$\frac{\omega^2}{B} = \frac{k_x^2}{\rho_x} + \frac{k_y^2}{\rho_y} + \frac{k_z^2}{\rho_z} \quad (2.1)$$

where $[\rho_x, \rho_y, \rho_z]$ and B are effective mass density tensor, and effective bulk modules of the metamaterial, respectively, k_x, k_y , and k_z represent wavevector components along the x, y , and z directions, and ω is the angular frequency. EMMs

have positive, anisotropic densities, and hence the equi-frequency contour is an ellipse (Figure 2. 1 (a)). HMMs can be designed to have positive and negative density components in different directions (e.g., $r_x > 0$, $r_z < 0$ in 2D case), therefore rendering a hyperbolic equi-frequency contour (Figure 2. 1 (b)).

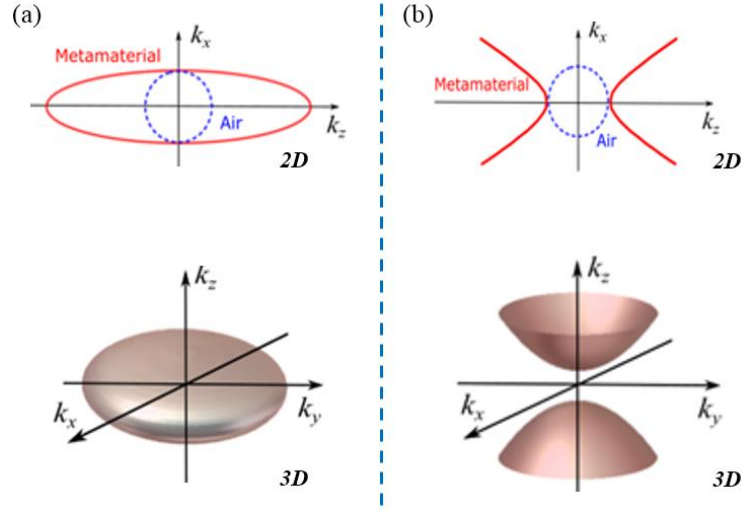


Figure 2. 1 Wave vector distribution of (a) elliptical and (b) hyperbolic high- k metamaterials.

An advantage of hyperbolic acoustic metamaterials is that their wave vector values can theoretically be unbounded, which implies unprecedented control over wave propagation. However, they tend to have more complicated designs compared to the simpler designs found in elliptical metamaterials. On the other hand, the elliptical equi-frequency contours in elliptical metamaterials imply their wave vectors are bounded, despite being higher than spherical equi-frequency contoured media. Although this implies their high- k capabilities are theoretically limited, they can be easier to realize. [69], [70]

2.2.2 Construction

The design of high- k acoustic metamaterials must adhere to the critical criterion that the lattice periodicity must be much smaller than the wavelength so that these structures can be treated as a continuous material. This criterion separates metamaterials from other artificial structures such as phononic crystals, wherein the lattice periodicity is on a scale comparable to the wavelength λ . Nonetheless, high- k acoustic metamaterials can be constructed in a variety of ways based on the intended working principle. The wave confinement property of Helmholtz resonators, for example, can be harnessed to realize metamaterial that could sustain high wave vectors at some frequencies. Therefore, the design Helmholtz resonator-based high- k metamaterials would generally consist of some form of holey arrays, such that each unit cell or subunit cell has a cavity-like region and a neck-like region, which are constituents of Helmholtz resonating elements (Figure 2. 2 (a)) [30], [31], [35], [38], [40], [41], [52], [71], [72]. Due to their cavity resonance characteristic, these Helmholtz resonator-based high- k metamaterials can yield a hyperbolic dispersion profile.

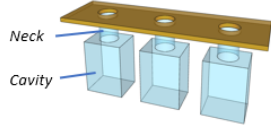
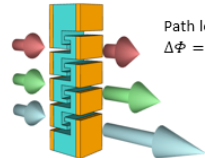
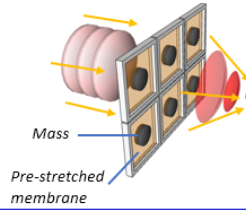
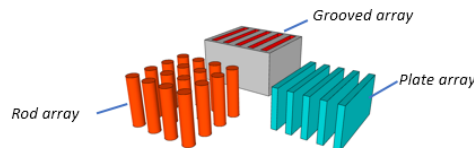
Metamaterial types	Construction schematic	Example high- k functionalities
(a) Helmholtz resonator-based metamaterials		<ul style="list-style-type: none"> • Pressure enhancement • Acoustic cloaking • Acoustic filters • Acoustic absorbers
(b) Space-coiling metamaterials		<ul style="list-style-type: none"> • Beam focusing and steering • Acoustic levitation • Superresolution imaging • Extraordinary absorption and transmission
(c) Membrane-type metamaterials		<ul style="list-style-type: none"> • Superresolution imaging • Superlenses and hyperlenses • Super absorbers • Energy harvesting
(d) Other types of arrays		<ul style="list-style-type: none"> • Sensing enhancement • Focusing • Acoustic filters • Cloaking

Figure 2. 2 Construction of different types of high- k acoustic metamaterials and some associated functionalities.

Space coiling metamaterials and metasurfaces have also been shown to exhibit high- k states, which were directly responsible for their sub-diffraction imaging capabilities [46], [73]–[76]. As discussed in section 1.2.3.3, there are a variety of ways of designing these types of high- k metamaterials, but the general idea remains to spatially elongate the propagating path of the acoustic waves to tailor phase shifts in the reflected or transmitted wavefronts. As discussed in section 1.2.3.3, the induced delay $\Delta\Phi$ is related to the total acoustic path L by $\Delta\Phi = k_0 L$ where k_0 is the free-space wave vector. The generation of high- k states by such metamaterials can trivially

be understood since the induced phases generated by such structures can result in focusing via constructive and destructive interferences of the incident or reflected wavefronts (Figure 2. 2 (b)).

Membrane-type acoustic metamaterials have particularly demonstrated high- k properties due to their ability to introduce wave-vector components perpendicular to the image plane, which are the components responsible for sub-diffraction imaging. The unit cells of these types of metamaterials generally involve a stretched elastic membrane-like material with some type of mass-like structure suspended on it (Figure 2. 2 (c)). The dispersion relations of these types of metamaterials could also be hyperbolic in shape, which evidences their abilities to withstand extraordinarily high- k states. Other metamaterial designs include rod arrays, plate, and groove arrays (Figure 2. 2 (d)) [14], [27], [33], [36], [37], [77], [78].

In all these designs, two general criteria can be deduced: First, the unit cells of these structures consist of two or more components. Second, there is a vast difference in the mass densities between the constituent materials. For example, the density of air is 1.1839 kg/m^3 while that of a plastic polymer (Vero™ plastic) is 1180 kg/m^3 , giving a solid-fluid ratio of about 996. Many of the metamaterials boast ratios of this magnitude or more. These two criteria mean that the metamaterials are anisotropic in nature.

2.3 Study methodology

Various methods are usually used to study acoustic metamaterials, of which experimental, numerical, and analytical methods are most common. In this dissertation work, primary use is placed on experimental methods to study high- k acoustic metamaterials. The experiments are usually done in an anechoic room on metamaterials designed and printed using a 3D printer. Numerical simulations and analytical methods are also employed to inform the experiments and validate the experimental data. The analytical studies make use of established relations in wave physics to understand, explain, and predict the metamaterial behavior.

In this dissertation work, the high- k acoustic metamaterials realized and investigated consist of arrays of plates (either circular or rectangular) separated by air gaps (Figure 2. 3). This is a simple yet profound way of realizing anisotropic metamaterials with dispersive effective parameters. It is shown in this work that such simple structures can educe many formidable properties characteristic of high- k acoustic metamaterials.

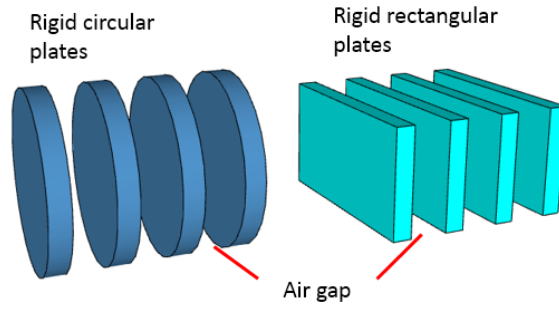


Figure 2. 3 Typical design format of the anisotropic metamaterials investigated in this work.

In this arrangement, air is the base medium which carries the acoustic waves, while the plates are generally fixed and regarded as rigid structures, like the walls of space-coiling and Helmholtz resonating structures. It is the interactions of the traveling waves in the air with the subunit plates at the intrinsic level, which produce the formidable high- k properties at the macroscopic level.

2.3.1 Simulation studies

COMSOL Multiphysics 5.3/5.4 and its Pressure Acoustics module software is employed to carry out simulation studies to verify and inform the design study of the metamaterials. Where the studies require the inclusion of losses in the model, the Thermoacoustics module is also included in the simulation and coupled with the Pressure Acoustics model so that thermal effects due to viscosity, which is responsible for the losses, are captured.

To satisfy the bulk modulus disparity criterion required to realize high- k acoustic metamaterials outlined in section 2.2.2 Construction , the two functional

materials featured in metamaterials are air, and a hard polymer. In the simulation settings, air, with a sound speed and density of 343m/s and 1.21 kg/m³ respectively, is used as the background (low bulk modulus) material. A typical polymer chosen for the high bulk modulus material is Acrylic, whose sound speed and density are 2730 m/s and 1190 kg/m³, respectively. In some simulations, hard-wall boundary conditions (Neumann) were used to simulate the metamaterial disks. A mesh criterion of between $\lambda_{\max}/20$ to $\lambda_{\max}/5$ is typically used to realize an effective simulation with a reasonable resolution, along with a perfectly matched layer simulation area to act as a sound absorber, preventing the formation of echoes in the test space. The simulation allows for simultaneous characterization of the wave propagation and attenuation properties in metamaterials.

2.3.2 Experimental studies

The simulation results are used as a basis to determine an optimal final design of the high- k acoustic metamaterial. Computer-Aided Design (CAD) software (Solidworks) is used to create the metamaterial designs, which are then realized using a 3D printing machine (Connex Object 500 or Formlabs Form 2). In section 2.4, the metamaterials used for studying the energy confinement and transport properties were constructed using steel plates. Most of the metamaterials studied in this work usually operate in the ultrasonic domain, where the wavelengths are less than 1.7cm. At this scale, the surface roughness can play a pivotal role in the performance of the metamaterials, where rougher surfaces decrease the performance by increasing the boundary layer

between the polymer and air. As such, the highest resolution is usually strived for when printing the devices. The Form 2 machine can achieve a resolution of up to 2.5 microns, while the Object 500 machine can achieve as low as 16 microns in resolution for horizontal builds.

2.3.3 Acoustic sensor development

The subwavelength structures of many high- k acoustic metamaterials, being in the millimeter scale, pose limitations in experimentally characterizing the acoustic fields inside the metamaterials since conventional microphones are typically too large fit in these gaps without severely disrupting the acoustic fields. As such, an appropriate sensor must be developed to properly characterize and study the deep subwavelength gaps of these high- k acoustic metamaterials.

An ideal acoustic probe used for spatial field mapping in metamaterials should act as a “point detector” with key characteristics, such as small size, omnidirectional response, and a broad working bandwidth. These characteristics will collectively help ensure precise acoustic field measurements at any location in the metamaterials over a broadband spectrum without much disturbance to the wave propagation. Many small acoustic probes based on capacitive, piezoelectric, Micro-Electro-Mechanical Systems (MEMS), and fiber optic techniques have been reported in the literature. However, these sensors inherently have one or more limitations, such as relatively large device sizes, strong directional response, and limited bandwidth [79], [80]. Commercial miniature probe microphones have been used for metamaterial characterizations [46], but they also suffer from large sizes (> 1 mm) and limited

bandwidth (audible range). Furthermore, because these microphones often rely on the use of rigid or flexible acoustic waveguiding tubes to indirectly measure the local acoustic fields, they inevitably introduce issues such as strong signal attenuation and distortions.

To this end, a miniature fiber optic microphone is developed to analyze the deep subwavelength structures of high- k acoustic metamaterials effectively. The fiber optic probe is comprised of a Fabry-Pérot cavity constructed by using a graphene diaphragm as one mirror and a single-mode fiber end face as another mirror (Figure 2. 3(a)). The signal from this optic probe is detected by using a white-light interferometry system [81].

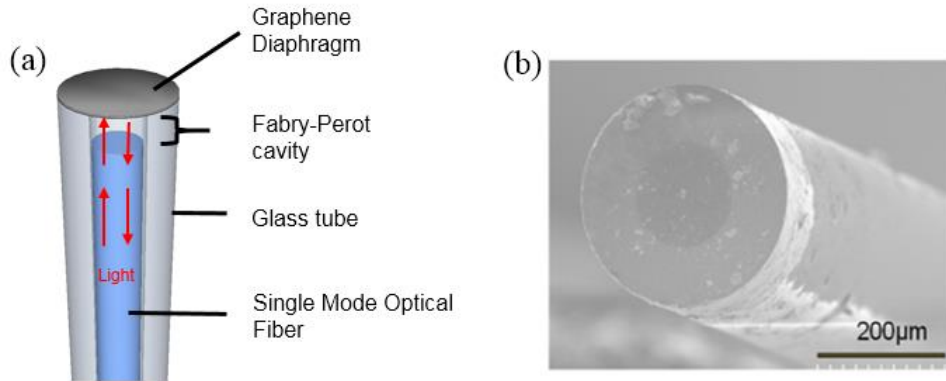


Figure 2. 4 (a) Diagram of the Fabry-Perot microphone tip showing key components. (b) Scanning electron microscopy (SEM) photograph of the Fabry-Perot microphone tip.

2.3.3.1 Sensor fabrication process

The fiber optic Fabry-Perot acoustic probe is constructed by using a single-mode fiber (FIS S97U7US5FISCU), a capillary glass tube (Polymicro TECHNOLOGIES, 1068150024; 323 μm and 150 μm outer and inner diameters respectively), and a multilayer graphene diaphragm as the acoustic pressure transducer. The fabrication process is illustrated in Figure 2. 4 and summarized as follows.

- a) The glass tube is end-polished by using an abrasive paper mounted on a rotating polishing platform and then cleaned (Figure 2. 4 (a)).
- b) A multilayer graphene film is suspended on water and then gently touched with the polished end of the tube (Figure 2. 4(b)). The adherence of the graphene to the tube is due to Van der Waals forces.
- c) A stripped, cleaned, and cleaved single-mode fiber is carefully inserted into the tube from the open end using a stage and microscopes so that a Fabry-Perot cavity with the desired length is formed between the fiber end face and the graphene diaphragm (Figure 2. 4(c)).
- d) A dab of liquid UV glue (DYMAX OP-66-LS) is used to fasten the fiber to the tube without completely sealing off the end, followed by UV curing for 1 minute (Figure 2. 4(d)).

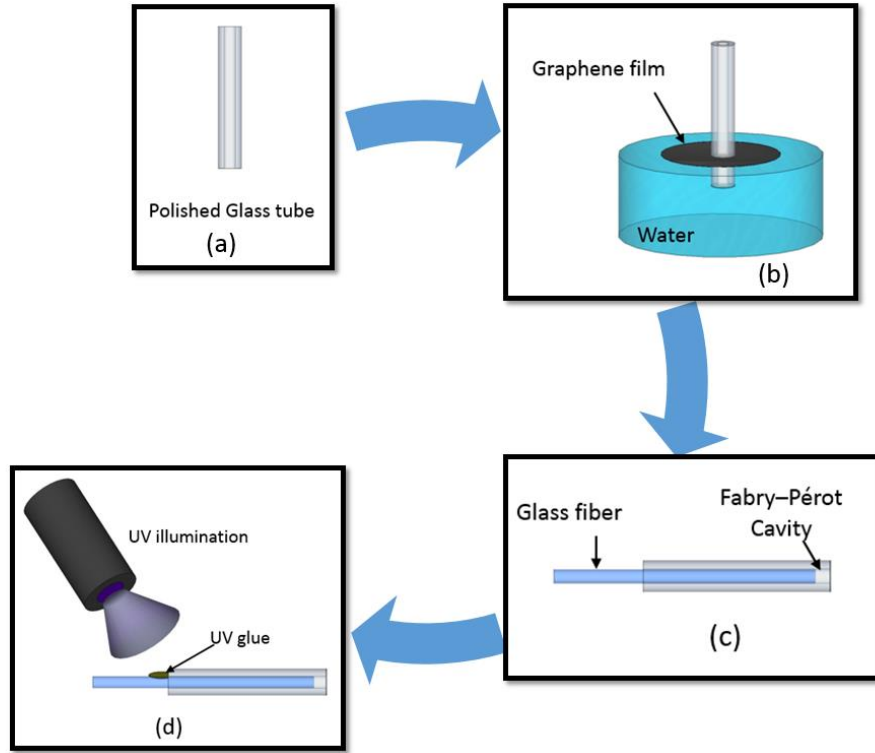


Figure 2. 4 Fiber optic microphone fabrication.

For a typically fabricated sensor, the finesse of the Fabry-Perot cavity is about 2, which makes it a low finesse sensor. However, owing to the extra-small thickness of the graphene film, the mechanical sensitivity of the sensor is quite high, which does not require the Fabry-Perot sensor to be high finesse for detecting the acoustic field. The low finesse sensor renders a large linear range. Additionally, due to the low-coherence optical detection system with a tunable Fabry-Perot filter -which can help mitigate instability factors due to the light source fluctuations and environmental disturbances- the sensor has superior stability. Throughout the experiments, the

sensor was proven to have comparable performance to a Brüel & Kjær (B&K) microphone (4939-L-002) in terms of the noise floor.

2.3.3.2 Properties of the fiber optic microphone

Graphene has unique mechanical properties, including ultra-small thickness (monolayer thickness of 0.34 nm), high stiffness (Young's Modulus as high as 1 TPa), and is highly stretchable (deformation up to 20%). These properties render the acoustic probe a high sensitivity, broad bandwidth, and large dynamic range [82]. Graphene-based acoustic probes working at the audible range (<20 kHz) have been previously reported. However, these sensors have been shown to exhibit strong directional dependence, making it difficult to obtain accurate spatial field mapping with them. To overcome this limitation, this fiber optic probe was made to have an aperture diameter of 323 μm . Because of this small size compared to the sound wavelength (e.g., $\lambda = 8.5$ mm at 40 kHz), an omnidirectional pressure response over a broad acoustic spectrum can be realized.

2.3.3.3 Characterization of the fiber optic microphone

Pressure Sensitivity: The pressure sensitivity of the fiber optic microphone is characterized using a speaker (Pettersson, LP 400) and a reference microphone (B&K, 4939-L-002). As illustrated in Figure 2. 5, the optical microphone was attached to the B&K microphone, and single frequency sweeping was performed for the frequencies ranging from 100 Hz to 40 kHz. Using the voltage outputs obtained

from both microphones and the known sensitivity data of the B&K microphone, the pressure sensitivity of the fiber optic probe at different frequencies was then obtained as $S_{fiber} = \frac{V_{fiber}}{V_{B\&K}} S_{B\&K}$, where S_{fiber} and $S_{B\&K}$ are the sensitivities of the fiber optic probe and the B&K microphone, respectively, and V_{fiber} and $V_{B\&K}$ are the voltage outputs of the fiber optic probe and the B&K microphone, respectively.

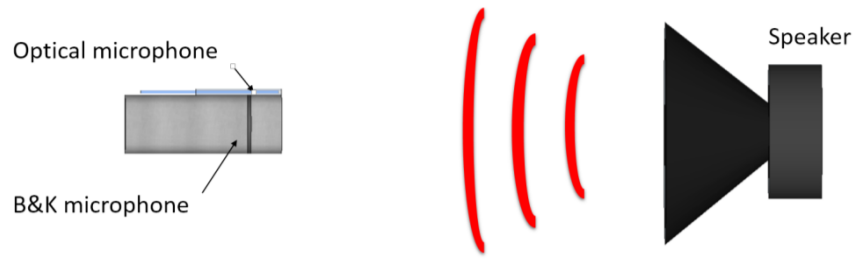


Figure 2. 5 Schematic of the characterization of the fiber optic acoustic probe using a B&K reference microphone.

Directivity: The directional response of the fiber optic probe was characterized by using a rotating stage (Newport URS75BPP) and the speaker. The probe was mounted on the stage so that the rotation center was aligned with the probe tip, as illustrated in Figure 2. 6. For each frequency ranging from 100 Hz to 40 kHz, the probe was rotated for 360 degrees with a step of 1 degree, and the output voltages were recorded and plotted as a function of the angle to the speaker to obtain the directionality plot.

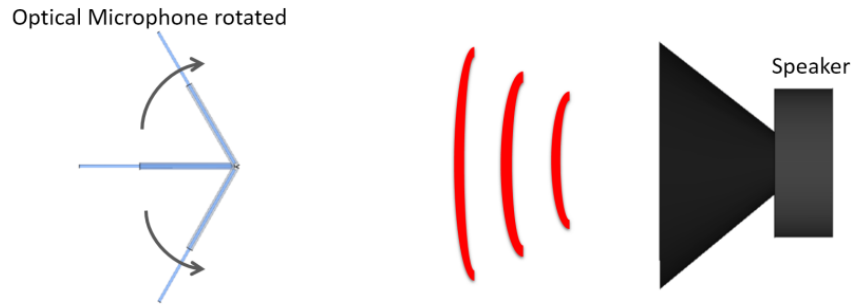


Figure 2. 6 Schematic of the directivity measurement of the fiber optic probe.

The results for the sensitivity, frequency response, and directivity characterization of the fiber optic probe are shown in Figure 2. 7. It is evident that the fiber optic probe manifests a good sensitivity in both audible (0.4 kHz–20 kHz) and ultrasonic frequency (20 kHz–40 kHz) regimes. The probe also exhibits almost perfect omnidirectional response at different frequencies (insets of Figure 2. 7). Therefore, this probe can truly act as an ideal “point detector,” which is essential for characterizing the wave propagation behaviors in metamaterials.

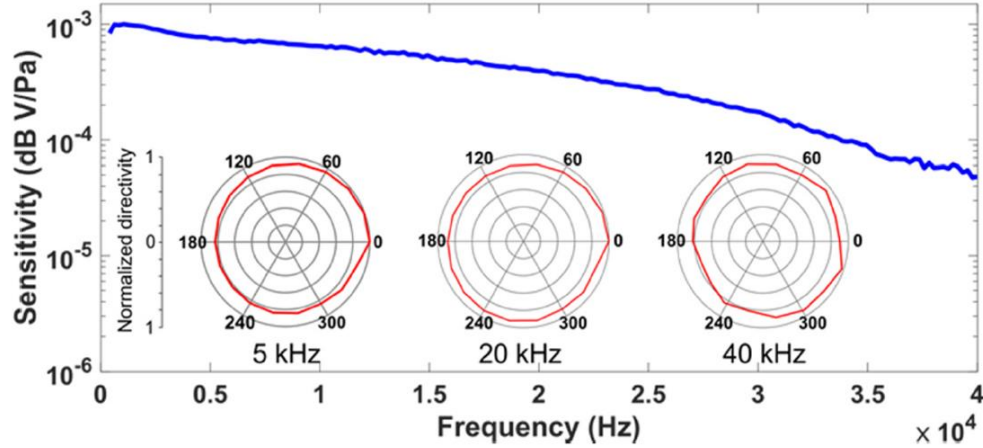


Figure 2. 7 Characterization of the fiber optic microphone probe. The frequency response reveals good sensitivity of up to 40 kHz. The directivity plots (inserts) reveal its omnidirectional response across the tested range.

2.3.3.4 Sensor interrogation system:

The cavity length of the tunable FP filter was initially tuned so that the fiber optic FP interferometry sensor worked at its quadrature point. In this case, the output voltage of the fiber optic probe ($V_{fiber}(t)$) was linearly proportional to the acoustic pressure. The fiber optic probe was mounted on a set of stages (Newport UTM50PE1 and VP25SA) controlled by a 3-axis motion controller (Newport Model ESP300, Figure 2. 8). The metamaterial was placed in front of the speaker. The fiber optic probe was precisely positioned in the metamaterial gaps for internal field mapping, as well as outside for external field mapping, by using the stages. The B&K reference microphone was positioned at the entrance of the metamaterial device (e.g., $x=0$ and $z=0$) in the free space. The metamaterial devices are typically characterized through a

frequency sweep with input harmonic sound frequencies ranging from 200 Hz to up to 50 kHz. After each frequency sweep, the optical microphone was precisely repositioned using the stages to another location so that a spatial mapping of the pressure field was obtained.

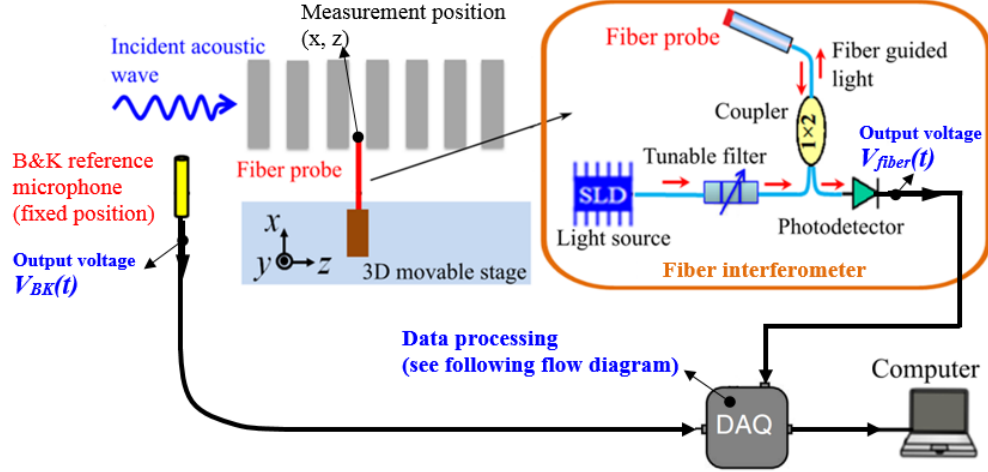


Figure 2. 8 Schematic of acoustic wave amplitude and phase measurements by using a reference microphone and fiber interferometer system.

The data processing flow diagram of the measurement signal is shown in Figure 2. 9. For each pure tone acoustic input signal, at each position (x, z) , the time domain voltage readings of both the fiber optic probe ($V_{fiber}(x, z, t)$) and the reference microphone ($V_{BK}(x, z, t)$) are recorded. A Fast Fourier Transform (FFT) is performed to obtain the corresponding complex frequency domain data $U_{fiber}(x, z, f)$ and $U_{BK}(x, z, f)$. The phase relative to the reference microphone at each position (x, z) and frequency f would then be obtained as $\Phi(x, y, f) = \text{Ang} \{U_{fiber}(x, z, f)/U_{BK}(x, z, f)\}$.

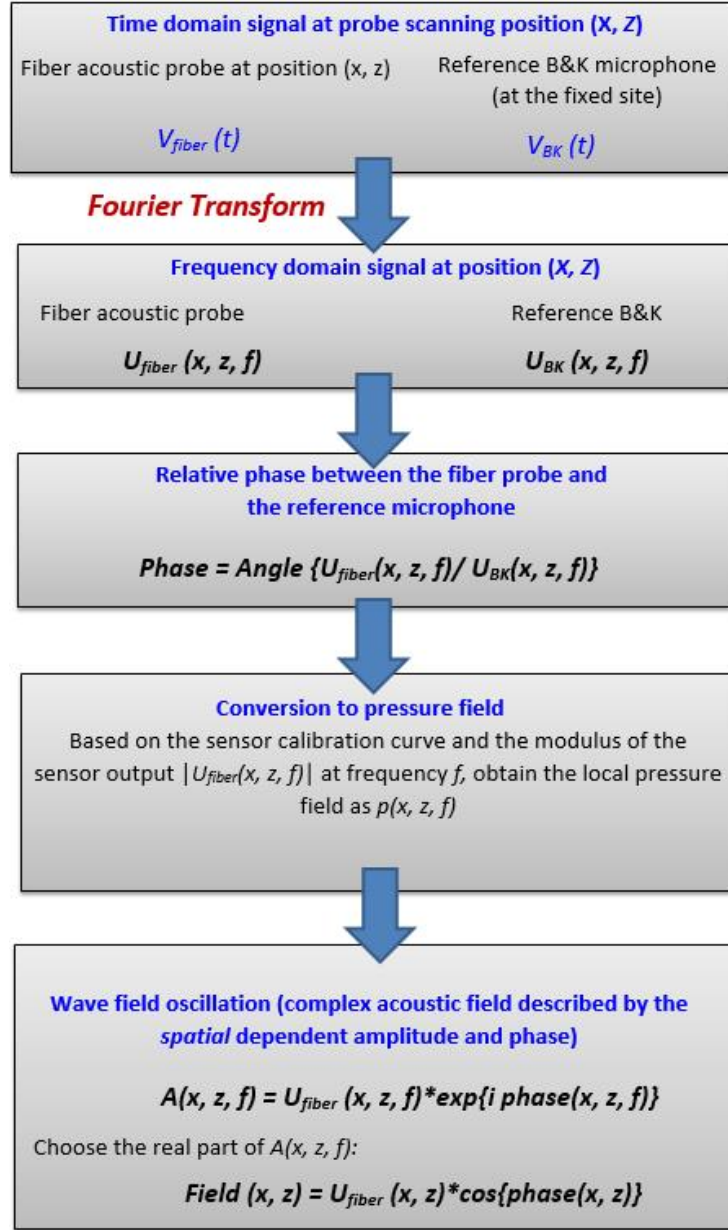


Figure 2. 9 Flow diagram of the data processing to obtain the complex acoustic fields (amplitude and phase) at the position (x, z) for each frequency f.

By using the calibration curve shown in Figure 2. 7 and the modulus of the complex frequency domain data $|U_{fiber}(x, z, f)|$, the acoustic pressure at each position

(x, z) and frequency f can be obtained as $p(x, z, f)$. Furthermore, the measured complex acoustic field was obtained as: $A(x, z) = p(x, z, f)e^{i\Phi(x, z, f)}$, which was used to obtain the real value of the pressure field as: $P(x, z, f) = \text{Real}(A(x, z, f)) = p(x, z, f)\cos(\Phi(x, z, f))$.

2.4 Properties of high- k acoustic metamaterials

Metamaterials that can sustain high wave vectors can display many characteristics that are attendant to the unique properties they enjoy. These properties can be summarized into three enhancements: enhancement of energy confinement and transport, control enhancement, radiation enhancement. In this section, these properties are analyzed with regard to acoustic metamaterials. As a case study, use will be made of variations of the anisotropic metamaterial types discussed in section 2.3. It is shown that such simple elliptical metamaterials can be designed to exhibit all three unique high- k metamaterial properties.

2.4.1 Energy confinement and transport

High- k metamaterials used for the manipulation of acoustic wave radiation and energy transport can be designed to have a close resemblance to low-dimensional semiconductors and metals used for controlling light-matter interactions such as quantum wells/wires, nanowires, graphene and their assemblies [12], [14], [27], [61], [68], [83], [84]. The high acoustic density of state (ADOS) they avail to the acoustic source for wave propagation enables the ability to enhance or suppress the radiation

efficiency of the source significantly. The radiated energies tend to have a preference for a channel with a high ADOS, enabling the transportation and containment of the wave energy within the high- k metamaterial structure. This closely resembles the photon transport behaviors of atom-nanowire coupled systems [83]. Additionally, the wave propagation direction across the high- k metamaterials can be altered by designing the metamaterials with asymmetric geometric characteristics, to enable radiation enhancement in one direction and suppression in the other [85], [86].

2.4.1.1 Analytical study of the energy confinement

It has been demonstrated that graded-index acoustic metamaterial waveguides can confine and transport acoustic waves in a similar manner to electromagnetic waveguides. An analytical model of such a device was developed in our research group [14]. Consider a simple two-dimensional (2D) case where the metamaterial is comprised of an array of solid plates placed in the air environment, and wave propagation is confined in the x - z plane as shown in Figure 2. 11

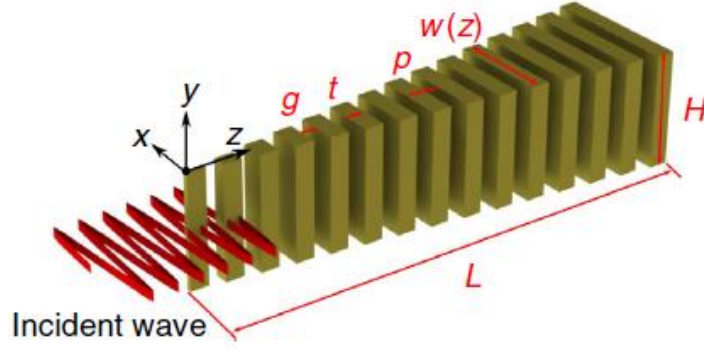


Figure 2. 11 2D acoustic metamaterial waveguide.

The equivalent medium model is developed to underscore the wave compression effect exhibited by a graded-index acoustic metamaterial waveguide.

The dispersion of this metamaterial has been determined to be [14]

$$k_{MM}(z, \omega) = \frac{\omega}{c_{air}} \sqrt{\frac{\rho_{air} B_{air}}{\rho_x B} \tan^2\left(\frac{\omega}{2} w \sqrt{\frac{\rho_x}{B}}\right) + 1} \quad (2.2)$$

where $\rho_x = \rho_{air} \rho_{steel} / [(1-F)\rho_{steel} + F\rho_{air}]$, $B = B_{air} B_{steel} / [(1-F)B_{steel} + FB_{air}]$ are effective density and bulk modulus of the metamaterial, respectively, ω is the frequency of the acoustic wave, and $w = w(z)$ is the width of the plates. F is the filling ratio of the rigid plates, which is defined by $F = (p - g)/p$, where p is the periodicity of the structure and g is the size of the air gap. The anisotropic nature of the metamaterial with a vast difference in effective densities ρ_x and ρ_z enables the propagation of acoustic waves with large wave vectors along the z -direction, enabling

a high refractive index metamaterial. The decreased speed and increased wave vector result in the compression of the acoustic waves in the medium, thus increasing its energy density. This can be seen in the closed-form pressure field equation that describes the spatial oscillation and response along the z-axis:

$$P(z, \omega) = \frac{(\rho_{air}\omega)^{1/2} (1 - n_{eff}^{-2})^{1/4}}{\cos[\arctan(\rho_x \rho_{air}^{-1} (n_{eff}^2 - 1)^{1/2})]} \exp[ik_{air} \int_{z_0}^z n_{eff} dz] \quad (2.3)$$

Here $n_{eff} = c_{air} k_{MM}(z, \omega) / \omega$ is the effective refractive index of the metamaterial structure. From equation 2.3 above, the traveling wave behavior, wave (pressure) amplification, energy localization, as well as spatial separation of frequencies in this class of metamaterial structures can be characterized. Based on equation 2.3, the pressure distribution along the propagation direction at 7.5 kHz is illustrated in Figure 2. 12

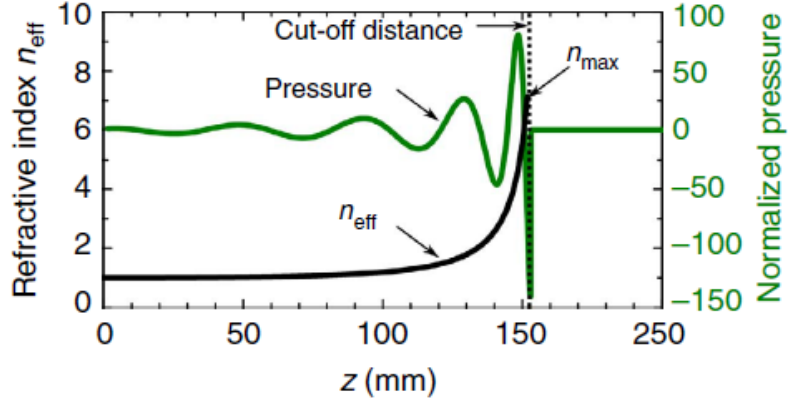


Figure 2. 12 Pressure and refractive index distribution along the metamaterial at 7.5 kHz, illustrating the wave compression effect.

It is clear from Figure 2. 12 above that the graded-index metamaterial waveguide provides a medium of increasing effective refractive index n_{eff} in the z -direction, which results in the increased wave vector and pressure amplitude in that direction. Because the acoustic energies tend to favor channels with high ADOS, the energy is confined to travel along the waveguide.

2.4.1.2 Experimental demonstration of energy confinement and transport

To better understand the energy confinement and transport and related properties of these types of high- k acoustic metamaterial, a double-tapered anisotropic metamaterial waveguide is realized for experimental studies (Figure 2. 13). The metamaterial waveguide has a double tapered configuration with three sections: two tapered end sections (sections 1 and 3) and a long uniform middle section (section 2).

Section 1 is used to ensure efficient wave coupling from the free-space into the metamaterial, which is similar to the light coupling scheme used in nanophotonic devices [ENREF 31](#) [87]. Section 2 plays an important role in maintaining stable wave propagation along the metamaterial waveguide, which is used for the characterization of wave-guiding and dispersion properties. Section 3 is used to overcome the wave impedance mismatch between the metamaterial and the surrounding medium so that the reflection modes are eliminated, and no standing wave interference occurs in the metamaterial waveguide.

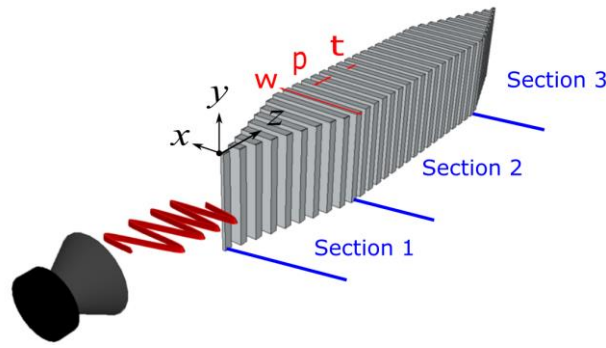


Figure 2. 13 Schematic of a double tapered metamaterial waveguide with three sections. It is comprised of an array of stainless plates spaced by air gaps with thickness $t=1.4$ mm and an array periodicity of $p=3.3$ mm. The uniform section (Section 2) is constructed with 100 plates of a constant width $w=20$ mm. Sections 1 and 3 are identical tapered structures, and the plate width w increases from 2 to 20 mm with a step of 0.5 mm. For simplicity, the metamaterial waveguide can be considered as a 2D system where the wave propagation is assumed to be confined in the x - z plane.

To verify this metamaterial's ability to effectively transport acoustic energy, a point-by-point pressure amplitude and phase measurements (i.e., one-dimensional (1D) field mapping) along the propagation axis of the metamaterial waveguide for various input sound frequencies is performed using the miniature fiber optic microphone. Representative measurement results for the entire metamaterial device are shown in Figure 2. 14 (a) and (b). First, it can be noted that at 5.5 kHz (Figure 2. 14 (a)), the measured pressure is nearly continuous along the metamaterial waveguide because the array periodicity ($p = 3.3$ mm) is much smaller than the sound wavelength (~ 62.5 mm) (i.e., $p \sim \lambda/18$). This confirms that the discrete metamaterial structure can be regarded as a continuous medium along the wave propagation direction [14]. The wave energy is effectively guided through this acoustic metamaterial at this frequency with a high DOS (the sound pressure levels inside the waveguiding sections -blue dotted lines- are higher compared to the tapered sections).

It should be noted, however, that energy propagation is halted for waves with frequencies beyond the stopband, as noted in Figure 2. 14 (b). For example, in Figure 2. 14 (b), a 12 kHz acoustic wave is seen to fall into the cut-off band of the metamaterial waveguide, and most of the propagating waves are trapped in Section 1 without entering the uniform waveguide region. This bandgap phenomenon is characteristic of high- k acoustic metamaterials.

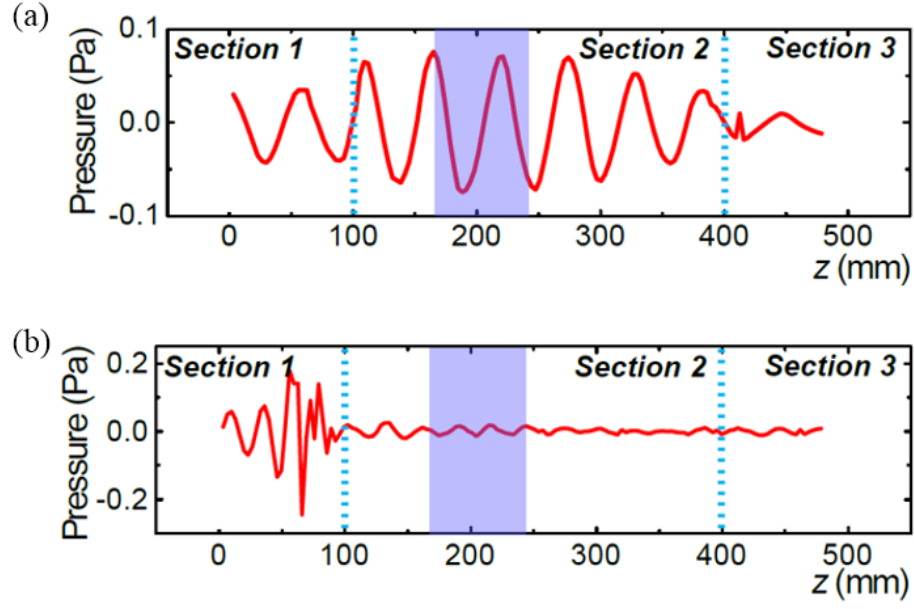


Figure 2. 14 (a) and (b) 1D pressure field mapping at an input sound frequency of 5.5 kHz and 12 kHz, respectively.

Furthermore, a 2D full spatial mapping of the internal and external pressure fields of the metamaterial structure was also performed to reveal more of the wave propagation characteristics in the metamaterial. Because the metamaterial structure is symmetric about the y - z plane, half of the x - z plane is measured. The measured 2D pressure fields for a segment of the metamaterial ($z=165$ mm to 225 mm, the blue highlighted region in Figure 2. 14 (a) and (b)) waveguide are shown in Figure 2. 15 (a) and (b). At 5.5 kHz (Figure 2. 14 (a)), the guided wave in the metamaterial is shown to propagate freely along the propagation (z) direction. However, it is strongly confined along the transverse (x) direction, as can be seen from the evanescent fields that decay outside the metamaterial region. By contrast, in Figure 2. 14 (b), the

acoustic waves at the cut-off band (12 kHz) are mostly prohibited from the metamaterial, producing a “silent zone” inside the metamaterial region. The small field oscillations observed inside the uniform waveguide may be due to the weak coupling of the external free space waves into the metamaterials from the boundary.

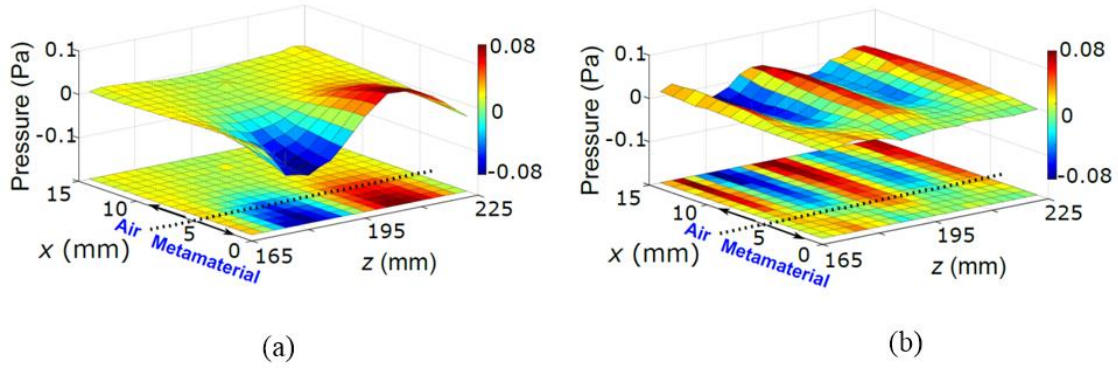


Figure 2. 15 (a) and (b) 2D field mapping at 5.5 kHz and 12 kHz for the specific region highlighted in Figure 2. 14 (a) and (b) ($z=165$ mm to 225 mm), respectively. The dashed line represents the metamaterial/air interface.

With the help of the spatial mapping, it is possible to distinguish the bounded surface waves from the unbounded free space waves propagating along the metamaterial/air interface. For instance, as shown in Figure 2. 14 (b), the wavefront periodicity for the acoustic waves propagating at the interface can be obtained as $\lambda=30$ mm, and the corresponding wavevector is $k=2\pi/30 \text{ mm}^{-1}$. This is almost the same as the free space wave vector $k_{air}=2\pi/29 \text{ mm}^{-1}$ at 12 kHz, indicating that these

are free space waves. On the other hand, if the traveling waves at the metamaterial/air interface have wavevectors larger than that of the free space waves, they should be classified as bounded surface modes [46]. This demonstrates how the acoustic metamaterial achieves high DOS within its frequency band.

2.4.1.3 Wave propagation mechanism

It is known that in conventional acoustic waveguides (e.g., acoustic tubes), the field confinement and waveguiding usually rely on hard-wall wave reflections (Figure 2. 16 (a), top). By using the measured 2D pressure field gradient, the air particle velocity fields are obtained, enabling the experimental exploration of the field confinement and waveguiding mechanism of this anisotropic metamaterial waveguide. Figure 2. 16 (b) shows the measured pressure and velocity fields (obtained from the pressure gradients) inside and outside of the metamaterial uniform section. Air particle oscillations inside the gaps can be induced by the internal and external pressure gradients, which spread beyond the arrayed structure. This enables gap-to-gap wave coupling through evanescent fields and renders sustainable guided-mode propagation along the metamaterial waveguide, as illustrated in the bottom of Figure 2. 16 (a). These experimental results, therefore, demonstrate that the waveguiding mechanism of anisotropic acoustic metamaterials is distinctively different from that of classical acoustic waveguide systems. It is interesting to note that the confinement and guiding of acoustic waves in the metamaterial waveguide closely resemble the optical guided modes supported by a dielectric slab waveguide. Therefore, it is possible to establish equivalences between these two waveguide

systems (Figure 2. 16(c)). This evanescent coupling method of wave propagation in this type of anisotropic high- k acoustic metamaterials is a key aspect that could explain many of their characteristics.

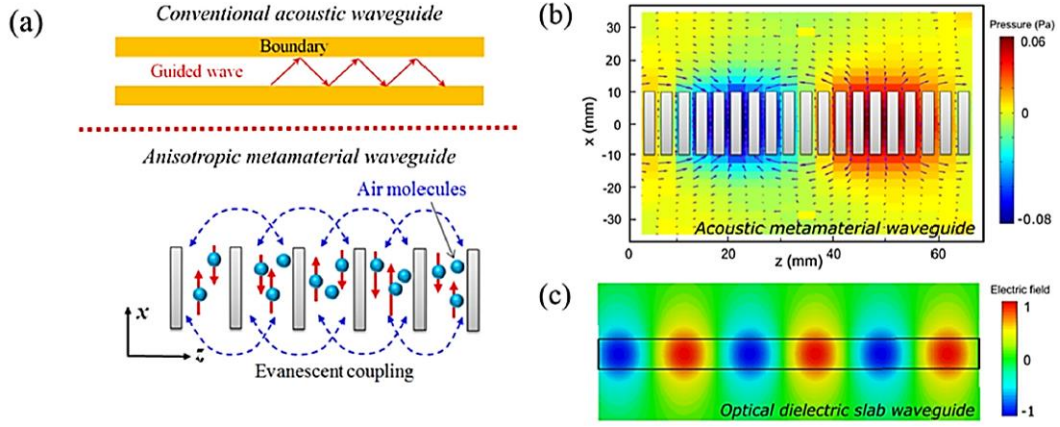


Figure 2. 16 Schematic of waveguiding mechanisms. (a), top: conventional acoustic waveguide and (bottom) metamaterial waveguide based on the microscopic perspective. (b) Measured pressure (colored map) and particle velocity fields (arrows) in the metamaterial waveguide. The length and direction of arrows indicate the magnitude and directions of air particle velocity. The gray bars represent the waveguide structure. (c) An optical analogy of the guided wave obtained by using finite-difference time-domain (FDTD) simulations. To establish an equivalence, the optical waveguide was chosen to have the same effective refractive index of $n=1.3$ as the acoustic metamaterial waveguide working at 5.5 kHz. Also, the normalized excitation frequency of the optical waveguide was chosen to be equal to that of the acoustic metamaterial waveguide, i.e. $f_{\text{optic}} = f_{\text{acoustic}} = w/\lambda = 0.32$, where $w=20$ mm is the width of the acoustic waveguide, and $\lambda=62.5$ mm is the sound wavelength at 5.5 kHz. The optical wavelength $\lambda = 1550$ nm and optical waveguide width of 500 nm were chosen to obtain the same normalized frequency. The length of the optical slab waveguide is 3.58 mm.

2.4.2 Enhancement of control

The underlying reason behind the existence of acoustic metamaterials is to acquire the ability to control acoustic wave propagation beyond what is possible with naturally occurring materials. It can, therefore, be expected that high- k acoustic metamaterials would likewise exercise additional control of acoustic waves. As outlined in section 2.2.2, a high- k acoustic metamaterial is artificially engineered by combining materials with vast differences in their material properties. The characteristics that the macrostructure takes on are, therefore, directly related to the geometry and assembly of its constitutive components. Additionally, the structures could be designed to enable the modification of the unit cells, which would bring about additional control of the wave propagation. When this is done, an active acoustic metamaterial is formed [42], [88]–[92][93].

There are, however, some unique ways in which high- k metamaterials enhance the control of acoustic waves that cannot readily be achievable with other metamaterial types. This can be seen by comparing the dispersion curves (i.e., k - ω relation) of high- k metamaterials and other low- k structures (Figure 2. 22). The group velocity of the propagating waves, which corresponds to the slope of the dispersion curve, is comparatively lower in the high- k region of high- k metamaterials than in the low- k structures. Because this temporal retardation of the acoustic waves comes as a direct consequence of the metamaterial's design, it follows that the high- k metamaterials could procure additional control of the waves. For example, the abrupt phase change necessary to bring about refraction of acoustic waves describable by

Snell's law of refraction has been discussed. This ability was identified to be a direct result of the metamaterial's ability to sustain high- k states, which, in space-coiling metamaterials, is due to temporal retardation of the waves.

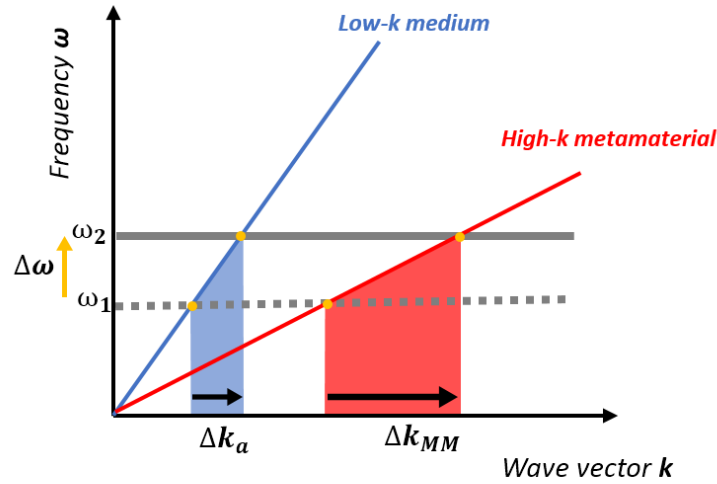


Figure 2. 22 Stimuli induced frequency change in high- k metamaterial versus low- k media. The frequency change $\Delta\omega$ brings about a larger momentum change in the high- k metamaterial Δk_{MM} than in the low- k medium Δk_a .

It is also discernable that any small stimulus which brings about a change in frequency ($\Delta\omega = \omega_2 - \omega_1$) would cause the attainment of comparatively more k -states in the high- k metamaterial; -states that are unattainable in low- k structures at that frequency (Figure 2. 22). As such, the momentum change Δk can be significantly

higher in high- k metamaterials than in low- k metamaterials, which implies that significant modifications of the wave properties are achievable by using a small external stimulus with high- k materials than with low- k metamaterials. Furthermore, the dispersion curve usually assumes a nonlinear shape, which means that the group velocity is frequency-dependent. There could be a frequency in which $\frac{d\omega}{dk}$ approaches zero, which would mean a complete arrest of the progression of the waves in the structure. In this way, such high- k metamaterial could pass some frequencies while stopping others, thus exerting more control over the acoustic wave propagation.

In the double-tapered experimental structure in Figure 2. 13, the dispersion of the metamaterial waveguide was experimentally obtained by implementing a Spatial Fourier Transform (SFT) of the measured acoustic fields in the uniform section. As illustrated in Figure 2. 18 (a), the wave-vector of traveling waves at a specific frequency can be found at the peak amplitude of the SFT results. Therefore, by varying the frequencies of the input acoustic waves, the dispersion curve of the metamaterial waveguide can be obtained (Figure 2. 18 (b)).

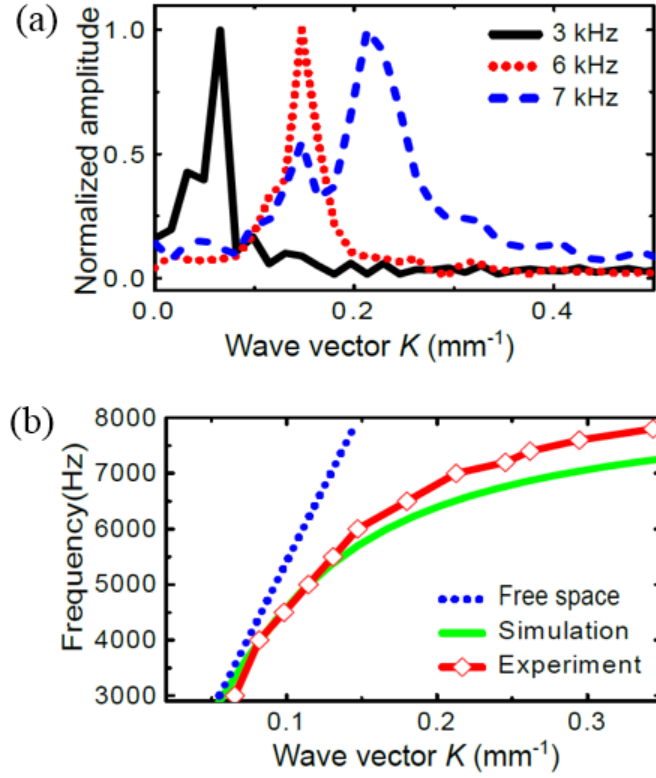


Figure 2. 18 (a) Normalized pressure amplitude as a function of wavevector at different input sound frequencies. (b) Experimentally obtained dispersion curve for the uniform waveguide section compared with that in air and that from FEM simulations.

Compared to the free space (air) dispersion, it is evident that the metamaterial allows wave propagation with a larger wavevector k_{MM} over a broad frequency range. The dispersion measurements provide clear experimental evidence that the wave-vector k can be parallel to the group velocity $v_g = 2\pi\partial f/\partial k$ in the anisotropic metamaterial, therefore realizing a positive effective refractive index larger than that of air (e.g., $n_{eff} = k_{MM}/k_{air} = 1.3$ at 5.5 kHz and $n_{eff} = 2.4$ at 7.8 kHz). The measured dispersion curve is found to be in good agreement with that calculated from

the effective medium model. In chapter 3, it will be shown that a high- k planar metamaterial receiver developed in this work is capable of achieving additional control over acoustic waves by allowing one of its physical parameters to be actively tunable.

2.4.2 Radiation enhancement

In electromagnetic metamaterials, the high DOS property is usually used to enhance spontaneous emission of photons [34], [57], [58], [61], [83], [94] using such mechanisms as Fabry-Perot resonances and the Purcell effect. The latter is a phenomenon where an atom radiates much faster in a wavelength-size resonant cavity than in the free space. This condition is can equally be observed in high- k acoustic metamaterials because, in principle, the implication of a high- k medium for wave propagation is that the wavelengths spatially compressed while the frequency is preserved (Figure 2. 19). Frequency preservation and wavelength reduction result in a concentration of the wave energy, thus enabling high- k acoustic metamaterials to achieve extraordinarily high wave energy densities within them. The acoustic equivalence of Purcell enhancement has been demonstrated [67], wherein an emitter embedded within a high- k structure produced elevated pressures. It has also been demonstrated that resonance effects from metamaterial cavities can be used to enhanced acoustic pressures from emitters [95], as well as the use of high- k rod arrayed acoustic metamaterials to enhance directional emission [23].

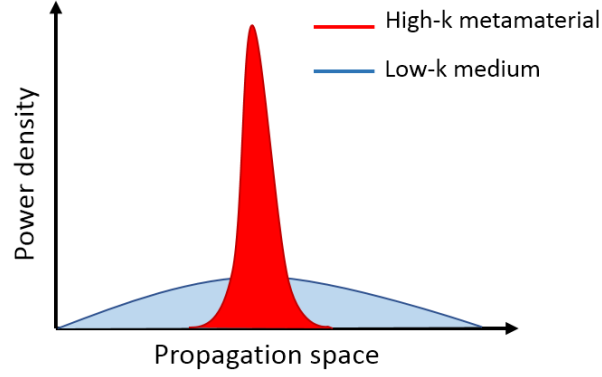


Figure 2. 19 Schematic of wave compression and energy density enhancement.

In chapter 4, it will be shown that the high- k acoustic metamaterial emitter developed in this work can yield extraordinary enhancement to the acoustic radiation power. By availing a high impedance medium to an embedded emitter, elevated power can be extracted from the source and coupled into free space. It should be noted that such an effect is similar to the Purcell effect common in electromagnetic metamaterials [34], [57], [58], [61], [83], [94] and that has been recently reported in acoustics [67].

2.5 Summary

The unique properties exhibited by high- k acoustic metamaterials deserve in-depth study and understanding. The fundamental criterion for creating a high wave vector medium for acoustic wave propagation is that there must be a vast difference in the mass densities between the constituent materials so that the lattice periodicity remains much smaller than the wavelength. A successful combination would create a material with enhanced acoustic energy transportation and radiation properties, as well as frequency-dependent energy enhancement characteristics. Exploiting these properties can lead to the development of new acoustic technologies, such as phonon routers, compact beam steering systems, passive and active acoustic filters, and switches.

This chapter has discussed the two categories of high- k acoustic metamaterials, namely elliptical and hyperbolic metamaterials, according to their equi-frequency contour plots. The typical properties exhibited by high- k acoustic metamaterials have been addressed, namely energy confinement and transport, radiation enhancement, and enhancement of control. High- k acoustic metamaterials exhibit radiation enhancement properties different from single cavity resonating materials. One method by which the metamaterial confines and transports the energy in acoustic waves was discussed and experimentally demonstrated using an anisotropic metamaterial waveguide. The design of these metamaterials, coupled with their unique characteristics, can give them the flexibility to tune their parameters, hence enhancing the control of their performance and characteristics. For example,

the frequency bandwidth of these metamaterials can be tuned by altering geometric parameters.

Because the metamaterials studied in this work are compact – their subwavelength unit cells being in the millimeter scale – a fiber optic probe was realized to enable their characterization without disrupting the acoustic field. The fiber optic acoustic point detector has a small size, broadband working range, and omnidirectional, making it ideal for use to perform spatial mapping of internal and external acoustic fields of the deep subwavelength structures of metamaterials. The optical sensing system and the metamaterial study method has also been discussed. This chapter has underscored the need to study high- k acoustic metamaterials along with the fascinating properties they can have and can serve as a framework to further the research in the area of high- k acoustic metamaterials.

Chapter 3: Low dimensional high- k acoustic metamaterials for reception

High- k acoustic metamaterials have incredible abilities to modify the acoustic waves within their subwavelength unit cells. Placing a sensor directly in the subwavelength cavities of the metamaterial can enable direct access to these modified waves within the structure. This would help provide access to high- k states and properties that typically occur well within or close to, the metamaterial medium. Metamaterials that allow for this type of capability can be very useful in a wide range of areas, including acoustic circuitry, acoustic filters, enhanced acoustic sensors, and sonars. In this chapter, reception-based high- k graded-index acoustic metamaterials are realized and studied. The exotic characteristics of this class of metamaterials are exposed through two main designs: a low-dimensional tapered planar metamaterial, and a conical shaped metamaterial. It is shown that, while maintaining a small, low-dimensional profile, these metamaterials can achieve strong wave confinement and energy enhancement properties, as well as spatial separation of frequency components within their structure, giving rise to a passive acoustic filter and switch.

Interestingly, this feat is analogous in functionality to the mammalian cochlea. For the first time, it is shown that such a simple structure is capable of functionally mimicking such a complex biological system. Additionally, the low-dimensional

planar metamaterial can be actively tuned, broadening the capability bandwidth of the structure. Such a tunable metamaterial platform enables the development of functional compact devices related to acoustic sensing and communication systems and expands the capabilities of the development of acoustic time-varying circuits and its related areas.

3.1 Motivation

A fundamental characteristic of high- k acoustic metamaterials is their ability to enhance control of their emissive and receptive characteristics, as discussed in section 2.4. When designing and realizing acoustic metamaterials, it is often desirable for the structures to have as small a footprint as possible so that they can easily be manipulated. Savings in terms of weight, complexity, and size, is usually beneficial because it enables effortless integration into small devices such as motherboards, and miniature platforms. The challenge, however, remains how to accomplish this feat because although the unit cells of these artificial structures are well in the subwavelength dimensions, the whole structure can often be bulky, posing severe limitations to their integration into other useful systems. For example, passive acoustic filters such as those developed using a technique called acoustic rainbow trapping can find immediate applications in areas such as electro-acoustic devices and circuits because they promise to relieve the electronic layer from some tasks such as filtering and amplification [12], [37], [96]. Ironically, however, because these devices tend to be bulky, with the whole structure usually measuring several wavelengths in size, their integration into where they find much use is hardly feasible. There have

been promising attempts to realize “acoustic rainbow trapping” metamaterials with a small footprint [38], but integrating sensing systems into such structures remains a challenge.

Furthermore, metamaterials that are only passive in design would have characteristics that are essentially frozen in scope, imposing limitations on their performance. Overcoming these challenges and further broadening the capability bandwidth of these passive metamaterial structures will provide obvious benefits in the study and uses of acoustic metamaterials, and they can enjoy such features as broader frequency bandwidths, energy transmission attenuation, beam steering, etc. [40], [43], [89], [91], [97] Since the unique characteristics possessed by acoustic metamaterials are afforded by the design and placement of their unit cell components, it follows that by enabling one or more of the physical parameters to be alterable, an active acoustic metamaterial can be realized [40], [89], [98], [99]. It, therefore, becomes easy to discern that low dimensional acoustic metamaterials with active tunable properties can be very desirable and holds the promise of solving the size constraint faced by many metamaterials while having a broad usability bandwidth.

In this chapter, low dimensional acoustic metamaterials with unique passive properties of signal amplification and filtering are developed and studied (Figure 3. 1(a) - (c)). One of these low dimensional metamaterials is capable of such active properties as switching and delay control (Figure 3. 1 (d)). With the capability of sustaining waves with wave vectors much higher than the surrounding free space, these devices enjoy unique characteristics of energy enhancement and enhancement of wave control. It is also shown here that this metamaterial design can achieve key

properties of bio-acoustic systems, such as wave trapping, amplification, and spectral decomposition present in mammalian cochleae (Figure 3. 1(b)).

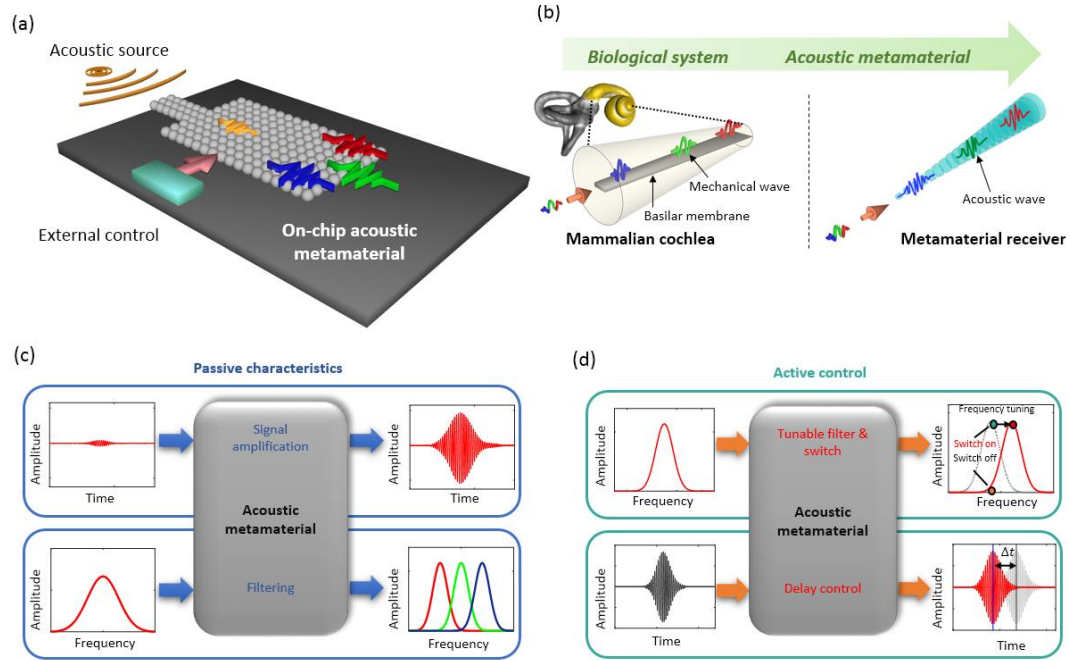


Figure 3. 1 (a) Schematic of the low-profile on-chip acoustic metamaterials with active capabilities. (b) Schematic showing the mechanical wave amplification and spatial frequency separation property of the mammalian cochlear (left), and equivalent pressure amplification and spatial separation of frequencies exhibited by the conical metamaterial receiver (right). (c) and (d) Illustration of the passive characteristics and active properties of the planar low dimensional “on-chip” acoustic metamaterial, respectively.

The planar acoustic metamaterial is designed to enable active reconfiguration of its geometry. The design makes use of a liquid to reconfigure the metamaterial in

real-time, giving rise to such active properties as frequency tuning and switching, as well as pulse retardation (Figure 3. 1 (d)). This tunable acoustic metamaterial has a low profile, which renders it suitable for integration in confined spaces such as embedding in mechanical components or inclusion into electrical components on the chip level. An area that can benefit from this feat is in electro-acoustic sensing systems by moving such tasks as amplification, filtering, and phasing from the electronic layer to the physical layer.

3.2 Metamaterial design, fabrication, and experimental setup

3.2.1 Design and fabrication

Two types of low dimensional acoustic metamaterial receivers are studied in this work: the planar “on-chip” acoustic metamaterial and the conical receiver acoustic metamaterial. The planar on-chip acoustic metamaterial is based on the graded-index class of acoustic metamaterials, with unit cells comprising of solid-fluid (polymer-air) anisotropic subunit composites. The entire metamaterial structure is tapered so that the gradual increase in the plate sizes produces a medium of increasing refractive index with minimal impedance mismatch.

The metamaterials consist of plates 1 mm thick and 5 mm in height. The width of the plates increases linearly from 1mm to 15 mm at the aft end. Two different periodicities were used in this study. To study the passive properties of the device, a metamaterial with a periodicity of 3 mm consisting of 30 plates with 2 mm

gaps was used (Figure 3. 2 (a), bottom). This design boasts a slightly higher frequency response and finer passive frequency filtering characteristics. For investigating the active properties, a metamaterial with a periodicity of 5 mm is used because its larger gaps of 4 mm reduced the capillary and meniscus effect observed when liquid is added, which improves its active performance compared to that with a 3 mm periodicity (Figure 3. 2 (a), top). This design has 18 plates as opposed to 30 in the previous design to maintain the overall length of 83 mm. The design also has “arms” with grooves used for fixing an acoustic sensor on the last gap during experiments, as well as a surrounding casing to render it capable of holding liquid. The devices were 3D printed (Connex Object500 printer) using a rigid polymer (Verowhite Plus).

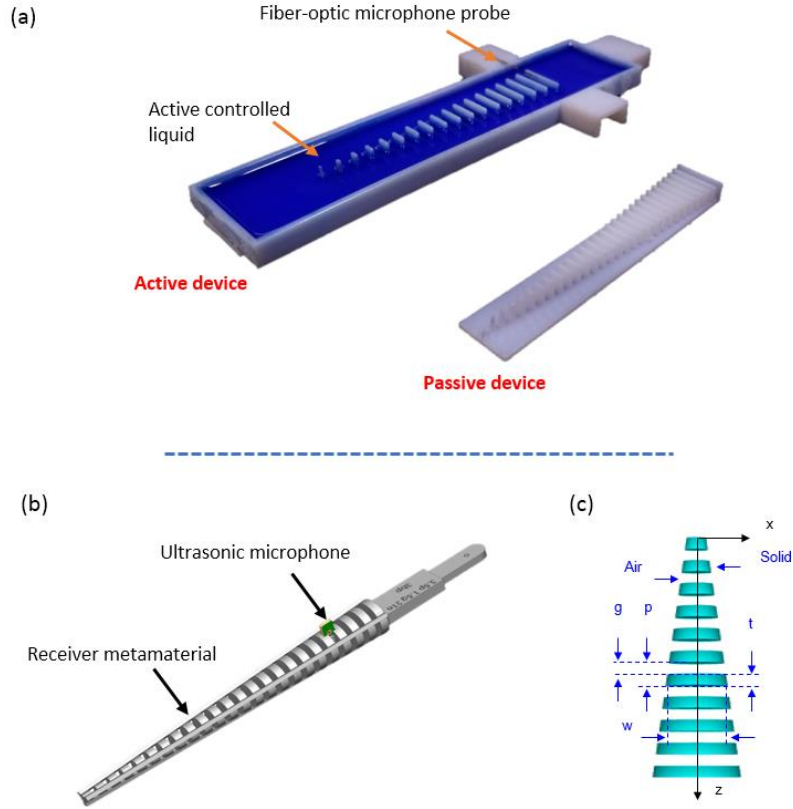


Figure 3. 2 (a) Photo of passive and active on-chip metamaterials. The passive device consists of 30 plates separated by 2 mm air gaps while the active device consists of 18 plates separated by 4 mm gaps. The active device is designed in a surrounding container to hold liquid, with arms for sensor attachment. Isopropanol (dyed blue in the picture) is used to actively tune the exposed plate heights of the metamaterial. (b) CAD rendering of the conical receiver metamaterial. The microphone used is a Sisonic ultrasonic microphone (SPU0410LR5H-QB). (c) The thickness of the plates and air gaps are $t = 2$ mm and $g = 1.5$ mm, respectively. The device consists of 24 plates, with widths w ranging from 2 mm to 8.95 mm.

For the conical receiver metamaterial (Figure 3. 2 (b)), its dimension needed to satisfy the Wentzel-Kramer-Brillouin (WKB) condition for the adiabatic

compression of the acoustic waves [100], [101], for which a length of $L \approx 6\lambda$ was chosen. Acoustic waves travelling through the reception metamaterial would encounter a serious impedance mismatch at the metamaterial-free space interface at the rear, which would create a backward traveling wave in the metamaterial. To minimize the influence of this backward traveling wave on the inserted microphone, three additional disks are included behind the design disk. The acoustic metamaterials were designed using 3D software (Solidworks) and were realized via 3D printing. A Stereolithography-type printer (Formlabs Form 2) was employed to realize the conical metamaterial structures out of a rigid polymer (White FLGPWH04).

3.2.2 Experimental setup

To conduct the experiments with the low-dimensional metamaterial receivers, each device was placed in front of an ultrasonic speaker (Pettersson, LP 400) with a reference microphone (B&K 4939-L-002) between them. The fiber optic microphone used to probe the subwavelength structures of the metamaterial was connected to its optical interrogation system comprising of a light source (ThorLabs 1310nm SM), a tunable filter (Micron-Optics FFP-TF2), a 2x1 coupler (Gould Fiber optics 1-28450 78) and a photodetector (New Focus Model 2011) (Figure 3. 3 (a)). The B&K reference microphone (Figure 3. 3 (b), top) was used to calibrate the fiber optic probe so that the acoustic pressure levels could be directly obtained from the probe readings. A stage (Newport UTM50PE1) was used to precisely position the probe between the metamaterial gaps for the characterization and spatial mapping. A DAQ (NI USB 6259) relayed signals between the sensors and speakers and a computer,

where the signals were generated and processed using LabVIEW software. For the planner on-chip acoustic metamaterial, the setup was such that it was flush with the surface, with the speaker 41.5cm away.

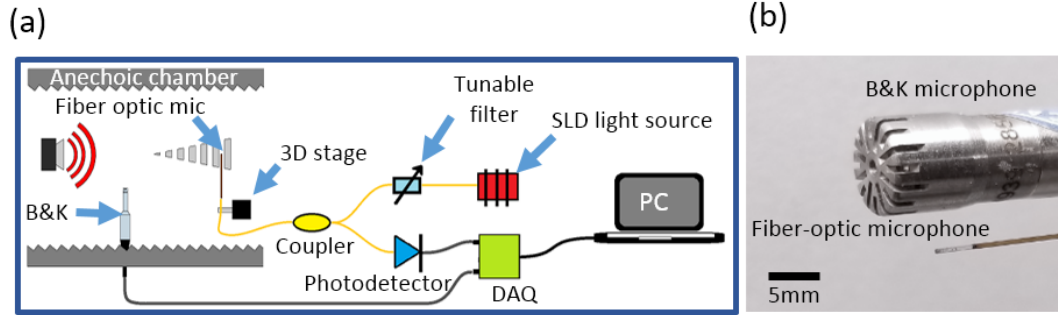


Figure 3.3 (a) Schematic of the experimental setup and the sensing system. The fiber optic detection system consists of a superluminescent diode (SLD) light source, tunable filter, coupler, and a photodetector connected to a computer through a data acquisition (DAQ) card. (b) Picture of the B&K reference microphone and the fiber optic microphone. The B&K has a diameter of 7 mm, while the fiber optic microphone is 323 μm in diameter.

3.3 Metamaterial characterization studies

The graded-index anisotropic metamaterial design that these metamaterials are based on has many rich reception-based properties. These properties come as a result of the interaction of acoustic waves with their subwavelength unit cells, and the properties are very similar in both types of metamaterials. Because these properties are best

demonstrated using the planar metamaterial, extensive use is made of this design to showcase the formidable properties afforded by this type of metamaterial. Care would, however, be taken to highlight the unique differences between the two, such as that afforded by the active component of the planar on-chip metamaterial.

To begin the study on the planar on-chip metamaterial, 2D FEM simulations are conducted on the metamaterial to gain an understanding of its wave propagation and guiding mechanisms. In Figure 3. 4 (a), it is evident from the frequency response curve of the 30-plate metamaterial that 2 distinct modes are supported: the fundamental mode at 18 kHz and a higher-order mode at 34 kHz. The first mode is discernable from the dispersion curve in Figure 3. 4 (b), which corresponds to the frequency where the vertical asymptote is reached at 18 kHz (cut-off frequency). Aside from the apparent amplitude difference between the two modes, there is a remarkable difference in their mode shapes, which can be observed by employing a FEM spatial pressure mapping of the last gap at the frequencies. It reveals that the fundamental mode shows a centrally located single peak, while the higher-order mode exhibits a tri-peak mode shape. This higher-order mode is consistent with the third-order modes because this metamaterial is capable of exciting only antisymmetric eigenmodes (Figure 3. 4 (a), insert).

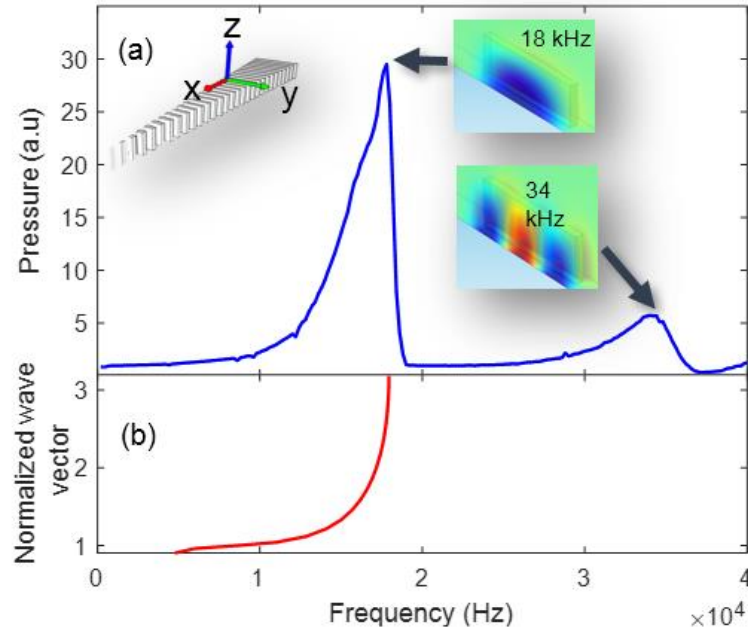


Figure 3. 4 (a) Simulation of the frequency response characteristics of the last gap of the planar passive acoustic metamaterial. The inserts are simulations of the mode shapes of the fundamental mode (18 kHz) and a higher-order mode (34 kHz). (b) Normalized dispersion curve of the last gap of the metamaterial from the simulation. Normalization is with respect to the free space wave vector.

These simulations are further experimentally verified by probing the last gap of the acoustic metamaterial using a low-profile fiber optic microphone (Figure 3. 5 (a) and (b)). These experimental scans from the gap center outward (y-axis) and upward (z-axis) agree with the simulation and are useful findings in understanding the optimal position for an acoustic pressure sensor placement.

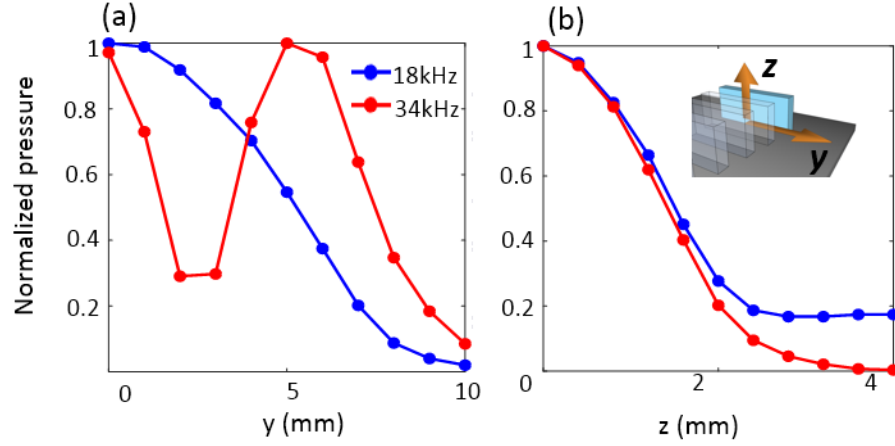


Figure 3. 5 Experimental scans of the last gap of the metamaterial to show the mode shapes of the first two modes. (a) shows outward scans (y-direction) from the center, while (b) shows upward scans (z-direction) from the center.

Next, a spatial mapping of the acoustic field of the metamaterial gaps and the surrounding space is done, which reveals the metamaterial's operation in confining 18 kHz acoustic waves towards its last plate (Figure 3. 6 (a)-(d)). The experimental results agree with the simulations, of which interesting observations can be made. First, the acoustic pressure field is observed to be continuous along the propagation direction of the metamaterial as a result of the metamaterial's periodicity being much smaller than the free-space wavelength ($\lambda_{18\text{ kHz}} \sim 19\text{ mm}$). Therefore this discrete metamaterial structure can be regarded as a continuous medium along the propagation direction[27]. Furthermore, it is also perceptible that the metamaterial gradually increases the wave vector in the propagation direction from $k_{air} = 332.6\text{ m}^{-1}$ to $k_{MM} = 1047.2\text{ m}^{-1}$ at the last gap, giving an effective refractive index of $n_{eff} =$

$k_{air}/k_{MM} = 3.15$ at 18 kHz. This observation is also substantiated in the metamaterial dispersion plot (Figure 3. 4 (b)), which verifies that this on-chip metamaterial is highly dispersive, boasting high- k states.

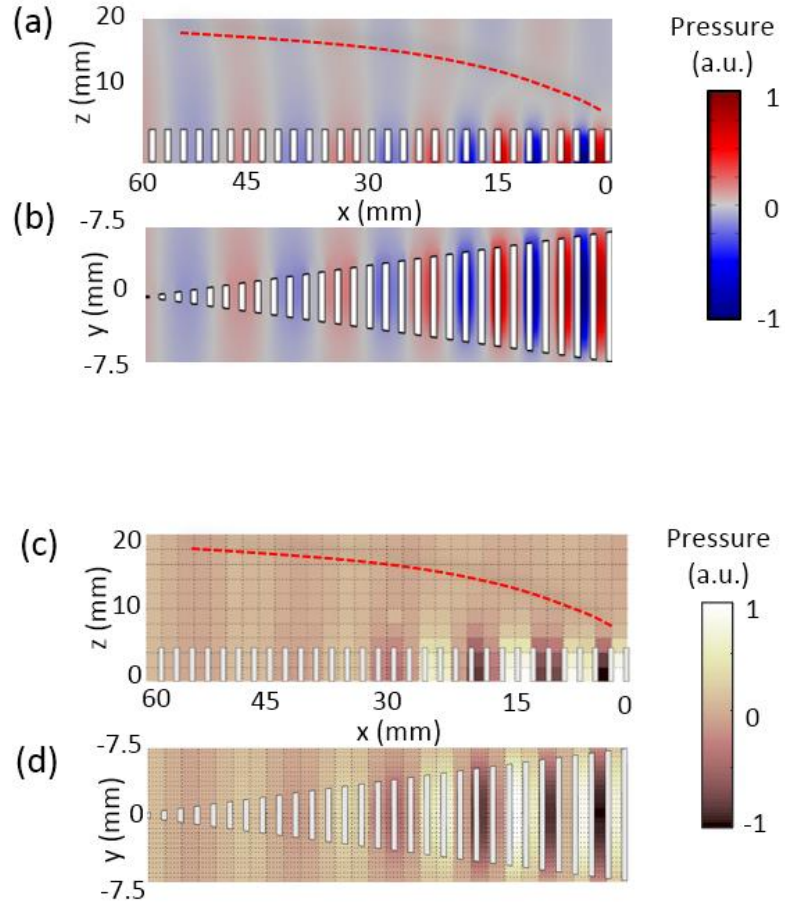


Figure 3. 6 Simulation (a) and (b) and experimentally obtained (c) and (d)) spatial mapping of the acoustic field of the metamaterial to an 18 kHz incident plane wave. The red dotted lines in (c) and (d) highlight the confining effect of the metamaterial due to the gradual change in refractive index across the space.

It is worth noting that this change in the wave vector of the propagating waves in the metamaterial space does not occur abruptly across the air – metamaterial interface in the x - y and x - z planes. Rather, this change is gradual and becomes more pronounced with the propagation of the wave in the metamaterial until the maximum wave vector condition for periodic structures $k_{max} = \pi/P$, where P is the periodicity,

is reached. This k_{max} condition corresponds to the wave vectors in the first Brillouin zone boundary [102], [103]. The interface between the unaffected free space propagating waves and the high- k waves results in a semi-cubical parabolic convergence phenomenon that can be perceived in the spatial mapping of the acoustic field (Figure 3. 6 (a)-(d) highlighted by the red dotted lines). Furthermore, the spatial concentration of the wave energy is achieved through the compression of the wavelength along the length of the metamaterial, which enables this metamaterial to achieve a higher acoustic density of states [14] (Figure 3. 7 (a) and (b)). This wave compression effect is a key phenomenon in graded-index acoustic metamaterials and produces sound amplification as well as introduces phase delays.

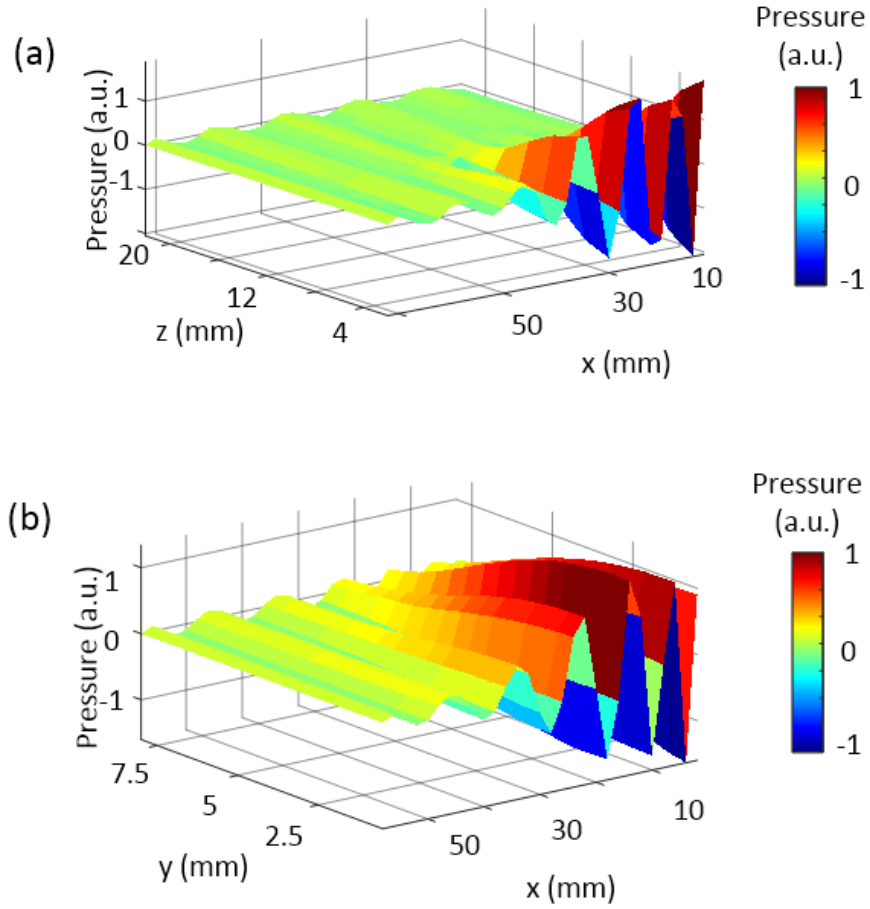


Figure 3. 7 3D plots of the experimentally obtained spatial field mapping of the acoustic field along the vertical plane (a) and the horizontal plane (b).

3.3.1 Role of vertical space above the on-chip metamaterial

It has been demonstrated that the x-y space (according to the coordinate system in the insert of Figure 3. 4 (a)) around this type of graded-index acoustic metamaterial is necessary for the propagating waves due to the evanescent coupling mechanism [27].

In addition to that, it is shown here that the vertical space (z-space) above the on-chip acoustic metamaterial plays a critical role in the functionality of this device. The open design allows for evanescent coupling of the acoustic waves in the adjacent gaps to take advantage of the space above the structure, such that this metamaterial assumes characteristics beyond a 2D device.

To observe this phenomenon, two simulation studies are performed on two types of unit cells. In Figure 3. 8 (a), the velocity field of a single periodicity of the uncovered metamaterial is simulated. It can be observed that the gap-to-gap coupling of the acoustic waves makes use of both the sides of the metamaterial gaps (arrows V_a) and the top of the metamaterial (arrows V_b). If the top of the metamaterial is covered (Figure 3. 8 (b)), the coupling is observed to make use of only the sides of the metamaterial.

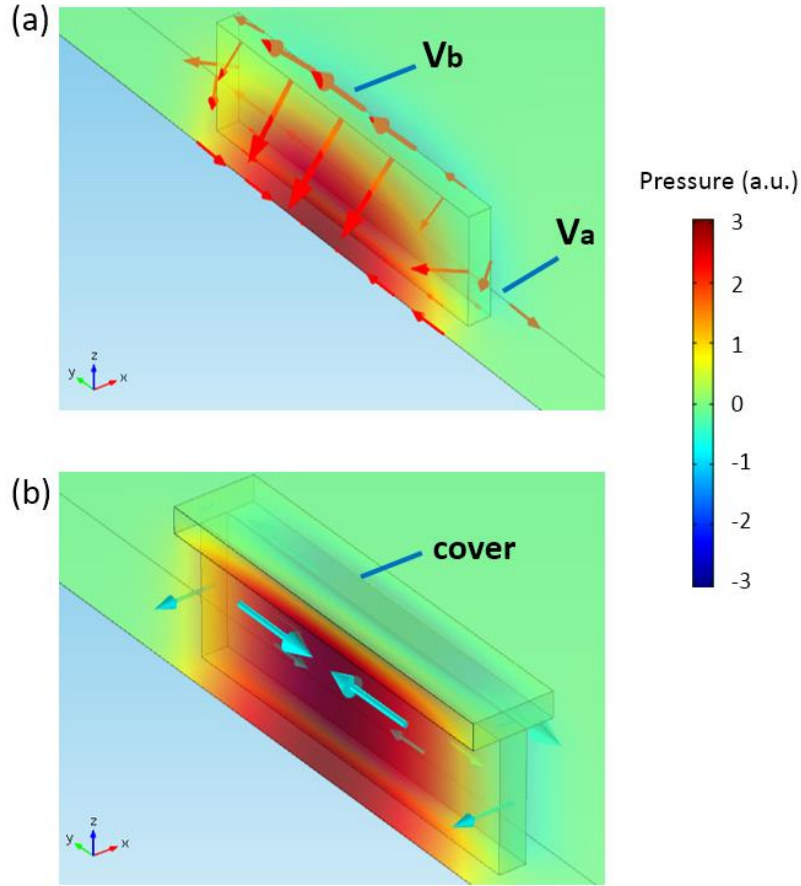


Figure 3. 8 (a) Simulated unit cell of an uncovered metamaterial structure. The plate is 1 mm thick, 5 mm tall, and 15 mm wide. The unit cell comprises of the plate and a 2 mm air gap (1 mm on each side), with an imposed repeated boundary condition to simulate infinite plates. The red arrows indicate the velocity profile of the air media. (b) A simulated unit cell of a covered metamaterial structure. The dimensions of the unit cell are similar to that in (a), except for the added 1 mm thick cover. The turquoise arrows indicate the velocity profile of the air media.

To demonstrate the effect that this phenomenon has on the metamaterial's frequency response, frequency sweep experiments are performed on three

metamaterials with different heights (Figure 3. 9 (a)). In one set of experiments, the top of the metamaterials is left open to enable the evanescent coupling of acoustic waves to take advantage of the top of the metamaterial gaps as in Figure 3. 8 (a). In this configuration, it can be observed from the frequency response of these metamaterials that the height of the metamaterial plates determines the optimal and cut-off frequency of the structures, with taller plates having lower cut-off frequencies and vice versa (Figure 3. 10 (a)).

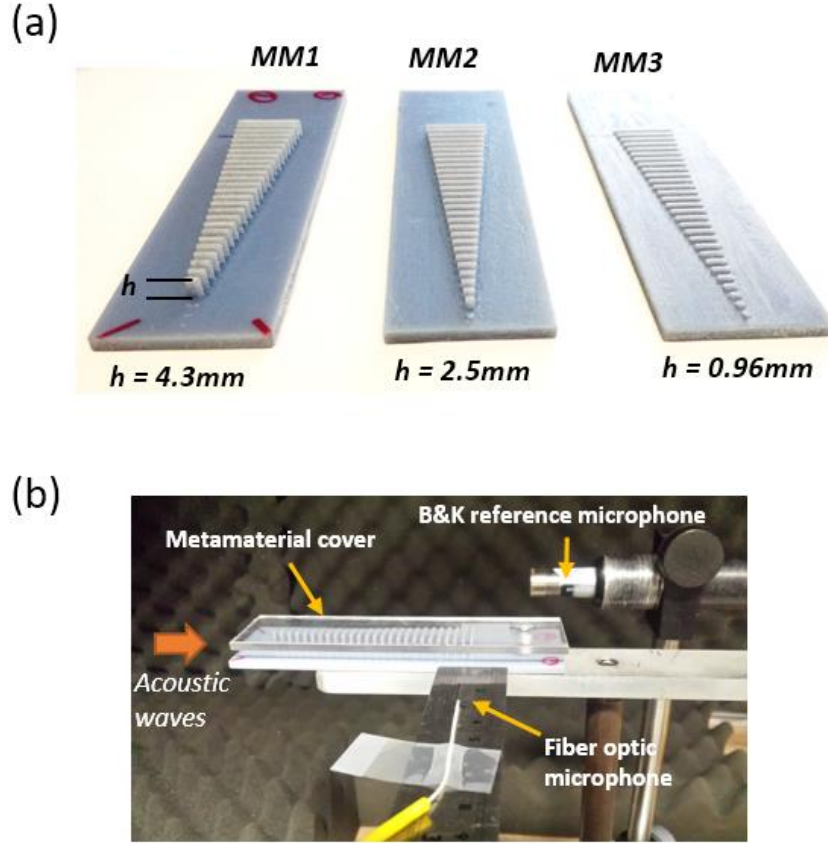


Figure 3. 9 (a) Metamaterials of different heights used to demonstrate the use of the space above the metamaterial structure. Each metamaterial shown has a periodicity of 2 mm with a gap size of 1 mm. The heights of the metamaterial plates are as shown. (b) Experimental setup of the showing MM1 covered with an acrylic plate.

In another configuration, the top of the metamaterial is covered (Figure 3. 9 (b)) to confine evanescent coupling to occur only through the sides of the structure, as in Figure 3. 8 (b). The frequency sweep in this configuration, as depicted in Figure 3. 10 (b), reveals that the height difference between the metamaterial plates plays no role in the cut-off frequency of the metamaterial. As such, achieving tunability by changing the plate height is not possible with the covered configuration. It can also be

observed that the covered devices have an overall lower working frequency than their uncovered counterparts, with the plate heights playing a role only in the gain of the devices. It should be noted that these metamaterials are printed with a coarser resolution compared to the prints used in the rest of this chapter. As such, the gains presented are comparatively lower than expected, which is due to the viscous and thermal losses in these structures.

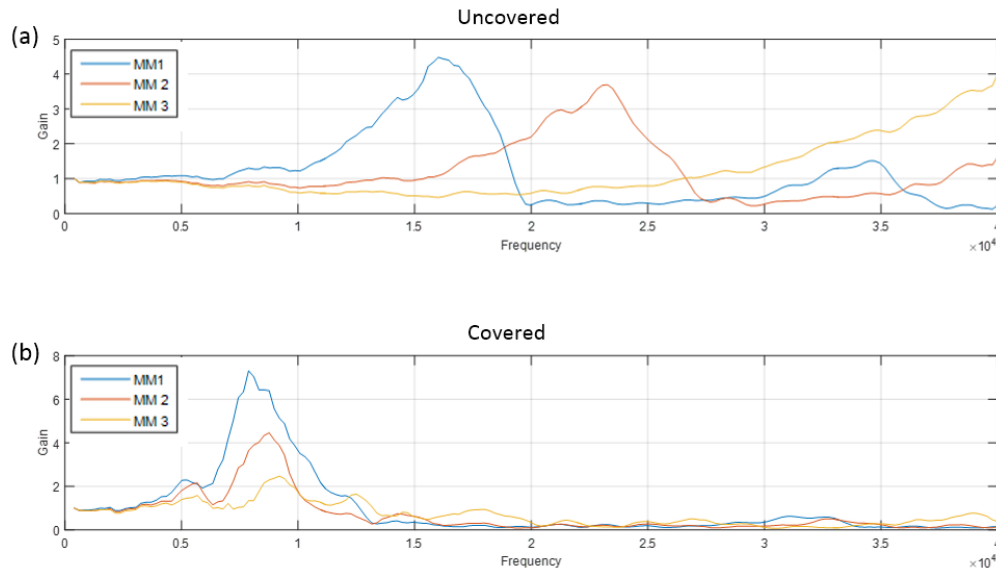


Figure 3. 10 (a) Frequency response of the uncovered metamaterials. (b) The frequency response of the covered metamaterials.

3.4 Broadband filtering effects of the receiver metamaterial

These low dimensional acoustic metamaterials are capable of broad-band filtering of acoustic waves. To see these characteristics at work, the on-chip metamaterial is subjected to a series of Gaussian pulses. First, to verify the ability to amplify acoustic pulses well within the working frequency bandwidth of its last plate, the passive metamaterial is insonified with a Gaussian pulse centered at 18 kHz with a 1 kHz bandwidth (Figure 3. 11 (a) and (b)). It is discernable from the time domain plots in Figure 3. 11 (a) that there is a markedly significant difference in amplitude between the pulses with and without the metamaterial. This signal amplification is also evident in the frequency domain of the pulses in Figure 3. 11 (b).

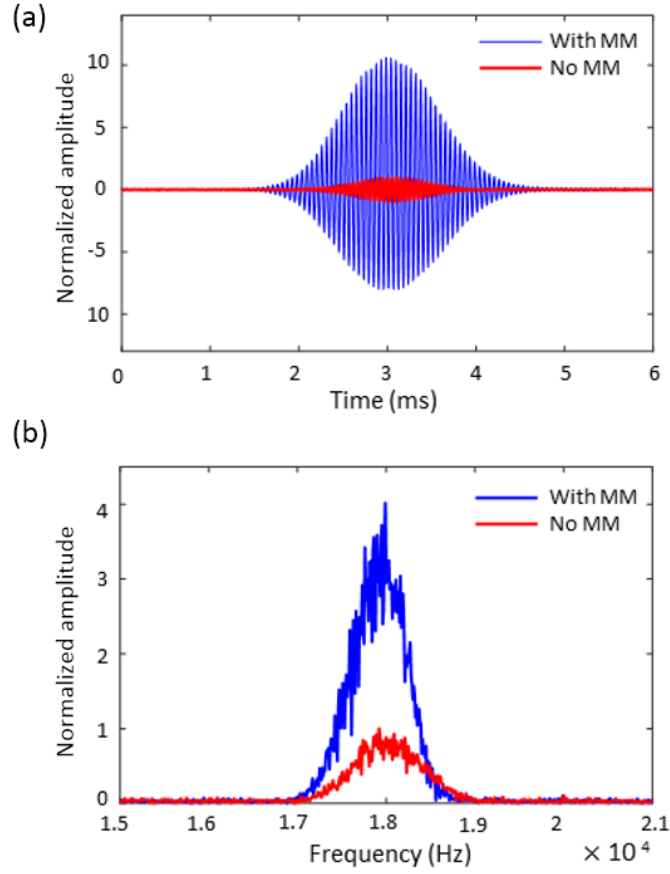


Figure 3. 11 (a) Time-domain comparison of an 18 kHz pulse with a bandwidth of 1 kHz through the metamaterial versus without the metamaterial. Normalization is with respect to the peak of the pulse without metamaterial. (b) Comparison of the FFT of the pulses in (a).

Next, the filtering effect that the metamaterial has on a pulse is verified by subjecting the metamaterial to a pulse with a center frequency of 20 kHz and a normalized bandwidth of 0.2. This pulse would have more than half of its frequency components beyond the cut-off frequency of the metamaterial. If the probe is inserted in the last gap of the metamaterial where the cut-off frequency is ~ 19 kHz and insonified, the pulse experiences both signal amplification and broadening in the time

domain, as depicted in Figure 3. 12 (a). A frequency analysis of the received pulses at the probe with and without the metamaterial shows that the former is devoid of all frequencies above 19 kHz, which accounts for the temporal pulse broadening effect (Figure 3. 12 (b)).

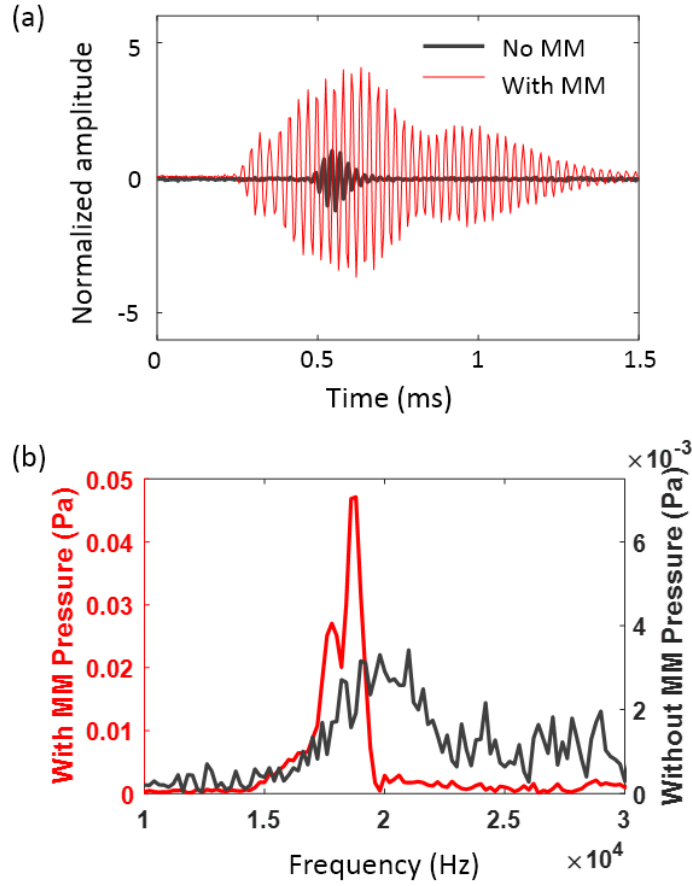


Figure 3. 12 (a) Time-domain comparison of a 20 kHz pulse with a bandwidth of 4 kHz through the metamaterial versus without the metamaterial showing the pulse broadening and filtering effect of the metamaterial. Normalization is with respect to the peak of the pulse without metamaterial. (b) Frequency domain comparison of the pulses in (a).

Interestingly, these signal amplification and filtering phenomena occur at different frequencies for each metamaterial gap, such that higher frequencies are amplified and eventually arrested at the front of the metamaterial where the width of the gaps are smaller (increasing x -direction). A frequency sweep of pure tones at each

gap demonstrates this feat, as illustrated in Figure 3. 13. This on-chip metamaterial is, therefore, a highly broadband structure whereby the required frequency band can be effectively achieved by placing the sensor at various positions within the structure. For example, the cut-off frequency – hence the passive bandwidth – at the 16th gap (Gap D in Figure 3. 13) of this on-chip device is ~ 27.8 kHz. Because of its ability to spatially separate frequencies along its length, it can thus act as a broadband passive acoustic filter.

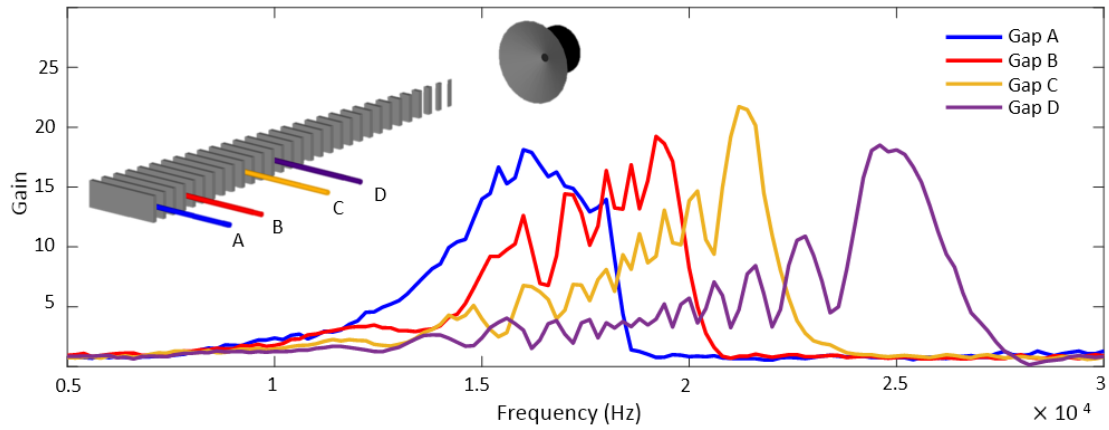


Figure 3. 13 Frequency response gain plots of different gaps of the metamaterial. Pure tone pulses at 200 Hz intervals were used. The gaps A-D correspond to locations 0, 9, 27, and 36 mm from the last gap.

3.5 Active tunable on-chip metamaterial

The bandwidth of the on-chip metamaterial device can be further broadened and arbitrarily modified by introducing an active component to the 5 mm periodic

metamaterial structure. The active component entails modifying the height h of the exposed plates using a liquid, such that h decreases with an increase in the liquid level (Insert in Figure 3. 14). A characterization of the last gap of the metamaterial structure using the fiber optic probe and reveals that as h is decreased, the frequency bandwidth of the metamaterial shifts to accommodate higher frequencies. For example, decreasing the height from 4.5 mm to 3.5 mm brings about a change in the cut-off frequency of the last gap from ~18 kHz to 20 kHz (Figure 3. 14).

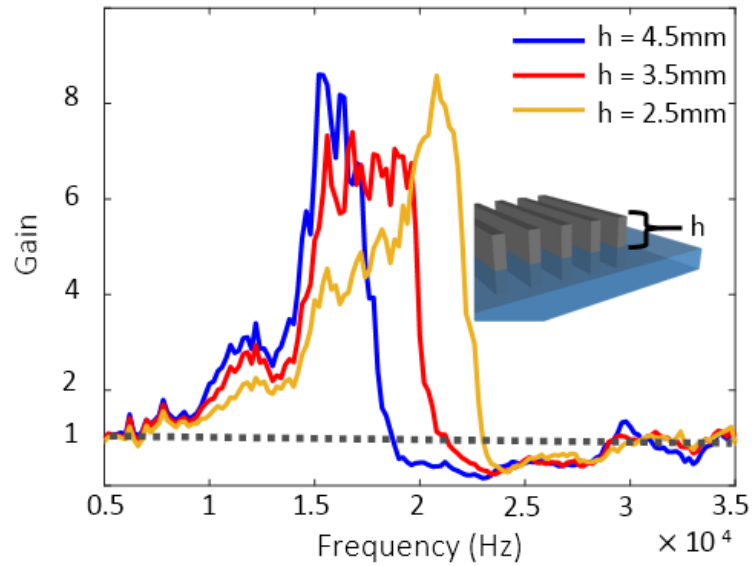


Figure 3. 14 Experimentally obtained gain plots at different plate heights. The insert depicts a schematic of the exposed plate height h .

Therefore, the bandwidth of the last gap of this on-chip device has been extended by 2 kHz with a change of 20% in the metamaterial structure. The dispersion curves at different plate heights in Figure 3. 15 demonstrate this

phenomenon, where the cut-off frequency corresponds to the frequency at which the group velocity $v_g = 2\pi \frac{\partial f}{\partial k} \rightarrow 0$. Because the group velocity of the propagating waves is comparatively lower in the high- k region of this metamaterial than in low- k and non-dispersive materials (such as air), the momentum change Δk is thus significantly higher in this high- k metamaterial (highlighted). This means that a slight change in h will produce a correspondingly substantial change in the bandgap of the structure, which is proof of this acoustic metamaterial's ability to enhance control of acoustic waves – a fundamental characteristic of high- k acoustic metamaterials.

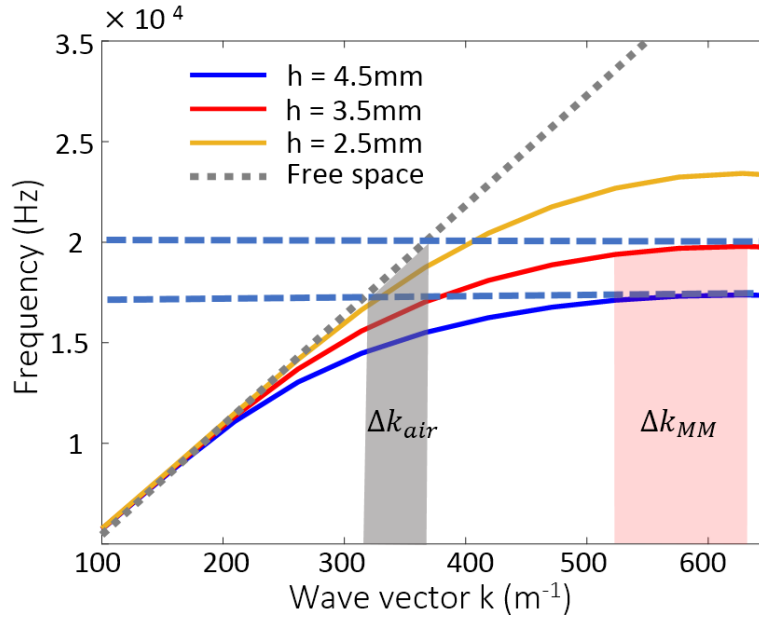


Figure 3. 15 Dispersion curves of the metamaterial at different plate heights and of air (grey dotted line) from the simulation.

In the experimentally obtained gain plots (Figure 3. 14 (a)), this tunability phenomenon is verified, and it is also evident when this metamaterial switches from amplification mode (passband) to attenuation mode (stopband) with respect to the unity gain line (dotted line). As such, this on-chip device can effectively be used to “switch on” and “switch off” the propagation of sound, which can be a useful function in signal processing.

An additional property that emerges as a direct consequence of being able to tune the dispersion of the metamaterial is temporal wave retardation. Because the wave vector can be parallel to the group velocity as evident from the dispersion curve, the metamaterial will have a frequency-dependent refractive index greater than that of air, which will cause a wave packet to experience temporal retardation when compared to its counterpart propagating in the free-space (Figure 3. 16 (a)-(d)).

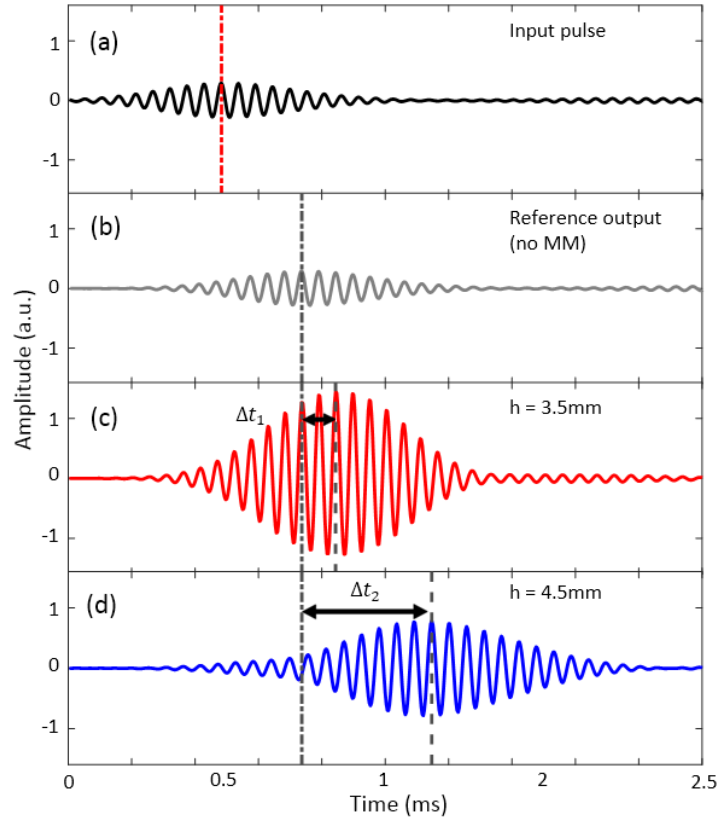


Figure 3. 16 (a)-(d) Comparison of an 18 kHz pulse with a bandwidth of 5.4 kHz (a) through the metamaterial at different plate heights. (b) indicates the reference output for a pulse propagating in the free-space (no metamaterial). The time pulse delays Δt_1 and Δt_2 are between the reference pulse (b) and the pulses through the metamaterial at 3.5 mm and 4.5 mm heights, respectively.

Since changing h results in a shift in the dispersion curve, a corresponding change in the pulse retardation results. For example, the group velocity v_g of the center frequency of the pulse (18 kHz) changes from 0 m/s at $h = 4.5$ mm to ~ 128.6 m/s at $h = 3.5$ mm. Additionally, because the frequency is not directly proportional to

the wave vector, the group velocity will be different from the phase velocity for a given wave packet. This implies that the phase velocities of different components of a wave packet also experience predictable changes when h is altered. These pulse retardation and phase manipulation capabilities of this on-chip acoustic metamaterial open many novel possibilities in the manipulation of acoustic waves. Analogies could thus be developed between electronic circuit components and acoustics, furthering the research in innovative acoustic circuits.

3.5 Metamaterial approximation of the mammalian cochlea

The signal amplification and filtering properties exhibited by these low dimensional high- k acoustic metamaterial receivers have close similarities in functionalities to the mammalian cochlea. To demonstrate this, the conical metamaterial and the cochlea system are both analyzed in this section.

3.5.1 The mammalian cochlea

Many mammals have specialized auditory capabilities that depend on wave manipulation and signal processing by their cochlear systems. This biological organ has two important functions: amplification of weak acoustic signals, and decomposition of complex acoustic signals into different frequency bands for spectral separation and analysis in the cerebral cortex of the brain [104]–[106]. It can do this due to unique wave response properties of the basilar membrane (BM), which is an

active pseudo-resonant structure with varying stiffness across its length [107]–[109]. Acoustic signals are admitted into the BM structure via a system of diaphragms and bones which convert the airborne acoustic waves into mechanical waves.

3.5.1.1 Analytical model of the basilar membrane of the mammalian cochlea

For simplicity, the coiled structure of the BM is representatively unwrapped (Figure 3. 17) so that an analytical comparison can be made between the BM and the acoustic metamaterial receiver. Here, the traveling wave properties principally depend on the stiffness variation $S(z)$ along the basilar membrane. As illustrated in Figure 3. 17, the BM structure is narrow near the base with the largest stiffness, and gradually becomes wider at the apex with a decreasing stiffness.

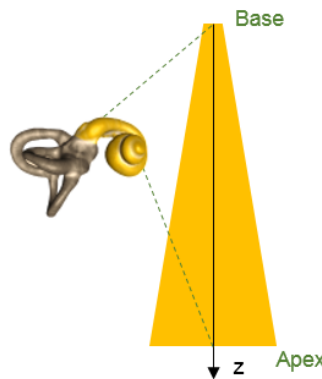


Figure 3. 17 Schematic of the biological cochlea uncoiled for simplicity.

The stiffness distribution along the BM can be approximately described as [110]:

$$S(z) = S_0 e^{-\frac{2z}{L_0}} \quad (3.1)$$

Here, z represents the propagation axis, the coefficient $S_0 = 1.0 \times 10^7 \text{ gs}^{-2} \text{ mm}^{-2}$, and $L_0 = 5 \text{ mm}$ is a characteristic length. The admittance of the mechanical wave along the BM propagation axis can be expressed as:

$$Y_{BM}(z, \omega) = \frac{i\omega}{S(z) + i\omega R + \omega^2 M} \quad (3.2)$$

where ω is the angular frequency, $R = 2.0 \text{ gs}^{-1} \text{ mm}^{-2}$ and $M = 1.5 \times 10^{-3} \text{ gmm}^{-2}$ are effective damping and mass of the BM, respectively, and are defined per unit area [110]. To establish an intuitive comparison between wave propagation in the BM and the acoustic metamaterial, the admittance Y_{BM} of the BM could be seen as analogous to the effective refractive index n_{eff} of the metamaterial. From equation 3.2, the wave admittance Y_{BM} is frequency and position-dependent, rendering dispersive and graded-index properties. Further, the wavenumber of the BM waves can be derived as:

$$k_{BM}(z, \omega) = \sqrt{\frac{-2i\omega\rho}{h} Y_{BM}} \quad (3.3)$$

where $\rho = 1.0 \times 10^{-3} \text{ g/mm}^3$ is the fluid density, and $h = 1 \text{ mm}$. From equation 3.3, it is evident that the wavenumber $k_{BM}(z, \omega)$ varies with position and frequency.

A plot of k_{BM} as a function of distance and frequency demonstrates this relationship (Figure 3. 18 (a) and (b)).

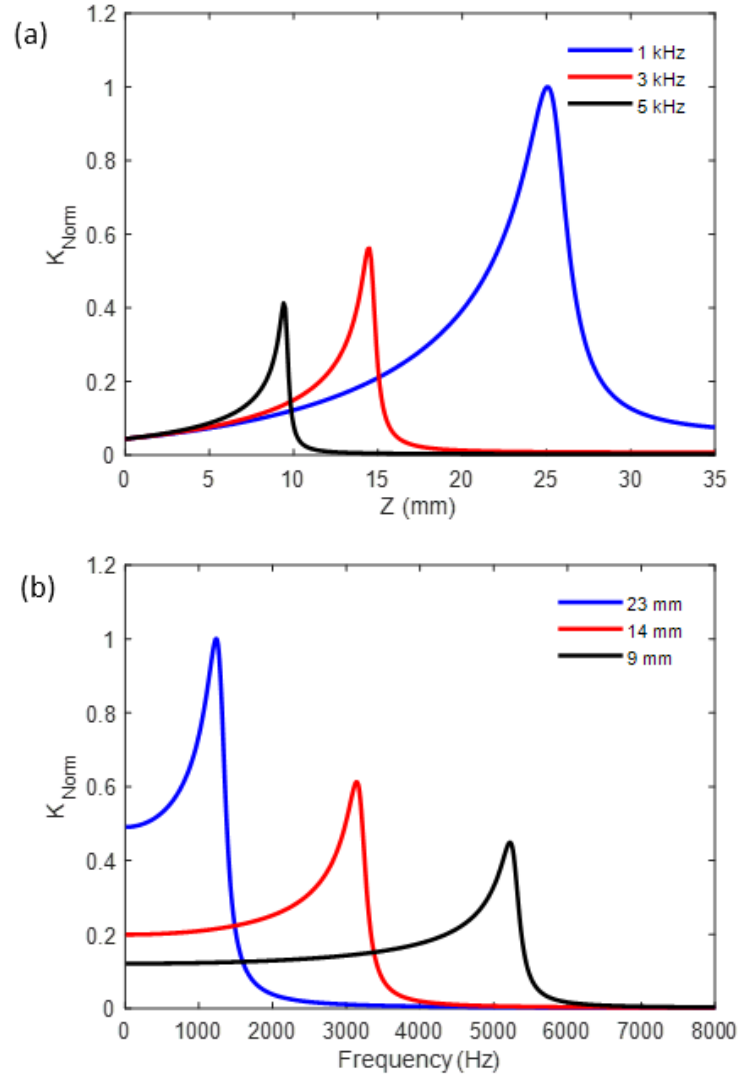


Figure 3. 18 Analytically obtained normalized wave vector as a function of distance (a) and frequency (b) of the basilar membrane of the biological cochlea for three frequencies.

As illustrated in Figure 3. 18 (a), in the BM, the wavenumber $k(z, \omega)$ of the travelling wave increases roughly exponentially with distance z for a given frequency. Also, for a given distance z , the wavenumber in the BM increases roughly exponentially with the frequency (Figure 3. 18 (b)). Correspondingly, the wavelength decreases as a wave travels from the base toward the apex of the BM, “piling up” the energy into increasingly smaller regions as the wave propagates. Once the wavenumber k_{BM} is known, the mechanical response of the cochlea can then be calculated using the Wentzel–Kramers–Brillouin approximation (WKB) method [111]. This response could be characterized by the displacement of the BM produced by a pure tone:

$$D(z, t) = Ak_{bc}(z, \omega)^{3/2} e^{-i[\omega t - \phi(z)]} \quad (3.4)$$

where $\phi(z) = \int_0^z k_{bc}(z, \omega) dz$ denotes the integral of the accumulating phase shift and gains or losses as the wave propagates along the BM, A is the wave amplitude at the base of the BM, and $\omega = 2\pi f$ is the driving frequency. From equations 3.3 and 3.4, it is evident that the mechanical wave motion of the BM is directly related to the wavenumber $k(z, \omega)$ (Figure 3. 18 (a), (b)). The mechanical waves propagate from the base of the BM toward the apex with decreasing wavelength but increasing in strength up to a position of peak amplitude, and beyond which they decay rapidly (Figure 3. 19 (a)).

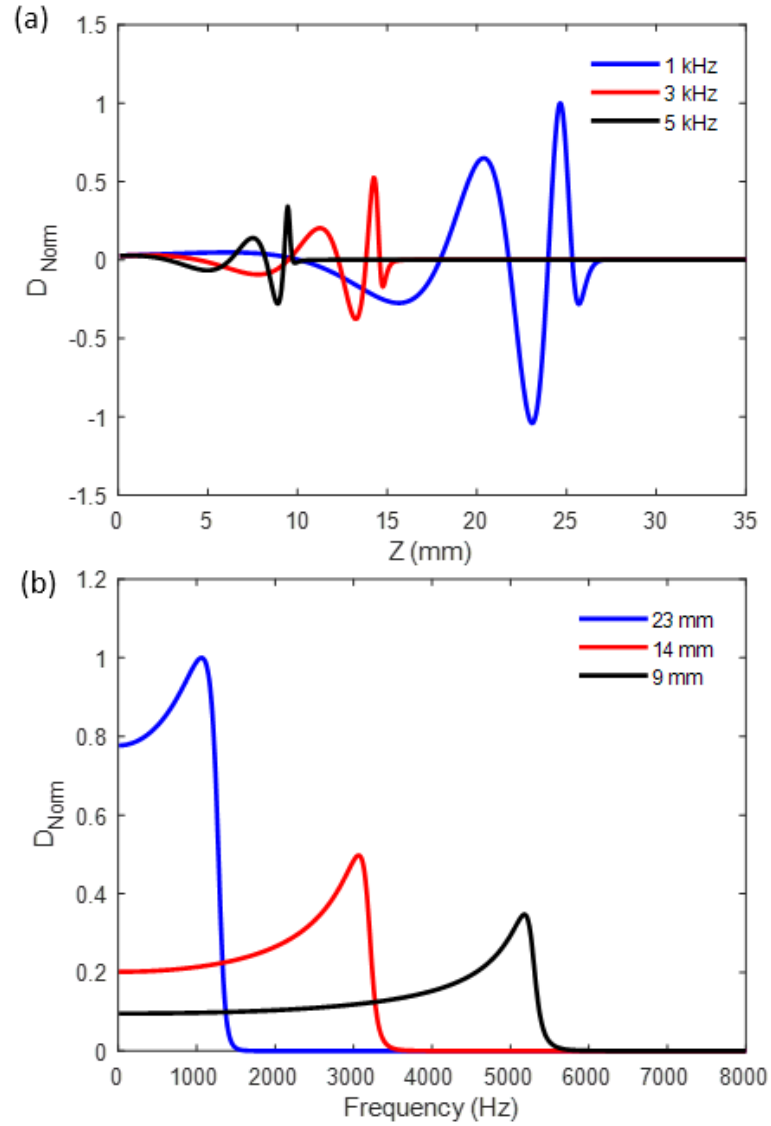


Figure 3. 19 Analytically obtained normalized displacement as a function of distance (a) and frequency (b) of the basilar membrane of the biological cochlea for three frequencies.

This progressive concentration of wave energy leads to an increase in the wave amplitude (displacement of BM), proportional to wavenumber k as the waves

travel. Near the cutoff point, the energy in the wave decreases rapidly, resulting in a rapid decay of the wave amplitude. These properties of the traveling waves in the BM also lead to a unique frequency response, in which local sections of the BM are tuned to specific frequency bands that vibrate with large amplitudes (Figure 3. 18 (a) and Figure 3. 19 (a)). As such, the cochlea effectively creates a spatial-spectrum map in which, close to the entrance of the cochlea (the base), the BM is most sensitive to high-frequency bands, and at the apex, the BM responds best to low frequencies. The cochlea is, therefore, capable of exceptional sound analysis in terms of both frequency and intensity. This implies that the BM of cochlea acts as a hydro-mechanical frequency analyzer – a feat that has proven to be pivotal to the mammal’s specialized auditory functions such as exceptional hearing sensitivity, remarkable frequency analysis, and signal processing capabilities. It must be emphasized that active mechanisms are involved in biological cochlea systems and play important roles for acoustic signal amplification and frequency selectivity, which presents a complex challenge for replication in research. [104], [105], [107], [110]

3.5.2 Metamaterial based artificial cochlea

These high- k anisotropic acoustic metamaterials can serve as an ideal platform for the development of a receiver that mimics the acoustic signal amplification, high-frequency selectivity, and acoustic spectrum analyzer functionalities of the cochlea. Like the cochlea, the low dimensional acoustic metamaterial receivers are capable of spatially separating frequencies across their length while amplifying the acoustic

signals. To illustrate these similarities and equivalences, a simple two-dimensional (2D) model of the 3D conical metamaterial of Figure 3. 2 (c) is used as an analytical model. Here, the solid plates are rectangular, and wave propagation is confined in the x - z plane. This type of arrangement where there is a gradual spatial variation of metamaterial's geometric parameters (the width w of the solid plates) over the wave propagation direction will result in corresponding changes in the metamaterial's wave dispersion

$$k_{MM}(z, \omega) = \frac{\omega}{c_{air}} \sqrt{\frac{\rho_{air}B_{air}}{\rho_x B} \tan^2 \left(f\pi \frac{w}{c_{eff}} \right) + 1} \quad (3.5)$$

where $\rho_x = \frac{\rho_{air}\rho_{solid}}{[(1-F)\rho_{solid}+F\rho_{air}]}$ and $B = \frac{B_{air}B_{solid}}{[(1-F)B_{solid}+FB_{air}]}$ are the effective density and bulk modulus of the metamaterial respectively, and $c_{eff} = \sqrt{1 - \eta i}$ is the effective sound speed in the metamaterial [112], [113]. Here, η is the analytically obtained effective loss factor of the metamaterial along the propagation direction, with $\eta = 0.03$ being in good agreement with the simulations and experiments. Similar to the wave dispersion of the BM in the cochlea, the graded-index metamaterial is capable of spatially tailoring the wavenumber $k(z, \omega)$ and rendering an approximately exponential increasing function with distance z for a given frequency (Figure 3. 20 (a) and (b)).

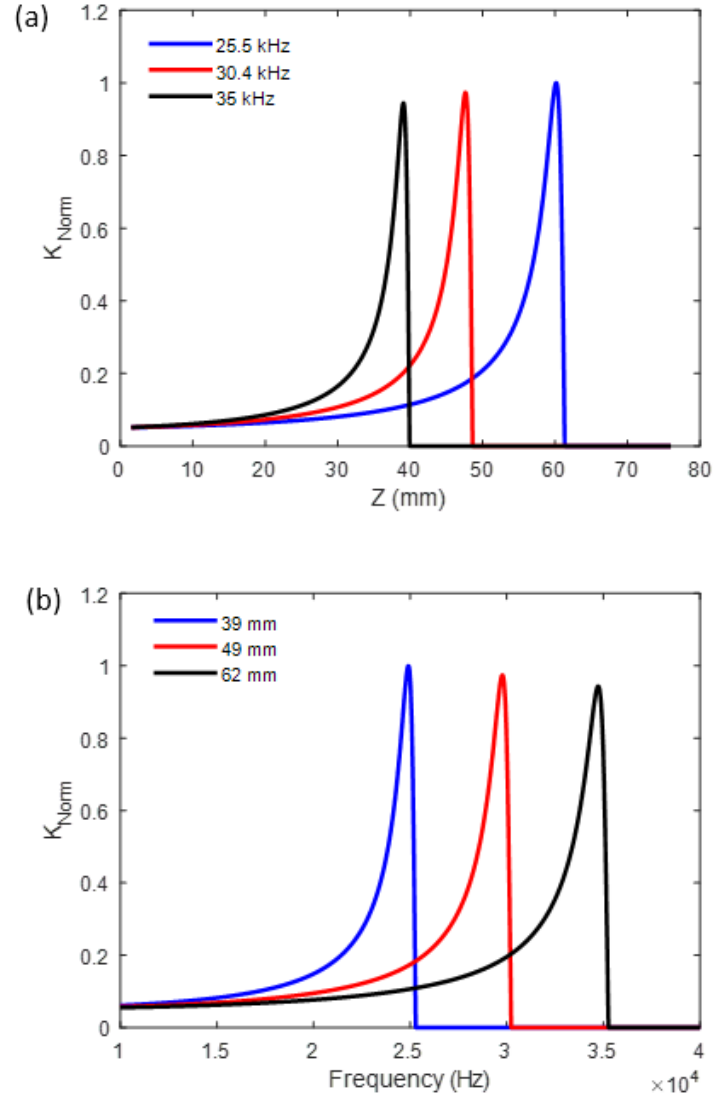


Figure 3. 20 Analytically obtained normalized wave vector as a function of distance (a) and frequency (b) in the metamaterial. Normalization is with respect to the free-space wave vector.

Interestingly, similar to the cochlea, the wave response of the metamaterial is also governed by the wavenumber $k(x, \omega)$ and can be characterized by the wave pressure field inside the metamaterial [14]:

$$P(z, \omega) = \frac{(\rho_{air}\omega)^{1/2}(1 - n_{eff}^{-2})^{1/4}}{\cos \left[\tan^{-1} \left(\rho_x \rho_{air}^{-1} (n_{eff}^2 - 1)^{1/2} \right) \right]} e^{-ik_{air} \int_{z_0}^z n_{eff} dz} \quad (3.6)$$

Here $n_{eff} = c_{air}k_{MM}(z, \omega)/\omega$ is the effective refractive index of the metamaterial structure. From equation 3.6 above, the traveling wave behavior, wave amplitude amplification (pressure amplification), energy localization, as well as spatial separation of frequencies of the metamaterial structure can be characterized (Figure 3.21 (a) and (b))

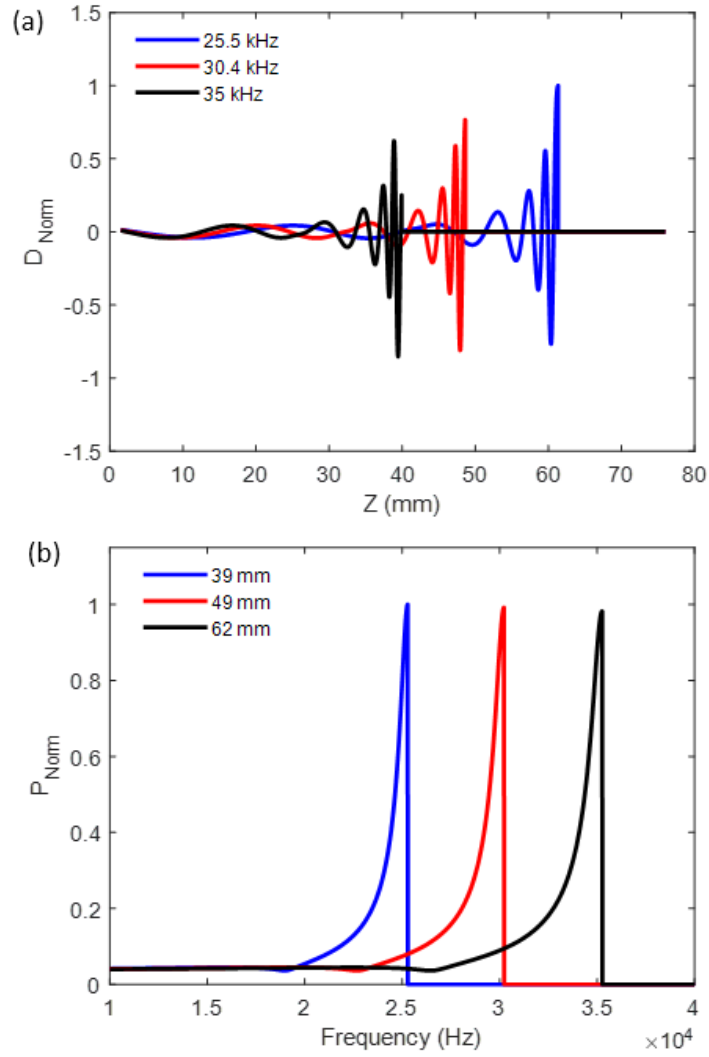


Figure 3. 21 Analytically obtained normalized on-axis pressure as a function of distance (a) and frequency (b) in the metamaterial.

Because the metamaterial's effective refractive index is a function of both the distance (z) and frequency [37], there comes a point along the metamaterial where each frequency component of the wave experiences a sufficiently high refractive

index to effectively arrest its forward progress in the metamaterial [12] (Figure 3. 20 (a) and Figure 3. 21(a)). This anisotropic tapering design thus gives rise to both strong wave compression and trapping effects, where different frequency components are amplified and subsequently confined at specific locations across the metamaterial structure in the propagation direction, resulting in a spatial band-pass filter bank phenomenon analogous to what is found in mammalian cochlear systems.[110], [114]

These analytically derived properties can be validated via simulations and experiments. To do so, use is made of the conical receiver (Figure 3. 22 (a)), which demonstrates the functional similarities between this structure and the on-chip metamaterial structure. In Figure 3. 22 (b), the localized trapping effects of three frequencies are simulated and displayed, which agrees with the analytical results in Figure 3. 20 (a) and Figure 3. 21 (a).

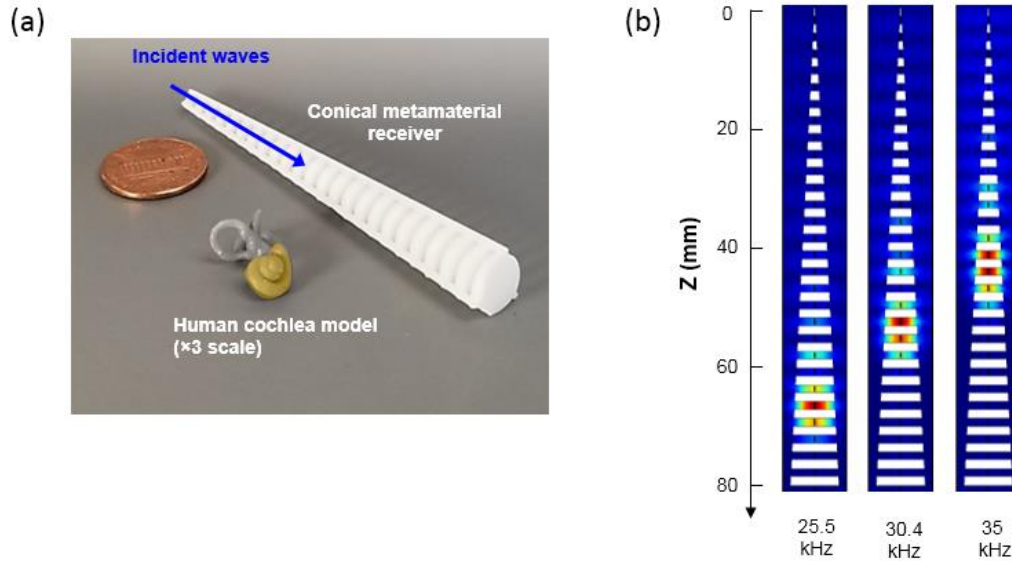


Figure 3. 22 (a) Photo of the metamaterial cochlea, 3D printed model of a human cochlea, and a coin for comparison. The coin is 19 mm in diameter. (b) FEM spatial pressure maps showing the spatial confinement and pressure amplification of waves propagating into the metamaterial. The distinct frequencies are spatially mapped to distinct locations in the metamaterial structure, which is similar in functionality to biological cochleae systems.

Furthermore, simulations and experimental results of the pressure field within the metamaterial structure show significant wave signal amplification over a broadband spectrum (over ten times gain across a 10 kHz bandwidth) as predicted by the analytical studies (Figure 3. 23 (a) and (b)). Moreover, the measured sharpness of the receiver metamaterial is similar to that of biological systems ($Q=7-10$). [114]

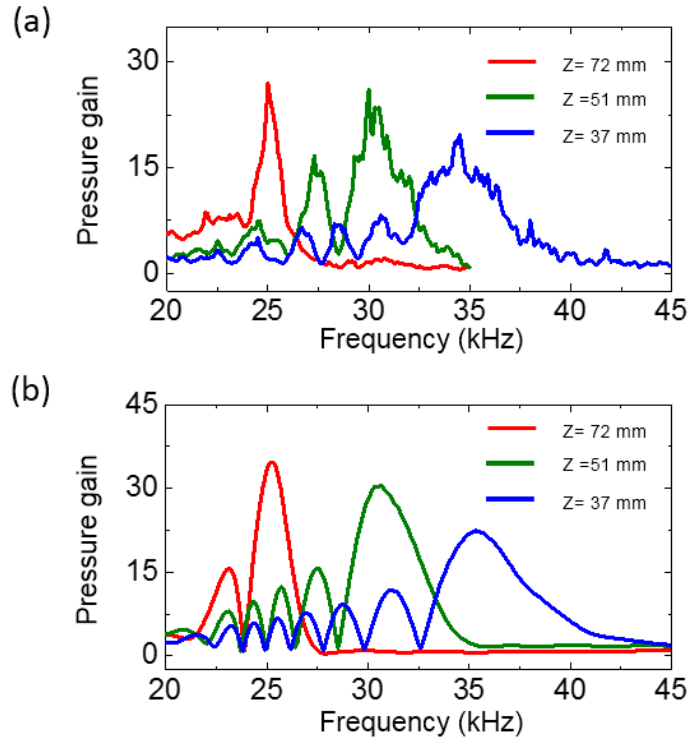


Figure 3. 23 Experimental (a) and simulated (b) pressure gain of the metamaterial as a function of frequency at three locations.

Using the fiber optic probe, the metamaterial gaps can also be probed to obtain the pressure as a function of distance for different frequencies (Figure 3. 24). The acoustic waves traveling within the structure are observed to experience the wave compression and pressure amplification phenomena as expected from the analytical results. This also pays striking resemblance to the displacement of the basilar membrane in Figure 3. 19 (a)

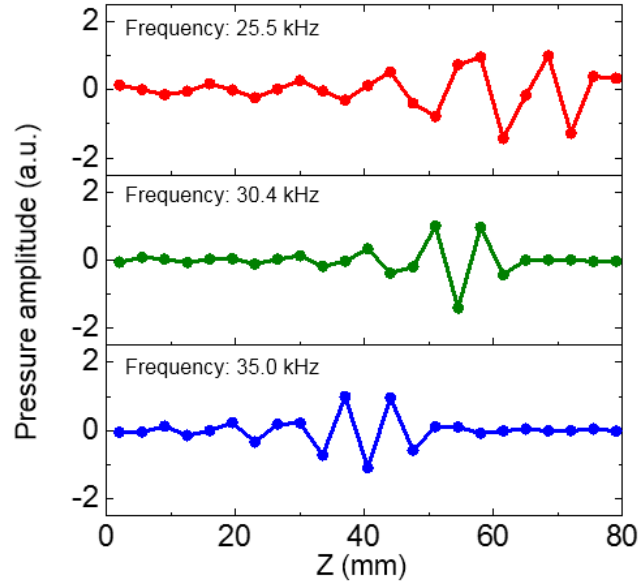


Figure 3. 24 Experimentally obtained pressure fields in the gaps of the metamaterial for three frequencies.

As such, this passive acoustic metamaterial structure can approximate the functionalities of the active, highly complex, and optimized mammalian cochlea. Compared with the biological cochlea, two unique features that the metamaterial enjoys over the biological systems that are worth summarizing: First, its passive nature demonstrates that a rather simple, metamaterial structure could directly amplify the signal, decompose frequency components, and realize acoustic filtering without using any complex electronic or active components. Second, its simplicity in design encourages quick and efficient realization using common methods such as 3D printing, which is cost-effective and allows for batch fabrication. The design of the metamaterial is relatively easy, which could rely on simple guidelines and full-wave simulations.

Despite their similarities, there are significant differences between the biological cochlea and the reception metamaterial. Here, one such difference is addressed. In the cochlea, the airborne sound waves passing from air to the BM experience a dramatic decrease in their wave velocities [115] (from $v_{air} = 340 \text{ m/s}$ to $v_{BM} = 15 \text{ m/s}$). This wave transition leads to a significantly reduced sound wavelength (by a factor of 23), which is essential for the capability of the relatively small-sized BM to perform exceptionally well in the low-frequency sound regime. By contrast, the acoustic waves in the metamaterial structure pass directly from the free-space into the metamaterial without any transition between airborne sound and membrane mechanical waves. Although the wave speed in metamaterial will be only modestly reduced ($n_{eff} \cong 2$), the wavelength is not comparatively significantly reduced. As a result, the frequency-size ratio of the metamaterial is comparatively higher, giving the metamaterial the ability to sustain much higher frequencies than a cochlea of the same size. Nevertheless, the coupling mechanism in the cochlea systems which make use of bones as mechanical lever-like structures results in much higher gains than possible in these acoustic metamaterials.

3.6 Summary

The high- k properties possessed by anisotropic acoustic metamaterials can be exploited to enhance the reception of acoustic waves. In this chapter, the two types of low dimensional anisotropic metamaterials were shown to possess similar properties in acoustic wave reception.

These low dimensional metamaterials were shown to extend the performance bandwidth of passive acoustic metamaterials by availing such new functionalities as signal amplification, passive acoustic filtering, and, in the case of the active on-chip acoustic metamaterial, frequency bandwidth tuning, switching, and pulse retardation control of the acoustic waves. In this study, the high- k on-chip acoustic metamaterials are shown to be capable of spatially separating frequencies across their length, where each gap corresponds to the resonant mode of a particular frequency, thus realizing a passive broadband acoustic filter.

With regards to the on-chip tunable metamaterial, the degree to which the wave vector can be parallel to the group velocity is shown to have a dependence on the plate height. As such, the refractive index exhibits a predictable dependence to the plate height throughout the measured frequency range, with high refractive indices corresponding to greater plate heights and vice versa. The result of this phenomenon is the active tuning of the frequency bandwidth of the metamaterial, which further produces pulse retardation and phase manipulation properties. Moreover, comparing the wavelengths to its thickness reveals that this thin on-chip metamaterial structure can confine acoustic waves with wavelengths up to six times larger than its thickness,

which is a key advantage possessed by this device. The high refractive index exhibited by the higher plate heights induces a delay in the wave packet due to the group velocity being slower in the metamaterial than in air. These properties can be manipulated to further the study and realization of acoustic devices and their applications.

Analytical comparisons demonstrated many similarities between these anisotropic metamaterial structures and the basilar membrane of the mammalian cochlea. They successfully enhanced acoustic sensing via wave compression, as well as spatially separated acoustic waves across the length according to their frequencies – a filtering feat exhibited in the basilar membrane of the mammalian cochlea. Such profound findings can have an immediate impact on the design of functional acoustic devices such as broadband acoustic transducers.

Chapter 4: Bio-inspired High- k acoustic metamaterial for emission enhancement

Many biological organisms rely on sound to interact with one another and their environments – a feature that explains the highly optimized nature of their designs to enhance sound production. Man-made systems have long benefited from the designs found in nature to realize more efficient and effective acoustic systems. Recently, artificial structures such as acoustic metamaterials have grown in popularity in the scientific community because of the extra degrees of control and manipulation they provide acoustic waves, making them prime candidates for exploiting many biological designs that occur in nature. As discussed in Chapter 2, the architecture of these artificially engineered structures takes advantage of some basic physical laws and principles, such as resonance in Helmholtz cavities or spring-mass systems, to infuse the propagating waves with additional useful properties. Some of these properties lend themselves to enhance acoustic radiation, with such mechanisms as the Purcell effect common in their electromagnetic counterparts. In this chapter, it is shown that high- k anisotropic acoustic metamaterials could be designed to exhibit strong radiative properties that render direct amplification of the pressure fields, as well as improved directionality. Parametric studies are carried out to understand the effects of certain geometrical factors on its performance. The properties deduced by

this acoustic metamaterial can find immediate use in real-world applications such as fault detection, noise identification, acoustic communication, and sonar navigation.

4.1 Motivation

It is well known that the behavior of acoustic waves in a medium has a strong dependency on the geometric properties of that medium. This property is exploited in nature, where biological systems enhance emitted sounds via such mechanisms as cavity resonance. Small insects and animals such as the cicada, water boatman, and frogs, for instance, have miniaturized but very efficient sound generation organs capable of producing intense and conditioned acoustic signals, facilitating their communication, mating, and foraging abilities [80], [116], [117]. They use their abdominal resonance chambers to confine acoustic waves in a small volume [80], [118], [119] so that the local pressure fields are amplified. In cicadas, for example, a pair of tymbals on each side of the abdomen is used to drive a cavity in their abdomen which serves as a Helmholtz resonator (Figure 4. 1 (a)). Other insects like crickets modify their environment to enhance the intensity of their mating calls. Some cricket species, such as the mole cricket [120], create an external resonating cavity by burrowing specific shapes in the earth (Figure 4. 1 (b)), which act as an acoustic hornlike structure that amplifies the sounds they produce with their tegmen via stridulation. By placing themselves in the cavity, these insects act as the acoustic source, whose signal is greatly amplified by the surrounding cavity.

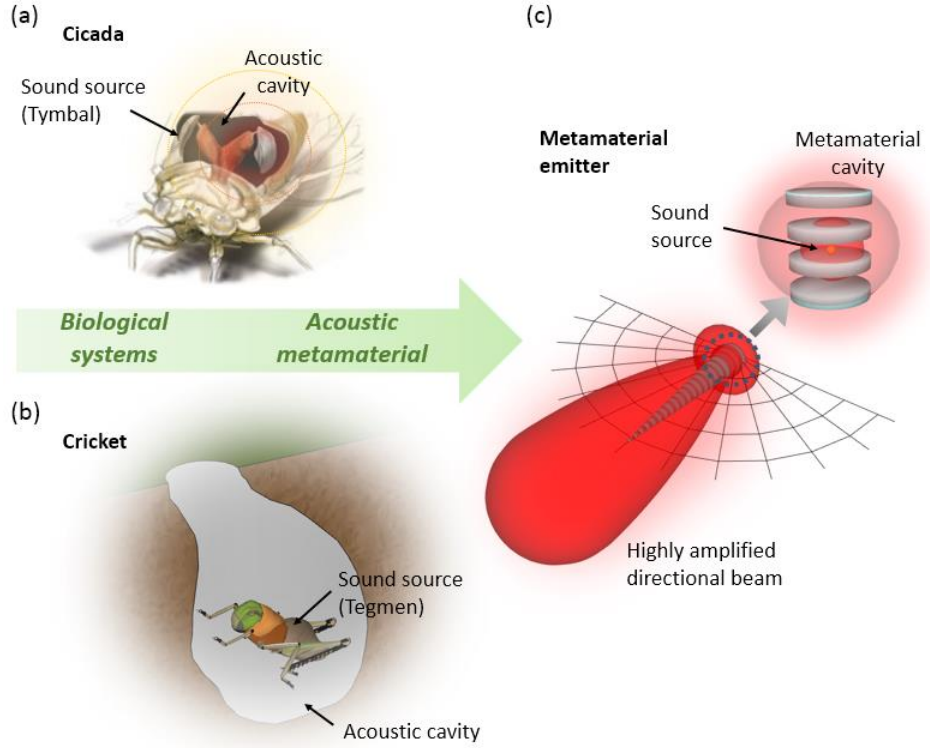


Figure 4. 1 Sound enhancement mechanism in small insects such as the cicada [121] (a) and the cricket (b) using acoustic resonators. (c) Equivalent strong confinement and intensification of acoustic fields in acoustic metamaterial cavities for the enhancement of directional emission of sound.

In addition to the optimized tuning between the sizes of their cavities and their calling frequencies which maintain tonal purity, the systems of these insects are designed to provide exceptional impedance matching, which increases the effective size of the sound source and enable a near-perfect transfer of the acoustic energy to the free space [122]. These phenomena have easily been replicated in research, where

resonating cavities are commonly used to enhance the acoustic properties of waves, producing frequency-dependent, highly intense sounds. It has been discussed that the emergence of acoustic metamaterials is as a result of the need to enact extra control of wave propagation, and these artificially engineered structures equally rely on the axiom that the structural parameters play a strong role in tailoring the properties of the wave propagation through the medium. Because of this, it follows that acoustic metamaterials provide a fertile platform for replicating some of the designs found in nature. For example, Fabry Perot -like cavities in some acoustic metamaterial designs have been used to enhance sound pressures [123]. Also, placing an acoustic emitter right in a high impedance medium would enhance its radiation power [95], [124]–[126]. This effect has been referred to as the acoustic Purcell effect, derived from the enhanced spontaneous emission rate that a quantum source experiences due to a change in its surrounding environment [67]. Such properties can be identified as a result of the high- k states that these metamaterials are capable of sustaining.

In chapter 2, it was discussed that metamaterials with anisotropic designs were equally capable of enhancing acoustic radiation, in terms of both pressure and directivity (Figure 4. 1 (c)). To thoroughly investigate this idea, numerical simulations and experimental results are presented in this chapter. This is done by employing parametric studies to understand how the design parameters affect the performance of the metamaterial emitter. Next, using a characteristic emitter, experimental results are reported, which demonstrate the metamaterial emitter's extraordinary ability to enhance the acoustic radiation.

4.2 Metamaterial design

The acoustic metamaterial emitter comprises two main sections: the metamaterial cavity region and the coupler region (Figure 4. 2). The geometric properties of the metamaterial are determined by the intended working frequency of the specific gap. As will be presented in this section, this working frequency depends on many factors, but a good starting point is the relation $d = 2c/\pi f$, where d is the disk diameter, c is the sound speed in air, and f is the frequency. In this study, a working frequency of 25 kHz is chosen as the design frequency for the metamaterial, and as a starting point, a periodicity of 3 mm is chosen with a disk thickness of 2 mm.

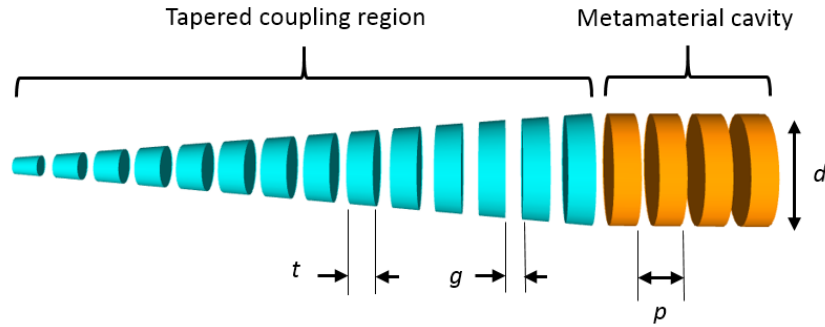


Figure 4. 2 Schematic of the acoustic metamaterial emitter. It comprises two regions: the metamaterial cavity and the tapered coupling region. The parameters shown are the disk thickness t , gap thickness g , periodicity p , and the diameter of the uniform disks d .

At the working frequency, this criterion satisfies the maximum wave vector criterion for periodic structures given by $k_{max} = \pi/P$ which corresponds to the wave vectors at the first Brillouin zone boundary [103], [127]. This would result in a high refractive index n for pressure amplification [14], given by $n = k_{max}/k_0$, where k_0 is the free-space wave vector. The lower limit of P is governed by such factors as boundary layer effects and surface roughness.

4.3 Parametric studies

In this section, the different design parameters are investigated for their effect on the radiation performance of the acoustic metamaterial. The parameters investigated here are the metamaterial cavity design, taper design, metamaterial periodicity, embedded emitter size, and temperature effects. FEM simulations are primarily employed to investigate these parameters. Besides, where necessary, use is made of analytical methods to explain their mechanisms.

4.3.1 Acoustic metamaterial cavity

It has been discussed that some biological systems make use of an acoustic cavity to enhance their production of sound (Figure 4. 1). A similar idea is employed in designing the acoustic metamaterial emitter. The metamaterial cavity is a region of uniform, equally spaced disks (Figure 4. 2) and plays an important role in setting the working frequency of the metamaterial and housing the emitter element. The number

of uniform disks in the metamaterial cavity plays an important role in the performance of the metamaterial. Cavities from 2 disks to 10 disks are investigated via FEM simulations by performing a frequency sweep, and the acoustic pressure is measured at 40 cm away (Figure 4. 3).

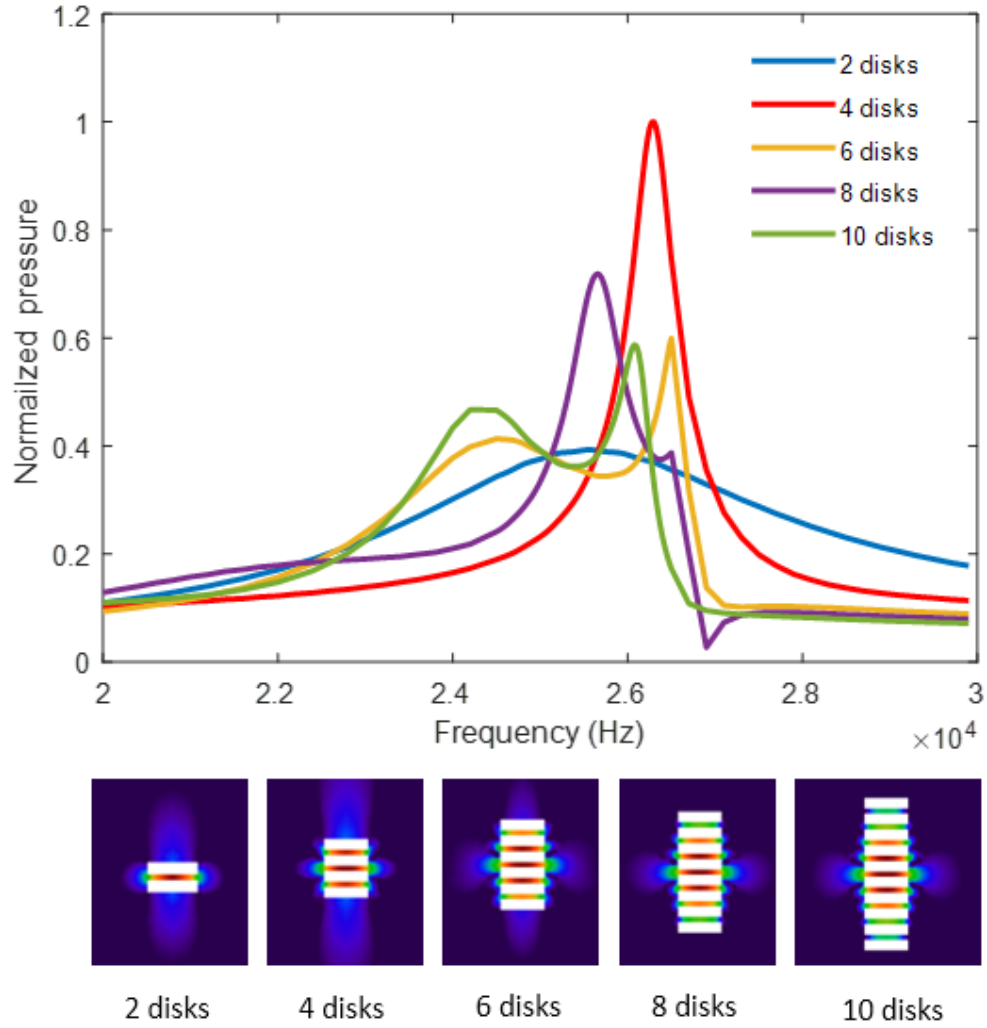


Figure 4. 3 (Top) Normalized pressure amplitude for the different metamaterial cavities (bottom). Normalization is with respect to the peak pressure of the data.

It can be seen from Figure 4. 3 above that a metamaterial cavity made of four disks provides the maximum gain at the design frequency of 25 kHz. Conversely, the conventional acoustic cavity made up of 2 disks provides the least of the pressure amplification. Also, the comparatively poor performance of the other cavities (6, 8, and 10 disks) is evident, and the ripples in the frequency plots may be as a result of interference effects of the reflected wavefronts between the metamaterial-air boundary.

4.3.1.1 Analytical studies on radiation enhancement

The high- k metamaterial cavity developed in this work can achieve intense enhancement of the acoustic radiation power of an acoustic source embedded in it. To better understand how this feat is accomplished, consider a small spherical acoustic source placed in the metamaterial cavity, as illustrated in Figure 4. 4 (a).

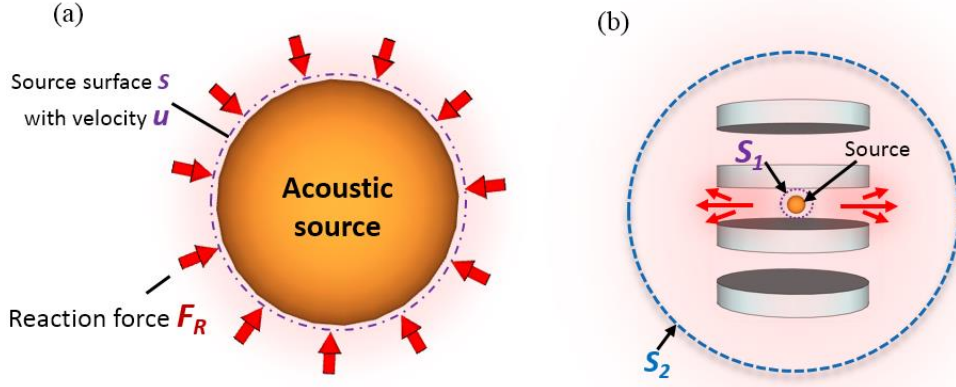


Figure 4.4 Sound source radiation in free-space and metamaterial structure. (a) Schematic of acoustic radiation of a spherical monopole source placed in air. (b) Radiation of a spherical source in a metamaterial cavity comprised of four disks 8 mm in diameter and 2 mm thick, separated by 1 mm gaps. S_1 and S_2 represent the near-field (on the source surface) and far-field regions, respectively.

The velocity at every point on the surface can be defined as:

$$u = u_0 e^{i\omega t} \quad (4.1)$$

where ω is the vibrating angular frequency and u_0 is a constant whose value is determined by the strength of the external power supply. The surrounding medium always maintains contact with the sphere so that the motion is transferred to the medium, which in turn exerts a reaction force on the source such that energy is transferred. This force is simply the integral of the acoustic pressure over the surface and can be expressed as [128]

$$F_R = - \iint_S p(\vec{r}) dS \quad (4.2)$$

Where S is the surface area of the sphere, $p(\vec{r})$ is the pressure, and r is the radius. The negative sign indicates that this F_R is the reaction of the medium on the source. The complex radiation impedance is defined as

$$Z = -\frac{F_R}{u_0} = \frac{1}{u_0} \iint_S p(\vec{r}) dS = R + iX \quad (4.3)$$

Where R , known as the radiation resistance, is associated with power transfer to the medium, and X is the radiation reactance. The radiation resistance is the most useful for acoustic radiation since it is proportional to the radiation power Π_{rad} , which is given by:

$$\Pi_{rad} = \frac{1}{2} u_0^2 \text{Re}[Z] = \frac{1}{2} u_0^2 R \quad (4.4)$$

This acoustic metamaterial cavity comprising of 4 disks can improve the radiation resistance, which would produce the desired effect of improving the radiation power from equation 4.3 (Figure 4. 4 (b)). As a proof-of-principle, simulations are carried out to demonstrate that such a metamaterial cavity is capable of significantly amplifying the radiation reaction force F_r applied to the sound source (Figure 4. 5), which is essential for the enhancement of source-medium interaction and acoustic radiation.

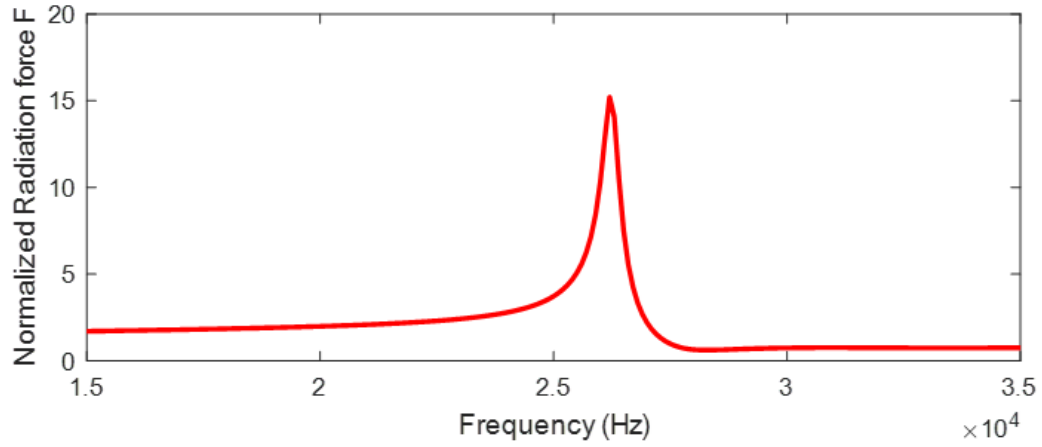


Figure 4. 5 Normalized radiation reaction force in the metamaterial cavity depicted in Figure 4. 4 (b). Normalization is with respect to the radiation force F_{r_air} in free-space, calculated using F_{r_MM}/F_{r_air} , where F_{r_MM} is the radiation reaction force in the metamaterial.

Since $R \propto F_R \propto \Pi_{rad}$, it follows that a stronger radiation force bearing on the source would induce a larger reaction force from the source in the form of radiation resistance, thus causing the source to transfer more power into the surrounding medium. The radiation enhancement could be evaluated by the ratio of radiation resistance R_{MM} of source in metamaterial to the radiation resistance R_{free} in free space:

$$Radiation\ Enhancement = \frac{R_{MM}}{R_{free}} = \frac{\Pi_{MM}}{\Pi_{free}} \quad (4.5)$$

which is also the enhancement of sound emission power. As shown in Figure 4. 6 (a) and (b), it is evident that the radiation resistance, as well as radiation power of a source, is greatly amplified by the metamaterial cavity when compared with the same sound source placed in free space.

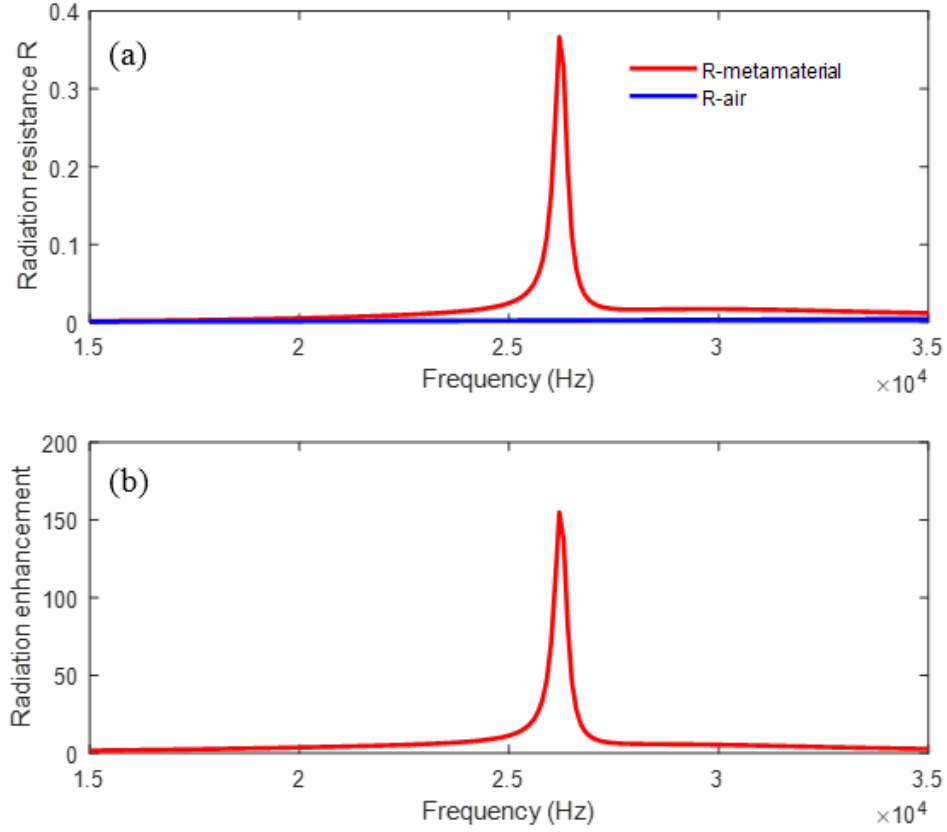


Figure 4. 6 (a) Radiation resistances of a monopole source in the metamaterial cavity as compared with the same source placed in the free space. (b) The acoustic radiation power enhancement in the metamaterial cavity. A finite element method (COMSOL Multiphysics 5.4) is used to analyze pressure and velocity fields generated by a sound source, which are used in equations 4.2 - 4.5 to calculate reaction force, radiation resistance, and radiation enhancement factors.

It is worth noting that the radiation enhancement exhibited by the metamaterial differs from that of a conventional acoustic cavity comprised of a pair of disks. As demonstrated in Figure 4. 7 (a), the induced radiation enhancement spectrum of the metamaterial cavity (comprised of four disks) exhibits a strong

asymmetric line-shape, corresponding to the metamaterial dispersion curve shown in Figure 4. 7 (b) (blue shaded regions in Figure 4. 7 (a) and (b)) and achieves a maximum power enhancement of ~ 150 at around 26 kHz. By contrast, the conventional acoustic cavity has a symmetrical Lorentzian-like resonance curve with a much lower pressure enhancement (~ 26 at around 24 kHz). Additionally, the line-shape of this conventional acoustic cavity's pressure enhancement spectrum does not correspond with the metamaterial dispersion curve.

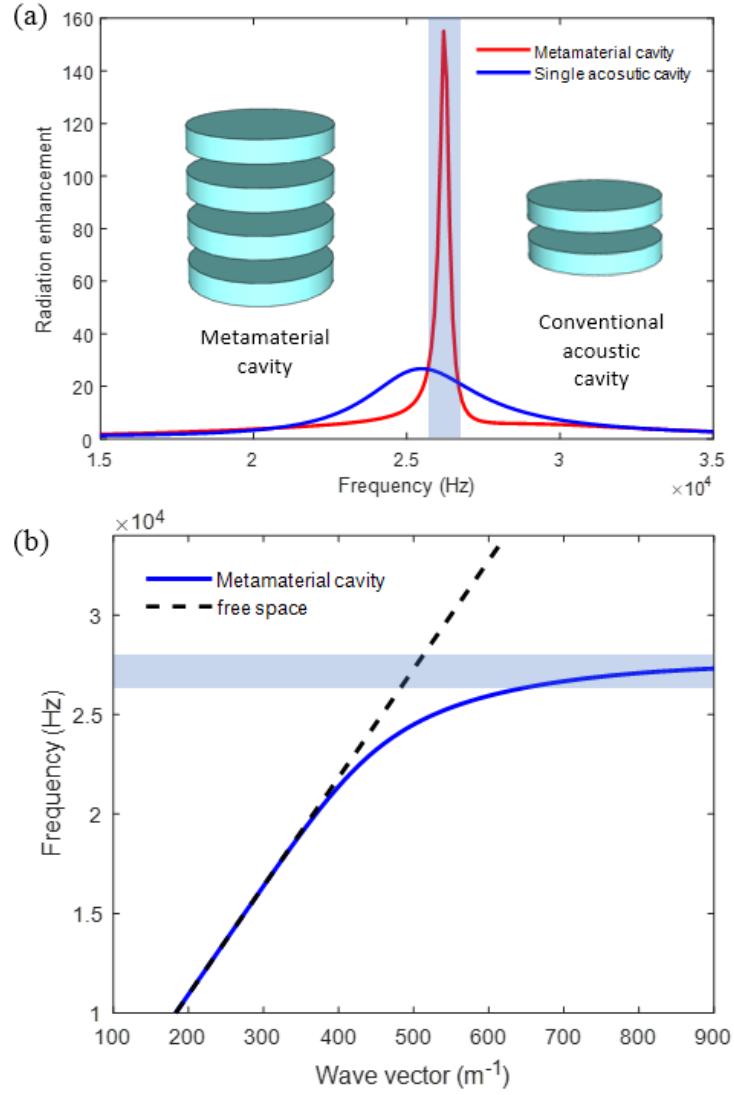


Figure 4. 7 (a) Comparison between a conventional acoustic cavity and a metamaterial cavity for sound radiation enhancement. The radiation enhancement spectrum in the metamaterial cavity as compared with that of a conventional acoustic cavity comprised of a unit cell of the metamaterial cavity. (b) The dispersion plot of the metamaterial cavity comprised of four disks (blue) compared with the free-space dispersion (black dashed line) from the simulation. The blue shading in (a) and (b) indicate the working frequency region.

4.3.1.2 Accounting for radiation losses

In terms of the acoustic metamaterial emitter, this work is focused on enhancing the far-field acoustic radiation. The acoustic power radiated into the far-field

Π_{rad_far} could be calculated as:

$$\Pi_{rad_far} = \iint_{S_2} Re(P \times u) \cdot \hat{n}_{s_2} dS \quad (4.6)$$

Where the surface S_2 encloses an area that extends far away ($d > 10\lambda$) from the source to ensure that only the far-field radiation component is taken into account (Figure 4. 4 (b)). In practice, the acoustic metamaterials would experience losses due to viscous and thermal effects. The emitted waves from the embedded vibrating source could be essentially understood to couple into two modes; radiative and non-radiative modes. The former makes its way into the far-field by coupling into the free space and is thus useful for acoustic communication and sonar echolocation. The latter, which essentially is a metamaterial guided mode, is trapped in the metamaterial structures and dissipated as heat due to viscous and thermal effects. If a comparison is made between the power radiated through the two surfaces S_1 (total power) and S_2 (far-field radiated power), this radiation loss due to viscous and thermal effects can be effectively assessed (Figure 4. 8 (a)).

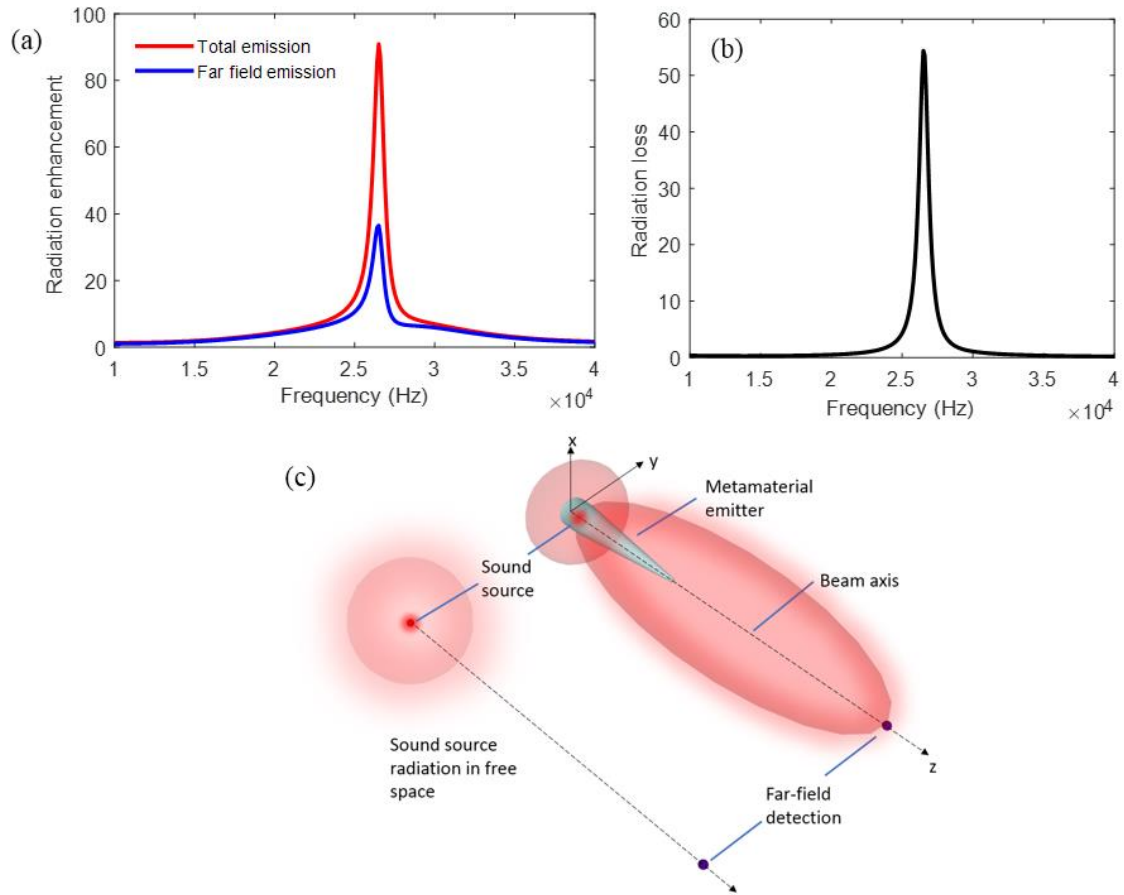


Figure 4. 8 Far-field emission gain of metamaterial emitter. (a) The total radiation and far-field radiation enhancement of the metamaterial cavity with viscous-thermal dissipation. (b) Radiation loss in the metamaterial emitter. (c) Schematic for describing the emission enhancement, which is defined as the ratio of far-field radiation power measured on the metamaterial emitter's beam axis (right) to the power produced by the sound source without using metamaterial structures (left).

The total power Π_{total} is evaluated as:

$$\Pi_{total} = \iint_{S_1} \text{Re}(P \times u) \cdot \hat{n}_{s_1} dS \quad (4.7)$$

Where the surface S_1 is encloses the emitter in the metamaterial. The radiation loss can thus be evaluated as:

$$\Pi_{loss} = \Pi_{total} - \Pi_{rad_far} \quad (4.8)$$

It is discernible from Figure 4. 8 (b) that the radiation losses can be quite significant, accounting for over 50% of the total radiation power. Since the far-field acoustic radiation is what is useful for tasks like for sonar echolocation, the far-field emission gain G_{far} can be used to describe how well the metamaterial emitter improves sonar performance. As illustrated in Figure 4. 8 (c), G_{far} is defined as the ratio of far-field emission power measured on the metamaterial emitter's beam axis to the power produced by the sound source without using metamaterial structure. Notably, the far-field emission gain combines metamaterial emitter's radiation enhancement as well as its directivity. These two factors describe how effective the metamaterial emitter is at enhancing sound radiation and concentrating the acoustic power in a specified direction. This gain can be expressed as:

$$G_{far} = \left(\frac{\Pi_{rad_far}}{\Pi_{free}} \right) \cdot \left(\frac{4\pi}{\theta_{HPBW}} \right) \quad (4.9)$$

The term $\frac{\Pi_{rad_far}}{\Pi_{free}}$ in equation 4.9 represents the far-field radiation enhancement of the metamaterial emitter while the term $4\pi/\theta_{HPBW}$ is the emitter's directivity, where θ_{HPBW} is approximated as half-power beamwidth of the emission beam. In practice, the sound pressure is a more useful quantity in assessing acoustic emission than the sound power because it is the quantity that is readily measured using acoustic sensors such as microphones. Since sound pressure is proportional to the square root of acoustic power, the emission gain based on pressure field measurements could be obtained as:

$$G_t = \sqrt{G_{far}} \quad (4.10)$$

Here, G_t represents emission gain characterized by the pressure field.

It is, therefore, evident that a high- k acoustic metamaterial cavity of 4 disks can yield extraordinary enhancement to the acoustic radiation power. By availing a high impedance medium to an embedded emitter, elevated power can be extracted from the source and coupled into free space. It should be noted that such an effect is similar to the Purcell effect common in electromagnetic metamaterials [34], [57], [58], [61], [83], [94] and that has been recently reported in acoustics [67].

4.3.2 Acoustic metamaterial coupler

The coupler region of the metamaterial emitter comprises of air-spaced disks with a tapered profile. This region serves two main purposes: first, to gradually match the impedance of the metamaterial cavity to that of the air, so that the amplified acoustic waves retains as much of its energy as possible as while being introduced into the free space. Second, it serves to tailor the beam profile, increasing its directionality. The parameter to be investigated here is how long this region needs to be, hence the tapering angle, to produce the optimal response. In Figure 4. 9, different sized tapers are added to the four-disk metamaterial cavity, and the far-field pressures are obtained.

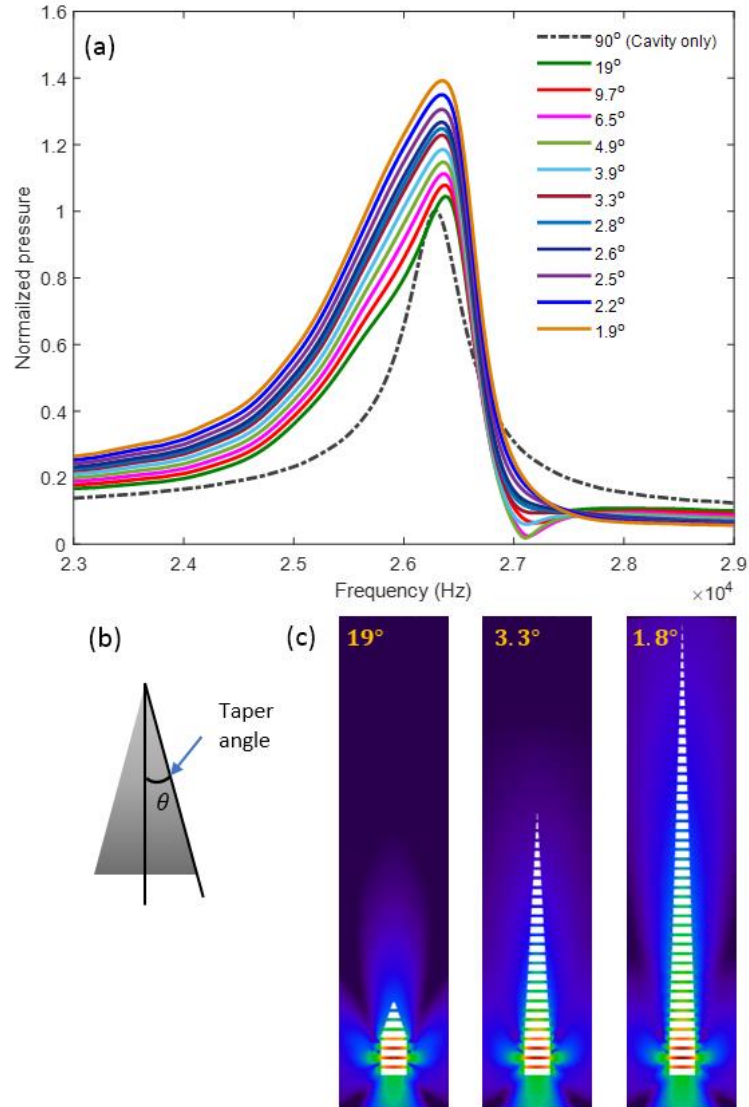


Figure 4. 9 (a) Normalized pressure as a function of frequency for different taper angles. Normalization is with respect to the maximum pressure for the 4-cavity data (grey dashed line). The taper angles correspond to adding increments of four 1 mm spaced disks. (b) Schematic illustrating the taper angle. (c) Simulation pictures depicting some taper angles and their respective lengths.

In Figure 4. 9 above, the taper angles are obtained by adding increments of 4 disks to the metamaterial cavity. For example, 19°, 9.7°, 6.5°, and 4.9° correspond to 4, 8, 12, and 16 disks respectively added to the 4-disk metamaterial cavity. Also included are the cavity only results (90°) and a 30-disk taper (2.6°). A general increase in pressure amplitude can be observed with smaller taper angles. This observation is reasonable because of the more gradual matching of the acoustic impedance provided by the longer structure, since the impedance change per unit length x , given by $\frac{dZ}{dx}$ is smaller in the longer configuration.

It must be noted that because the metamaterial structure is inherently lossy (Figure 4. 8), two opposing factors affect the coupler's performance: on one side, a longer coupler provides a more gradual matching of the impedance, thus minimizing losses that may arise as a result of impedance mismatch. On the other side, the longer coupler provides a longer lossy medium for the propagating waves, so that the non-radiative modes are more fully trapped in the metamaterial structure and dissipated as heat due to viscous and thermal effects. A plot of the maximum normalized pressures for taper angle illustrates this trend (Figure 4. 10)

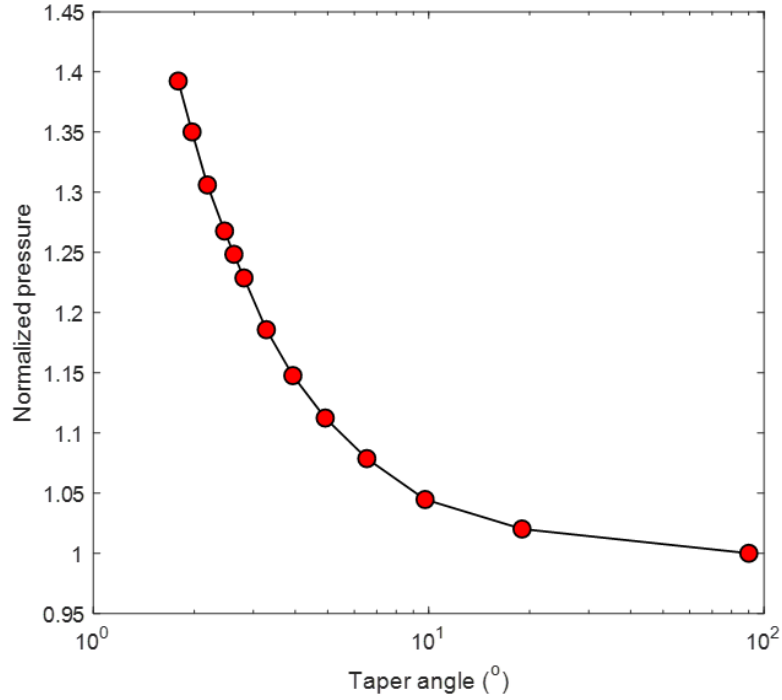


Figure 4. 10 Maximum normalized pressure as a function of the taper angle. Normalization is with respect to the maximum cavity-only pressure.

However, because the tapering profile implies that the loss per unit length is decreasing along the propagating direction, a nonlinear degradation of the pressure profiles with increasing taper angles is observable, as indicated in Figure 4. 10.

Besides the radiation enhancement, the metamaterial emitter also engineers the beam pattern of the sound wave, achieving highly directional emission from a small size device. The directional beam emitted by the metamaterial emitter is evidence that it acts as a mode-area transformer, gradually changing the tightly confined source mode into a large-mode-area guided wave – an essential factor to the generation of a directional beam (Figure 4. 11).

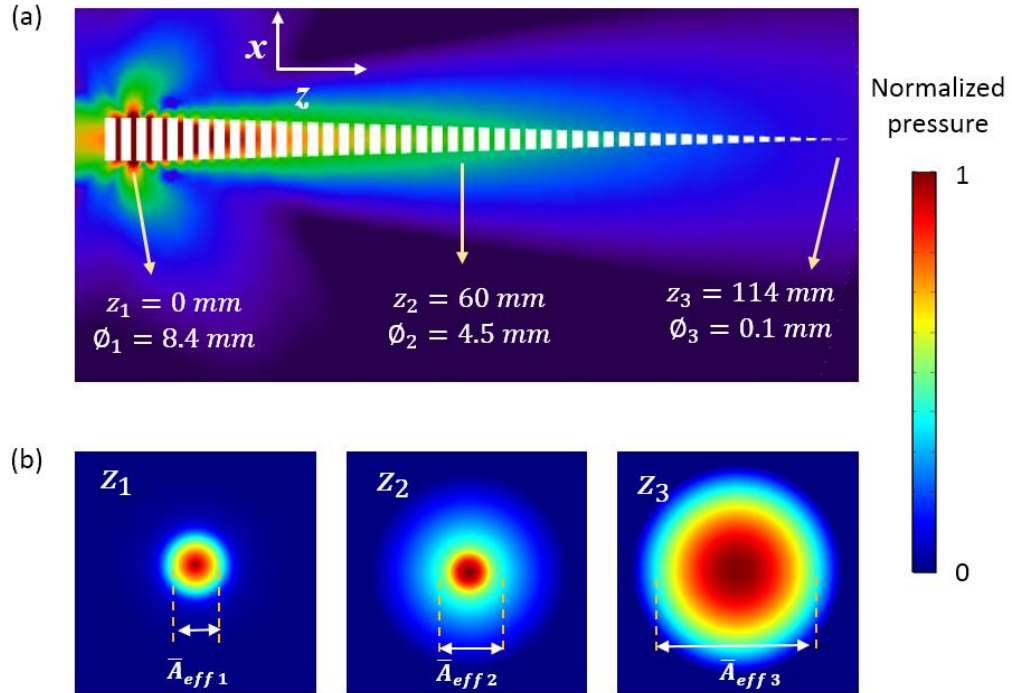


Figure 4. 11 (a) FEM photos depicting the pressure field distribution of the metamaterial emitter. (b) The change of mode field distribution of the guided mode propagating along the z -axis in the regions identified in (a). ϕ_1 to ϕ_3 indicate the diameters of the corresponding air gaps in regions z_1 to z_3 .

As shown in Figure 4. 11 (b), the effective mode area \bar{A}_{eff} (measured by the transverse mode field diameter) gradually increases along the propagation direction because of the progressive decrease in the metamaterial emitter's wave confinement. The radiation pattern of the metamaterial emitter in the far-field region could be described by using the piston model [128]:

$$D(\theta) = \frac{J_1(k\bar{A}_{eff} \sin(\theta))}{k\bar{A}_{eff} \sin(\theta)} \quad (4.11)$$

where θ is the angular width of the acoustic beam, k is the wave vector in free space, \bar{A}_{eff} is the effective radius of the output mode field, and J_l represents the first-order Bessel function. It is clear from equation 4.11 that a larger mode area A_{eff} leads to a narrower emission beam pattern. This mode-area transformer effect in the metamaterial emitter is comparable to that of an acoustic horn, where the gradually expanding mode field is guided by the horn's walls to a directional beam pattern at its opening due to the large mode area [129]. It is worth noting that while conventional horn structures require large physical aperture size to achieve highly directional beam pattern [128], [130], [131], the opposite directivity-aperture size relation exists with the metamaterial: a smaller aperture size (measured by the cone diameter) will support larger mode field area and therefore higher directivity. Such an inverse relationship could present a useful advantage held by the metamaterial emitter because it could relax the large size criterion necessary for achieving directional emission at various frequencies.

Furthermore, this beam shaping is greatly enhanced by the tapered region, wherein the directivity, as indicated by the half-power beamwidth (θ_{HPBW}) is comparatively higher than the cavity-only metamaterial. At 25.5 kHz for example, the tapered metamaterial with the cavities has $\theta_{HPBW} = 26^\circ$, while the cavity-only metamaterial has $\theta_{HPBW} = 46^\circ$ (Figure 4. 12)

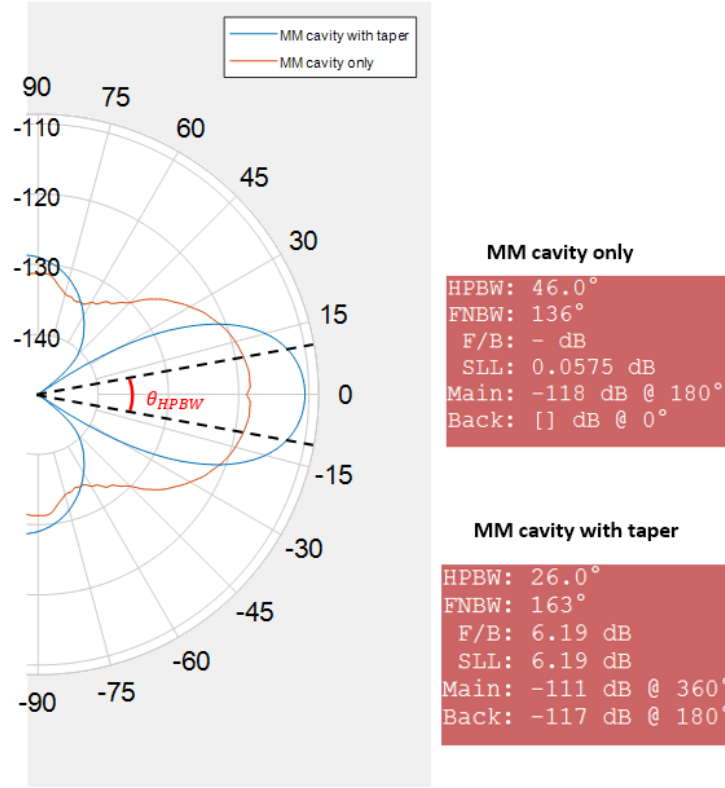


Figure 4. 12 Comparison of the directivities of the metamaterials comprising of the cavity and tapered coupling region and a cavity-only metamaterial.

4.3.2.1 Tapered structure without the metamaterial cavity

If the metamaterial is designed without the cavity region (of uniform disks) and the emitter is placed in the last gap of a tapered metamaterial structure, the resulting performance is different and suboptimal when compared to a metamaterial structure comprising of the cavity and the tapered coupler region. Figure 4. 13 depicts the simulated results obtained for different taper angles.

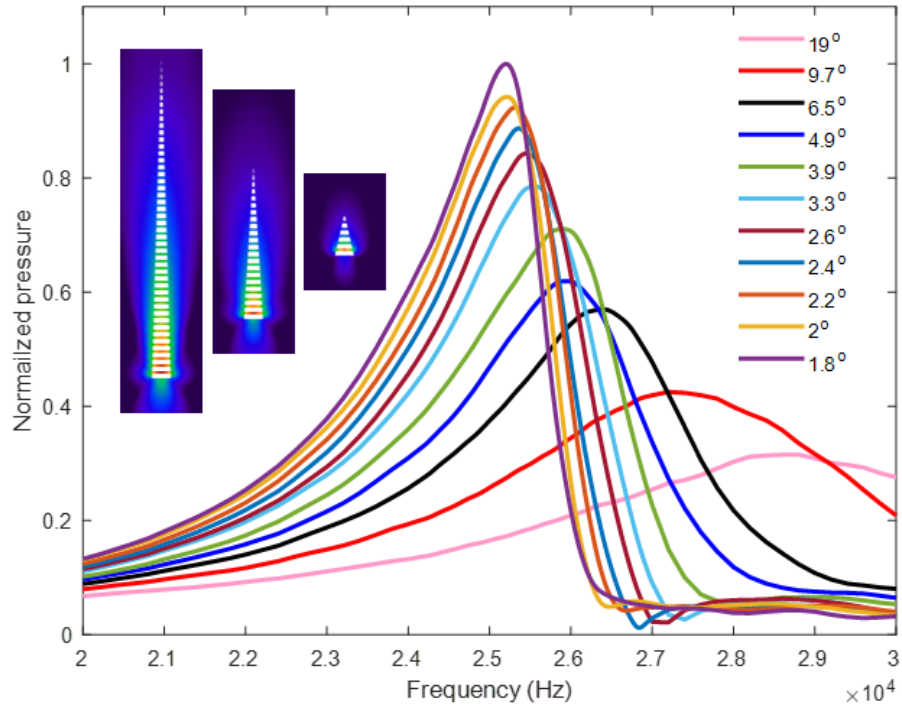


Figure 4. 13 Normalized pressure (to peak pressure in data) as a function of frequency for different taper angles for a metamaterial taper only. The inserts are simulation pictures of the metamaterial taper angle profiles for 19°, 3.9°, and 1.8°, respectively.

Two observations can be made in Figure 4. 13 above. First, the peak frequency of the structures increases with a decrease in the taper angle. Second, the gain also decreases with a decrease in the taper angle. As discussed in section 4.3.1, the metamaterial cavity defines the working frequency of the structure by availing multiple gaps of uniform sizes for the tailoring of the waves. There is a strong dependency of the geometric properties of these uniform disks on the working

frequency of the structure, with larger disks corresponding to lower design frequencies and vice versa. This can provide a reason for the anomalous observed effects, since, in this taper-only configuration, the average size of the disks closest to the emitter (which would serve as the metamaterial cavity) comparatively smaller due to the taper, and therefore boast higher cutoff frequencies. Furthermore, the decrease in gain as the taper angle is increased comes as a result of poor impedance matching in the shorter and steeper angled structures.

4.3.3 Gap thickness

So far, optimal values have been identified for the metamaterial cavity and the metamaterial coupler. It has been observed that a metamaterial cavity comprised of four disks coupled produced the highest far-field pressures, and a tapered coupling region made of 40 disks or more is ideal for both coupling the enhanced radiation into the free space as well as tailoring the beam profile. In this study, the periodicity of the entire metamaterial structure is changed by altering the thickness of the air gaps that separate the disks while keeping the disk thickness at 2 mm, as illustrated in Figure 4. 14 (b). The normalized far-field pressure is obtained and plotted for different gap sizes in Figure 4. 14 (a)

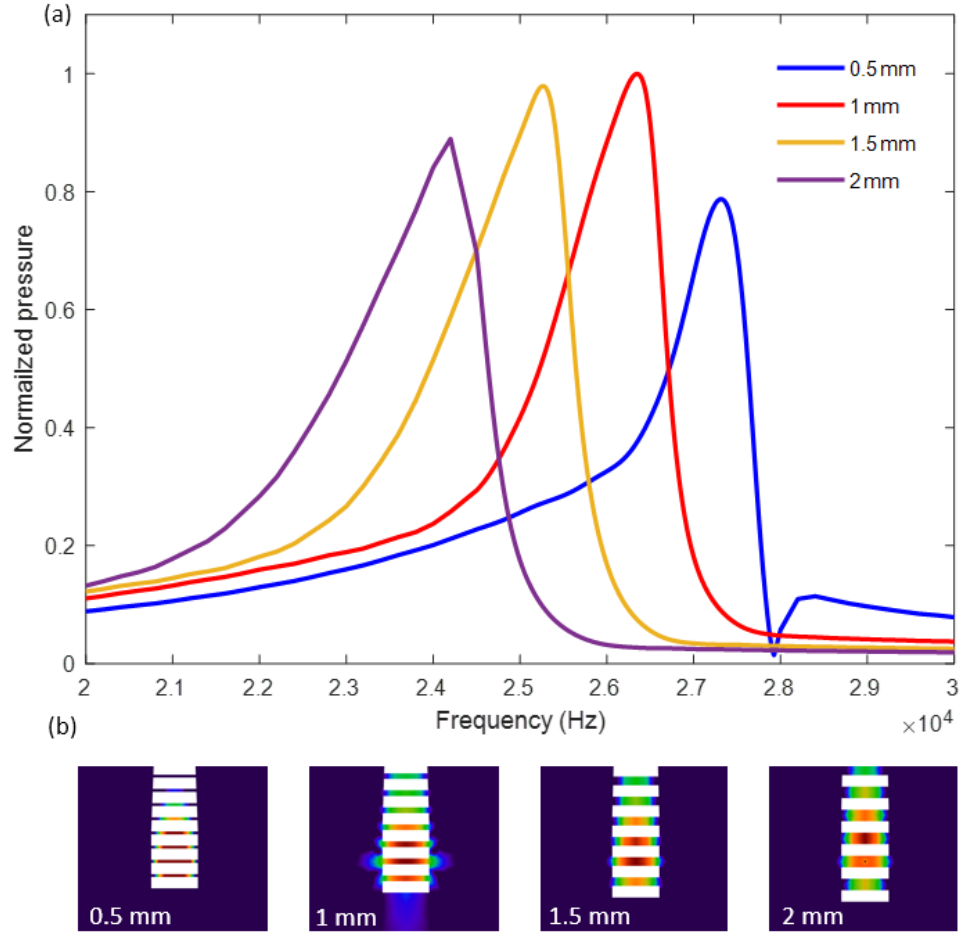


Figure 4. 14 (a) Normalized (to maximum pressure data) far-field pressure as a function of frequency for different metamaterial gap thicknesses. (b) Simulation photos of the different gap sizes.

From Figure 4. 14 (a) above, the gap size can be seen to have two net effects on the performance of the metamaterial structure. First, there is a decrease in gain with an increase in the air gap thickness. This can be understood when the effective refractive index of the structure is observed which can be analytically expressed as

$$n_{eff}(z, f) = \sqrt{\frac{\rho_{air} B_{air}}{\rho_x B} \tan^2 \left(f \pi w \sqrt{\frac{\rho_x}{B}} \right) + n_{air}^2} \quad (4.12)$$

where $\rho_x = \rho_{air} \rho_{solid} / [(1-F)\rho_{solid} + F\rho_{air}]$, $B = B_{air} B_{solid} / [(1-F)B_{solid} + FB_{air}]$ are effective density and bulk modulus of the metamaterial, respectively, f is the wave frequency, and $w = w(z)$ is the diameter of the metamaterial disk at distance z . Also, F is the filling ratio of the rigid disks, which is defined by $F = (p - g)/p$, where p is the periodicity of the structure and g is the size of the air gap. From equation 4.12 above, the effective refractive index of the structure will decrease as the gap thickness is increased. This will result in a decrease in the pressure amplification effect of the metamaterial, as observed in the closed-form pressure field equation given in equation 2.3 of chapter 2. This idea can also be intuitively understood by considering what would happen if the gaps got infinitely large. In such a scenario, the structure becomes almost identical to the free space where the refractive index is unity. In such a case, all the metamaterial properties are lost as the frequency response curve flattens out. In the case of the 0.5 mm air gap, while the cutoff frequency is high, the overall amplitude is very small because the evanescent coupling mechanism for wave propagation in the structure is overwhelmed by losses due to viscous and thermal effects.

A second effect observable from Figure 4. 14 (a) is that the optimal frequency of the metamaterial is decreased with an increase in gap thickness. This phenomenon can also be observed in the dispersion curve of different gaps in Figure 4. 15.

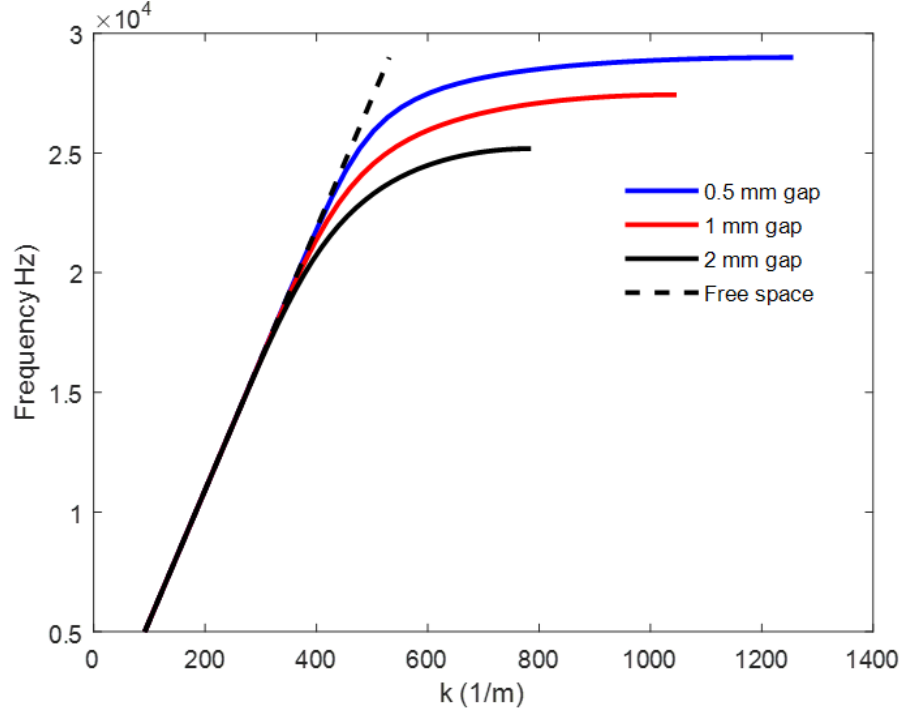


Figure 4. 15 Dispersion plots for metamaterial unit cells with different gap sizes from numerical simulations.

The cutoff frequencies correspond to the frequencies where $2\pi \frac{\partial f}{\partial k} \rightarrow 0$, and from the plots above, it is observable from the dispersion curve that thinner air gaps result in higher cutoff frequencies. It is also possible to deduce the frequency of peak amplitude from the dispersion curve. The peak amplitude is expected to occur at the frequency at which the wave vector k_{peak} is

$$k_{peak} \cong (1 - e^{-1})k_{max} \quad (4.13)$$

Where k_{max} is the asymptotic wave vector. As an example, $k_{max} \approx 785 \text{ m}^{-1}$ for the 2 mm gap and $k_{peak} \approx 496 \text{ m}^{-1}$ which corresponds to $\sim 23.3 \text{ kHz}$ in the

dispersion curve. From Figure 4. 14 (a), the peak frequency for the metamaterial with 2 mm gap thickness occurs at ~23.4 kHz, which is close to the dispersion-deduced value. Equation 4.13 can thus serve as a good starting point, where the peak pressure amplitude is to be expected. However, it does not account for external factors such as severe losses as in the 0.5 mm case, where all characteristic metamaterial amplification is absent due to viscous and damping effects. From the simulation results, a 1 mm thick air gap should be selected to achieve the optimal performance at 25 kHz.

4.3.4 Size of the emitter

Having determined the optimal parameters for the metamaterial cavity, taper, gap, and disk thicknesses, an optimized metamaterial can be constructed. Next, the size of the embedded emitter is investigated for its effects on metamaterial performance. In Figure 4. 16, numerical simulations are carried out for emitter sizes ranging from 0.5 mm to 8 mm embedded in the metamaterial.

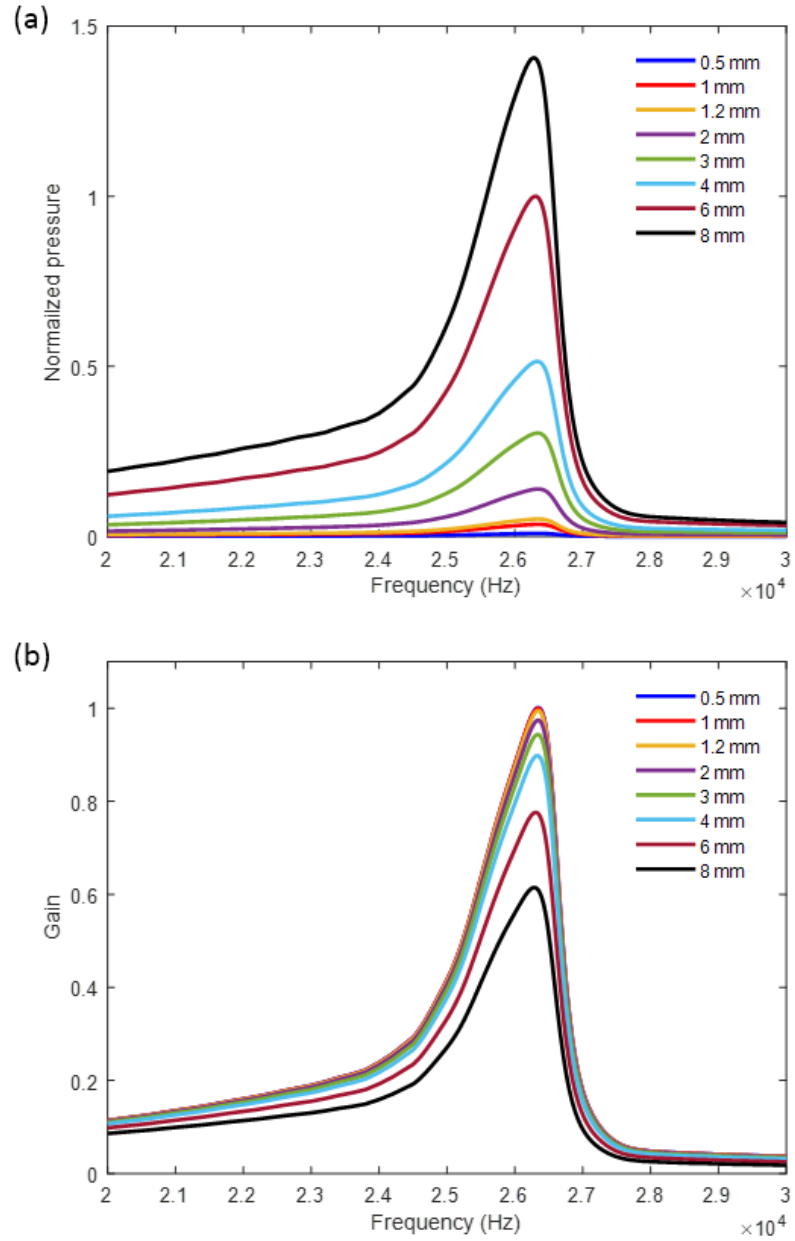


Figure 4. 16 (a) Normalized (to maximum pressure data) far-field pressure as a function of frequency for different emitter sizes. (b) Normalized gain plots for the emitter sizes. The gain is obtained as the ratio between the settings with and without the metamaterials. Normalization is with respect to maximum gain data.

It is expected that larger emitters would result in greater far-field pressures since such sources can push more energy into the surrounding medium by displacing more air molecules. This is observed in the pressure amplitude plots (Figure 4. 16 (a)), where the amplitudes of the frequency response curves increase with the size of the emitter. However, the opposite trend is observed in the gain plots, where larger emitters boast lower overall gains than smaller emitters (Figure 4. 16 (b)). These larger emitters accelerate the air molecules with greater magnitudes so that they emerge from the emitter cavity with high velocities unsuitable for efficient evanescent coupling into the adjacent gaps.

Conversely, it can also be expected that miniature emitters would be unable to accelerate the air molecules enough to enable efficient evanescent coupling. To illustrate this trend, the maximum gain is plotted as a function of the emitter size, in Figure 4. 17.

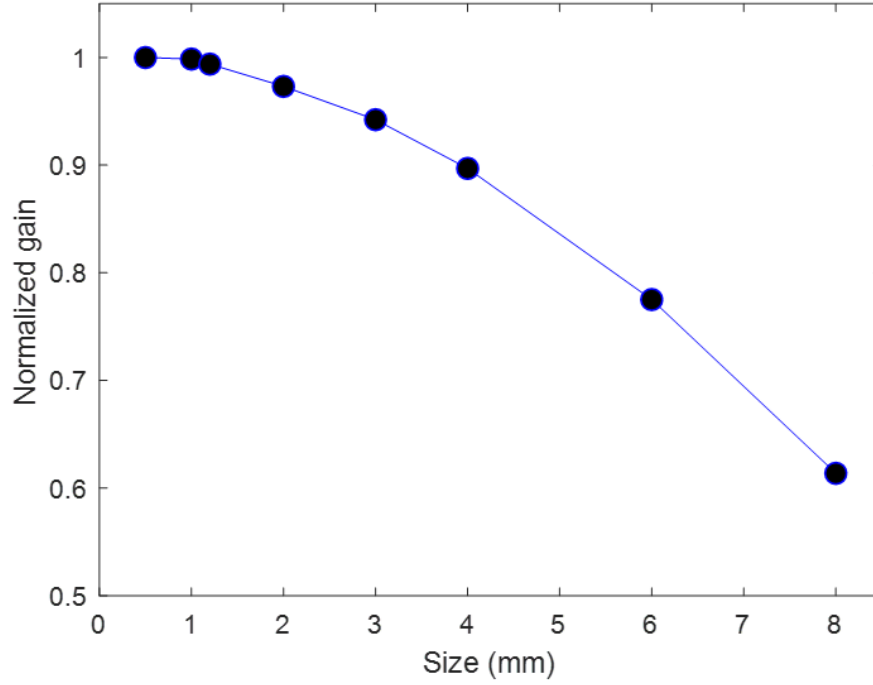


Figure 4. 17 Normalized gain as a function of emitter size.

The observable plateau at 1 mm and 0.5 mm indicates that an emitter sized in this range provides the most efficient matching of the mode fields, which maximizes the coupling between the emitter element and the metamaterial medium [132]. The trend in Figure 4. 17 suggests that emitters smaller than 0.5 mm may experience a drop in performance due to their inability to impart sufficient energy to the surrounding air molecules to enable efficient evanescent coupling— a consequence of sub-optimal mode-field matching. These results provide useful information for specific applications of the metamaterial emitter. Embedding a large emitter in the metamaterial emitter is suitable for applications that require high pressure output regardless of gain. Conversely, comparative investigations that need to showcase the

metamaterial's performance would be best suited with miniature emitters. The metamaterial emitter's performance is therefore optimized for emitters around 1 mm but can equally work for larger emitters.

4.3.5 Ambient temperature effects

Finally, the effects of the environmental conditions on the metamaterial's performance are investigated. In natural media such as air, the velocity of acoustic waves through them have a temperature dependency. Like heat, sound propagation entails the vibration of molecules. If the average kinetic energy of molecules in the medium is high, as indicated by the high temperature of the medium, then they move faster. As such, they can pass acoustic pressure waves comparatively quicker than in low-temperature environments. The temperature-dependent sound speed equation is given by [130]:

$$c(T) = c_{273} \cdot \sqrt{\frac{T}{273}} \quad (4.14)$$

Here, T is the absolute temperature (in Kelvin) and c_{273} is the speed of sound in air at 273 K, which has a value of 331.3 m/s. From equation 4.14 above, it is expected that a 1 K change in temperature would result in a 0.6 m/s change in the speed of sound in air. Also, the change in air density with temperature is given by

$$\rho(T) = \frac{p_0}{R \cdot T} \quad (4.15)$$

where $p_0 = 101325$ Pa is the atmospheric pressure, $R = 287.058$ J/kg · K is the universal gas constant, and T is the temperature in Kelvin. Substituting equations 4.14 and 4.15 into equation 2.2, the analytically derived metamaterial dispersion can be obtained for different temperatures and plotted, as shown in Figure 4. 18.

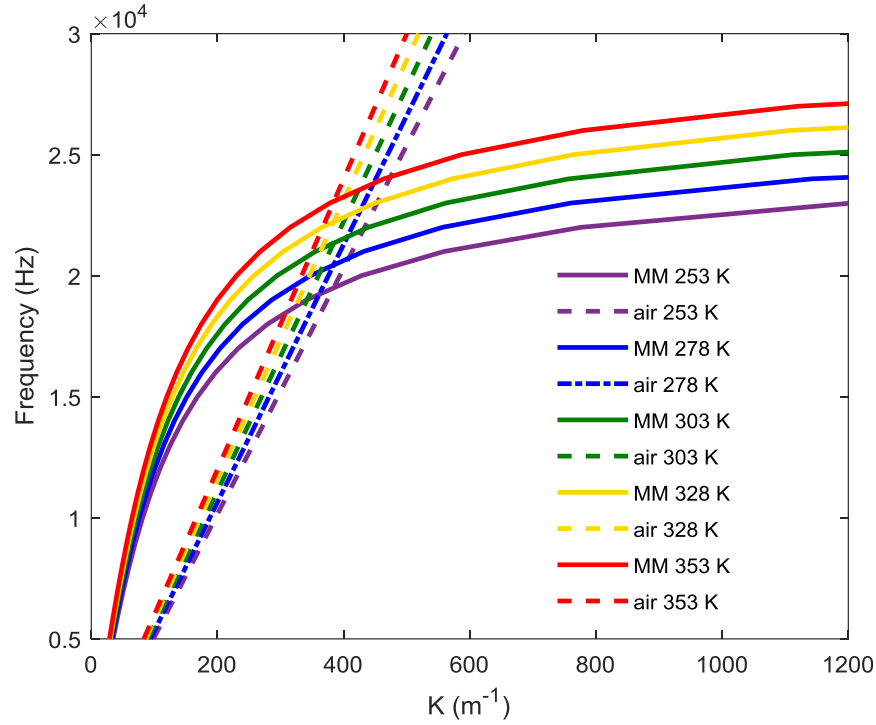


Figure 4. 18 Analytically obtained metamaterial dispersion plots (solid lines) as a function of temperature for different temperature values. The corresponding free space dispersion curves are also shown (dotted lines).

Because of its highly dispersive nature, this metamaterial structure is expected to have a comparatively higher frequency-dependent temperature rate of change than the free space. This is evident from the slope of the dispersion curve at a given frequency, which corresponds to the sound speed. It can, therefore, be expected that the peak and cutoff frequencies of the metamaterial structure will increase as the temperature rises. To investigate how this effect behaves within the artificially engineered metamaterial parameters, a numerical study is carried out where the ambient temperature of the base medium (air) is changed from 253 K to 353 K, and the results are plotted (Figure 4. 19). It is important to note that in this study, the

material properties of the polymer, which makes up the disks, are not considered since wave propagation within the structure is only via the base medium (air) due to the vast difference in bulk moduli between these two media.

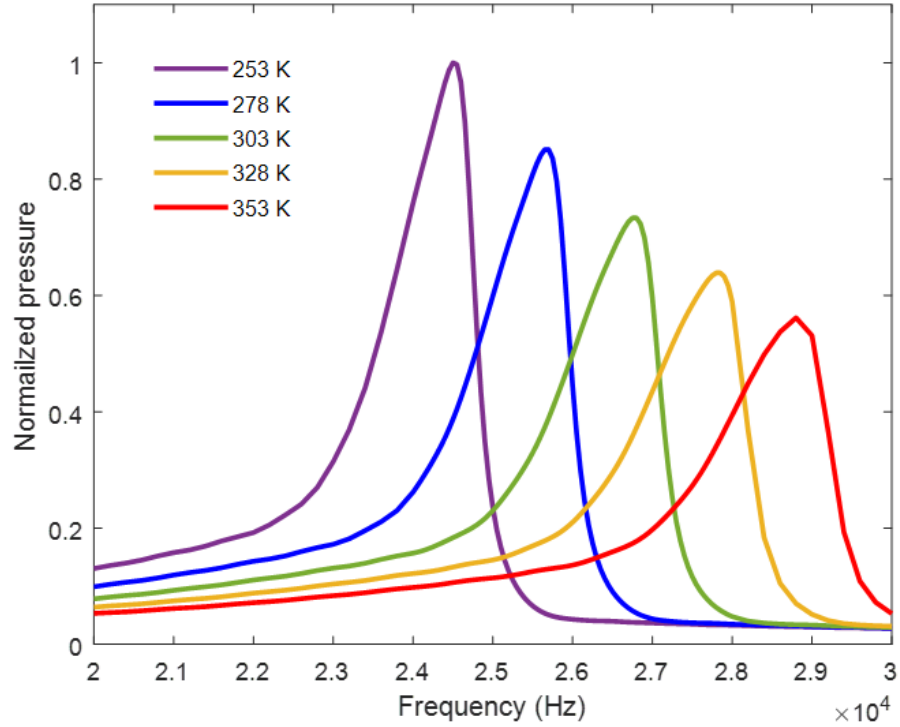


Figure 4. 19 Normalized far-field pressure plots for the metamaterial as a function of frequency for different ambient air temperatures.

Figure 4. 19 indicates that changes in the temperature have noticeable effects on the performance of the metamaterial structure. The working frequency of the metamaterial is strongly dependent on the ambient air temperature, with high

temperatures increasing the cutoff frequency. A decrease in the overall pressure amplification effect can also be observed. The air molecules within the metamaterial gaps possess higher kinetic energies at higher temperatures, which is further increased during the pressure perturbations caused by sound propagation. Degradation of the evanescent coupling mechanism would result from this, which is a similar phenomenon in the emitter size studies discussed in 4.3.4.

4.4 Experimental and numerical studies on a 25.6 kHz metamaterial emitter

The parametric studies discussed in section 4.3 provides a set of guidelines for realizing an optimal metamaterial emitter. As an earlier endeavor in this work, it was demonstrated that a metamaterial structure with roughly similar parameters is capable of providing equally extraordinary enhancements to acoustic wave radiation. To realize the metamaterial, a Stereolithography-type printer (Formlabs Form 2) was employed, and a rigid polymer (White FLGPWH04) was used. In this study, the metamaterial emitter's design comprises of 28 plates separated by 1 mm air gaps. The diameters of the plates range from 8.24 mm (last three plates) to 2 mm at the tip of the metamaterial. The design also features an emitter holder at the base(behind the 3-plate metamaterial cavity), with a pinhole measuring 1.2 mm in diameter to simulate a point source (Figure 4. 20).

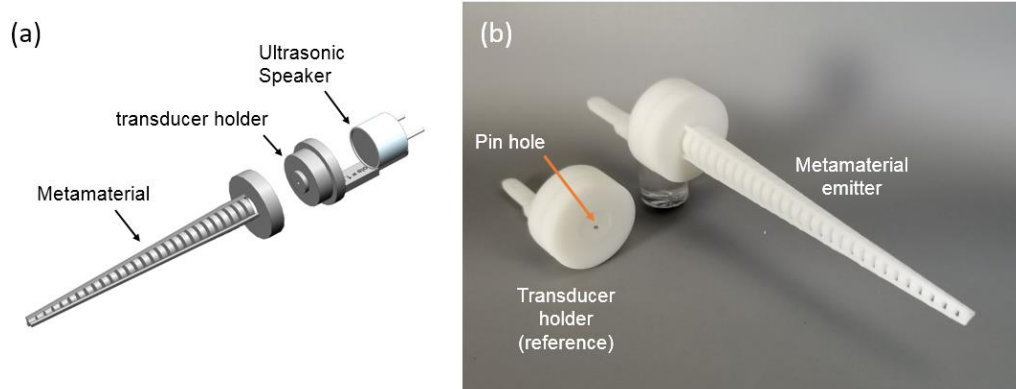


Figure 4. 20 (a) Exploded CAD model of metamaterial emitter assembly. The ultrasonic speaker is a commercially available unit with a center frequency of 25 kHz. (b) Photograph of metamaterial emitter realized studied in this work. The Transducer holder features a pinhole 1.2 mm in diameter to serve as a point source.

Such a metamaterial design strongly modifies the acoustic radiation of a transducer embedded inside the metamaterial by offering extraordinary acoustic wave confinement – a direct consequence of the metamaterial’s ability to support high- k states [60], [67]. The metamaterial achieves this by availing a high effective impedance medium Z_{MM} for the propagation of acoustic waves (Figure 4. 6). As discussed in section 4.3.1, an embedded emitter in this high impedance environment would experience enhanced radiation Π_{rad} , according to $\Pi_{rad} = \frac{1}{2}u_0^2 Re[Z_{MM}]$, where u_0 is a constant related to the external power supply. To smoothly deliver the enhanced acoustic energy into the free space with minimal impedance mismatch, the metamaterial cavity is padded with 24 disks spaced with one-millimeter gaps, which are tapered in profile in the propagation direction. As discussed in section 4.3.2, this

region is essential to couple the acoustic energy from the metamaterial to the air while retaining as much of the enhanced energy as possible, so that the sound waves are discharged from the metamaterial emitter with a greatly elevated pressure field.

Figure 4. 21 (a) and (b) shows the pressure amplitude and gain plots obtained experimentally and via numerical simulations.

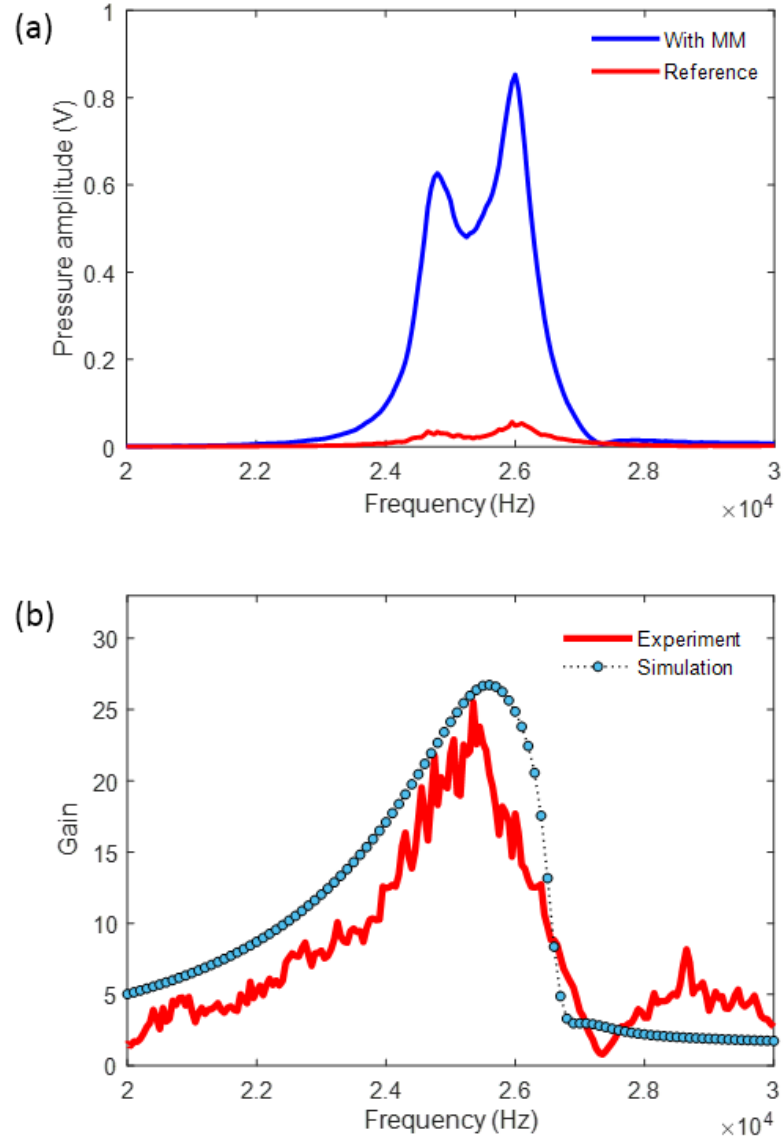


Figure 4. 21 (a) Emission spectrum of the emitter with and without the metamaterial (blue and red respectively) measured from 100 cm away. (b) Experimentally obtained and simulated emission gain of the metamaterial emitter, which is the ratio of the on-axis pressure amplitude of the emitter with and without metamaterial. The simulated data were equally obtained from 100 cm away.

The results show that a large increase in the sound source pressure level (on-axis pressure) is realized (Figure 4. 21 (b)). When compared to the same setup without the metamaterial structure, the emission sound pressure is greatly enhanced around its design frequency (~26.6 gain), and this observation is consistent across the experimental results and the numerical simulations. This prove-of-concept study enables the development of a compact acoustic emitter with high output power and extraordinary beam directivity, capable of mimicking the high-efficiency sound radiation and acoustic beam control functionality found in bio-acoustic systems.

The highly directional nature of the metamaterial emitter is also demonstrable in this design. The directivity and the effective aperture of the metamaterial emitter at the working frequency is displayed in Figure 4. 22.

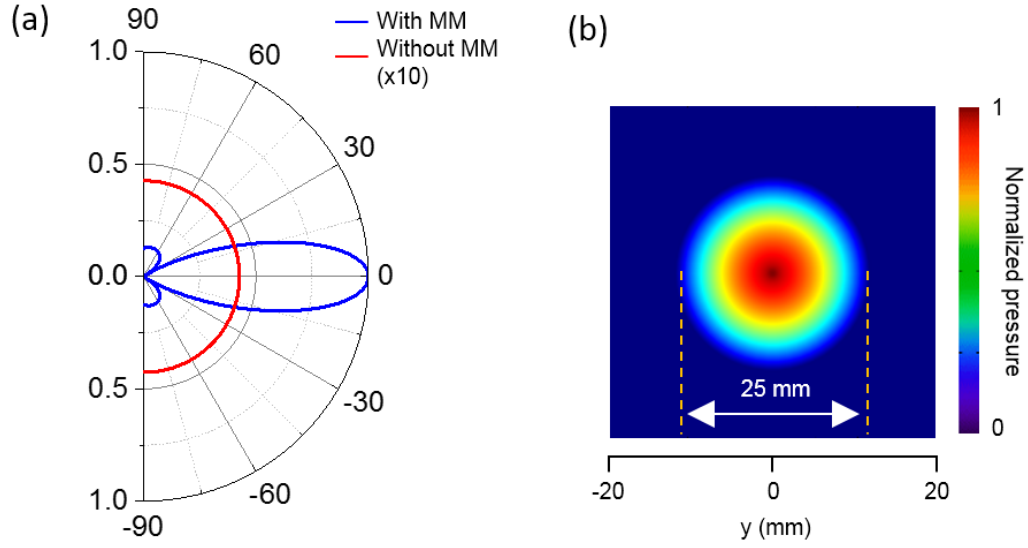


Figure 4.22 (a) Normalized directivity of the metamaterial emitter and the reference from the simulation. (b) The effective aperture of the metamaterial emitter obtained from the tip of the device.

The half-power beamwidth of the metamaterial is related to the wavelength through the equation [133]

$$\theta_{HPBW} = \alpha_{BW} \frac{\lambda}{d} \quad (4.16)$$

where α_{BW} is the beamwidth factor, λ represents the wavelength, and d is the effective aperture size of the system. A smaller value of θ_{HPBW} indicates higher directivity. The beamwidth factor α_{BW} usually assumes values like 70° in parabolic antennas. From the numerical simulations, d and θ_{HPBW} can be obtained for the metamaterial emitter, which would help obtain the beamwidth factor of this device.

From Figure 4. 22 (b), $d = 2.5$ cm at 25.6 kHz and $\theta_{HPBW} \cong 26^\circ$, giving $\alpha_{BW_{MM}} = 45.5^\circ$. In conventional sonar systems, achieving a higher angular resolution (smaller θ_{HPBW}) would usually require a large effective aperture size for a given wavelength. This condition is greatly relaxed in this high- k acoustic metamaterial emitter since, in addition to the large effective aperture size, it has a smaller beamwidth factor α_{BW} .

Notably, the highly directional characteristic of the metamaterial emitter is present across a large bandwidth, as evident in the experimentally obtained directivity contour plot in Figure 4. 23.

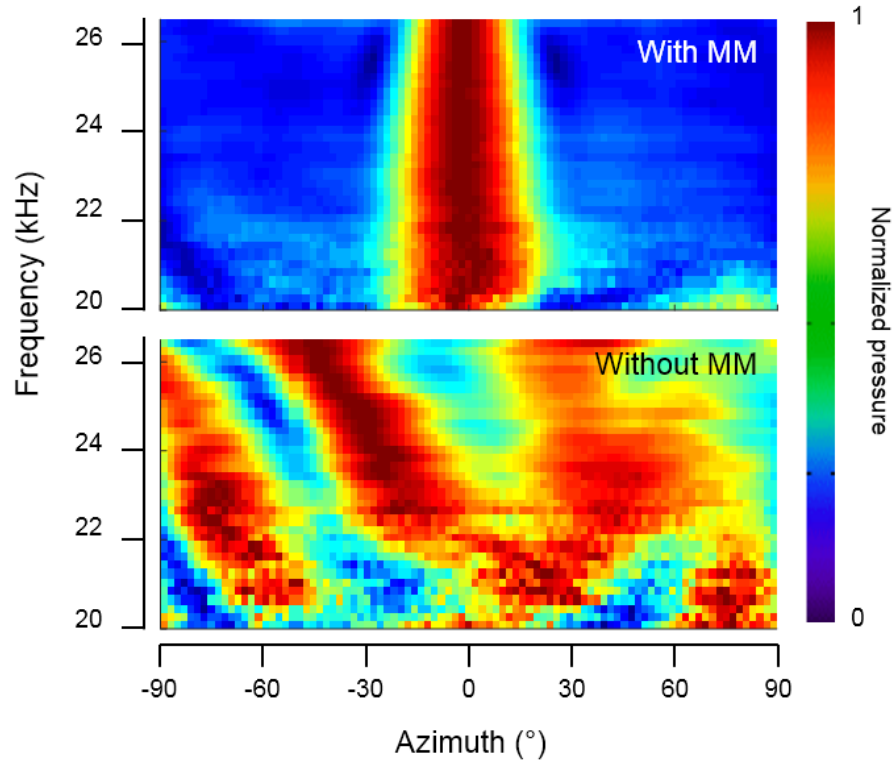


Figure 4. 23 Experimentally obtained contour plot of normalized emission amplitude as a function of frequency and azimuth for the case with the metamaterial (top) and without the metamaterial (bottom).

When compared with the system without the metamaterials, the directional advantages of the metamaterial emitter are obvious. Such a system be very useful in realizing a highly directional sonar system, as would be discussed in chapter 5.

4.5 Summary

High- k acoustic metamaterials provide a fertile platform for replicating some of the formidable phenomena found in nature. Similar to the acoustic radiation enhancement techniques found in nature, the high- k acoustic metamaterial emitter in this study has demonstrated the ability to greatly enhance the production and radiation of acoustic waves from an embedded emitter by making use of both metamaterial cavity and tapered coupling regions.

This chapter aimed at realizing an acoustic metamaterial for enhancing acoustic radiation and understanding the effect of different parameters on the performance of the metamaterial. In investigating the optimal size for of the metamaterial cavity, it was demonstrated that a cavity comprising of for disks measuring 8.25 mm in diameter and 2 mm in thickness, and spaced by 1 mm air gaps was optimal for enhancing acoustic waves of a centrally placed emitter over a 30 kHz bandwidth. Adding more disks to the metamaterial cavity degraded the far-field performance, while the two -disk configuration did not correspond to the metamaterial dispersion curve. The tapered metamaterial coupling region was identified to serve two key functions: to efficiently couple the enhanced acoustic waves from the cavity region to the free space with minimal losses; and to tailor the radiated pattern, producing a more directional beam. From numerical simulations, it was found that more gentle tapers are generally more favorable compared to steeper configurations. Furthermore, it was also found that the thickness of the metamaterial

gaps is an important parameter that can modify the optimal design frequency of the metamaterial emitter.

The emitter size was demonstrated to play a role in the pressure amplitude and gain from the metamaterial emitter. While larger emitters provide greater pressure amplitude, they boasted comparatively lower gains when compared with the system without the metamaterial. Also, in investigating the ambient temperature effects on the metamaterial emitter's performance, it was found that lower temperatures increased the far-field gain of the metamaterial while reducing its optimal and cutoff frequency. Such an effect provides more evidence in the metamaterial's ability to enhance the control of acoustic waves since a larger effect is achieved (pressure amplitude and frequency change) by changing the stimulus (temperature change).

Experimental studies performed for a characteristic 25.6 kHz acoustic metamaterial emitter demonstrated its ability to provide various enhancements to acoustic wave radiation. Notably, the metamaterial sonar introduced here opens a promising way into real-world applications. Compared with its no-metamaterial counterpart, the metamaterial emitter achieved an acoustic pressure gain of over 25 times at the design frequency. The waves were also emitted in a highly directional pattern commensurate with acoustic horns, thus acting as a mode-area transformer. Remarkably, the metamaterial emitter achieved this phenomenon in a manner unconventional to acoustic horns, where the mode-area instead decreases with aperture size. As such, although using different mechanisms, this metamaterial emitter can achieve similar emission enhancement features as found in some small animals and insects.

Chapter 5: Bio-inspired High- k acoustic metamaterial

SONAR

In nature, bio-acoustic systems for perception and navigation are generally highly optimized and are efficiently tailored to their specific applications. Echolocating animals possess remarkable bio-sonar systems to facilitate their navigation, communication, and foraging activities. Achieving such advanced levels of efficiency and functionality usually require these organs to be quite complex, and therefore pose formidable challenges for their replication in research. In recent years, the advent of acoustic metamaterials has opened new possibilities in the study of acoustics and has provided a novel platform for the development of new devices and applications in the field. In this chapter, it is also shown that a compact bio-inspired sonar system can be realized by using a high- k metamaterial emitter and receiver combination, and this system is demonstrated to have significantly improved detection range, the ability for small target size detection, and high spatial resolution for differentiation of closely spaced targets. Furthermore, using a robotic platform with a simple tracking algorithm, it is shown that the metamaterial enhanced sonar system demonstrated superior tracking abilities when compared to a similar system without the metamaterials.

5.1 Motivation

For many biological organisms in nature, sound is a critical means through which their surrounding is perceived. These animals are equipped with highly efficient bio-acoustic transducers for sound generation, detection, and manipulation, to which they owe their remarkable perception, communication, navigation, and preying capabilities. Some animals such as bats and dolphins (Figure 5. 1 (a) and (b)) combine their acoustic emitting and receiving systems to form a sophisticated sonar system for navigation and foraging [134]–[138]. They can produce exceptionally directional sonar beams that selectively “illuminate” a specific volume of space and enable accurate target detection and tracking of small objects in noisy and cluttered environments. This feature also enables efficient information processing by reducing echo interference in cluttered environments.

Acoustic metamaterials, on the other hand, present a new paradigm for manipulating acoustic waves and therefore offer a comprehensive and versatile platform for the development of novel bio-inspired acoustic devices with unique properties and functionalities. With these artificially engineered structures, researchers are capable of manipulating sound waves in ways that are unconventional in naturally occurring materials, and thus giving rise to such novel functional devices as super-resolution and hyper-resolution imaging devices, acoustic beamforming, acoustic sensing systems, acoustic cloaks, and acoustic filters [8], [14], [51], [67], [68], [139]. Such abilities could lend themselves to enhancing conventional sonar systems towards achieving similar functionalities as their biological counterparts. There have been

research advancements in sonar technologies in recent years. However, such efforts are generally relegated to the electronic layer in the form of complex signal processing techniques [112], [113], [133], [140]–[163]. In chapter 3, it was demonstrated that a high- k acoustic metamaterial based on the graded-index design was capable of enhancing acoustic reception and displayed many properties that are found in the much complex biological cochlea. In chapter 4, an acoustic metamaterial was realized that was capable of enhancing the acoustic emission of an embedded emitter, as well as educing such desirous properties as radiation enhancement and directionality. If these two acoustic metamaterials can be combined, it would be possible to realize a sonar system with enhanced capabilities.

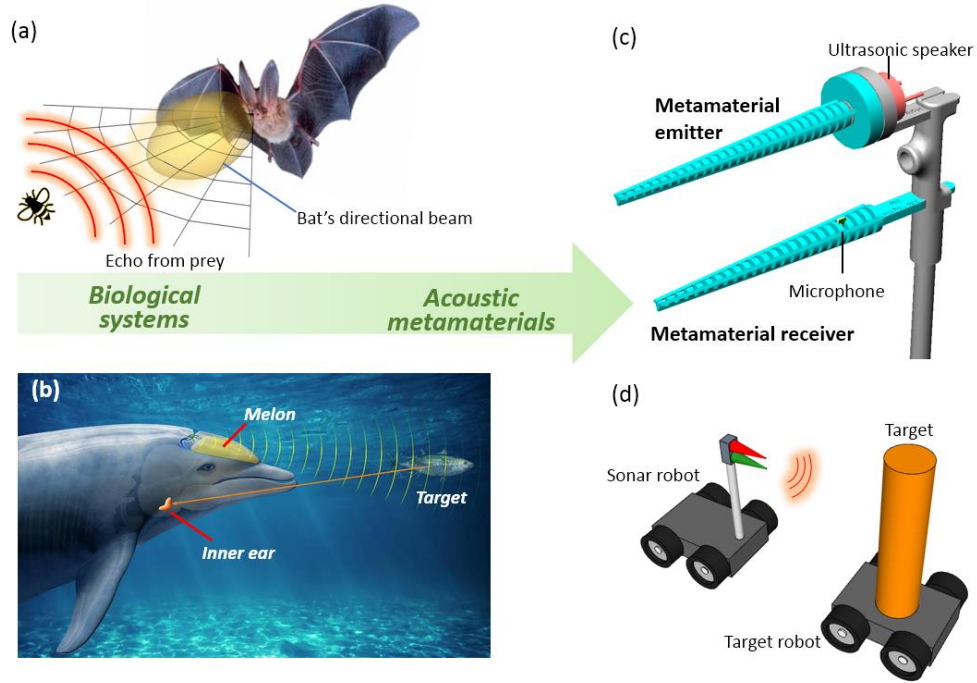


Figure 5. 1 Schematic of biological sonar systems in the bat (a) and the dolphin (b). (c) CAD model of the metamaterial sonar system comprised of an emitter and receiver pair of metamaterials. (d) Schematic of the metamaterial sonar robot tracking and following a target robot with a mounted target.

In this chapter, the acoustic metamaterials developed in the previous chapters are employed as a multifunctional bioinspired sonar platform that would benefit from the unique properties and functionalities possessed by these structures such as high-efficiency sound radiation, acoustic beam control, wave trapping, and amplification. By combining the metamaterial transmitter and receiver (Figure 5. 1 (c)), superior long-distance ranging and navigation, small target detection, and high-resolution acoustic imaging over conventional systems are achieved. It is also experimentally

demonstrated that a robotic sonar platform equipped with the acoustic metamaterials is capable of superior target detection and tracking (Figure 5. 1 (d)). This work represents a significant leap forward from the existing sonar-based robots that are plagued with limited performance and functionalities.

5.2 Analytical studies

It is possible to apply well established analytical studies on the metamaterial sonar to demonstrate the advantages that the metamaterial sonar system provides over a conventional sonar system. To evaluate the advantages of using metamaterials, three key factors are investigated as figures of merit for the metamaterial sonar; the enhancement of echolocation range, detectable target size, and target differentiation capability.

5.2.1 Conventional sonar system

Consider a sonar comprised of an emitter and a receiver (Figure 5. 2) that detects a target with a range of R_1 and R_2 from the emitter and receiver, respectively. For simplicity, the space between emitter and receiver is small, such that $R_1 \cong R_2$.

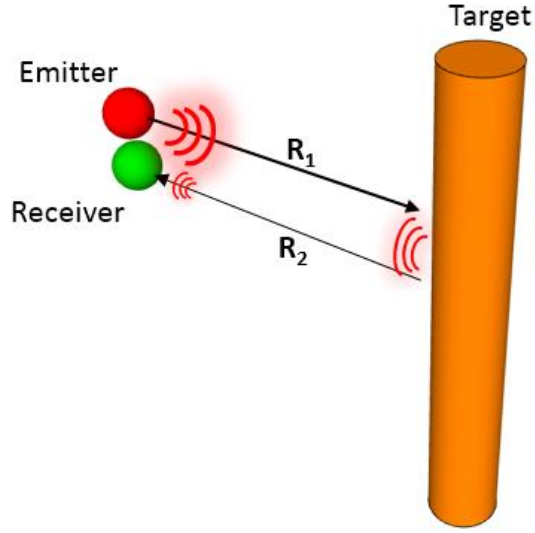


Figure 5. 2 Schematic of the sonar system for use in deriving the metamaterial sonar equation.

It is assumed here that the emitter is a small acoustic source radiating energy in all directions (three-dimensional case) so that the power density of acoustic waves propagating at the target location may be expressed as [164]:

$$S_t = \frac{W_e}{4\pi R_1^2} \quad (5.1)$$

where S_t is the sound power density at the target location R_1 , and W_e represents the transmitted power of the emitter. The acoustic waves incident onto the target from the emitter is reflected as echo signals which are picked up by the receiver of the sonar. The power density of echo waves detected by the receiver would depend on the crosssectional area of the target, can be written as:

$$S_r = \left(\frac{W_e}{4\pi R_1^2} \sigma \right) \cdot \frac{1}{4\pi R_2^2} \approx \frac{W_e}{16\pi^2 R_1^4} \cdot \sigma \quad (5.2)$$

where σ represents the scattering cross-section of the target, which is approximately proportional to the size of the target. To estimate the detection range of the sonar, it is assumed that the minimum power density detectable by the receiver is $S_{r_{min}}$, and as such the maximum detection range of sonar can be derived as:

$$R_{max} = \left(\frac{W_e}{16\pi^2 S_{r_{min}}} \sigma \right)^{\frac{1}{4}} \quad (5.3)$$

For convenience, the radiation power W_e of the sound source is converted to the radiation pressure P_{max} by $P_{max}^2 = W_e$, since the sound pressure field, rather than sound power, is generally the quantity being measured. Equation 5.3 can then be rewritten as:

$$R_{max} = \left(\frac{P_{max}^2}{16\pi^2 S_{r_{min}}} \sigma \right)^{\frac{1}{4}} \quad (5.4)$$

5.2.2 Metamaterial sonar system

The effects of the metamaterial emitter and receiver are now introduced, which has been demonstrated to provide significant gains in both emission and signal reception. By considering the emission gain G_t (measured by the far field pressure), equation 5.1 can be modified to depict the transmission gain as:

$$S_t = \frac{P_{max}^2 G_t^2}{4\pi R_1^2} \quad (5.5)$$

Similarly, with the reception pressure gain G_r , equation 5.2 can be rewritten as:

$$S_r = \frac{P_{max}^2 G_t^2 G_r^2}{16\pi^2 R_1^4} \sigma \quad (5.6)$$

The performance enhancement of a sonar comprised of metamaterial emitter and receiver may, therefore, be evaluated by its maximum detection range:

$$R_{max} = \left(\frac{P_{max}^2 G_t^2 G_r^2}{16\pi^2 P_{rmin}^2} \sigma \right)^{\frac{1}{4}} \quad (5.7)$$

From equation 5.7, it is evident that the maximum detection range of sonar could be drastically enhanced by using a metamaterial emitter and receiver system with significant emission and reception gains and provide obvious advantages for acoustic navigation, surveillance, and communication. Moreover, a sonar capable of detecting small objects is highly desirable for target recognition and tracking applications. Since a smaller object will have a lower scattering cross-section, the minimum detectable cross-section σ_{min} could be an effective figure of merit to characterize the sonar's ability to detect small-sized targets, which is expressed as:

$$\sigma_{min} = \frac{16\pi^2 P_{rmin}^2}{P_{max}^2 G_t^2 G_r^2} R^4 \quad (5.8)$$

Here $P_{r\min}^2 = S_{r\min}$ is the minimum detectable pressure of the sensor embedded in the metamaterial receiver. The inverse-squared relationship in equation 5.8 provides compelling evidence that using high gain metamaterials strongly enhances the minimum target cross-sectional area of the structure, thus significantly increasing the capability for small target detection. Vehicles or robotic systems equipped with a sonar system often need to perform tasks in highly cluttered environments, which requires the sonar system to discriminate and differentiate closely spaced targets – an important feature for path planning and collision avoidance [143], [165], [166]. Therefore, the system's angular resolution is a good figure of merit to evaluate the system's imaging capability. The angular resolution in terms of the distance between two targets can be expressed as [164]:

$$\phi_R = 2R \sin \frac{\theta_{HPBW}}{2} \quad (5.9)$$

Where R is the slant range aim, and θ_{HPBW} is the beamwidth given by $\theta_{HPBW} = \alpha_{BW} \lambda/d$, as discussed in chapter 4.4. In this relation, α_{BW} is the beamwidth factor, λ is the free-space wavelength, and d represents the effective aperture size of the system. In conventional sonar systems, achieving a higher angular resolution (smaller θ_{HPBW}) would usually require a large effective aperture size for a given wavelength. This condition is greatly relaxed in this high- k acoustic metamaterial sonar system since the metamaterials boast a large effective aperture size. As such, a higher resolution can be achieved with a relatively small-sized device, which is a useful advantage of the metamaterial sonar system.

5.3 Sonar experimental characterization

To demonstrate how the metamaterial sonar system addresses the factors mentioned above, namely enhancement of echolocation range, detectable target size, and target differentiation capability, the performances of the sonar system with and without the metamaterials are experimentally compared. The photographs in Figure 5. 3 (a) and (b) depict the sonar system with and without the metamaterials, respectively. For the receiver subsystem, a MEMS microphone was used (SPU0410LR5H-QB), and the orientation of its aperture was such that was always normal to the acoustic velocity field. This means that in the metamaterial, the axis of the aperture was perpendicular to the sonar axis (Figure 5. 1 (c)) since the velocity field in the metamaterial gaps is normal to the metamaterial axis, as discussed in Section 2.4.1 [27]. Conversely, for the receiver subsystem without the metamaterial, the axis was parallel to the sonar axis (Figure 5. 3 (b)). To properly align the sonar systems, a small laser was embedded in the metamaterial holders (red dot in Figure 5. 3 (a) and (b)).

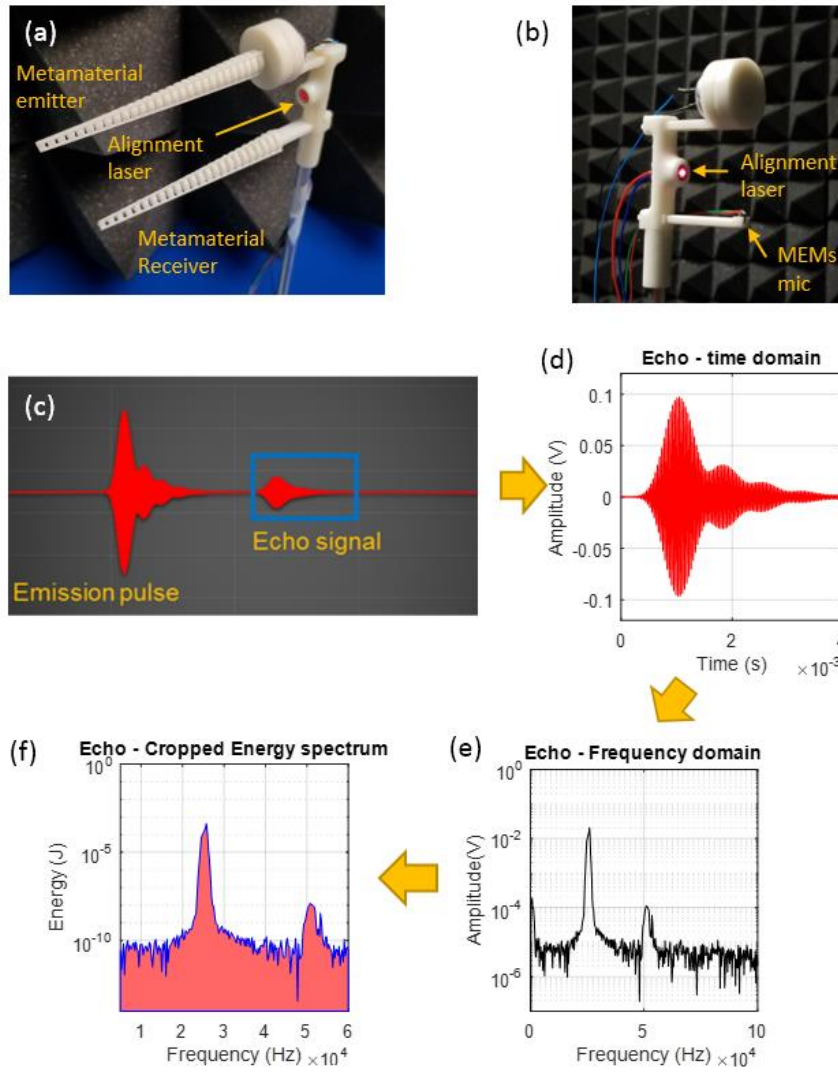


Figure 5. 3 (a) Photo of the metamaterial sonar system. The alignment laser is used as a visual reference of the metamaterial axis. (b) Photo of the sonar system without metamaterials. (c)-(f) Flow chart for obtaining the echo energy. (c) The entire waveform obtained from the receiver. The echo is cropped from the signal (d), and a Fourier transform is carried out on the signal to expose all its frequency components. (e) The energy is then calculated from a cropped frequency spectrum (f).

In the echolocation experiments in this section, the energy is obtained from the receiver and analyzed according to the schematic in Figure 5. 3 (c)-(f). The time-domain echo is cropped from the total signal received from the microphone. A Fourier analysis is then done on the pulse to reveal its frequency components, with values up to 100 kHz. Next, a cropped frequency spectrum is obtained, with frequency bounds $f_1 = 5$ kHz and $f_2 = 60$ kHz. Finally, the energy is obtained using Parsevelli's theorem, given by [167]:

$$E = \int_{f_1}^{f_2} |X(f)|^2 df \quad (5.10)$$

where $X(f)$ is the Fourier transform of the echo signal. The average of the energies from three echoes are plotted. The MATLAB codes for performing these routine calculations are presented in Appendix A5 and A6

5.3.1 Echolocation range

A schematic of the experimental setup for the echolocation range and detectable target size experiments is shown in Figure 5. 4 (a). In the experiment for investigating the echolocation range, a target with a diameter of 89 mm and a height of 1.5 m is used. The distance between the target and the sonar system ranged from 15 cm to 10.5 m. Figure 5. 4 (b) compares the performance of the sonar systems with and without metamaterial. This set of experiments was carried out in an open space so that

reflections from walls and other objects were minimized. As such, the noise floor of both systems (with and without metamaterials) could be assessed.

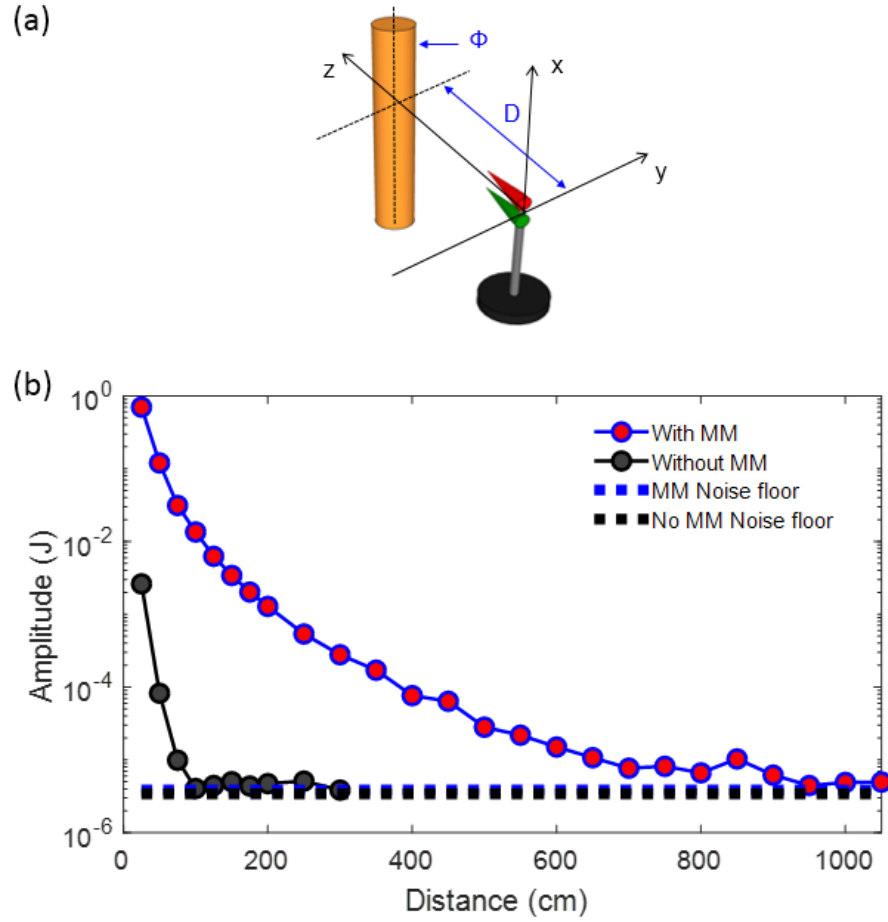


Figure 5. 4 (a) Schematic of the target size and distance experiments. (b) Echo energy as a function of distance for a target with and without metamaterials. The target was 89 mm in diameter and 1.5 m tall.

By comparing the normalized energy between the metamaterial sonar and the sonar without the metamaterials, it is apparent that the metamaterial sonar significantly extends the echolocation range about nine times with respect to the identical system without metamaterials. This is despite the slightly higher noise floor of the metamaterial sonar system, which comes as a result of the metamaterial amplifying all frequencies in the given bandwidth, whether they are part of the signal or noise.

5.3.2 Target size

In another set of experiments for investigating the detectable target size carried out in a closed chamber, each sonar system was presented with different sized targets located 55 cm away. The targets ranged from 1.3 mm to 400 mm in diameter and 40 cm height. In Figure 5. 5, the exceptional advantage of the metamaterial sonar possesses in detecting these targets is observed.

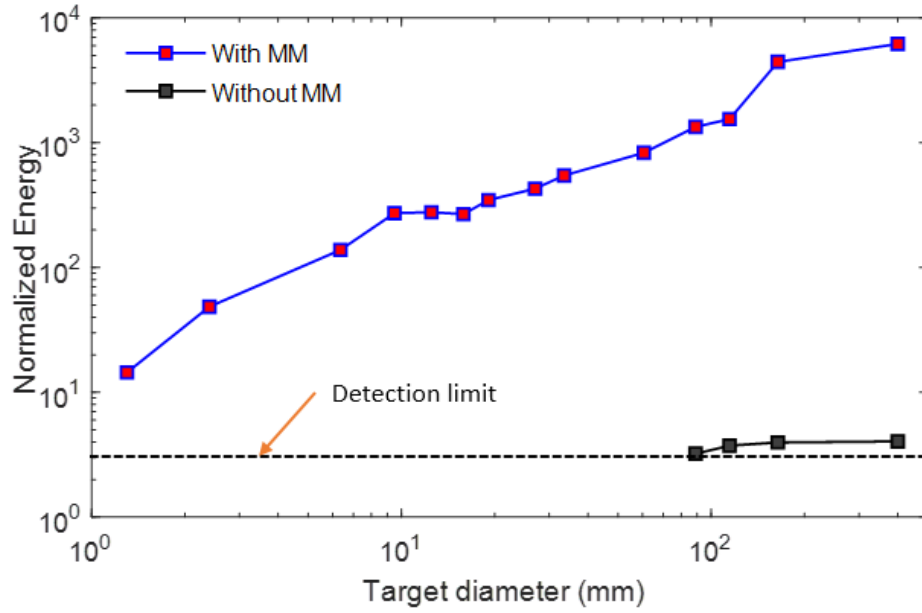


Figure 5. 5 Normalized echo energy for different target sizes with and without metamaterials.

The targets were 40 cm tall and were placed 55 cm away from the sonar setup.

In this set of experiments, the detection limit is defined as the limit beyond which the object's echo is indistinguishable from the background noise from the wall reflections. To better understand this, a power spectral plot for the targets is done and presented in Figure 5. 6 through Figure 5. 10.

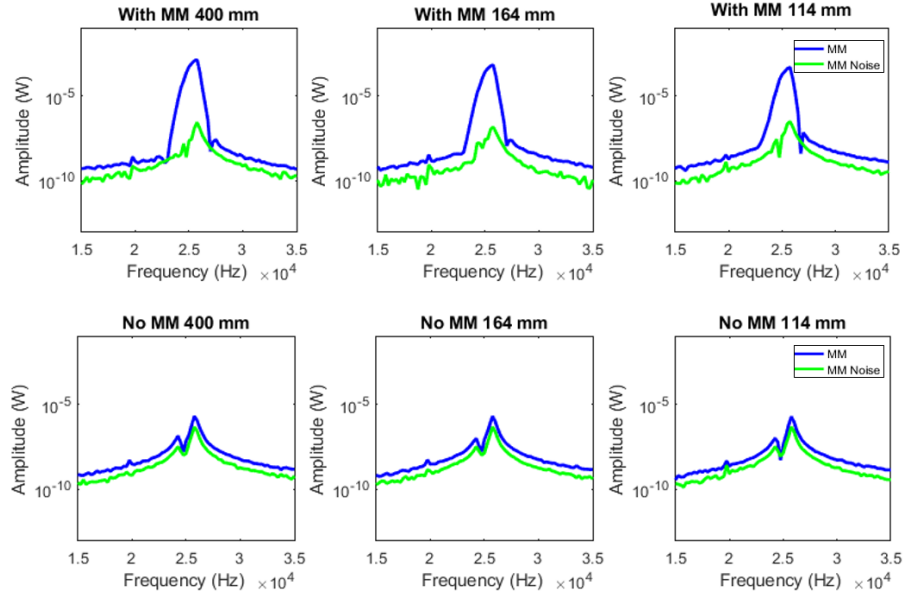


Figure 5. 6 Power spectrum of the 400 mm, 164 mm and 114 mm targets with metamaterial (top row) and without metamaterial (bottom row).

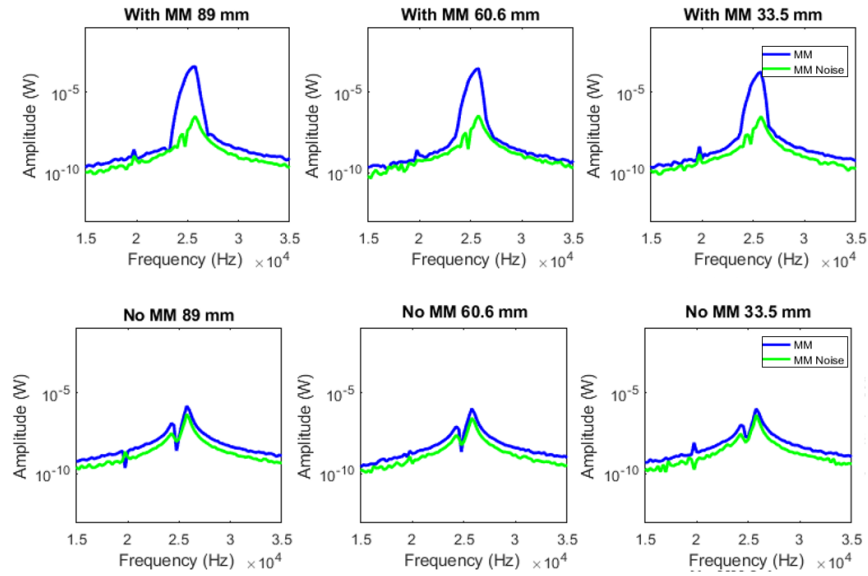


Figure 5. 7 Power spectrum of the 89 mm, 60.6 mm, and 33.5 mm targets with metamaterial (top row) and without metamaterial (bottom row).

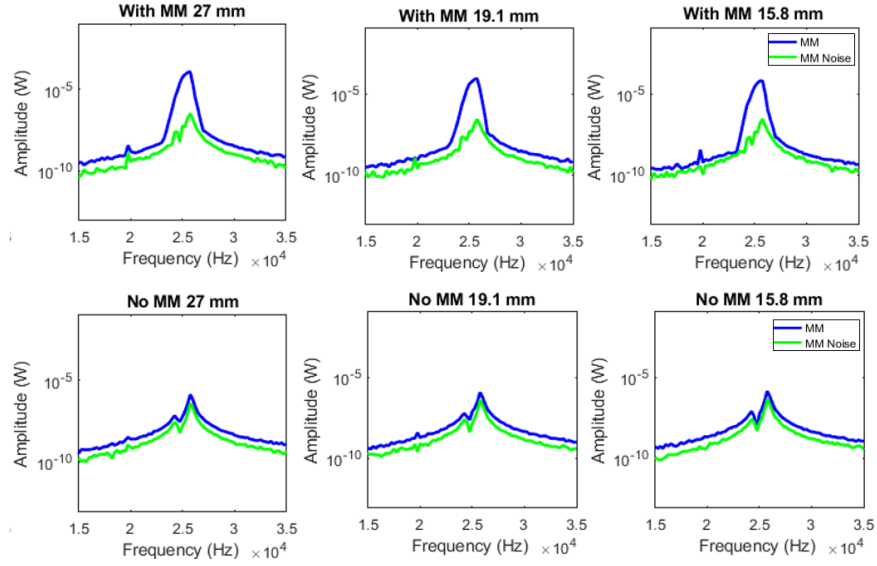


Figure 5. 8 Power spectrum of the 27 mm, 19.1 mm, and 15.8 mm targets with metamaterial (top row) and without metamaterial (bottom row).

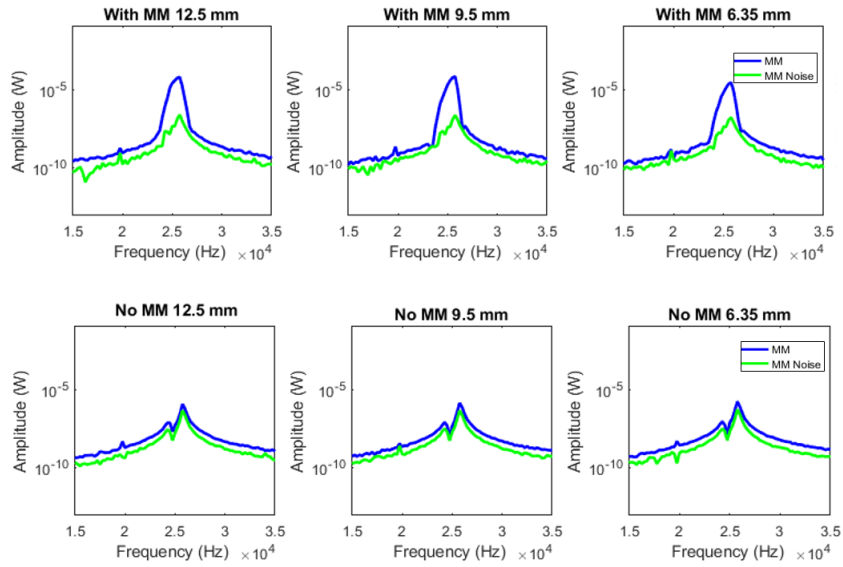


Figure 5. 9 Power spectrum of the 12.5 mm, 9.5 mm, and 6.35 mm targets with metamaterial (top row) and without metamaterial (bottom row).

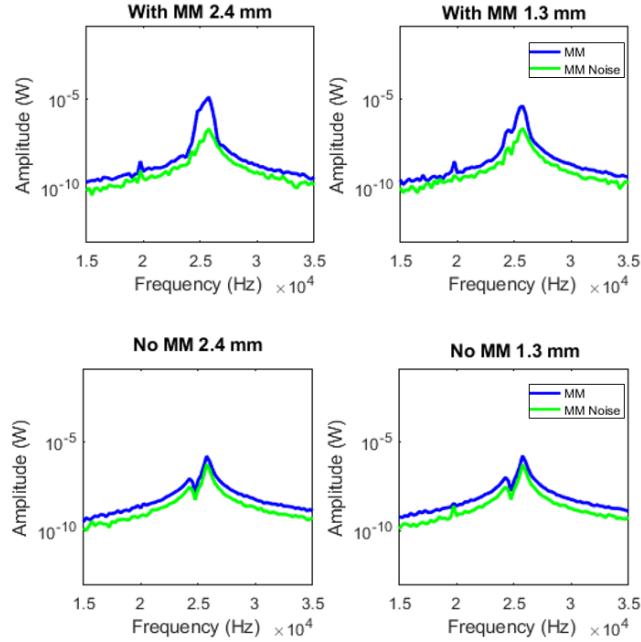


Figure 5. 10 Power spectrum of the 2.4 mm and 1.3 mm targets with metamaterial (top row) and without metamaterial (bottom row).

In the power spectral plots presented, the “Noise” data (green plots) represent data obtained when the targets were completely removed from before the sonar system. As such, the obtained power at the microphone is from background reflections. It can be observed from Figure 5. 7 through Figure 5. 10 that the received power from the sonar system without the metamaterials are constant from the 89 mm target and below, and barely distinguishable from the noise. As such, the sonar system without metamaterials reached its detection limit with the 89 mm target, while the metamaterial sonar did not reach its limit even with the smallest target. Therefore, the metamaterial sonar enhances the minimum detectable target size by over a factor of 68.

Additionally, a comparison of the time domain data between both sonar systems demonstrates the superior echo enhancement provided by the metamaterial system (Figure 5. 11 and Figure 5. 12). Such obvious advantages provided by the metamaterial system perceptible even without heavy signal processing could be very useful for platforms with limited processing power.

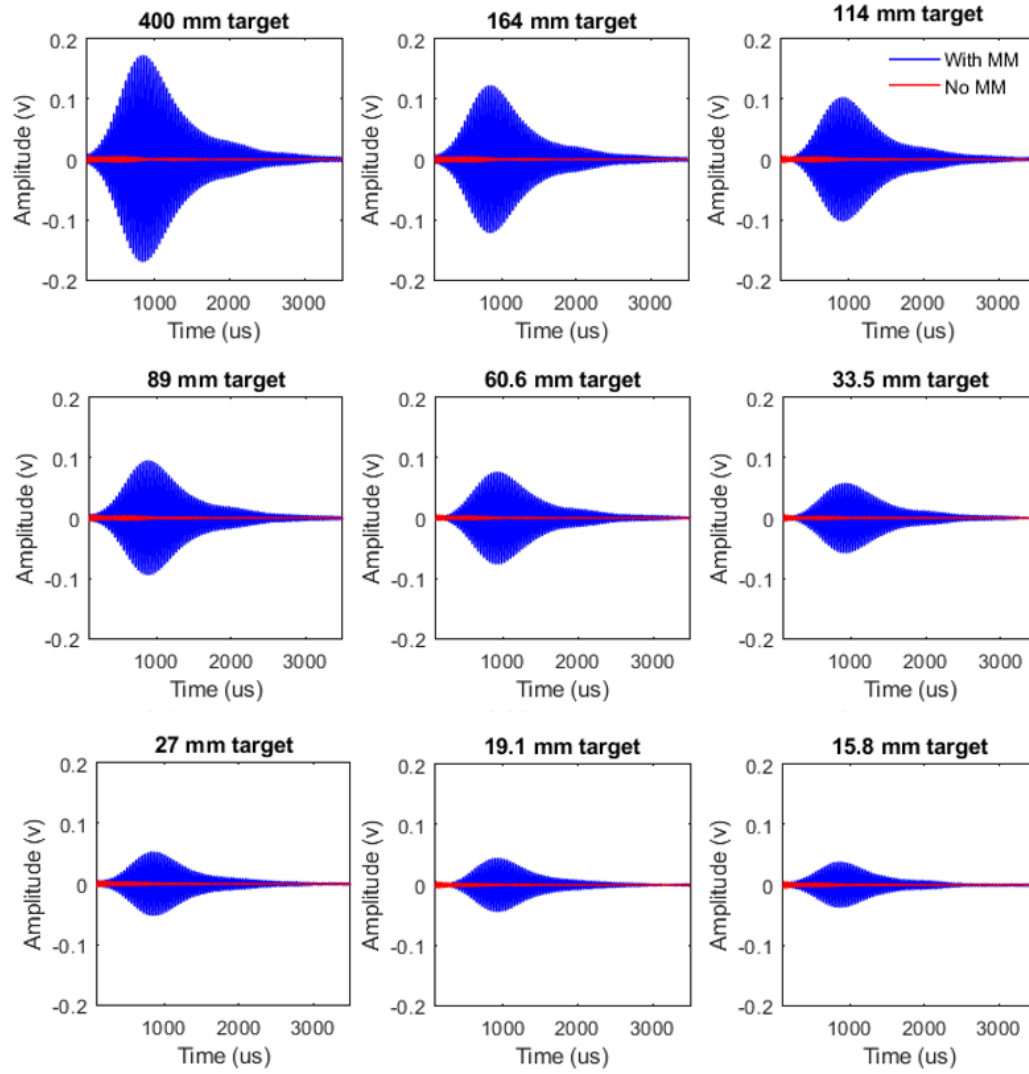


Figure 5. 11 Time domain data for the echoes of different targets with metamaterial (blue) and without metamaterial (red). Targets from 400 mm to 15.8 mm are shown.

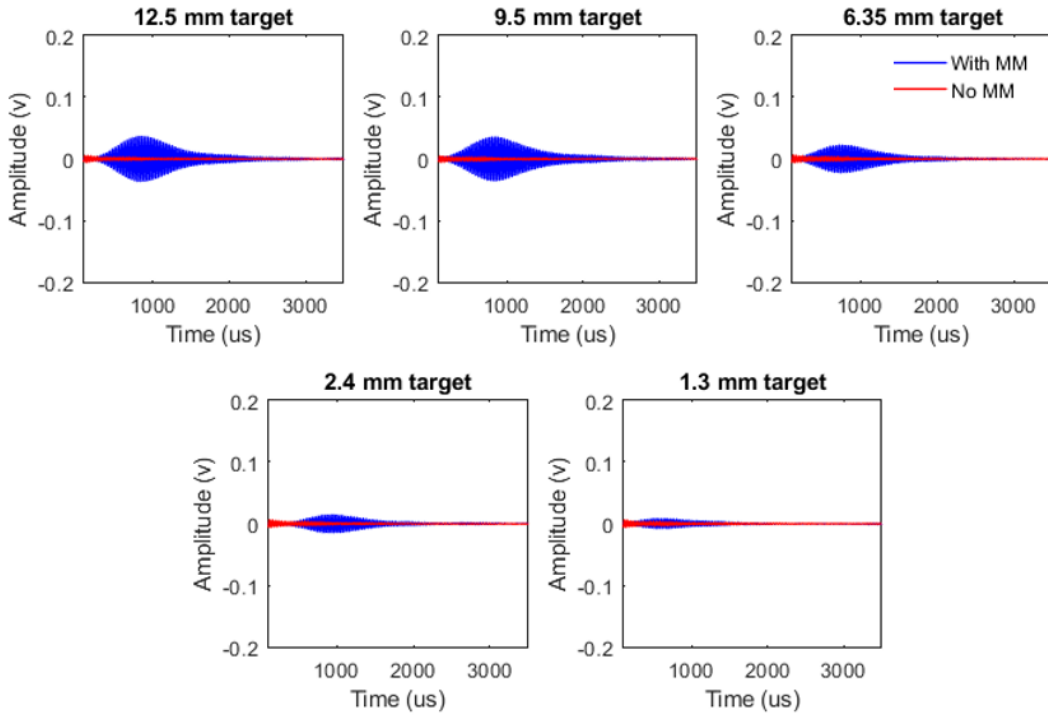


Figure 5.12 Time domain data for the echoes of different targets with metamaterial (blue) and without metamaterial (red). Targets from 12.5 mm to 1.3 mm are shown.

It is interesting to note that the echo signal produced by a 1.3 mm target with the metamaterial sonar system was markedly larger than that of the 400 mm target from the sonar system without metamaterials, as evident in Figure 5.11 and Figure 5.12.

5.3.3 Target separation

Next, the ability of the sonar systems to assess the gaps between two targets as well as differentiate (in terms of size) the targets are investigated. The setup for these

experiments is shown in Figure 5. 13, where two targets measuring 89 mm and 60 mm in diameter and 40 cm tall are placed in a plane perpendicular to the sonar axis and 55 cm away from the sonar system. The sonar system was mounted on a rotating stage which positioned the system so that it scanned from $\theta = 0^\circ$ to $\theta = 180^\circ$.

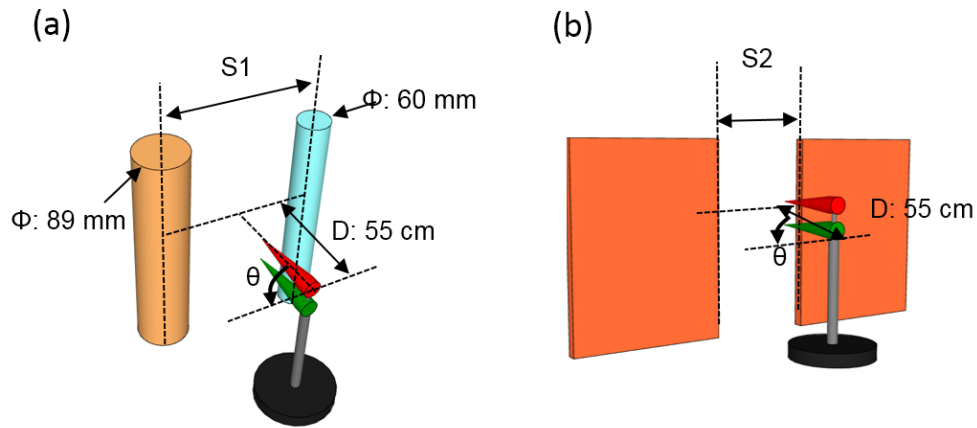


Figure 5. 13 Schematic of the target separation experiments. (a) Two pipes measure 89 mm and 60 mm in diameter and 40 cm tall, respectively (b) Gap experiments using two boards placed to form a gap in front of the sonar system.

In the pipe separation experiments in Figure 5. 14 (a), it can be seen that the metamaterial sonar can differentiate targets when the distance between the two targets larger than 17 cm. Furthermore, echoes from the targets are also observed to carry information of their relative size difference, since the echoes from the left target are comparatively larger than that from the right target, which corresponds to its larger

size. It is thus clear that the metamaterial sonar system has a higher angular resolution and can easily differentiate these closely spaced targets until the image profile of the two pipes become seriously overlapped, which indicates the resolution limit of the sonar system. By contrast, because of the poor angular resolution, the conventional sonar suffers from limited imaging ability and is incapable of resolving the closely spaced targets (Figure 5. 14 (b)).

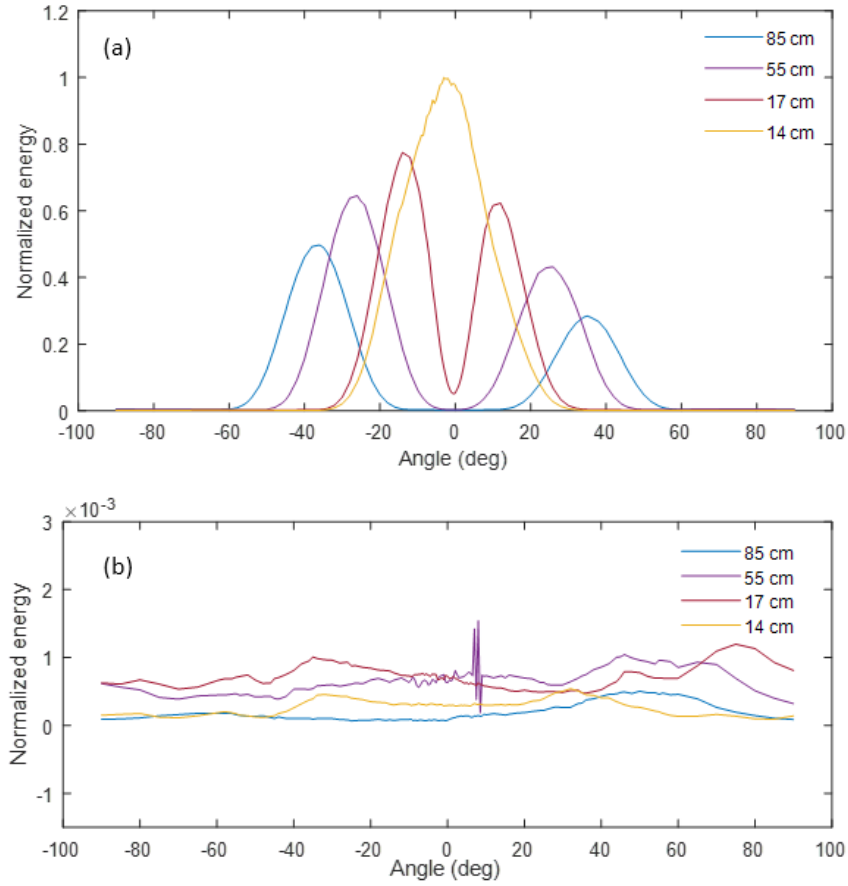


Figure 5. 14 Experimental results of the target separation detection using the sonar setup with the metamaterials (a) and without the metamaterials (b). Normalization is with respect to the maximum energy value from the metamaterial sonar system.

Next, the minimum separation resolvable by the sonar system in a high-echo power setup is investigated (Figure 5. 13 (b)). Presenting the sonar system with two flat panels ensures that most of the power is reflected to the system and mimics targets with a maximum surface area. Such a situation challenges the sonar's ability to resolve gaps in high echo power environments. As evident in Figure 5. 15 (a), the metamaterial sonar

system could resolve the gap between the panels up to 20 cm. By contrast, the sonar system without the metamaterials was incapable of identifying the gaps, since the low directivity and angular resolution ensured that it was consistently overwhelmed by the echoes from both panels at all angles (Figure 5. 15 (b)).

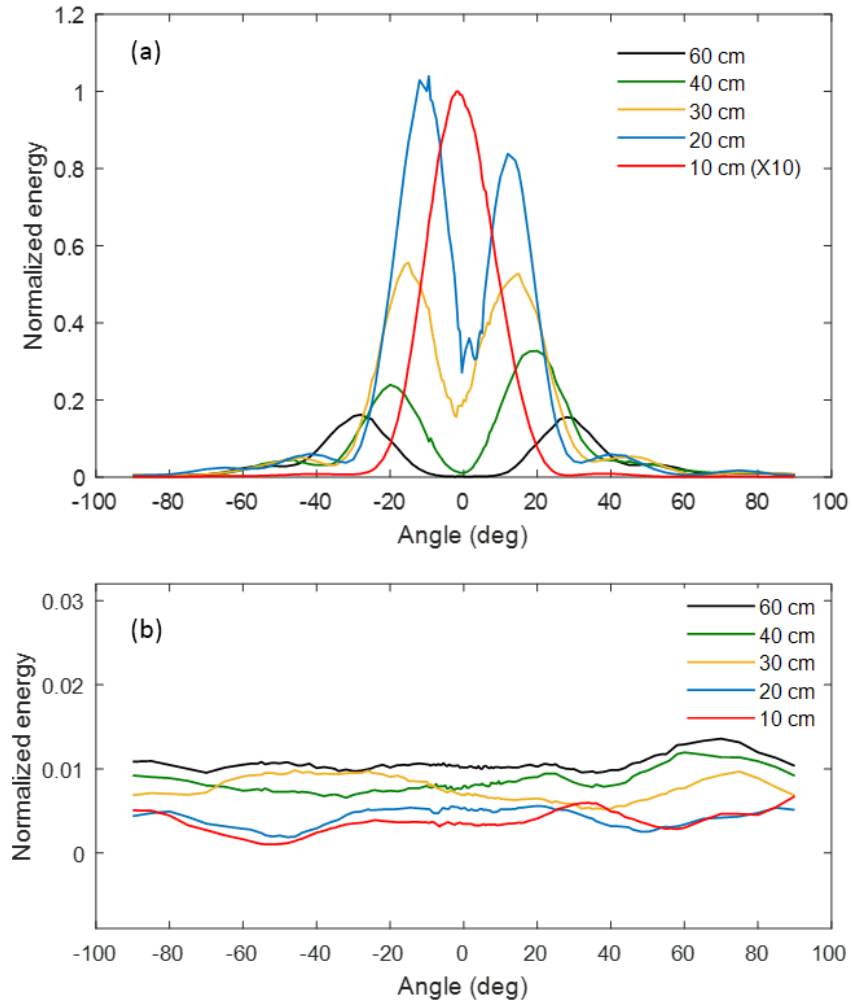


Figure 5.15 Experimental results of the gap separation detection using the sonar setup with the metamaterials (a) and without the metamaterials (b). Normalization is with respect to the maximum energy value from the metamaterial sonar system.

5.3.4 High-frequency metamaterial sonar

The acoustic metamaterials studied in chapters 3 and 4 were optimized to operate around 25.6 kHz, a frequency that closely matches the working frequency of some commercially available transducers. However, the principles of these metamaterial designs are for a wide range of frequencies and can be employed to design acoustic metamaterials to work with transducers with higher frequencies. In an earlier endeavor, a metamaterial pair designed to operate at around 40 kHz was realized and studied. A comparison between the characteristics of the 40 kHz structures and the 25 kHz structures reveal very similar behaviors. Figure 5. 16 (c) – (f) shows the experimentally obtained results of the 40 kHz emitter.

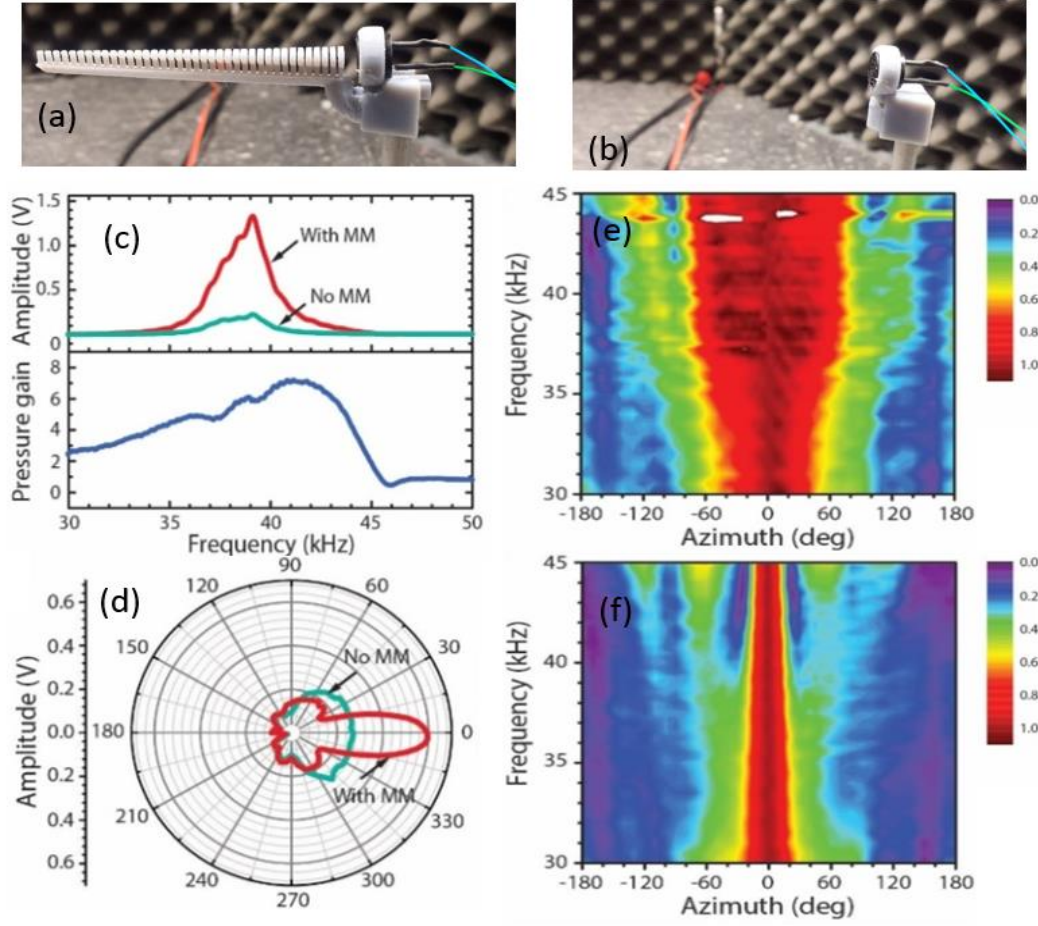


Figure 5.16 Photographs of the emitter equipped with the metamaterial (a) and without the metamaterial (b). (c) The frequency response of the metamaterial emitter measured by a reference microphone placed in the far-field. The pressure gain plot is defined as the ratio of the signal amplitude measured with the metamaterial to that measured without the metamaterial. (d) Emission directivity at 40 kHz. (e) and (f) show contour plot of the normalized emission amplitude as a function of frequency and azimuth for the case without the metamaterial (e) and with the metamaterial (f). Normalization is with respect to the peak azimuthal pressure for each frequency.

The 40 kHz metamaterial emitter in Figure 5. 16 (a) comprises 38 circular plates 1.15mm thick spaced with 0.35 mm air gaps giving a periodicity of 1.5 mm. The last plate diameter measures 5.7 mm. As expected, this metamaterial shows significant amplification (~8 times gain) of the acoustic pressure field when compared to the system without the metamaterials (Figure 5. 15 (c)), although such gain values are modest compared with the 25.6 kHz metamaterial emitter discussed in chapter 4. Such a smaller gain is expected due to a few reasons. First, the metamaterial print quality is comparatively low in resolution; thus, surface roughness resulted in greater losses in the structure, reducing the overall gain. This is further exacerbated by the higher frequency operation of the design, which gives rise to a low wavelength to roughness ratio, causing more energy loss. Furthermore, because high frequencies attenuate faster in a medium, it is expected that comparatively lower acoustic pressure would be recorded by a receiver placed at similar distances.

Figure 5. 16 (d)-(f) reveals the highly directional nature of this metamaterial emitter (~ 60°), with directivity increasing with the frequency. This is a similar phenomenon that was observed with the 25.6 kHz metamaterial. By contrast, the emitter shows poor directional emission without the metamaterial.

In Figure 5. 17, the 40 kHz metamaterial receiver characteristics are displayed. The dimensions of this receiver are similar to that of the emitter. Although this design is not optimized, it boasts useful advantages over the un-enhanced system (Figure 5. 17 (b)). It shows a four-times enhancement at ~43 kHz, which is well within the bandwidth of the MEMS microphone (Appendix C3).

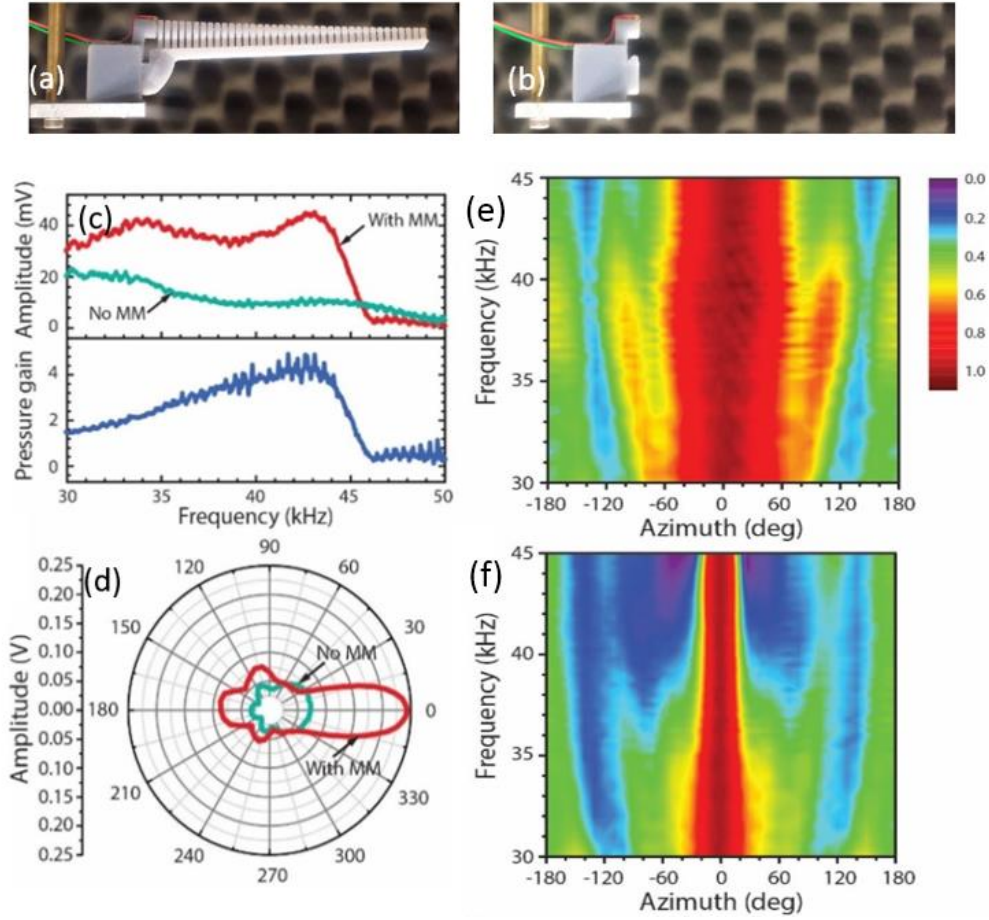


Figure 5.17 Photographs of the receiver (MEMS microphone) equipped with the metamaterial (a) and without the metamaterial (b). (c) The frequency response of the metamaterial receiver measured by the ultrasonic MEMS microphone. The bottom plot is the gain plot obtained by normalizing the plot with metamaterial with the data without metamaterial. (d) Reception directivity at 40 kHz. (e) and (f) show contour plots of the normalized reception amplitude as a function of frequency and azimuth for the case without the metamaterial (e) and with the metamaterial (f). Normalization is with respect to the peak azimuthal pressure for each frequency.

Similarly, the directivity of the 40 kHz metamaterial receiver shows comparable behavior to that of the metamaterial emitter and their low-frequency counterparts. This makes this receiver an ideal pair for the 40 kHz metamaterial emitter to realize a high gain, high-frequency metamaterial sonar system.

A sonar system was then formed with the 40 kHz metamaterials, and target size and separation experiments were conducted similar to the 25.6 kHz metamaterial sonar system. The results are displayed in Figure 5. 18.

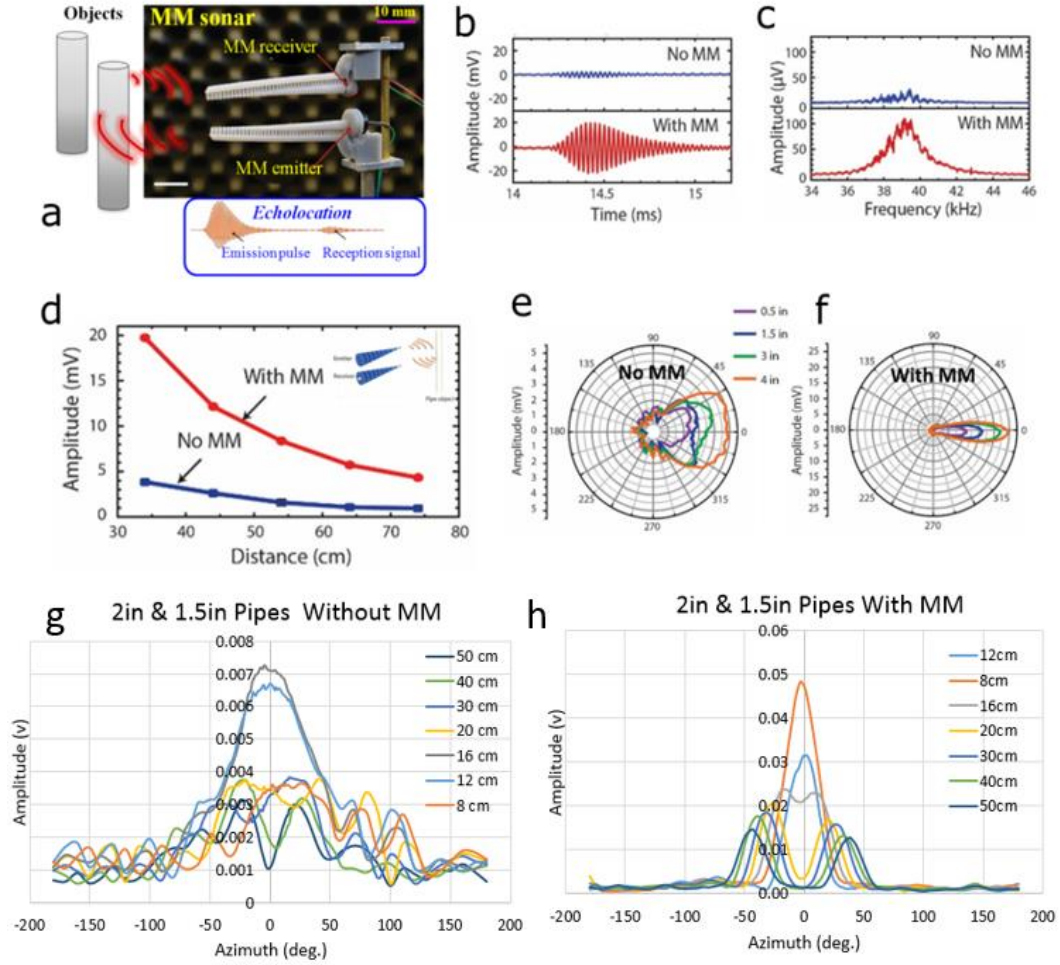


Figure 5. 18 (a) Photograph of the 40 kHz metamaterial sonar. (b) and (c) show echo signals (time and frequency domains respectively) detected by the metamaterial sonar as compared with the conventional sonar system (without using metamaterials). (d) The detection range enhancement. (e) and (f) show the directivity patterns of the active echolocation of pipes with different sizes for the cases without metamaterials and with metamaterials, respectively. (g) and (h) Experimental results of the target separation detection using the 40 kHz sonar setup without the metamaterials (g) and with the metamaterials (h).

The target separation experiments shown in Figure 5. 18 made use of two cylindrical targets (63.5 mm and 38.1 mm in diameter, and 40 cm in height) placed at different separation distances between them, which were insonified with the sonic sensing system 100 cm away. This system was able to distinguish the targets up to a separation of 16 cm, which is quantitatively better than the performance achieved with the 25.6 kHz metamaterial, which was placed almost half the distance (55 cm). This is mostly due to the shorter wavelengths of the 40 kHz, which increases the resolving power of the system (equation 5.9). In these experiments, minimal signal processing was done compared to what was presented for the 25.5 kHz metamaterials. However, the results still demonstrate the superiority of the metamaterial sonar system over a conventional system.

5.4 Metamaterial enhanced robotic tracking

In this section, a small robotic platform with a simple tracking algorithm is used to showcase the advantages the high- k acoustic metamaterials avail to a conventional sonar system. Use is made of the 40 kHz metamaterial, which is mounted on a small four-wheeled robot (Figure 5. 19). The metamaterial sonar system is fixed to a rotating servo, which acts as the “neck” of the system to orient the sonar in a specified direction. A long rod suspends the system at a sufficient distance from the ground to avoid unwanted echoes from the ground.

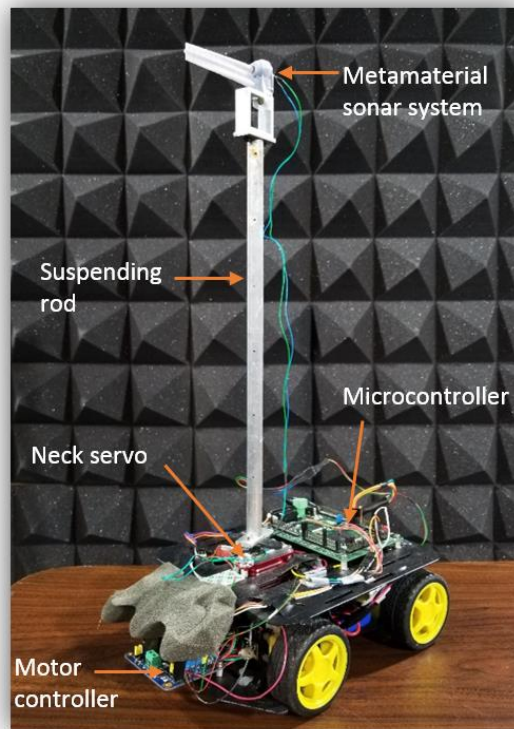


Figure 5. 19 Photograph of the four-wheeled sonar tracking robotic platform with the metamaterials.

5.4.1 Localization scheme

Similar to some bat species that scan their environment with rapid head and ear movements [140], [168]–[170], the robot steers the sonar to alternately point its sonar beam toward the left and the right directions at 100 ms intervals, emitting clicks and receiving echoes at each steer, as illustrated in Figure 5. 20.

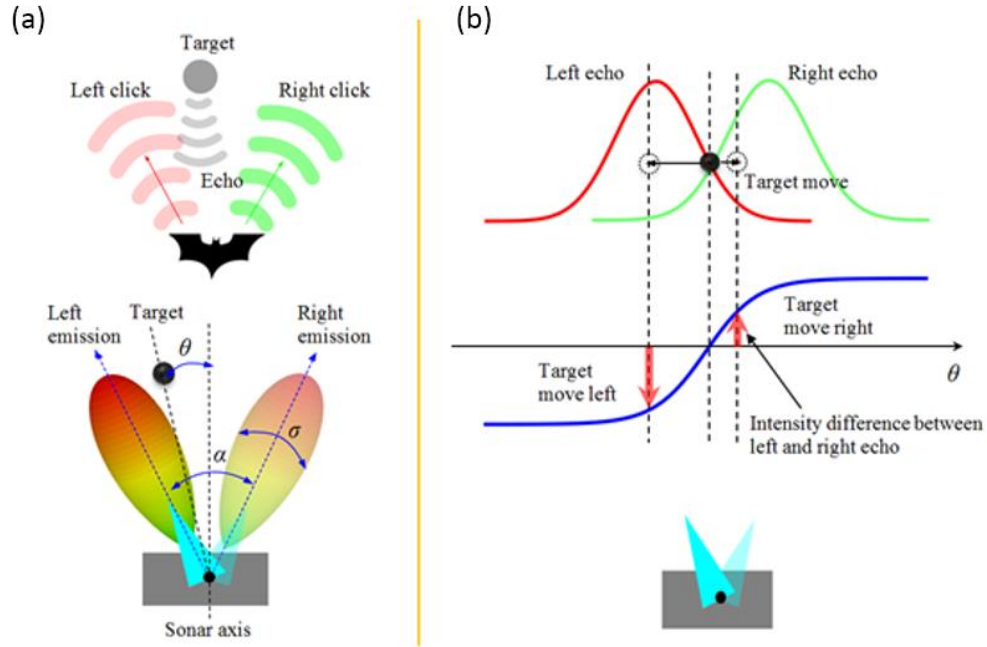


Figure 5. 20 (a) Schematic of the tracking method showing the relationship between the target and the two emitted clicks. (b) Schematic of the directional cues used for robot tracking. The intensity difference is used to infer the target's position.

The amplitude of the left and right echoes reflected from a target (such as a pole-like object) can be expressed as:

$$A_L = A(r)e^{\theta^2/\sigma^2} \quad (5.11)$$

and

$$A_R = A(r)e^{-\theta^2/\sigma^2} \quad (5.12)$$

where $A(r)$ is a function of the radial distance r between the target and metamaterial sonar, θ represents the azimuth of the target relative to the sonar, and σ is the metamaterial beamwidth. Similar to the Egyptian fruit bat's optimal localization strategy [171], [172], the sonar robot directs the maximal slope of its emission beam pattern onto the center of the target, thus maximizing changes in echo intensity that result from the motion of the target. Correspondingly, α is the optimal angle between the pair of clicks, and the azimuthal motion of the target relative to the metamaterial could be characterized by comparing the intensity difference between the left and the right echo signals:

$$A_d = \frac{A_L - A_R}{A_L + A_R} = \frac{e^{\frac{\alpha\theta^2}{\sigma^2}} - e^{\frac{-\alpha\theta^2}{\sigma^2}}}{e^{\frac{\alpha\theta^2}{\sigma^2}} + e^{\frac{-\alpha\theta^2}{\sigma^2}}} \quad (5.13)$$

When the maximum slope of the beam is directed toward the center of the object (Figure 5. 20 (b)), any motion of the object relative to the metamaterial sonar will result in the largest possible change between the left and right echo. The sign of A_d in equation 5.13 identifies the direction of target relative to the axis of the sonar, with a negative sign corresponding to the left while a positive sign indicates the right.

5.4.2 Tracking control scheme

A simple tracking scheme is implemented to demonstrate the functionality and effectiveness of the robotic platform in performing tracking maneuvers using the metamaterial sonar sensing system. The parameters needed for this tracking are the angle between the target and the sonar axis and the distance between the robot and the target (θ and d , respectively). Equation 5.13 is implemented to experimentally construct an $A_d - \theta$ mapping, while the distance d is approximated by the time delay between the maximum echo using

$$d = \frac{ct}{2} \quad (5.14)$$

where $t/2$ is the time of flight of the echo, and c is the speed of sound in air. A digital signal processing (DSP) board mounted on the robot serves as the brain of the robot, effectuating both robot control and target tracking algorithms. The control scheme aims at keeping a fixed following distance d_0 between the robot and the target as well as centralize the target on the sonar axis (minimize θ). As illustrated in Figure 5. 21, the tracking scheme consists of providing motor inputs from a simple decision-making process based on the parameters obtained (θ and d).

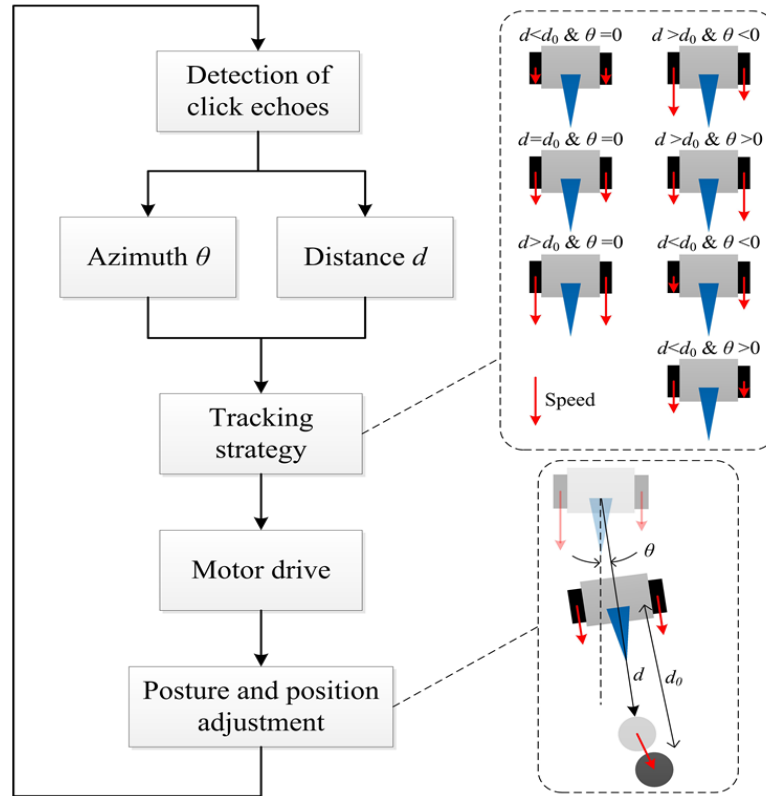


Figure 5.21 Schematic of the control scheme used for target localization, tracking, and following.

5.4.3 Robotic tracking experiments

A cylindrical target measuring 63.5 mm in diameter and 40 cm in height was placed on a second robotic platform. This platform was programmed to navigate simple paths so that the sonar robot with the simple tracking scheme discussed in section 5.4.2 would track and follow. The first set of experiments (Figure 5.22) investigates the sonar robot's ability to detect the object moving in a straight path. In this set of

experiments, the sonar robot is still and oriented perpendicular to the direction of the moving object (insert in Figure 5. 22 (a)). The target robot travels a total distance of 2.2 m, and the perpendicular distance between the target's path and the sonar system is 33 cm. The robot is tasked to orient the sonar (turn the neck servo) to track the moving target. This experiment exposes the sonar system's spatial and temporal resolution, with the difficulty of this task increases with the distance from the robot.

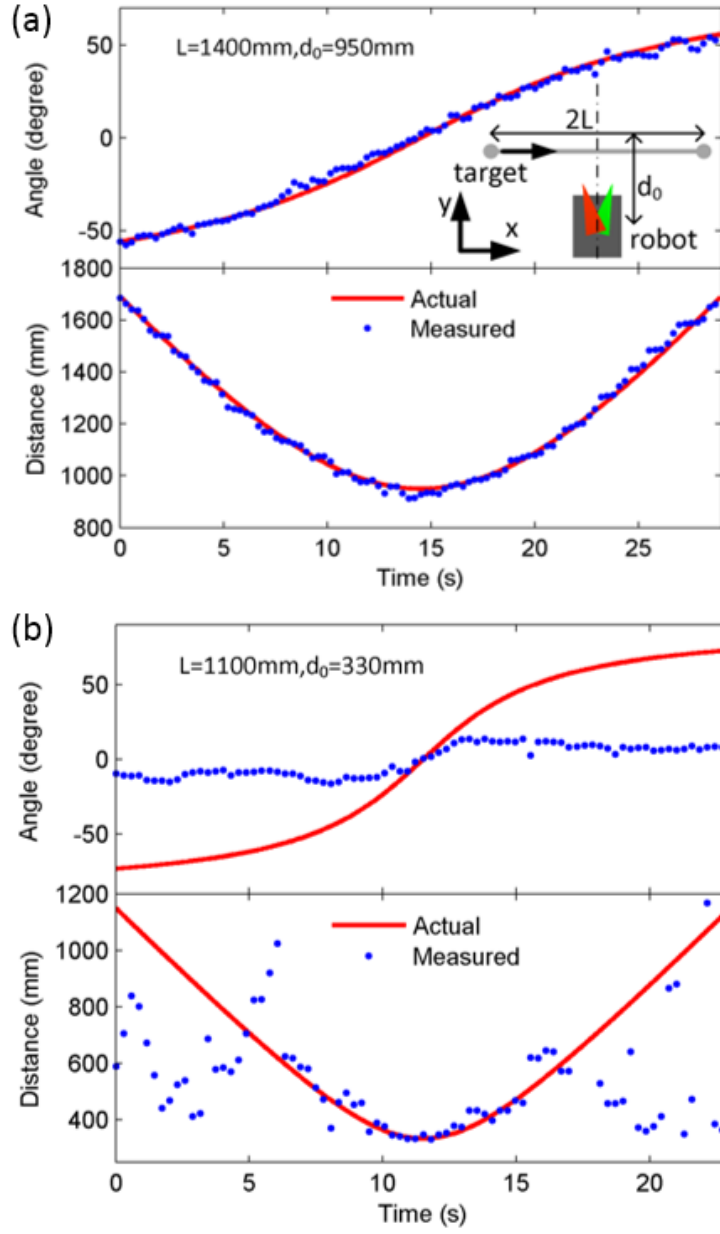


Figure 5. 22 Sonar tracking of a target moving in a straight line. The “Actual” results (red) are from the target robot, while the “Measured” results are from the sonar robot. (a) Tracking results for the metamaterial sonar. The insert in (a) is a schematic of the experimental setup. (b) Tracking results for the sonar without the metamaterials.

The results show that the metamaterial sonar was able to track the robot with superior accuracy in terms of distance and angle. This superior tracking capability is due to its good angular resolution and signal strength. By contrast, the sonar system without the metamaterials showed poor tracking capabilities, only achieving its optimal performance when the target was very close to the sonar.

In another set of experiments, the sonar robot was tasked to follow the target robot negotiating a circular path depicted in Figure 5. 23 (b).

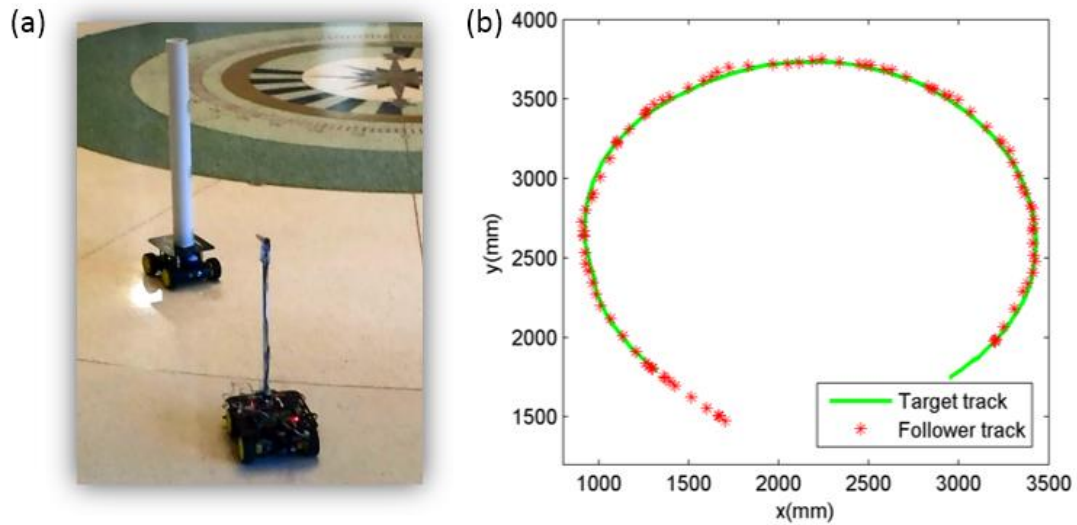


Figure 5. 23 (a) Photo of the metamaterial sonar-equipped robot tracking and following the target robot. (b) Results of the metamaterial equipped tracking robot tracking and following the target robot on a circular path.

The metamaterial sonar robot was able to follow the target robot with remarkable accuracy, which demonstrates the advantages that the high- k metamaterial sonar provides active echolocation and robotic tracking. Also, moderate interferences from nearby objects such as chairs did not degrade the metamaterial sonar robot's tracking performance. By contrast, due to the low resolution, low signal power, and low signal-to-noise ratio, the sonar robot without the metamaterials was incapable of tracking the target when subjected to the same circumstances.

5.5 Summary

Having established the metamaterial emitter's ability to enhance the radiation properties of a point source emitter in chapter 4, and the metamaterial receiver's formidable capabilities in sensing enhancement with similar features of mammalian cochleae systems in chapter 3, it is discernable that combining these systems can be very useful in improving sonar systems. This was demonstrated by combining the metamaterial emitter and receiver to form a metamaterial sonar. This system is specifically designed to make use of the pressure and directivity enhancement of both metamaterial emitter and receiver. The experimental data showed remarkable results, with drastic enhancement compared with the reference (no metamaterial) sonar system. The echolocation range experiments took particular advantage of the radiation pressure enhancement feature provided by the metamaterial sonar, extending the detectable range up to 9 times with the 25 kHz sonar system. When testing the sonar system with different target sizes at a fixed distance, the

metamaterial sonar reduced the minimum detectable object size by over a factor of 68. In the experiments to test the resolution of two targets 55 cm away, the metamaterial sonar system successfully resolved the targets up to a separation of 17 cm, while the system without the metamaterials was unable to resolve the target under the same settings. Moreover, the size difference between the two targets was noticeable with the metamaterial system. Such an experiment showcased the effect that a directional beam emission can have on target differentiation. These formidable properties were demonstrated to be valid for a metamaterial designed to operate at higher frequencies (~40 kHz).

The advantages that the metamaterial sonar system provides over conventional sonar systems could lend themselves in aiding tracking in a robotic sonar platform. It was shown that the sonar tracking robot equipped with a simple tracking algorithm was capable of superior tracking with the metamaterials. The results demonstrate the immense practical values that acoustic metamaterials have and show that the research in acoustic metamaterials transcends academic curiosity and could find immediate applications in solving real-world problems.

Chapter 6: Conclusion

Acoustic metamaterials promise to provide unprecedented control over acoustic waves than has been otherwise possible, which is an interesting proposition worth investigating. The idea that a medium with high wave vector values and high energy DOS could provide extraordinary control of acoustic wave propagation is revolutionizing the field of acoustics and has been explored in research in recent years. This dissertation work has focused on investigating the properties of such high wave vector acoustic metamaterials, as well as applications in which they could be used.

6.1 Summary of the dissertation work

6.1.1 Research question responses

This work set out to explore three key questions (Chapter 1.3), of which the responses are provided herein. First, the fundamental properties that electromagnetic high- k metamaterials possess have been identified in the realm of acoustics. Electromagnetic metamaterials exhibit unique and useful properties as energy confinement, wave radiation enhancement, energy transport, and enhanced dynamic control. These

properties are equally present amongst high- k acoustic metamaterials and were demonstrated in this work via numerical simulations, analytical studies, and experimental studies.

Second, a useful tool that enables accurate experimental studies of the intrinsic properties of high- k acoustic metamaterials is realized, studied, and used. This fiber optic microphone probe has an ultrathin profile, which enables accurate probing of the acoustic fields. Such a system removes the size limitations that conventional microphone systems inevitably introduce due to their bulky sizes, enabling the intrinsic characterization of even smaller metamaterial structures.

Third, the high- k properties of acoustic metamaterials have been leveraged in this work to realize acoustic metamaterials with practical applications that would enhance acoustic sensing and emission. Taking advantage of the wave confinement and transport, as well as the radiation enhancement properties of high- k acoustic metamaterials, these metamaterials are proven to provide exceptional advantages over conventional acoustic systems.

6.1.2 Research summary

To realize high- k acoustic metamaterials, the fundamental criterion is the need for the existence of a vast difference in the mass densities between the constituent materials to ensure that the lattice periodicity remains smaller than the working frequency of the structure. Two categories of high- k metamaterials have been identified according to their equi-frequency contour plots: elliptical and hyperbolic metamaterials. By sustaining waves with much higher wave vectors than their low- k metamaterial

counterparts or the free space, these high- k acoustic metamaterials can demonstrate useful properties such as energy confinement and transport, wave control enhancement, and enhancement of acoustic radiation. In this work, these properties were studied and explored via novel metamaterial designs.

A key challenge faced in the study of acoustic metamaterials is that the unit cells of these structures tend to be quite small, usually in the millimeter scale, making it difficult to directly measure the pressure fields inside the structures without compromising them. To overcome this challenge, a low-profile fiber optic microphone probe was developed, which was demonstrated to be robust, and have excellent sensitivity and omnidirectionality. This sensor is based on low coherence interferometry technique, which makes it very stable and less susceptible to electromagnetic interference. The studies carried out in this work benefited from extensive use of this fiber optic sensor to unearth the intrinsic characteristics of the acoustic metamaterials.

The ability to enhance control over the propagation of acoustic waves in or around them, as identified as one of the properties of high- k acoustic metamaterials, was exploited through metamaterial designs for acoustic reception. Notably, the metamaterials realized and studied for their receptive characteristics were low dimensional, which is a desirable quality because it enables easy integration into systems or subsystems where they can be used. Due to their highly dispersive nature, these structures possessed useful properties in modifying the acoustic waves in their subwavelength unit cell structures. They could produce intense pressure fields due to the wave compression effect in their anisotropic cavities. Placing a miniature acoustic

sensor within these cavities enabled direct access to these modified pressure fields. Another useful property shared by both metamaterials in this study is the ability to spatially separate frequencies across their length – a filtering feat analogous to what is found in the cochlea, which is a highly complex biological system in the mammalian ear. It was demonstrated that such comparatively simple systems could functionally mimic the highly complex functions of the mammalian cochlea.

One of these low-dimensional acoustic metamaterials for acoustic reception enhancement was also configured to enable active modification of its parameters, thus broadening the usability bandwidth of the device. By enabling a geometric parameter of the structure (height of exposed plates) to be arbitrarily alterable, an active metamaterial was realized, which further broadened the frequency bandwidth of the structure, as well as introduced other functionalities as switching and pulse delay control. The latter is a feature that combines the advantages of the high refractive index nature of the metamaterial with the dependency of the speed of the acoustic waves through the medium on the height of the exposed plates.

The well-established ability for radiation to be enhanced by electromagnetic metamaterials has recently garnered attention in the field of acoustics, where high- k metamaterials could be designed to enhance acoustic wave radiation equally. To exploit the radiation enhancement property of high- k metamaterials, a metamaterial emitter was designed, realized, and studied that was capable of greatly enhancing the radiative properties of an embedded emitter. The design availed a high impedance medium to the emitter so that doing work against this high impedance medium enabled the extraction of more energy from the emitter. This kind of effect is

analogous to the well-known Purcell effect in electromagnetics, where a quantum system's spontaneous emission rate is enhanced by its environment.

The metamaterial emitter's two regions play key roles in its ability to enhance the radiative properties of an embedded emitter efficiently. The emitter is placed in the metamaterial cavity region, which sets the working frequency of the structure in addition to providing enhancement of the emitter's acoustic radiation. The enhanced acoustic waves are then passed to the tapered coupling region, which serves to tailor the beam profile of the waves, enabling a more directional beam emission.

Additionally, this region helps to match the acoustic impedance from the high impedance metamaterial cavity to the low impedance free space. This is necessary to minimize the impedance mismatch between these media, which would otherwise degrade the radiative performance of the structure. As such, the acoustic beam thus emerges from the metamaterial with highly elevated pressures, as well as having a directional profile that proves useful for many applications. Interestingly this region served as a mode-area transformer with an opposite size-aperture relationship to conventional systems like horns.

Like other metamaterials, the metamaterial emitter's performance is highly dependent on the geometric properties of the design. These optimal design parameters were identified through parametric studies that showed the effects of the number of unit cells in the cavity region, the optimal length of the tapered coupling region, the optimal size of the gaps, and the effects of the emitter size as well as ambient air temperature. This study provides a framework for designing an optimal metamaterial emitter. It was identified that a metamaterial cavity of 4 unit cells is optimal for

radiation enhancement. Also, the coupling region needed to be long enough to match the impedance to that of air without supporting severe internal losses due to viscous and thermal effects. For this metamaterial emitter, it was found that the taper angle of the coupling region needed to be at most 2° .

Useful findings emerged in investigating extrinsic factors to the metamaterial's design. One of such is the performance of the acoustic metamaterial given different sized emitters. Larger emitters would result in higher far-field pressure amplitudes but result in generally smaller gain values compared to small-sized emitters. This observation is reasonable given the wave propagation mechanism of the structure and can be useful to inform different use cases of the metamaterial. Also, it was found that the ambient temperature has significant effects on the metamaterial's performance compared to its effect on free-space wave propagation. Higher temperatures shift the optimal frequency of the structure to higher values while decreasing the overall gain of the device. The fact that a small change in the temperature leads to a comparatively larger change in the performance of the propagating waves in the metamaterial is another way that this metamaterial enhances the control of acoustic waves through it, which is a fundamental property of high- k acoustic metamaterials.

The practical applications of acoustic metamaterials have been a key factor in driving research and innovation in this area. By combining the high- k metamaterial emitter and receiver, a metamaterial sonar is realized, which, for the first time, demonstrates the use of acoustic metamaterials in enhancing sonar systems. Such a system takes advantage of the radiation enhancement, reception enhancement, and

directivity of the metamaterials to provide remarkable enhancement to sonar systems. It is analytically determined that the metamaterials should provide significant enhancement to the performance of sonar systems, and this is experimentally proven using a batch of tests. The acoustic metamaterials extended the detectable range of a conventional sonar system up to 9 times. This is despite the higher noise floor of the metamaterial sonar system, which comes as a result of the metamaterial amplifying all frequencies in the bandwidth, be it part of the signal or noise. As such, the metamaterial sonar system maintained a higher signal-to-noise ratio. The metamaterial system also excelled in its ability to identify targets of different sizes, reducing the minimum detectible object size by over a factor of 68 when compared to the conventional system without the metamaterials.

Sonar systems used for tracking and navigation are often tasked with resolving the gap between objects in which the system's resolution would determine its performance. The metamaterial sonar system showed superior abilities in this task due to its comparatively high angular resolution. Cylindrical targets were resolvable up to a separation of 17 cm while preserving some information about the size of the objects. The conventional sonar system was unable to resolve the objects due to its low resolution and signal-to-noise ratio.

The advantages that these high- k acoustic metamaterials have in sonar systems lend themselves in applications such as robotic tracking. Using a metamaterial sonar system designed for 40 kHz, which is the operating frequency of some commercially available transducers, these advantages were demonstrated on a robotic platform. An algorithm inspired by the foraging clicks of some bats (such as the Egyptian fruit bat)

was used, with which the metamaterial sonar system demonstrated superior tracking capabilities compared to the system without the metamaterials.

6.1.3 Delineation of High- k properties in this study

Notably, all the properties of high- k metamaterials were exhibited by the metamaterials developed and studied in this dissertation work.

Energy confinement and transport: The double-tapered acoustic metamaterial developed to understand the waveguiding properties of anisotropic graded-index acoustic metamaterials demonstrated acoustic energy transporting characteristics, where the acoustic waves were gradually amplified and transported through the device. Also, the metamaterial receivers demonstrated the ability to confine acoustic waves via wave compression, wherein the acoustic pressures were enhanced.

Radiation enhancement: It was demonstrated that the acoustic metamaterial emitter enhanced the acoustic pressure of an embedded emitter and releasing these enhanced pressure fields into the far-field. This was identified to be as a result of availing a high acoustic impedance medium to the embedded emitter.

Enhancement of control: Due to their frequency selective nature, all the metamaterials in this work enhanced the control of acoustic waves through them. Additionally, the metamaterial receivers exhibited filtering characteristics that were position-dependent. Notably, the on-chip metamaterial receiver provided an extra degree of control by enabling the active configuration of one of its parameters, providing extra functionalities to the passive system.

6.2 Major contributions

The original contributions of this dissertation work are summarized as follows

Contribution 1: An enhanced understanding of the fundamental properties of high- k acoustic metamaterials has been obtained. Key properties possessed by high- k electromagnetic metamaterials, namely enhancement of control, confinement and transport of energy, and radiation enhancement, have been identified in acoustic metamaterials and exploited in this work. These equivalences established between electromagnetic metamaterials and acoustic metamaterials establishes a reference point through which the study of acoustic metamaterials can be furthered.

Contribution 2: A low profile fiber optic probe has been developed that enables the study of the intrinsic properties of acoustic metamaterials. Using this probe, for the first time, direct measurement of the pressure fields inside the metamaterials has been achieved without seriously disrupting these fields. This has enabled the unearthing of properties that were previously unattainable via experimental studies. Using this tool, the wave propagation mechanism in graded-index acoustic metamaterial waveguides has been experimentally demonstrated. Unlike conventional waveguides that make use of wall-to-wall reflections to confine and transport acoustic waves, the anisotropic metamaterial waveguides in this work make use of gap-to-gap coupling of the evanescent fields to propagate acoustic waves. This mechanism closely resembles the optical guided modes supported by dielectric slab waveguide systems.

Contribution 3: A low dimensional on-chip acoustic metamaterial has been developed that allows for active tuning of its properties. For the first time, a graded-index acoustic metamaterial whose properties can be tuned using a liquid has been developed. By changing the plate height of a tapered graded-index metamaterial, such phenomena as signal amplification, filtering, switching, and active pulse retardation and their related properties were achieved. This metamaterial design thus extended the usability of an otherwise passive structure over a broader bandwidth.

Contribution 4: A refined understanding of how to design high- k acoustic metamaterials for acoustic emission enhancement has been obtained. Far-field radiation enhancement is achieved by embedding an acoustic source in a high-impedance metamaterial cavity, which enables the transfer of more power from the source. The metamaterial cavity size, tapering angle of the coupling region, the effect of gap thickness, the effect of size of the emitter, and ambient temperature effects on the metamaterial radiation performance were studied. Experimental demonstrations of emission enhancement were also presented.

Contribution 5: A bio-inspired metamaterial receiver and emitter has been developed and used to realize a compact metamaterial sonar system to enhance sonar tracking. The high- k metamaterial receiver was shown to functionally approximate the signal amplification and spatial filtering of acoustic signals that are

performed by the mammalian cochlea. Combining this metamaterial receiver with the metamaterial emitter produced a compact bio-inspired sonar system. By providing signal amplification, increased directionality, and a high signal-to-noise ratio, the metamaterials extended the detection range, reduced the minimum detectable target size, and improved target differentiation capabilities of a conventional sonar system. Using a robotic platform with a bio-inspired tracking scheme, the metamaterial sonar system demonstrated superior tracking performance over a similar sonar system without the metamaterials.

6.3 Future work

Upon the completion of this dissertation work, the following recommendations for future work are proposed.

1. **Broadband acoustic metamaterial cochlea.** In this dissertation work, it was found that the gaps of the metamaterial receivers correspond to specific resonant frequencies. One advantage that the basilar membrane of the cochlea has is its possession of sensory cells throughout its structure for picking up the vibrations of the membrane. Unlike this complex structure, the metamaterial receiver developed in this work made use of a single microphone in one of its gaps. If microphone receivers can be placed in more gaps, the frequency bandwidth of the structure can be greatly increased. A robust signal processing scheme could be developed that could perform such tasks as the summation of the signals from the microphones, enabling or disabling

microphones, etc. Such a system would consider the phase shifts induced by the metamaterial medium in performing the signal processing. This would greatly increase the performance and functionality of the metamaterial receiver.

2. **Broadband, tunable metamaterial emitter.** Using one sound source in the metamaterial emitter limits the bandwidth of the amplified emitted signals. This can be broadened by placing emitters in different gaps along the metamaterial emitter. Research on this topic is currently being carried out by colleagues in our research group, where disk-like piezoelectric emitters are being investigated for their ability to perform this task. Furthermore, in this study, the size of the air gaps has been shown to have predictable effects on the metamaterial's frequency response. This idea could be exploited to design a metamaterial emitter that is tunable by changing the gap size of the structure.
3. **Flexible acoustic metamaterial antenna.** Adding more degrees of freedom to the metamaterial would enhance the usability of the device. As an earlier endeavor in this work, the feasibility of this idea was demonstrated, with promising applications in robotic sensing and echolocation tasks. A flexible metamaterial would relax pivoting constraints placed on the current sonar system so that the actuating servos could be arbitrarily placed or replaced by other actuation mechanisms. Such a system may be useful for weight distribution in smaller robotic platforms such as drones. To complete this study, the maximum bending radius of such a structure would need to be

determined so that bending losses are minimized. Such a metamaterial could be investigated for emission and reception functionalities.

4. **Robust bio-inspired echolocation.** The echolocation scheme presented in this work was a proof-of-concept endeavor that demonstrated the capability of acoustic metamaterials to enhance sonar navigation and tracking. This could serve as a framework for investigating and realizing a more robust bio-inspired echolocating robotic platform. In nature, echolocating animals such as bats typically use broadband chirp calls for navigation and foraging. Such a scheme enables a more comprehensive mapping of the environment due to the different response characteristics of the different frequencies. This idea can be incorporated using a broadband metamaterial emitter like that proposed in suggestion 2. Further, the metamaterial sonar system could be mounted on a 3D mobile robot platform, such as a small drone. Such a scheme would closely resemble what is found in nature amongst such animals as echolocating bats.

Appendix A: MATLAB codes

A1: Metamaterial analytical model - frequency

```
%---Metamaterial Frequency Pressure Field-----

% %---Brief Description
% This code plots the ref. index, pressure gain, and wavenumber as
% a function of frequency at a prescribed distance in the metamaterial.

clear all;
close all;
clc;

z = 62.0*10^-3;    %Distance (m).

%=====PARAMETERS=====

%-----Metamaterial Parameters-----

p=3.5*10^-3;          % periodicity in m
g=0.5*10^-3;          % Gap size in m
Z = 7.6*10^-2;        % Total MM length m
w_0=1.5*10^-3;        % First plate dimension m
w_L=8*10^-3;          % Last plate dimension m

%-----Physical parameters-----
R_air=1.2;             % Density of air, unit kg*m^-3
B_air=142*10^3;        % Bulk modulus of air (Adiabatic), unit Pa
R_solid=1.19*10^3;     % Density of polymer, unit kg*m^-3
B_solid=3*10^9;        % Bulk modulus of Solid Pa
loss = 0.03;          % Effective loss factor along the x direction

%-----calculated parameters-----

F = (p-g)/p;          % filling ratio of plates in air
R_z =F*R_solid+(1-F)*R_air; % Density of acoustic metamaterial medium in z
R_x = R_air*(1-li*loss); %Effective density of metamaterial using loss
factor
B = B_air*B_solid/((1-F)*B_solid+F*B_air); % Bulk modulus of acoustic
metamaterial medium
c_air =sqrt(B_air/R_air); % Sound speed in air.
c_eff = c_air*sqrt(1-li*loss); % Effective sound speed using loss factor
theta = atan(0.5*(w_L-w_0)/Z); % Metamaterial slope angle

index = 1;

%---Containers-----

f = 10000:10:40000;
X = zeros(size(f));
N_eff = zeros(size(f));
Y2 = zeros(size(f));
L = zeros(size(f));
```

```

P = zeros(size(f));
K_eff = zeros(size(f));

for f = 10000:10:40000
    lamda=c_air./f;      % the wavelength of sound wave
    k_air = 2*pi/lamda;   % free space wave number of the sound wave

    w_z = w_0+2.*z.*tan(theta);
    n_eff = sqrt((R_air*B_air/(R_x*B))*(tan(f*pi.*w_z./c_eff).^2 +1));
    n_eff0= sqrt((R_air*B_air/(R_x*B))*(tan(f*pi.*w_0./c_eff).^2 +1));

    k_eff = (2*pi*f/c_air)*n_eff;
    k_eff0 = (2*pi*f/c_air)*n_eff0;

    % n_eff for integration until z
    a=0:1*10^-5:z;
    ww_z = w_0+2.*a.*tan(theta);
    nn_eff = real( sqrt((R_air*B_air/(R_x*B))*(tan(f*pi.*ww_z./c_eff).^2
+1)));

    if imag(n_eff)>=0
        p_amp = ((2*pi*R_air*f)^0.5*(1-n_eff.^-
2)^0.25)./cos(atan(R_x*R_air^-1*(n_eff^2-1)^0.5));
        p0_amp = ((2*pi*R_air*f)^0.5*(1-n_eff0.^-
2)^0.25)./cos(atan(R_x*R_air^-1*(n_eff0^2-1)^0.5));

        int_n = trapz(a, real(nn_eff));

        p = (p_amp/abs(p0_amp))*exp(1i*k_air*int_n);
        n=n_eff;
        k = k_eff;
        k0= k_eff0;
    else
        p=0;
        n=0;
        k=0;
    end
    P(index)=abs(p);
    X(index)= f;
    N_eff(index) = n;
    %K_eff(index) = k./k0;
    K_eff(index) = real(k)./real(k0);
    Y2(index) = n_eff0;
    L(index) = w_z;
    index=index+1;
end

figure(1)
subplot (3,1,1)
Y3=N_eff./Y2;
plot(X,real(N_eff), 'b', 'linewidth',2)
xlabel ('Frequency (Hz)')
ylabel ('N_{eff}')
name = sprintf('Effective refractive index at %d mm', 1000*z);
title (name);

```

```

subplot (3,1,2)
plot(X,real(K_eff), 'r', 'linewidth',1)
ylabel ('K_{eff}')
xlabel ('Frequency (Hz)')
name3 = sprintf('Wave vector at %d mm', 1000*z);
title (name3);

subplot (3,1,3)
plot(X,real(P), 'k', 'linewidth',1)
ylabel ('Normalized Pressure')
xlabel ('Frequency (Hz)')
name2 = sprintf('Normalized pressure at %d mm', 1000*z);
title (name2);

```

A2: Metamaterial analytical model - spatial

```
%---Metamaterial Spatial Pressure Field-----

% %---Brief Description
% This code plots the ref. index, pressure gain, and wavenumber as a
% function of distance in the metamaterial at a prescribed
% frequency.

clear all;
close all;
clc;

f = 25500;    %Frequency (Hz)

%=====PARAMETERS=====

%-----Metamaterial Parameters-----
p=3.5*10^-3;      % periodiciy in m
g=0.5*10^-3;      % Gap size in m
Z = 7.6*10^-2;    % Total MM length m
w_0=1.5*10^-3;    % First plate dimension m
w_L=8*10^-3;      % Last plate dimension m

%-----Physical parameters-----
R_air=1.2;         % Density of air, unit kg*m^-3
B_air=142*10^3;    % Bulk modulus of air (Adiabatic), unit Pa
R_solid=1.19*10^3; % Density of polymer, unit kg*m^-3
B_solid=3*10^9;    % Bulk modulus of Solid Pa
loss = 0.03;       % Effective loss factor along the x
direction

%-----calculated parameters-----
F = (p-g)/p;       % filling ratio of plates in air
R_z = F*R_solid+(1-F)*R_air; % Density of acoustic metamaterial
medium in z
R_x = R_air*(1-li*loss); %Effective density
of metamaterial using loss factor
B = B_air*B_solid/((1-F)*B_solid+F*B_air); % Bulk modulus of
acoustic metamaterial medium
c_air = sqrt(B_air/R_air); % Sound speed in air.
c_eff = c_air*sqrt(1-li*loss); % Effective sound speed using loss
factor
lamda=c_air./f;     % the wavelength of sound wave
k_air = 2*pi/lamda; % free space wave number of the sound wave
theta = atan(0.5*(w_L-w_0)/Z); % Metamaterial slope angle
index = 1;

%---Containers-----
z=w_0:1*10^-5:Z;
X = zeros(size(z));
```

```

N_eff = zeros(size(z));
Y2 = zeros(size(z));
L = zeros(size(z));
P = zeros(size(z));
K_eff = zeros(size(z));

for z=w_0:1*10^-5:Z
    w_z = w_0+2.*z.*tan(theta);
    n_eff = sqrt((R_air*B_air/(R_x*B))*(tan(f*pi.*w_z./c_eff).^2
+1));
    n_eff0= sqrt((R_air*B_air/(R_x*B))*(tan(f*pi.*w_0./c_eff).^2
+1));

    k_eff = (2*pi*f/c_air)*n_eff;
    k_eff0 = (2*pi*f/c_air)*n_eff0;

    % n_eff for integration until z
    a=0:1*10^-5:z;
    ww_z = w_0+2.*a.*tan(theta);
    nn_eff = real(
sqrt((R_air*B_air/(R_x*B))*(tan(f*pi.*ww_z./c_eff).^2 +1)));

    if imag(n_eff)>=0
        p_amp = ((2*pi*R_air*f)^0.5*(1-n_eff.^-
2)^0.25)./cos(atan(R_x*R_air^-1*(n_eff^2-1)^0.5));
        p0_amp = ((2*pi*R_air*f)^0.5*(1-n_eff0.^-
2)^0.25)./cos(atan(R_x*R_air^-1*(n_eff0^2-1)^0.5));

        int_n = trapz(a, real(nn_eff));

        p = (p_amp/abs(p0_amp))*exp(1i*k_air*int_n);
        n=n_eff;
        k = k_eff;
        k0= k_eff0;
    else
        p=0;
        n=0;
        k=0;
    end
    P(index)=real(p);
    X(index)= z;
    N_eff(index) = n;
    K_eff(index) = real(k)./real(k0);
    Y2(index) = n_eff0;
    L(index) = w_z;
    index=index+1;
end

figure(1)
subplot (3,1,1)

```

```

Y3=N_eff./Y2;
plot(1000.*X,real(N_eff), 'b', 'linewidth',2)
xlabel ('z (mm)')
ylabel ('N_{eff}')
name = sprintf('Effective refractive index at %d Hz', f);
title (name);

subplot (3,1,3)
plot(1000.*X,real(P), 'k', 'linewidth',1)
ylabel ('Normalized Pressure')
xlabel ('z (mm)')
name2 = sprintf('Normalized pressure at %d Hz', f);
title (name2);

subplot (3,1,2)
plot(1000.*X,real(K_eff), 'r', 'linewidth',1)
ylabel ('K_{eff}')
xlabel ('z (mm)')
name3 = sprintf('Wave vector at %d Hz', f);
title (name3);

```

A3: Cochlea analytical model- dispersion plotter

```
%----- Calculate dispersion of BM in the frequency

%   Brief description

% This code plots the dispersion of the basement membrane if the
cochlea

clear all; close all;
clc;

S0=10.^7; % Unit  $\text{gs}^{-2} \text{mm}^{-2}$ ; the stiffness coefficient
d0=5;      % Unit mm; the characteristic length 5mm
Z= 15;     % Position unit mm, z= 15mm, 10mm, 7mm, 5mm is
used
R=2.0;     % Damping along the BM, in  $\text{gs}^{-1} \text{mm}^{-2}$ 
M=1.5.*10.^-3; % Effective mass per unit area of the BM in
 $\text{g/mm}^2$ 
roh= 1.0.*10.^-3; % Fluid density (water), in  $\text{g/mm}^3$ 
h=1;       % the coefficient (height of the BM cavity), in
mm

f=[0:10:20000]; % Frequency Hz
S=S0.*exp(-Z./d0); % Stiffness distribution along the propagation
direction
Omega=2.*pi.*f; % Angular frequency
Y_bm0=(i.*Omega)./(S0+(i.*Omega.*R)-(Omega.^2.*M)); % Wave
admittance at z=0 position (start point)
K0=sqrt((-2.*i.*Omega.*roh).*Y_bm0./h); % Wavenumber at
z=0 position (start point)
Y_bm=(i.*Omega)./(S+(i.*Omega.*R)-(Omega.^2.*M)); % Admittance
K=sqrt((-2.*i.*Omega.*roh).*Y_bm./h); % Wavenumber unit
 $\text{mm}^{-1}$ 
Neff=K./K0; % Effective index
of the cochlea
Y1=real(Neff);
Y2=imag(Neff);

plot(f,Y1);

xlabel('Frequency (Hz)')
ylabel('K_Norm')
title(sprintf('Bio Cochlea Wave vector at %d mm', Z))
```

A4: Cochlea analytical model- spatial

```
% ====MAMMALIAN COCHLEA SPATIAL CALAULATIONS =====

%-----Brief description----
% This code will plot the normalized displacement and wave vectors
for a
% prescribed frequency on the basement membrane of the mammalian
cochlea.

clear all;
close all;
clc;

%==== Frequency ====
f=1000; % Frequency

%== Parameters====

S0=10.^7; % Unit  $gs^{(-2)} mm^{(-2)}$ ; the stiffness coefficient
d0=5; % Unit mm; the characteristic length 5mm
Z= 15; % Position unit mm, z= 15mm, 10mm, 7mm, 5mm is
used
R=2.0; % Damping along the BM, in  $gs^{-1} mm^{(-2)}$ 
M=1.5.*10.^-3; % Effective mass per unit area of the BM in
g/mm^2
roh= 1.0.*10.^-3; % Fluid density (water), in g/mm^3
h=1; % the coefficient (height of the BM cavity), in
mm
Omega=2.*pi.*f; % Angular frequency

%== Normalized Displacement calculations=====

Y_bm0=(i.*Omega)./(S0+(i.*Omega.*R)-(Omega.^2.*M)); % Wave
admittance at z=0 position (start point)
K0=sqrt((-2.*i.*Omega.*roh).*Y_bm0./h); % Wavenumber at
z=0 position (start point)
Disp0=abs(K0.^(3/2)); % The displacement at the z=0 point,
Disp0=K0.^(3/2)

m=1; % Data Index

for z=0.1:0.05:35 % propagation direction z, in mm
    a=0:0.05:z; % Integration range
    S=S0.*exp(-a./d0); % Stiffness distribution along the
propagation direction
    Y_bm=(i.*Omega)./(S+(i.*Omega.*R)-(Omega.^2.*M));
    K=sqrt((-2.*i.*Omega.*roh).*Y_bm./h);
    % SS=real(K);
```



```

integ=trapz(a,K);
Disp=K(end).^(3/2).*exp(-i.*integ);    % Displacement of the
membrane
Disp_norm=Disp./Disp0;                 % Displacement of the
membrane normalized to                 %the displacement at the z=0
point
X(m)=z;
Y(m)=real(Disp_norm);
m=m+1;
end

figure (1)
subplot(2,1,1)
plot(X,Y,'b','linewidth',1)
xlabel('Distance (mm)')
ylabel('Normalized Displacement')
title(sprintf('Bio Cochlea displacement at %d Hz', f))

%=== Normalized Wave vector calculations=====

Y_bm0=(i.*Omega)./(S0+(i.*Omega.*R)-(Omega.^2.*M)); % Wave
admittance at z=0 position (start point)
K0=sqrt((-2.*i.*Omega.*roh).*Y_bm0./h);           % Wavenumber at
z=0 position (start point)
Z=[0:0.1:35]; % propagation direction z, in mm
S=S0.*exp(-Z./d0); % Stiffness distribution along the
propagation direction
Y_bm=(i.*Omega)./(S+(i.*Omega.*R)-(Omega.^2.*M));
K=sqrt((-2.*i.*Omega.*roh).*Y_bm./h);
Neff=K./K0; % Normalized wavevector (Effective index of
the cochlea)
Y1=real(Neff); % Real part of admittance
Y2=imag(Neff); % Imagine part of admittance

%====Figures=====
subplot(2,1,2)
plot(Z,Y1,'r','linewidth',1);
xlabel('Distance (mm)')
ylabel('K_Norm')
title(sprintf('Bio Cochlea Wave vector at %d Hz', f))

```

A5: Sonar target size plotter

```
%-----Target Size Experiments Plotter-----
clear all; close all; clc;
%-----Code procedure:
% Acquire data
% Properly crop pulse echo data
% Remove DC offset
% FFT
% Find energy
% Save for every trial, and average 3 trials for each distance

%=====
folder = 'F:\OneDrive\Flies!\School Work\SAL\Data\Week of May 13
2019 Experiments\Target size experiments v2\With MM\'; %With MM
file path
folder2 = 'F:\OneDrive\Flies!\School Work\SAL\Data\Week of May 13
2019 Experiments\Target size experiments v2\Without MM\'; %Without
MM file path

%====FFT stuff=====
Fs = 1000000; % Sampling frequency 1M from LabVIEW code
T = 1/Fs; % Sampling period
L = 4000; % Length of signal chosen for analysis;
t = (0:L-1)*T; % Time vector

freq_a = 5000; %Enter cropped frequency range (Lower bound): 250
Hz - 100 kHz at 250 Hz multiples
freq_b = 60000; %Enter cropped frequency range (Upper bound):
250 Hz - 100 kHz at 250Hz multiples

fl = (freq_a/250)+1; %cropped freq range- lower
bound; 81 = 20kHz; 93 = 23kHz
fu = (freq_b/250)+1; %cropped freq range- lower bound;
121 = 30kHz; 109 = 27kHz

%===== Containers=====

MMecho = zeros(14,1); %to hold With MM energy data
Refecho = zeros(14,1); % to hold Ref ene data

MMPower_raw=zeros(221,14); %to store the raw power spectral data
RefPower_raw=zeros(221,14); %to store the raw power spectral data

Noise_MMPower_raw=zeros(221,14); %to store the raw power spectral
data
Noise_RefPower_raw=zeros(221,14); %to store the raw power spectral
data
```

```

Noise_MM_echo = zeros(14,1);    %to hold With MM noise floor energy
data
Noise_Ref_echo = zeros(14,1);    %to hold Ref noise floor energy data

%Pipe = zeros(10,1);
Pipes = [400 164 114.6 89 60.6 33.5 27 19.1 15.85 12.5 9.5 6.35 2.4
1.3];
Pipes2 = uint8([400 164 114.6 89 60.6 33.5 27 19.1 15.85 12.5 9.5
6.35 2.4 1.3]);

%=====WITH METAMATERIAL CALCULATIONS=====

figure(1)

for i = 1:14

subplot(2, 7, i)

    pipe = i-2;
echo_start =13000;    % MM echo starts at 14000pts -Distance is
55.5cm
echo_start2 =13000;    % Noise floor echo is same as pipe echo window

echo_end = echo_start + 3999;
echo_end2 = echo_start2 + 3999;

%% Import data from text file.

for j = 1:3
    subfolder2 = [num2str(j)];
subfolder = [num2str(pipe)];
filename =
fullfile(folder,subfolder,subfolder2,'waveforms','1Deg.txt');

delimiter = {' '};
startRow = echo_start;
endRow = echo_end;

formatSpec = '%f%[\n\r]';

%% Open the text file.
fileID = fopen(filename,'r');

dataArray = textscan(fileID, formatSpec, endRow-startRow+1,
'Delimiter', delimiter, 'TextType', 'string', 'HeaderLines',
startRow-1, 'ReturnOnError', false, 'EndOfLine', '\r\n');

%% Close the text file.
fclose(fileID);

Deg = [dataArray{1:end-1}];
%% Clear temporary variables

```



```

% @@@-----Noise floor per target-----@@@

%% Import data from text file.

for m = 1:3
    subfolder2 = [num2str(m)];
    subfolder = [num2str(pipe)];
    subfolder3 = 'Noise floor\';
    filename =
    fullfile(folder,subfolder,subfolder3,subfolder2,'waveforms','1Deg.tx
t');

    delimiter = {' '};
    startRow = echo_start2;
    endRow = echo_end2;

    formatSpec = '%f%[\n\r]';

    %% Open the text file.
    fileID = fopen(filename,'r');

    dataArray = textscan(fileID, formatSpec, endRow-startRow+1,
'Delimiter', delimiter, 'TextType', 'string', 'HeaderLines',
startRow-1, 'ReturnOnError', false, 'EndOfLine', '\r\n');

    %% Close the text file.
    fclose(fileID);

    Deg = [dataArray{1:end-1}];
    %% Clear temporary variables
    clearvars filename delimiter startRow endRow formatSpec fileID
dataArray ans;

    %=====End of Import file=====
    meanDeg = mean(Deg);
    Deg2=Deg-meanDeg;    % Remove DC offset

    %====Compute the FFT and Power =====
    Y = fft(Deg2);
    P2 = abs(Y/L);
    P1 = P2(1:L/2+1);
    P1(2:end-1) = 2*P1(2:end-1);
    Power = P1.^2;

    %==== Crop the frequency range =====
    f = Fs*(0:(L/2))/L;          %original freq range
    f2 = f(f1:fu)';
    Power2=zeros(size(f2));

    for k=1:size(f2)
        Power2(k)=Power(k+f1);    %cropped power
    end
    Ptot2(:,j)=Power2;    %Total power for each of the 3 trials

```

```

end

%=== Get the average of the 3 Power vs freq. data

Ptot2_avg = zeros(size(f2));
for k=1:ss(1)
    Ptot2_avg(k,1)=(Ptot2(k,1)+Ptot2(k,2)+Ptot2(k,3))/3;
end

%===== Calculate the energy =====
ene2 = trapz(f2, Ptot2_avg); % Area under FFT^2 graph = energy -
Parseval's theorem

%===== Populate the MM Noise echo vector=====
Noise_MM_echo(i,1) = ene2;

Noise_MMPower_raw(:,i)=Ptot2_avg;

end

%=====WITHOUT METAMATERIAL
CALCULATIONS=====

%figure(6)
for i = 1:14

subplot(2,7,i)

    pipe = i-2;
    echo_start =13000; % MM echo starts at 14000pts -Distance is
55.5cm
    echo_end = echo_start + 3999;

%% Import data from text file.

for j = 1:3
    subfolder2 = [num2str(j)];
    subfolder = [num2str(pipe)];
    filename =
fullfile(folder2,subfolder,subfolder2,'waveforms','1Deg.txt');

    delimiter = {' '};
    startRow = echo_start;
    endRow = echo_end;

    formatSpec = '%f%[\n\r]';

    %% Open the text file.
    fileID = fopen(filename,'r');

```



```

        hold off
    end

    %====Compute the FFT and Power =====
    Y = fft(Deg2);
    P2 = abs(Y/L);
    P1 = P2(1:L/2+1);
    P1(2:end-1) = 2*P1(2:end-1);
    Power = P1.^2;

    %==== Crop the frequency range =====
    f = Fs*(0:(L/2))/L;          %original freq range
    f2 = f(f1:fu)';
    Power2=zeros(size(f2));

    for k=1:size(f2)
        Power2(k)=Power(k+f1); %cropped power
    end
    Ptot2(:,j)=Power2; %Total power for each of the 3 trials

end

%== Get the average of the 3 Power vs freq. data

Ptot2_avg = zeros(size(f2));
for k=1:ss(1)
    Ptot2_avg(k,1)=(Ptot2(k,1)+Ptot2(k,2)+Ptot2(k,3))/3;
end

%===== Calculate the energy =====
ene2 = trapz(f2, Ptot2_avg); % Area under FFT^2 graph = energy -
Parseval's theorem

%===== Populate the MM Noise echo vector=====
Noise_Ref_echo (i,1) =ene2;
Noise_RefPower_raw(:,i)=Ptot2_avg;

end

%=====
%
%          NORMALIZATION CALCS
%=====
%

MMnorm = MMecho./Noise_MM_echo; %Normalized MM data
Refnorm = Refecho./Noise_Ref_echo; %Normalized Reference data

```

```

Noise_floor = MMecho./MMecho;      % Noise floor = vector of ones

%=====
%=====PLOTS=====

figure (2)

plot(Pipes, MMnorm, 'linewidth',1, 'Color', [0 0 1], 'LineStyle','-
',...
     'Marker','s', 'MarkerFaceColor',[1 0 0],'Displayname', 'With
MM')
hold on
plot(Pipes, Refnorm, 'linewidth',1, 'Color', [0 0 0], 'LineStyle','-
',...
     'Marker','s', 'MarkerFaceColor',[0.24705882370472
0.24705882370472 0.24705882370472], 'Displayname', 'Without MM')
plot(Pipes, Noise_floor,'linewidth',3, 'Color', [0 0 1],
'LineStyle',':', 'Displayname', 'Noise floor')

set(gca, 'YScale', 'log')
grid on

xlabel('Target diameter (mm) ')
ylabel('Energy SNR')
title('Target Size Plotter')
legend

hold off
figure (3)

plot(Pipes, MMecho, 'linewidth',1, 'Color', [0 0 1], 'LineStyle','-
',...
     'Marker','s', 'MarkerFaceColor',[1 0 0],'Displayname', 'With
MM')
hold on
plot(Pipes, Refecho, 'linewidth',1, 'Color', [0 0 0], 'LineStyle','-
',...
     'Marker','s', 'MarkerFaceColor',[0.24705882370472
0.24705882370472 0.24705882370472], 'Displayname', 'Without MM')
plot(Pipes, Noise_MM_echo,'linewidth',3, 'Color', [0 0 1],
'LineStyle',':', 'Displayname', 'MM Noise floor')
plot(Pipes, Noise_Ref_echo,'linewidth',3, 'Color', [0 0 0],
'LineStyle',':', 'Displayname', 'No MM Noise floor')

set(gca, 'YScale', 'log')
grid on

xlabel('Target diameter (mm) ')
ylabel('Amplitude (J)')
title('Target Size Plotter')
legend

```

```

%===Power plot analysis=====

%====With MM: Select 2 points for analysis====
a = 1;
b = 2;
% ===Without MM: 2 points as well====
c = 1;
d = 2;

figure (3)
for i = 1:14
subplot(2,7,i)
    name = sprintf('MM');
    name2 = sprintf('MM Noise');

    plot(f2,MMPower_raw(:,i), 'linewidth',2, 'Color', [0 0 1],
'Displayname',name)
    hold on
    plot(f2,Noise_MMPower_raw(:,i), 'linewidth',2, 'Color', [0 1 0],
'Displayname',name2)

    set(gca, 'YScale', 'log')
    xlabel('Frequency (Hz) ')
    ylabel('Amplitude (W)')
    name3 = sprintf('With MM %d mm', Pipes(i));
    title(name3);
    legend

    axis([15000 35000 .1E-12 0.1])
end

figure (4)
for i=1:14

subplot(2,7,i)
    name = sprintf('No MM');
    name2 = sprintf('No MM Noise');

    plot(f2,RefPower_raw(:,i), 'linewidth',2, 'Color', [0 0 1],
'Displayname',name)
    hold on
    plot(f2,Noise_RefPower_raw(:,i), 'linewidth',2, 'Color', [0 1 0],
'Displayname',name2)

    set(gca, 'YScale', 'log')
    xlabel('Frequency (Hz) ')
    ylabel('Amplitude (W)')
    name3 = sprintf('No MM %d mm', Pipes(i));
    title(name3);
    legend
    axis([15000 35000 .1E-12 0.1])

end

```

A6: Sonar echolocation range plotter

```
%-----Pipe Distance Experiments Plotter - Re-selected noise----
-----

clear all; close all; clc;
%-----Code procedure:
% Acquire data
% Properly crop pulse echo data
% Remove DC offset
% FFT
% Find energy
% Save for every trial, and average 3 trials for each distance

%=====
folder = 'F:\OneDrive\Flies!\School Work\SAL\Data\Week of March 18
2019 Experiments\Pipe Distance Experiments\With MM\'; %With MM
file path
folder2 = 'F:\OneDrive\Flies!\School Work\SAL\Data\Week of March 18
2019 Experiments\Pipe Distance Experiments\Without MM\'; %Without
MM file path

%====FFT stuff=====
Fs = 1000000; % Sampling frequency 1M from LabVIEW code
T = 1/Fs; % Sampling period
L = 4000; % Length of signal chosen for analysis;
t = (0:L-1)*T; % Time vector

freq_a = 5000; %Enter cropped frequency range (Lower bound):
250Hz - 100kHz at 250Hz multiples
freq_b = 60000; %Enter cropped frequency range (Upper bound):
250Hz - 100kHz at 250Hz multiples

fl = (freq_a/250)+1; %cropped freq range- lower
bound; 81 = 20kHz; 93 = 23kHz
fu = (freq_b/250)+1; %cropped freq range- lower bound;
121 = 30kHz; 109 = 27kHz

%===== Containers=====
ene=zeros(3,1); %to hold the calculated energies for each
trial
ene2=zeros(5,1); %to hold the calculated noise floor energies
for each trial

MMecho = zeros(25,1); %to hold With MM energy data
Refecho = zeros(10,1); % to hold Ref ene data

Noise_MM_echo = zeros(25,1); %to hold With MM noise floor energy
data
Noise_Ref_echo = zeros(10,1); %to hold Ref noise floor energy data
```

```

distance = zeros(25,1);
distance2 = zeros(10,1);

%=====WITH METAMATERIAL CALCULATIONS=====

for i = 1:25

    dist_index = i;
    step1=25;
    step2=50;

    if i <=8
        dist = step1*i;
    else
        dist =step1*8 + 50*(i-8);
    end

    echo_start = round(dist*2*10000/340)+10000;
    echo_end = echo_start + 3999;

    %% Import data from text file.
    %
    for j = 1:3
        subfolder2 = [num2str(j)];
        subfolder = [num2str(dist)];
        filename =
            fullfile(folder,subfolder,subfolder2,'waveforms','1Deg.txt');

        delimiter = {' '};
        startRow = echo_start;
        endRow = echo_end;

        formatSpec = '%f%[\n\r]';

        %% Open the text file.
        fileID = fopen(filename,'r');

        dataArray = textscan(fileID, formatSpec, endRow-startRow+1,
            'Delimiter', delimiter, 'TextType', 'string', 'HeaderLines',
            startRow-1, 'ReturnOnError', false, 'EndOfLine', '\r\n');

        %% Close the text file.
        fclose(fileID);

        Deg = [dataArray{1:end-1}];
        %% Clear temporary variables
        clearvars filename delimiter startRow endRow formatSpec fileID
        dataArray ans;

        %=====End of Import file=====
        meanDeg = mean(Deg);
        Deg2=Deg-meanDeg;    % Remove DC offset

        %====Compute the FFT and Power =====
        Y = fft(Deg2);

```

```

P2 = abs(Y/L);
P1 = P2(1:L/2+1);
P1(2:end-1) = 2*P1(2:end-1);
Power = P1.^2;

%==== Crop the frequency range (specified lower and upper bound
ranges)=====
f = Fs*(0:(L/2))/L;          %original freq range
f2 = f(fl:fu)';
Power2=zeros(size(f2));

for k=1:size(f2)
    Power2(k)=Power(k+80);    %cropped power
end

%===== Calculate the energy =====
ene(j,1) = trapz(f2, Power2); % Area under FFT^2 graph = energy -
Parseval's theorem

end

%===== Populate the echo vector=====
MMecho(i,1) = mean(ene);
distance(i,1) = dist;

end
%=====Clear reusable variables=====
clearvars Deg Deg2 i j k dist ene

%=====WITHOUT METAMATERIAL
CALCULATIONS=====

for i = 1:10

    dist_index = i;
    step1=25;
    step2=50;

    if i <=8
        dist = step1*i;
    else
        dist =step1*8 + 50*(i-8);
    end

    echo_start = round(dist*2*10000/340)+10000;
    echo_end = echo_start + 3999;

    %% Import data from text file.
    %
    % Auto-generated by MATLAB on 2019/03/25 03:50:51
    for j = 1:3
        subfolder2 = [num2str(j)];
        subfolder = [num2str(dist)];
        filename =
        fullfile(folder2,subfolder,subfolder2,'waveforms','1Deg.txt');

```

```

delimiter = {' '};
startRow = echo_start;
endRow = echo_end;

formatSpec = '%f%[^\\n\\r]';

%% Open the text file.
fileID = fopen(filename, 'r');

dataArray = textscan(fileID, formatSpec, endRow-startRow+1,
'Delimiter', delimiter, 'TextType', 'string', 'HeaderLines',
startRow-1, 'ReturnOnError', false, 'EndOfLine', '\\r\\n');

%% Close the text file.
fclose(fileID);

Deg = [dataArray{1:end-1}];
%% Clear temporary variables
clearvars filename delimiter startRow endRow formatSpec fileID
dataArray ans;

%====end of Import file=====
meanDeg2 = mean(Deg);
Deg2=Deg-meanDeg2;    % Remove DC offset

%====Compute the FFT and Power =====
Y = fft(Deg2);
P2 = abs(Y/L);
P1 = P2(1:L/2+1);
P1(2:end-1) = 2*P1(2:end-1);
Power = P1.^2;

%==== Crop the frequency range (20K-30K)=====
f = Fs*(0:(L/2))/L;          %original freq range
f2 = f(f1:fu)';

Power2=zeros(size(f2));

for k=1:size(f2)
    Power2(k)=Power(k+80);    %cropped power
end

%==== Calculate the energy =====
ene(j,1) = trapz(f2, Power2);    % Area under FFT^2 graph = energy -
Parseval's theorem

end

%==== Populate the echo vector=====
Refecho (i,1) = mean(ene);
distance2(i,1) = dist;
end

```

```

%=====
==
%                               NOISE FLOOR CALCS
%=====
==

%=====Noise With Metamaterial
Calculations=====

for i = 1:25

    dist_index = i;
    step1=25;
    step2=50;

    if i <=8
        dist = step1*i;
    else
        dist =step1*8 + 50*(i-8);
    end

    echo_start = 1000;                %Echo window is far beyond the signals
    echo_end = echo_start + 3999;

    %% Import data from text file.
    for j = 1:3
        subfolder2 = [num2str(j)];
        subfolder = [num2str(dist)];
        filename =
        fullfile(folder,subfolder,subfolder2,'waveforms','1Deg.txt');

        delimiter = {' '};
        startRow = echo_start;
        endRow = echo_end;

        formatSpec = '%f%[\n\r]';

        %% Open the text file.
        fileID = fopen(filename,'r');

        dataArray = textscan(fileID, formatSpec, endRow-startRow+1,
        'Delimiter', delimiter, 'TextType', 'string', 'HeaderLines',
        startRow-1, 'ReturnOnError', false, 'EndOfLine', '\r\n');

        %% Close the text file.
        fclose(fileID);

        Deg = [dataArray{1:end-1}];
        %% Clear temporary variables
        clearvars filename delimiter startRow endRow formatSpec fileID
        dataArray ans;

        %=====End of Import file=====
        meanDeg = mean(Deg);

```



```

Deg2=Deg-meanDeg;    % Remove DC offset

%====Compute the FFT and Power =====
Y = fft(Deg2);
P2 = abs(Y/L);
P1 = P2(1:L/2+1);
P1(2:end-1) = 2*P1(2:end-1);
Power = P1.^2;

%==== Crop the frequency range (20K-30K)=====
f = Fs*(0:(L/2))/L;          %original freq range
f2 = f(f1:fu)';
Power2=zeros(size(f2));

for k=1:size(f2)
    Power2(k)=Power(k+80);    %cropped power
end

%===== Calculate the energy =====
ene(j,1) = trapz(f2, Power2);    % Area under FFT^2 graph = energy -
Parseval's theorem

end

%===== Populate the echo vector=====
Noise_MM_echo (i,1) = mean(ene);
distance(i,1) = dist;

end

Noise_MM_echo2 = ones(size(Noise_MM_echo));
Noise_MM_echo2=mean(Noise_MM_echo).*(Noise_MM_echo2;

%=====Clear reusable variables=====
clearvars Deg Deg2 i j k dist ene

%=====Noise Without MM calculations=====

for i = 1:10

    dist_index = i;
    step1=25;
    step2=50;

    if i <=8
        dist = step1*i;
    else
        dist =step1*8 + 50*(i-8);
    end

    echo_start = 95000;
    echo_end = echo_start + 3999;

    %% Import data from text file.

    for j = 1:3

```

```

    subfolder2 = [num2str(j)];
    subfolder = [num2str(dist)];
    filename =
    fullfile(folder2,subfolder,subfolder2,'waveforms','1Deg.txt');

    delimiter = {' '};
    startRow = echo_start;
    endRow = echo_end;

    formatSpec = '%f%[\n\r]';

    %% Open the text file.
    fileID = fopen(filename,'r');

    dataArray = textscan(fileID, formatSpec, endRow-startRow+1,
    'Delimiter', delimiter, 'TextType', 'string', 'HeaderLines',
    startRow-1, 'ReturnOnError', false, 'EndOfLine', '\r\n');

    %% Close the text file.
    fclose(fileID);

    Deg = [dataArray{1:end-1}];
    %% Clear temporary variables
    clearvars filename delimiter startRow endRow formatSpec fileID
    dataArray ans;

    %====end of Import file=====
    meanDeg2 = mean(Deg);
    Deg2=Deg-meanDeg2;    % Remove DC offset

    %====Compute the FFT and Power =====
    Y = fft(Deg2);
    P2 = abs(Y/L);
    P1 = P2(1:L/2+1);
    P1(2:end-1) = 2*P1(2:end-1);
    Power = P1.^2;

    %==== Crop the frequency range (20K-30K)=====
    f = Fs*(0:(L/2))/L;          %original freq range
    f2 = f(f1:fu)';

    Power2=zeros(size(f2));

    for k=1:size(f2)
        Power2(k)=Power(k+80);    %cropped power
    end

    %===== Calculate the energy =====
    ene(j,1) = trapz(f2, Power2);    % Area under FFT^2 graph = energy -
    Parseval's theorem

end

%===== Populate the echo vector=====
Noise_Ref_echo (i,1) = mean(ene);
distance2(i,1) = dist;

```

```
end
```

```
Noise_Ref_echo2 = ones(size(Noise_Ref_echo));  
Noise_Ref_echo2=mean(Noise_Ref_echo).*Noise_Ref_echo2;
```

```
%=====PLOTS=====
```

```
figure (1)
```

```
plot(distance, MMEcho, 'linewidth',1, 'Color', [0 0 1],  
      'LineStyle','-','...'  
      'Marker','o', 'MarkerFaceColor',[1 0 0], 'Displayname', 'With  
MM')  
hold on  
plot(distance2, Refecho, 'linewidth',1, 'Color', [0 0 0],  
      'LineStyle','-','...'  
      'Marker','o', 'MarkerFaceColor',[0.24705882370472  
0.24705882370472 0.24705882370472], 'Displayname', 'Without MM')  
plot(distance, Noise_MM_echo2, 'linewidth',3, 'Color', [0 0 1],  
      'LineStyle',':', 'Displayname', 'MM Noise floor')  
plot(distance2, Noise_Ref_echo2, 'linewidth',3, 'Color', [0 0 0],  
      'LineStyle',':', 'Displayname', 'No MM Noise floor')  
  
set(gca, 'YScale', 'log')  
grid on  
  
xlabel('Distance (cm) ')  
ylabel('Amplitude (J) ')  
title('Pipe Distance Plotter')  
legend
```

A7: Microphone calibration plotter

```
%%MICROPHONE SENSITIVITY PLOTTER

%This code will calculate and plot the sensitivity data for a given
mic
%based on a given Reference Mic.

%Procedure:
% Insert the microphone data in the Calibration Data excel
spreadsheet
% referenced in the code
% Run it.

clear all
close all
clc
%-----
%% Import B&K Calibration data
[~, ~, raw] = xlsread('F:\OneDrive\Flies!\School Work\SAL\Sensors &
Transducers\Microphones\Mic Calibration Plotter\Combined Calibration
Data.xlsx','Sheet1','A2:B201'); %

raw(cellfun(@x) ~isempty(x) && isnumeric(x) && isnan(x),raw)) =
{' '};

%% Exclude rows with non-numeric cells
I = ~all(cellfun(@x) (isnumeric(x) || islogical(x)) &&
~isnan(x),raw),2); % Find rows with non-numeric cells
raw(I,:) = [];

%% Create output variable
data = reshape([raw{:}],size(raw));

%% Allocate imported array to column variable names
Frequency_Cal = data(:,1);
BK_SensitivitydB_Cal = data(:,2);

%% Clear temporary variables
clearvars data raw I;

%=====
%% Import the Subject Microphone data
[~, ~, raw] = xlsread('F:\OneDrive\Flies!\School Work\SAL\Sensors &
Transducers\Microphones\Mic Calibration Plotter\Combined Calibration
Data.xlsx','Sheet1','C3:E201'); % NOTE: Adjust the last number as
needed to ensure that this scope covers the max frequency in the
spreadsheet.

raw(cellfun(@x) ~isempty(x) && isnumeric(x) && isnan(x),raw)) =
{' '};
```

```

%% Exclude rows with non-numeric cells
I = ~all(cellfun(@(x) (isnumeric(x) || islogical(x)) &&
~isnan(x),raw),2); % Find rows with non-numeric cells
raw(I,:) = [];

%% Create output variable
data = reshape([raw{:}],size(raw));

%% Allocate imported array to column variable names
FrequencyHzCh1 = data(:,1);
Optical_Mic_Voltage = data(:,2);
BK_Voltage = data(:,3);

%% Clear temporary variables
clearvars data raw I;

% Calculate

BKSensAtFreq = zeros(size(BK_SensitivitydB_Cal)); % Handle to
interpolate the frequency data from the B&K sensitivity data
Pressure = zeros(size(BK_SensitivitydB_Cal)); % Handle for the
calculated actual SPL = B&K voltage reading / B&K sensitivity at
that particular freq.
OptMicSens = zeros(size(Optical_Mic_Voltage)); % Handle to
calculate the sensitivity of the Optical mic from Opt. mic measured
voltage /actual pressure
for m = 1:size(Optical_Mic_Voltage)
    BKSensAtFreq(m,1) = interp1(Frequency_Cal,BK_SensitivitydB_Cal,
FrequencyHzCh1(m,1)); % Interpolate the Reference Mic's sensitivity
at each experimental frequency
end
for n = 1:size(Optical_Mic_Voltage)
    Pressure(n,1) = BK_Voltage(n,1)/((4.3*10^-
3)*10^(BKSensAtFreq(n,1)/20)); % SPL = V_BK/Sensitivity;
Sensitivity (V/Pa) = 10^((dB/20)) since sensitivity data is in dB
V/Pa.

% Note: the (4.3*10^-3) is as a result of the fact that the
reference sensitivity of the B&K is 4.3mv/Pa.

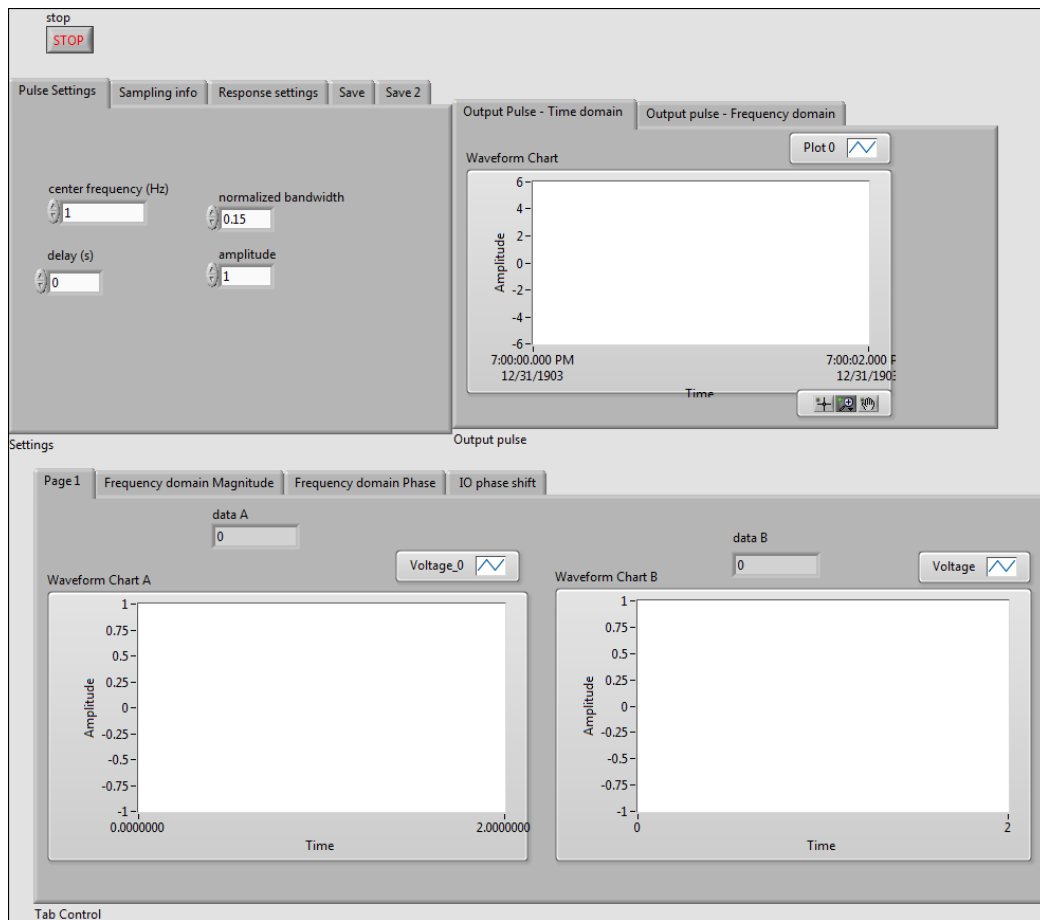
% That is, 0dB is a refence sensitivity corresponding to 4.30mV/Pa
for this 4939 ultrasonic B&K mic. See B&K calibration doc.
end
for p = 1:size(Optical_Mic_Voltage)
    OptMicSens(p,1) = Optical_Mic_Voltage(p,1)/Pressure(p,1);
end

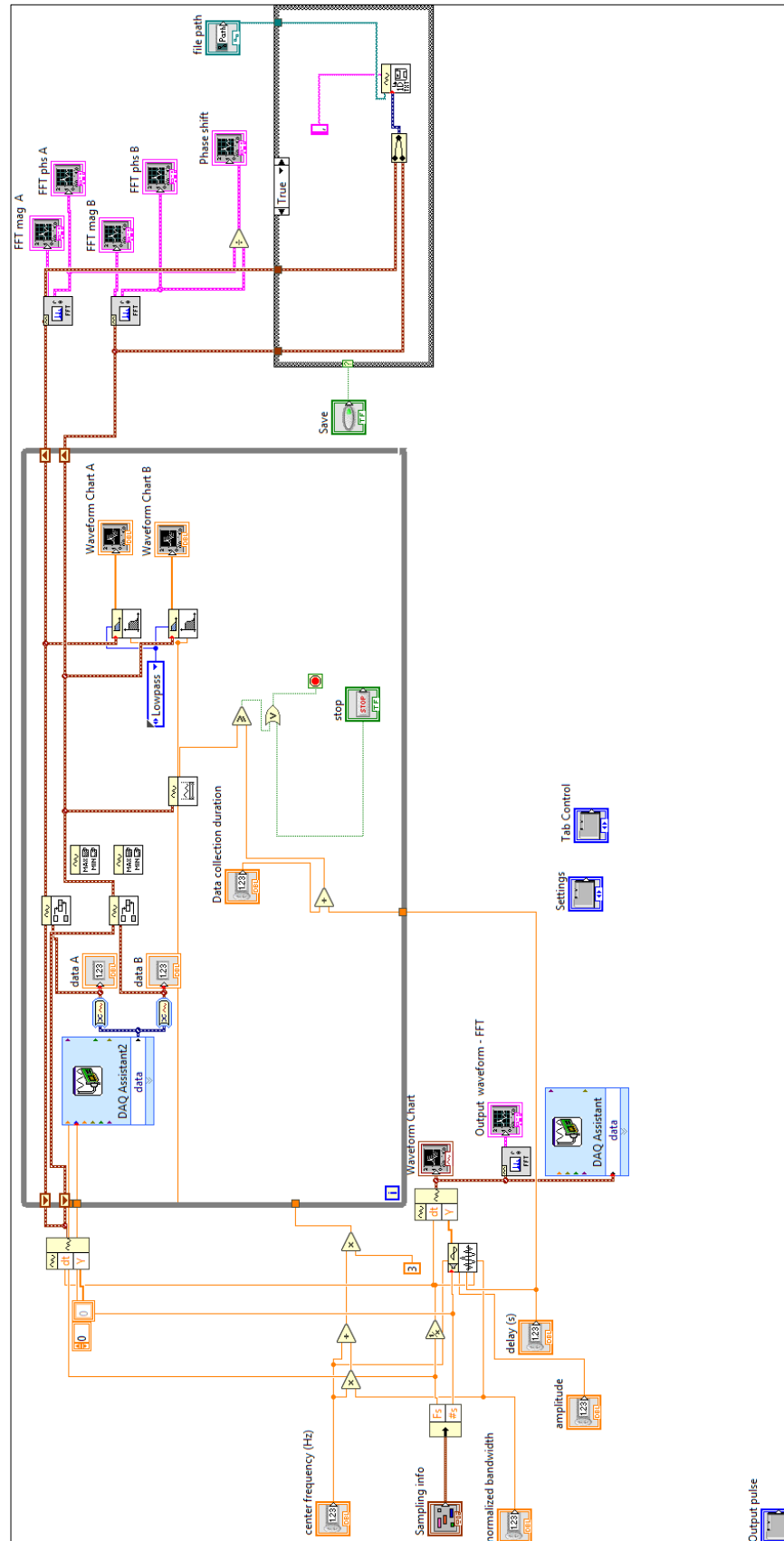
figure(1)
plot(FrequencyHzCh1, OptMicSens,'b', 'linewidth', 2)
xlabel('Frequency (Hz)');
ylabel('Sensitivity (V/Pa)');
grid on
set(gca, 'YScale', 'log')

```

Appendix B: LabVIEW code

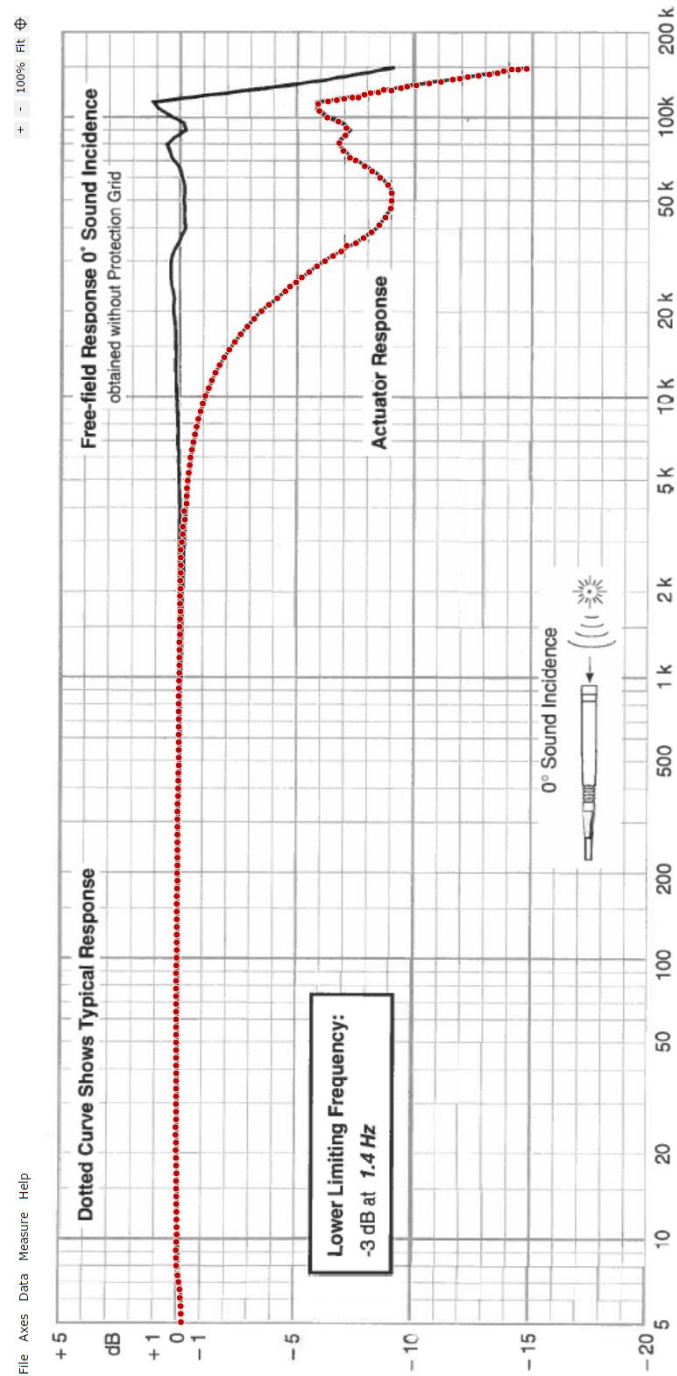
Pulse retardation analyzer





Appendix C: Calibration data

C1: Brüel & Kjær 4939 Ultrasonic microphone datasheet



C2: Optical microphone sensitivity calculator

This calibration data is using the actuator response data from the 4939 B&K calibration datasheet.

Note: 0dB is referenced to 4.3mv/Pa @ 250 Hz

BK_SensitivitydB_Cal	Frequency [Hz]	Optical_Mic_Voltage	BK_Voltage
-0.270186805	200	2.36E-04	7.80E-03
-0.261704913	400	2.60E-02	3.64E-01
-0.250963667	600	3.77E-02	3.80E-01
-0.216457503	800	8.73E-02	7.96E-01
-0.200878081	1000	1.53E-01	1.30E+00
-0.15421862	1200	1.90E-01	1.58E+00
-0.113364969	1400	1.98E-01	1.64E+00
-0.054987397	1600	1.39E-01	1.12E+00
-0.048977837	1800	1.52E-01	1.17E+00
-0.041054305	2000	2.02E-01	1.58E+00
-0.058144813	2200	2.41E-01	1.92E+00
0	2400	2.76E-01	2.40E+00
0	2600	2.99E-01	2.50E+00
0	2800	5.49E-01	4.49E+00
0	3000	6.81E-01	5.84E+00
0	3200	6.34E-01	5.57E+00
0	3400	6.49E-01	5.88E+00
0	3600	5.63E-01	5.34E+00
0	3800	5.73E-01	5.24E+00
0	4000	6.28E-01	5.69E+00
0	4200	6.15E-01	5.80E+00
0	4400	6.35E-01	5.97E+00
0	4600	5.69E-01	5.79E+00
0	4800	5.44E-01	5.42E+00
0	5000	6.05E-01	5.95E+00
0	5200	5.05E-01	4.96E+00
0	5400	5.59E-01	5.17E+00
0	5600	6.61E-01	6.63E+00
0	5800	5.30E-01	5.82E+00
0	6000	3.34E-01	3.63E+00
0	6200	3.81E-01	3.56E+00
0	6400	4.21E-01	4.24E+00

BK_SensitivitydB_Cal	Frequency [Hz]	Optical_Mic_Voltage	BK_Voltage
0	6600	3.88E-01	4.19E+00
0	6800	3.16E-01	3.54E+00
0	7000	3.38E-01	3.41E+00
0	7200	3.75E-01	3.69E+00
0	7400	4.23E-01	4.10E+00
0	7600	4.63E-01	4.78E+00
0	7800	3.98E-01	4.36E+00
0	8000	4.15E-01	4.28E+00
0	8200	5.12E-01	5.24E+00
0	8400	5.02E-01	5.01E+00
0	8600	5.42E-01	5.62E+00
0	8800	5.21E-01	5.54E+00
0	9000	5.60E-01	5.93E+00
0	9200	6.61E-01	6.90E+00
0	9400	5.86E-01	6.30E+00
0	9600	5.98E-01	6.12E+00
0	9800	6.36E-01	6.79E+00
0	10000	6.42E-01	6.76E+00
0	10200	6.64E-01	7.28E+00
0	10400	6.13E-01	6.47E+00
0	10600	6.56E-01	6.80E+00
0	10800	6.79E-01	7.18E+00
0	11000	6.04E-01	6.31E+00
0	11200	6.82E-01	7.33E+00
0	11400	5.91E-01	6.59E+00
0	11600	5.70E-01	6.03E+00
0	11800	5.40E-01	6.02E+00
0	12000	5.34E-01	5.63E+00
0	12200	5.69E-01	6.13E+00
0	12400	5.09E-01	5.85E+00
0	12600	4.15E-01	4.85E+00
0	12800	4.91E-01	5.53E+00
0	13000	4.45E-01	5.12E+00
0	13200	4.14E-01	4.64E+00
0	13400	4.20E-01	5.01E+00
0	13600	4.04E-01	4.93E+00
0	13800	4.40E-01	5.45E+00
0	14000	4.18E-01	4.94E+00
0	14200	3.81E-01	4.66E+00
0	14400	4.76E-01	5.77E+00

BK_SensitivitydB_Cal	Frequency [Hz]	Optical_Mic_Voltage	BK_Voltage
0	14600	4.59E-01	5.43E+00
0	14800	5.41E-01	6.55E+00
0	15000	5.03E-01	6.38E+00
0	15200	5.68E-01	6.71E+00
0	15400	6.83E-01	8.08E+00
0	15600	6.33E-01	7.85E+00
0	15800	6.10E-01	7.81E+00
0	16000	6.78E-01	8.93E+00
0	16200	6.02E-01	7.58E+00
0	16400	6.89E-01	8.45E+00
0	16600	6.87E-01	8.95E+00
0	16800	6.96E-01	9.32E+00
0	17000	6.77E-01	9.31E+00
0	17200	6.65E-01	8.98E+00
0	17400	7.92E-01	1.01E+01
0	17600	7.67E-01	1.04E+01
0	17800	6.11E-01	9.13E+00
0	18000	6.91E-01	9.78E+00
0	18200	6.67E-01	9.72E+00
0	18400	6.93E-01	9.98E+00
0	18600	7.07E-01	1.01E+01
0	18800	6.65E-01	9.71E+00
0	19000	6.74E-01	1.05E+01
0	19200	6.90E-01	1.01E+01
0	19400	6.86E-01	1.02E+01
-0.138709482	19600	6.88E-01	1.01E+01
-0.139324282	19800	6.72E-01	1.02E+01
-0.136153733	20000	7.10E-01	1.05E+01
-0.129197835	20200	6.26E-01	1.04E+01
-0.179022166	20400	6.08E-01	9.19E+00
-0.219526144	20600	6.07E-01	9.54E+00
-0.223783274	20800	5.74E-01	9.08E+00
-0.272969571	21000	5.58E-01	9.12E+00
-0.381441763	21200	5.21E-01	8.57E+00
-0.38962726	21400	5.06E-01	8.36E+00
-0.421471185	21600	4.90E-01	8.13E+00
-0.462778482	21800	4.41E-01	7.78E+00
-0.504085778	22000	4.30E-01	7.28E+00
-0.531198018	22200	4.20E-01	7.52E+00
-0.591432057	22400	4.15E-01	7.70E+00

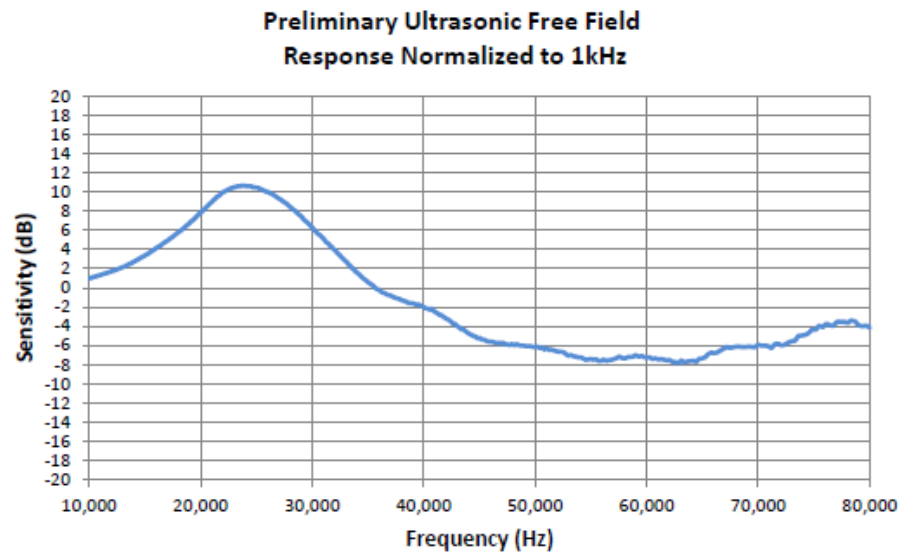
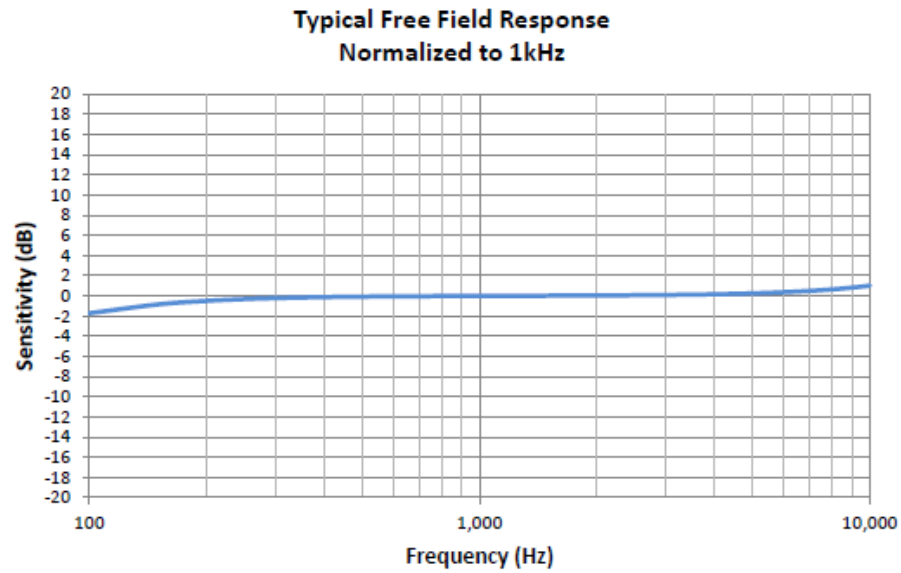
BK_SensitivitydB_Cal	Frequency [Hz]	Optical_Mic_Voltage	BK_Voltage
-0.656397782	22600	4.12E-01	7.53E+00
-0.721363507	22800	3.98E-01	7.47E+00
-0.791060918	23000	3.84E-01	7.27E+00
-0.860758328	23200	4.11E-01	7.59E+00
-0.958845853	23400	3.89E-01	7.73E+00
-1.047470007	23600	3.84E-01	7.73E+00
-1.155020903	23800	3.90E-01	7.65E+00
-1.300425285	24000	4.11E-01	7.96E+00
-1.431634609	24200	3.88E-01	8.08E+00
-1.581770677	24400	3.88E-01	7.93E+00
-1.760296858	24600	3.69E-01	8.05E+00
-1.957749783	24800	3.83E-01	8.11E+00
-2.164666078	25000	3.76E-01	8.11E+00
-2.399972488	25200	3.68E-01	7.84E+00
-2.649473955	25400	3.52E-01	8.00E+00
-2.932097222	25600	3.67E-01	8.37E+00
-3.214720488	25800	3.54E-01	8.58E+00
-3.530465555	26000	3.47E-01	8.19E+00
-3.841691915	26200	3.54E-01	8.38E+00
-4.195503446	26400	3.35E-01	8.56E+00
-4.537852442	26600	3.05E-01	8.21E+00
-5.233949075	26800	2.99E-01	7.86E+00
-5.551023841	27000	2.91E-01	7.79E+00
-5.879390759	27200	2.95E-01	7.86E+00
-6.219220212	27400	2.82E-01	7.63E+00
-6.559049665	27600	2.46E-01	7.51E+00
-6.908448979	27800	2.65E-01	7.37E+00
-7.139343172	28000	2.58E-01	7.49E+00
-7.529281283	28200	2.57E-01	7.56E+00
-7.854915679	28400	2.50E-01	7.32E+00
-8.190380125	28600	2.49E-01	7.75E+00
-8.522319413	28800	2.30E-01	7.88E+00
-8.781284251	29000	2.35E-01	7.41E+00
-9.00691431	29200	2.06E-01	7.46E+00
-9.040335464	29400	2.15E-01	7.28E+00
-9.042212046	29600	2.26E-01	7.94E+00
-8.887416301	29800	1.97E-01	7.78E+00
-8.547560986	30000	1.90E-01	7.40E+00
-8.205814721	30200	2.05E-01	7.76E+00
-7.892671549	30400	2.18E-01	8.07E+00

BK_SensitivitydB_Cal	Frequency [Hz]	Optical_Mic_Voltage	BK_Voltage
-7.502768579	30600	2.09E-01	8.04E+00
-7.261972988	30800	1.72E-01	7.71E+00
-6.986363833	31000	1.74E-01	7.50E+00
-6.810013588	31200	1.69E-01	7.33E+00
-7.064246741	31400	1.61E-01	7.01E+00
-7.105630101	31600	1.55E-01	7.24E+00
-6.767909141	31800	1.60E-01	7.93E+00
-6.295321052	32000	1.57E-01	7.87E+00
-5.957717373	32200	1.43E-01	7.34E+00
-5.903551108	32400	1.60E-01	7.46E+00
-6.325191513	32600	1.61E-01	8.09E+00
-6.694050018	32800	1.53E-01	8.21E+00
-7.006128294	33000	1.50E-01	8.15E+00
-7.356060056	33200	1.43E-01	8.36E+00
-7.611571083	33400	1.42E-01	8.32E+00
-8.12184771	33600	1.37E-01	8.22E+00
-8.46242259	33800	1.24E-01	8.10E+00
-9.012892634	34000	1.23E-01	8.33E+00
-8.689117545	34200	1.38E-01	8.59E+00
-9.417513169	34400	1.32E-01	8.66E+00
-10.06955117	34600	1.40E-01	8.40E+00
-9.682239092	34800	1.33E-01	8.69E+00
-10.61858041	35000	1.41E-01	8.64E+00
-11.11799084	35200	1.39E-01	9.28E+00
-11.62105884	35400	1.30E-01	9.07E+00
-12.71817098	35600	1.34E-01	8.93E+00
-13.17219983	35800	1.31E-01	8.77E+00
-13.52213159	36000	1.18E-01	8.30E+00
-14.39927359	36200	1.23E-01	8.33E+00
	36400	1.30E-01	8.45E+00
	36600	1.28E-01	8.12E+00
	36800	1.40E-01	8.14E+00
	37000	1.35E-01	8.05E+00
	37200	1.42E-01	8.30E+00
	37400	1.35E-01	8.31E+00
	37600	1.28E-01	8.20E+00
	37800	1.34E-01	7.81E+00
	38000	1.28E-01	7.47E+00
	38200	1.25E-01	7.76E+00
	38400	1.37E-01	8.12E+00

BK_SensitivitydB_Cal	Frequency [Hz]	Optical_Mic_Voltage	BK_Voltage
	38600	1.32E-01	7.57E+00
	38800	1.44E-01	7.30E+00
	39000	1.49E-01	7.85E+00
	39200	1.48E-01	7.99E+00
	39400	1.57E-01	8.12E+00
	39600	1.56E-01	7.94E+00
	39800	1.63E-01	8.09E+00
	40000	1.69E-01	8.52E+00

C3: SPU0410LR5H-QB Ultrasonic MEMS microphone frequency response

FREQUENCY RESPONSE CURVE



Appendix D: List of publications

1. **Ganye, Randy**, Yongyao Chen, Haijun Liu, Hyungdae Bae, Zhongshan Wen, and Miao Yu. "Characterization of wave physics in acoustic metamaterials using a fiber optic point detector." *Applied Physics Letters* 108, no. 26 (2016): 261906.
2. **Randy Ganye**, Yongyao Chen, Haijun Liu, Hyungdae Bae, Xinjing Huang, Hyun-Tae Kim, Liuxian Huang, Luxe Travisano, "Bio-inspired metamaterial sonar," *Nature communications*, In preparation
3. **Randy Ganye**, Yongyao Chen, John Surina, and Miao Yu, "On-chip acoustic metamaterial with active tunable properties," *Advanced Materials*, In preparation
4. **Randy Ganye**, Luxi Huang, Andrew Russel, and Miao Yu, "Parametric studies on a graded index metamaterial emitter," *Scientific Reports*, In preparation
5. Liuxian Zhao, Eitan Laredo, Olivia Ryan, Amirhossein Yazdkhasti, Hyun-Tae Kim, **Randy Ganye**, Timothy Horiuchi, Miao Yu, "Ultrasound Beam Steering with Flattened Acoustic Metamaterial Luneburg Lens" *Applied Physics Letters* 116.7 (2020): 071902.
6. Eslami, Babak, **Randy Ganye**, Chris Bunai, and Chandrasekhar Thamire. "Smart Fasteners and Their Application in Flanged Joints." In *ASME 2011 International Mechanical Engineering Congress and Exposition*, pp. 707-714. American Society of Mechanical Engineers Digital Collection, 2011.

Bibliography

- [1] Y. Li, B. Liang, Z. M. Gu, X. Y. Zou, and J. C. Cheng, “Reflected wavefront manipulation based on ultrathin planar acoustic metasurfaces,” *Sci. Rep.*, 2013.
- [2] N. Yu *et al.*, “Light propagation with phase discontinuities: generalized laws of reflection and refraction,” *Science*, vol. 334, no. 6054, pp. 333–7, Oct. 2011.
- [3] H. Esfahlani, M. S. Byrne, M. McDermott, and A. Alù, “Acoustic Supercoupling in a Zero-Compressibility Waveguide,” *Research*, 2019.
- [4] M. Molerón, M. Serra-Garcia, and C. Daraio, “Visco-thermal effects in acoustic metamaterials: from total transmission to total reflection and high absorption,” *New J. Phys.*, vol. 18, no. 3, p. 033003, Mar. 2016.
- [5] Y. Li and B. M. Assouar, “Acoustic metasurface-based perfect absorber with deep subwavelength thickness,” *Appl. Phys. Lett.*, vol. 108, no. 6, 2016.
- [6] S. Huang, X. Fang, X. Wang, B. Assouar, Q. Cheng, and Y. Li, “Acoustic perfect absorbers via Helmholtz resonators with embedded apertures,” *J. Acoust. Soc. Am.*, vol. 145, no. 1, 2019.
- [7] H. Chen and C. T. Chan, “Acoustic cloaking in three dimensions using acoustic metamaterials,” *Appl. Phys. Lett.*, vol. 91, no. 18, p. 183518, Oct. 2007.
- [8] J. Zhao, Z. N. Chen, B. Li, and C.-W. Qiu, “Acoustic cloaking by extraordinary sound transmission,” *J. Appl. Phys.*, vol. 117, no. 21, p. 214507, Jun. 2015.
- [9] F. Lemoult, N. Kaina, M. Fink, and G. Lerosey, “Wave propagation control at

- the deep subwavelength scale in metamaterials,” *Nat. Phys.*, vol. 9, 2012.
- [10] S. A. Cummer and B. L. Popa, “Wave fields measured inside a negative refractive index metamaterial,” *Appl. Phys. Lett.*, 2004.
 - [11] G. Ma and P. Sheng, “Acoustic metamaterials: From local resonances to broad horizons,” *Sci. Adv.*, vol. 2, no. 2, p. e1501595, Feb. 2016.
 - [12] J. Zhu *et al.*, “Acoustic rainbow trapping,” *Sci. Rep.*, vol. 3, no. 1, p. 1728, Dec. 2013.
 - [13] F. Cai, F. Liu, Z. He, and Z. Liu, “High refractive-index sonic material based on periodic subwavelength structure,” *Appl. Phys. Lett.*, vol. 91, no. 20, p. 203515, Nov. 2007.
 - [14] Y. Chen, H. Liu, M. Reilly, H. Bae, and M. Yu, “Enhanced acoustic sensing through wave compression and pressure amplification in anisotropic metamaterials,” *Nat. Commun.*, vol. 5, no. 1, p. 5247, Oct. 2014.
 - [15] S. Zhang, C. Xia, and N. Fang, “Broadband acoustic cloak for ultrasound waves,” *Phys. Rev. Lett.*, vol. 106, no. 2, p. 024301, Jan. 2011.
 - [16] C. Shen and Y. Jing, “Side branch-based acoustic metamaterials with a broadband negative bulk modulus,” *Appl. Phys. A*, vol. 117, no. 4, pp. 1885–1891, Dec. 2014.
 - [17] F. Bongard, H. Lissek, and J. R. Mosig, “Acoustic transmission line metamaterial with negative/zero/positive refractive index,” *Phys. Rev. B*, vol. 82, no. 9, p. 094306, Sep. 2010.
 - [18] T. Brunet *et al.*, “Soft 3D acoustic metamaterial with negative index,” *Nat. Mater.*, vol. 14, no. 4, pp. 384–388, Apr. 2015.

- [19] V. M. García-Chocano *et al.*, “Acoustic cloak for airborne sound by inverse design,” *Appl. Phys. Lett.*, vol. 99, no. 7, p. 074102, Aug. 2011.
- [20] G. Memoli, M. Caleap, M. Asakawa, D. R. Sahoo, B. W. Drinkwater, and S. Subramanian, “Metamaterial bricks and quantization of meta-surfaces,” *Nat. Commun.*, vol. 8, no. 1, p. 14608, Apr. 2017.
- [21] Z. Tian *et al.*, “Programmable Acoustic Metasurfaces,” *Adv. Funct. Mater.*, vol. 29, no. 13, p. 1808489, Mar. 2019.
- [22] M. A. B. Andrade, A. L. Bernassau, and J. C. Adamowski, “Acoustic levitation of a large solid sphere,” *Appl. Phys. Lett.*, vol. 109, no. 4, p. 044101, Jul. 2016.
- [23] C. Ma, S. Gao, Y. Cheng, and X. Liu, “Acoustic metamaterial antennas for combined highly directive-sensitive detection,” *Appl. Phys. Lett.*, vol. 115, no. 5, p. 053501, Jul. 2019.
- [24] Z. Li *et al.*, “Broadband gradient impedance matching using an acoustic metamaterial for ultrasonic transducers,” *Sci. Rep.*, vol. 7, no. 1, p. 42863, Mar. 2017.
- [25] C. Ma, S. Kim, and N. X. Fang, “Far-field acoustic subwavelength imaging and edge detection based on spatial filtering and wave vector conversion,” *Nat. Commun.*, vol. 10, no. 1, p. 204, Dec. 2019.
- [26] X. Yu, Z. Lu, L. Cheng, and F. Cui, “On the sound insulation of acoustic metasurface using a sub-structuring approach,” *J. Sound Vib.*, vol. 401, pp. 190–203, Aug. 2017.
- [27] R. Ganye, Y. Chen, H. Liu, H. Bae, Z. Wen, and M. Yu, “Characterization of wave physics in acoustic metamaterials using a fiber optic point detector,”

- Appl. Phys. Lett.*, vol. 108, no. 26, p. 261906, Jun. 2016.
- [28] A. Marzo, S. A. Seah, B. W. Drinkwater, D. R. Sahoo, B. Long, and S. Subramanian, “Holographic acoustic elements for manipulation of levitated objects,” *Nat. Commun.*, vol. 6, no. 1, p. 8661, Oct. 2015.
- [29] W. Kan *et al.*, “Broadband Acoustic Cloaking within an Arbitrary Hard Cavity,” *Phys. Rev. Appl.*, vol. 3, no. 6, p. 064019, Jun. 2015.
- [30] H. Chen and C. T. Chan, “Acoustic cloaking and transformation acoustics,” *Journal of Physics D: Applied Physics*. 2010.
- [31] N. Kaina, F. Lemoult, M. Fink, and G. Lerosey, “Negative refractive index and acoustic superlens from multiple scattering in single negative metamaterials,” *Nature*, vol. 525, no. 7567, pp. 77–81, 2015.
- [32] L. Vinet and A. Zhedanov, “A ‘missing’ family of classical orthogonal polynomials,” *Nat. Mater.*, vol. 13, no. 4, pp. 352–355, Nov. 2010.
- [33] J. Li, L. Fok, X. Yin, G. Bartal, and X. Zhang, “Experimental demonstration of an acoustic magnifying hyperlens,” 2009.
- [34] A. Poddubny, I. Iorsh, P. A. Belov, and Y. Kivshar, “Hyperbolic metamaterials,” *Nat. Photonics*, vol. 7, no. 12, pp. 948–957, 2013.
- [35] N. Fang *et al.*, “Ultrasonic metamaterials with negative modulus,” 2006.
- [36] C. Shen, Y. Xie, N. Sui, W. Wang, S. A. Cummer, and Y. Jing, “Broadband Acoustic Hyperbolic Metamaterial,” *Phys. Rev. Lett.*, vol. 115, no. 25, p. 254301, Dec. 2015.
- [37] Y. Y. Chen, R. Zhu, M. V Barnhart, and G. L. Huang, “Enhanced flexural wave sensing by adaptive gradient-index metamaterials,” *Sci. Rep.*, vol. 6, no.

- 1, p. 35048, Dec. 2016.
- [38] L. Zhao and S. Zhou, “Compact Acoustic Rainbow Trapping in a Bioinspired Spiral Array of Graded Locally Resonant Metamaterials,” *Sensors*, vol. 19, no. 4, p. 788, Feb. 2019.
 - [39] H. Li *et al.*, “Ultrathin Acoustic Parity-Time Symmetric Metasurface Cloak,” *Research*, vol. 2019, pp. 1–7, Aug. 2019.
 - [40] B.-I. Popa, D. Shinde, A. Konneker, and S. A. Cummer, “Active acoustic metamaterials reconfigurable in real time,” *Phys. Rev. B*, vol. 91, no. 22, p. 220303, Jun. 2015.
 - [41] K. J. B. Lee, M. K. Jung, and S. H. Lee, “Highly tunable acoustic metamaterials based on a resonant tubular array,” *Phys. Rev. B*, vol. 86, no. 18, p. 184302, Nov. 2012.
 - [42] F. Langfeldt, J. Riecken, W. Gleine, and O. von Estorff, “A membrane-type acoustic metamaterial with adjustable acoustic properties,” *J. Sound Vib.*, vol. 373, pp. 1–18, Jul. 2016.
 - [43] X. Yu, Z. Lu, F. Cui, L. Cheng, and Y. Cui, “Tunable acoustic metamaterial with an array of resonators actuated by dielectric elastomer,” *Extrem. Mech. Lett.*, vol. 12, pp. 37–40, Apr. 2017.
 - [44] P. Wang, F. Casadei, S. Shan, J. C. Weaver, and K. Bertoldi, “Harnessing Buckling to Design Tunable Locally Resonant Acoustic Metamaterials,” *Phys. Rev. Lett.*, vol. 113, no. 1, p. 014301, Jul. 2014.
 - [45] S. F. Mahmoud, *Electromagnetic Waveguides: theory and applications*. The Institution of Engineering and Technology, Michael Faraday House, Six Hills

Way, Stevenage SG1 2AY, UK: IET, 1991.

- [46] Y. Xie, W. Wang, H. Chen, A. Konneker, B.-I. Popa, and S. A. Cummer, “Wavefront modulation and subwavelength diffractive acoustics with an acoustic metasurface,” *Nat. Commun.*, vol. 5, no. 1, p. 5553, Dec. 2014.
- [47] B. Xie, K. Tang, H. Cheng, Z. Liu, S. Chen, and J. Tian, “Coding Acoustic Metasurfaces,” *Adv. Mater.*, vol. 29, no. 6, p. 1603507, Feb. 2017.
- [48] Y. Xie *et al.*, “Acoustic Holographic Rendering with Two-dimensional Metamaterial-based Passive Phased Array,” *Sci. Rep.*, vol. 6, no. July, pp. 1–6, 2016.
- [49] K. Melde, A. G. Mark, T. Qiu, and P. Fischer, “Holograms for acoustics,” *Nature*, vol. 537, no. 7621, pp. 518–522, Sep. 2016.
- [50] G. W. Milton, M. Briane, and J. R. Willis, “On cloaking for elasticity and physical equations with a transformation invariant form,” *New J. Phys.*, 2006.
- [51] L. Zigoneanu, B.-I. Popa, and S. A. Cummer, “Three-dimensional broadband omnidirectional acoustic ground cloak,” *Nat. Mater.*, vol. 13, no. 4, pp. 352–355, Apr. 2014.
- [52] F. Lemoult, M. Fink, and G. Lerosey, “Acoustic Resonators for Far-Field Control of Sound on a Subwavelength Scale,” *Phys. Rev. Lett.*, vol. 107, no. 6, p. 064301, Aug. 2011.
- [53] S. Zhang, L. Yin, and N. Fang, “Focusing ultrasound with an acoustic metamaterial network,” *Phys. Rev. Lett.*, vol. 102, no. 19, May 2009.
- [54] C. M. Park, J. J. Park, S. H. Lee, Y. M. Seo, C. K. Kim, and S. H. Lee, “Amplification of acoustic evanescent waves using metamaterial slabs,” *Phys.*

Rev. Lett., vol. 107, no. 19, Nov. 2011.

- [55] J. J. Park, C. M. Park, K. J. B. Lee, and S. H. Lee, “Acoustic superlens using membrane-based metamaterials,” *Appl. Phys. Lett.*, vol. 106, no. 5, Feb. 2015.
- [56] C. Shen, Y. Xie, N. Sui, W. Wang, S. A. Cummer, and Y. Jing, “Broadband Acoustic Hyperbolic Metamaterial,” *Phys. Rev. Lett.*, 2015.
- [57] T. Galfsky, H. N. S. Krishnamoorthy, W. Newman, E. E. Narimanov, Z. Jacob, and V. M. Menon, “Active hyperbolic metamaterials: enhanced spontaneous emission and light extraction,” *Optica*, 2015.
- [58] T. Galfsky, H. N. S. Krishnamoorthy, W. D. Newman, E. Narimanov, Z. Jacob, and V. M. Menon, “Simultaneous enhancement of decay rate and light extraction from active hyperbolic metamaterial,” in *CLEO: QELS - Fundamental Science, CLEO_QELS 2015*, 2015.
- [59] P. R. West, N. Kinsey, M. Ferrera, A. V. Kildishev, V. M. Shalaev, and A. Boltasseva, “Adiabatically tapered hyperbolic metamaterials for dispersion control of high-K waves,” *Nano Lett.*, 2015.
- [60] Z. Jacob, I. I. Smolyaninov, and E. E. Narimanov, “Broadband Purcell effect: Radiative decay engineering with metamaterials,” *Appl. Phys. Lett.*, vol. 100, no. 18, p. 181105, Apr. 2012.
- [61] D. Lu, J. J. Kan, E. E. Fullerton, and Z. Liu, “Enhancing spontaneous emission rates of molecules using nanopatterned multilayer hyperbolic metamaterials,” *Nat. Nanotechnol.*, vol. 9, no. 1, pp. 48–53, Jan. 2014.
- [62] J. Li, Z. Liang, T. Feng, C. H. Chan, S. Han, and S. Lee, “Experimental demonstration of acoustic and electromagnetic metamaterials with conical

- dispersion,” in *2013 7th International Congress on Advanced Electromagnetic Materials in Microwaves and Optics*, 2013, pp. 238–240.
- [63] J. Mei, G. Ma, M. Yang, Z. Yang, W. Wen, and P. Sheng, “Dark acoustic metamaterials as super absorbers for low-frequency sound,” *Nat. Commun.*, vol. 3, no. 1, p. 756, Jan. 2012.
 - [64] M. Oudich, B. Djafari-Rouhani, Y. Pennec, M. B. Assouar, and B. Bonello, “Negative effective mass density of acoustic metamaterial plate decorated with low frequency resonant pillars,” *J. Appl. Phys.*, vol. 116, no. 18, p. 184504, Nov. 2014.
 - [65] M. Ambati, N. Fang, C. Sun, and X. Zhang, “Surface resonant states and superlensing in acoustic metamaterials,” *Phys. Rev. B - Condens. Matter Mater. Phys.*, 2007.
 - [66] X. Zhou, M. Badreddine Assouar, and M. Oudich, “Subwavelength acoustic focusing by surface-wave-resonance enhanced transmission in doubly negative acoustic metamaterials,” *J. Appl. Phys.*, vol. 116, no. 19, p. 194501, Nov. 2014.
 - [67] M. Landi, J. Zhao, W. E. Prather, Y. Wu, and L. Zhang, “Acoustic Purcell Effect for Enhanced Emission,” *Phys. Rev. Lett.*, vol. 120, no. 11, p. 114301, Mar. 2018.
 - [68] F. Zangeneh-Nejad and R. Fleury, “Acoustic Analogues of High-Index Optical Waveguide Devices,” *Sci. Rep.*, vol. 8, no. 1, p. 10401, Dec. 2018.
 - [69] K. Y. Bliokh and F. Nori, “Transverse spin and surface waves in acoustic metamaterials,” *Phys. Rev. B*, vol. 99, no. 2, p. 020301, Jan. 2019.

- [70] Z. Gu *et al.*, “Experimental realization of broadband acoustic omnidirectional absorber by homogeneous anisotropic metamaterials,” *J. Appl. Phys.*, vol. 117, no. 7, p. 074502, Feb. 2015.
- [71] C. Shen, J. Xu, N. X. Fang, and Y. Jing, “Anisotropic Complementary Acoustic Metamaterial for Canceling out Aberrating Layers,” *Phys. Rev. X*, vol. 4, no. 4, p. 041033, Nov. 2014.
- [72] Y. Zhu and B. Assouar, “Multifunctional acoustic metasurface based on an array of Helmholtz resonators,” *Phys. Rev. B*, vol. 99, no. 17, p. 174109, May 2019.
- [73] S. K. Maurya, A. Pandey, S. Shukla, and S. Saxena, “Double Negativity in 3D Space Coiling Metamaterials,” *Sci. Rep.*, vol. 6, no. 1, p. 33683, Dec. 2016.
- [74] J. Chen, J. Xiao, D. Lisevych, A. Shakouri, and Z. Fan, “Deep-subwavelength control of acoustic waves in an ultra-compact metasurface lens,” *Nat. Commun.*, vol. 9, no. 1, p. 4920, Dec. 2018.
- [75] Y. Xie, B.-I. Popa, L. Zigoneanu, and S. A. Cummer, “Measurement of a Broadband Negative Index with Space-Coiling Acoustic Metamaterials,” *Phys. Rev. Lett.*, vol. 110, no. 17, p. 175501, Apr. 2013.
- [76] Z. Liang *et al.*, “Space-coiling metamaterials with double negativity and conical dispersion,” *Sci. Rep.*, vol. 3, no. 1, p. 1614, Dec. 2013.
- [77] J. Zhu *et al.*, “A holey-structured metamaterial for acoustic deep-subwavelength imaging,” *Nat. Phys.*, vol. 7, no. 1, pp. 52–55, Jan. 2011.
- [78] N. Jiménez, T. J. Cox, V. Romero-García, and J.-P. Groby, “Metadiffusers: Deep-subwavelength sound diffusers,” *Sci. Rep.*, vol. 7, no. 1, p. 5389, Dec.

2017.

- [79] R. Groschup and C. U. Grosse, “MEMS microphone array sensor for air-coupled impact-echo,” *Sensors (Switzerland)*, vol. 15, no. 7, pp. 14932–14945, 2015.
- [80] Young and Bennet-Clark, “The role of the tymbal in cicada sound production,” *J. Exp. Biol.*, 1995.
- [81] M. Yu and B. Balachandran, “Acoustic Measurements Using a Fiber Optic Sensor System,” *J. Intell. Mater. Syst. Struct.*, vol. 14, no. 7, pp. 409–414, Jul. 2003.
- [82] D. R. Smith, D. Schurig, and J. B. Pendry, “Negative refraction of modulated electromagnetic waves,” *Appl. Phys. Lett.*, vol. 81, no. 15, pp. 2713–2715, 2002.
- [83] a V Akimov *et al.*, “Generation of single optical plasmons in metallic nanowires coupled to quantum dots,” *Nature*, vol. 450, no. 7168, pp. 402–406, 2007.
- [84] Z. Tian and L. Yu, “Rainbow trapping of ultrasonic guided waves in chirped phononic crystal plates,” *Sci. Rep.*, vol. 7, no. 1, p. 40004, Feb. 2017.
- [85] B.-I. Popa and S. A. Cummer, “Non-reciprocal and highly nonlinear active acoustic metamaterials,” *Nat. Commun.*, vol. 5, no. 1, p. 3398, May 2014.
- [86] J. Li, C. Shen, A. Díaz-Rubio, S. A. Tretyakov, and S. A. Cummer, “Systematic design and experimental demonstration of bianisotropic metasurfaces for scattering-free manipulation of acoustic wavefronts,” *Nat. Commun.*, vol. 9, no. 1, p. 1342, Dec. 2018.

- [87] S. McNab, N. Moll, and Y. Vlasov, “Ultra-low loss photonic integrated circuit with membrane-type photonic crystal waveguides,” *Opt. Express*, vol. 11, no. 22, p. 2927, Nov. 2003.
- [88] J. P. Turpin, J. A. Bossard, K. L. Morgan, D. H. Werner, and P. L. Werner, “Reconfigurable and Tunable Metamaterials: A Review of the Theory and Applications,” *Int. J. Antennas Propag.*, vol. 2014, pp. 1–18, 2014.
- [89] B.-J. Kwon, J.-Y. Jung, D. Lee, K.-C. Park, and I.-K. Oh, “Tunable acoustic waveguide based on vibro-acoustic metamaterials with shunted piezoelectric unit cells,” *Smart Mater. Struct.*, vol. 24, no. 10, p. 105018, Oct. 2015.
- [90] X. Chen, P. Liu, Z. Hou, and Y. Pei, “Magnetic-control multifunctional acoustic metasurface for reflected wave manipulation at deep subwavelength scale,” *Sci. Rep.*, vol. 7, no. 1, p. 9050, Dec. 2017.
- [91] H. Chen, C. T. Chan, and P. Sheng, “Transformation optics and metamaterials,” *Nat. Mater.*, vol. 9, no. 5, pp. 387–96, May 2010.
- [92] W. Akl and A. Baz, “Analysis and experimental demonstration of an active acoustic metamaterial cell,” *J. Appl. Phys.*, vol. 111, no. 4, p. 044505, Feb. 2012.
- [93] F. Ma, J. Chen, and J. H. Wu, “Time-delayed acoustic sink for extreme sub-wavelength focusing,” *Mech. Syst. Signal Process.*, vol. 141, p. 106492, Jul. 2020.
- [94] W. Maryam, A. V. Akimov, R. P. Campion, and A. J. Kent, “Dynamics of a vertical cavity quantum cascade phonon laser structure,” *Nat. Commun.*, vol. 4, no. 1, p. 2184, Oct. 2013.

- [95] K. Song, S.-H. Lee, K. Kim, S. Hur, and J. Kim, “Emission Enhancement of Sound Emitters using an Acoustic Metamaterial Cavity,” *Sci. Rep.*, vol. 4, no. 1, p. 4165, May 2015.
- [96] S. Sun, Q. He, S. Xiao, Q. Xu, X. Li, and L. Zhou, “Gradient-index meta-surfaces as a bridge linking propagating waves and surface waves,” *Nat. Mater.*, vol. 11, no. 5, pp. 426–431, May 2012.
- [97] A. Baz, “The structure of an active acoustic metamaterial with tunable effective density,” *New J. Phys.*, vol. 11, no. 12, p. 123010, Dec. 2009.
- [98] Z. Chen *et al.*, “A tunable acoustic metamaterial with double-negativity driven by electromagnets,” *Sci. Rep.*, vol. 6, no. 1, p. 30254, Jul. 2016.
- [99] X. Zhu *et al.*, “Implementation of dispersion-free slow acoustic wave propagation and phase engineering with helical-structured metamaterials,” *Nat. Commun.*, vol. 7, no. 1, p. 11731, Sep. 2016.
- [100] D. F. P. Pile and D. K. Gramotnev, “Adiabatic and nonadiabatic nanofocusing of plasmons by tapered gap plasmon waveguides,” *Appl. Phys. Lett.*, vol. 89, no. 4, p. 041111, Jul. 2006.
- [101] L. M. Brekhovskikh, O. A. Odin, and M. D. Serotta, “Acoustics of Layered Media II,” *J. Acoust. Soc. Am.*, vol. 94, no. 4, pp. 2464–2464, Oct. 1993.
- [102] L. Brillouin, *Wave propagation in periodic structures: Electric filters and crystal lattices*. 1953.
- [103] E. B. Herbold, J. Kim, V. F. Nesterenko, S. Y. Wang, and C. Daraio, “Pulse propagation in a linear and nonlinear diatomic periodic chain: Effects of acoustic frequency band-gap,” *Acta Mech.*, vol. 205, no. 1–4, pp. 85–103, Jun.

2009.

- [104] L. Robles and M. A. Ruggero, “Mechanics of the mammalian cochlea,” *Physiol. Rev.*, vol. 81, no. 3, pp. 1305–52, Jul. 2001.
- [105] M. Ulfendahl, “Mechanical responses of the mammalian cochlea,” *Prog. Neurobiol.*, vol. 53, no. 3, pp. 331–380, Oct. 1997.
- [106] J. Meaud and K. Grosh, “The effect of tectorial membrane and basilar membrane longitudinal coupling in cochlear mechanics,” *J. Acoust. Soc. Am.*, vol. 127, no. 3, pp. 1411–1421, Mar. 2010.
- [107] P. Dallos, “The active cochlea,” *J. Neurosci.*, vol. 12, no. 12, pp. 4575–85, Dec. 1992.
- [108] Y. Raphael and R. A. Altschuler, “Structure and innervation of the cochlea,” *Brain Res. Bull.*, vol. 60, no. 5–6, pp. 397–422, Jun. 2003.
- [109] T. Reichenbach and A. J. Hudspeth, “The physics of hearing: fluid mechanics and the active process of the inner ear,” *Reports Prog. Phys.*, vol. 77, no. 7, p. 076601, Jul. 2014.
- [110] G. Ni, S. J. Elliott, M. Ayat, and P. D. Teal, “Modelling cochlear mechanics,” *Biomed Res. Int.*, vol. 2014, p. 150637, 2014.
- [111] A. Voros, “Wentzel-Kramers-Brillouin method in the Bargmann representation,” *Phys. Rev. A*, vol. 40, no. 12, pp. 6814–6825, Dec. 1989.
- [112] M. Kleiner, *Acoustics and audio technology*. 2011.
- [113] M. J. Buckingham, “Theory of acoustic attenuation, dispersion, and pulse propagation in unconsolidated granular materials including marine sediments,” *J. Acoust. Soc. Am.*, vol. 102, no. 5, pp. 2579–2596, Nov. 1997.

- [114] S. J. Elliott and C. A. Shera, “The cochlea as a smart structure,” *Smart Mater. Struct.*, vol. 21, no. 6, p. 064001, Jun. 2012.
- [115] S. Zerlin, “Traveling-Wave Velocity in the Human Cochlea,” *J. Acoust. Soc. Am.*, vol. 46, no. 4B, pp. 1011–1015, Oct. 1969.
- [116] J. Sueur, D. Mackie, and J. F. C. Windmill, “So Small, So Loud: Extremely High Sound Pressure Level from a Pygmy Aquatic Insect (Corixidae, Micronectinae),” *PLoS One*, vol. 6, no. 6, p. e21089, Jun. 2011.
- [117] M. J. Ryan and M. A. Guerra, “The mechanism of sound production in túngara frogs and its role in sexual selection and speciation,” *Curr. Opin. Neurobiol.*, vol. 28, pp. 54–59, Oct. 2014.
- [118] “A MODEL OF THE MECHANISM OF SOUND PRODUCTION IN CICADAS,” *J. Exp. Biol.*, 1992.
- [119] P. J. Fonseca and H.-C. B. Clark, “Asymmetry of tymbal action and structure in a cicada: a possible role in the production of complex songs,” *J. Exp. Biol.*, vol. 201, no. 5, 1998.
- [120] H. C. BENNET-CLARK, “The Tuned Singing Burrow of Mole Crickets,” *J. Exp. Biol.*, vol. 128, no. 1, pp. 383–409, 1987.
- [121] “Cicada / Cigarra on Behance.” [Online]. Available: <https://www.behance.net/gallery/25091969/Cicada-Cigarra>. [Accessed: 10-Mar-2020].
- [122] W. J. Bailey, H. C. Bennet-Clark, and N. H. Fletcher, “Acoustics of a small Australian burrowing cricket: the control of low-frequency pure-tone songs,” *J. Exp. Biol.*, vol. 204, no. Pt 16, pp. 2827–41, Aug. 2001.

- [123] K. Song *et al.*, “Sound Pressure Level Gain in an Acoustic Metamaterial Cavity,” *Sci. Rep.*, vol. 4, no. 1, p. 7421, May 2015.
- [124] M. Fink, F. Lemoult, J. de Rosny, A. Tourin, and G. Lerosey, “Subwavelength Focussing in Metamaterials Using Far Field Time Reversal,” 2013.
- [125] J. Zhao, L. Zhang, and Y. Wu, “Enhancing monochromatic multipole emission by a subwavelength enclosure of degenerate Mie resonances,” *J. Acoust. Soc. Am.*, vol. 142, no. 1, pp. EL24–EL29, Jul. 2017.
- [126] L. Zhang, J. Zhao, Y. Wu, and M. Landi, “Enhancement of low-frequency sound emission by metamaterial enclosures,” *J. Acoust. Soc. Am.*, vol. 142, no. 4, pp. 2577–2577, Oct. 2017.
- [127] M. BORN, “Wave Propagation in Periodic Structures,” *Nature*, vol. 158, no. 4026, pp. 926–926, Dec. 1946.
- [128] L. E. Kinsler, A. R. Frey, and C. E. Adams, “Fundamentals of Acoustics,” *Am. J. Phys.*, vol. 31, no. 10, pp. 812–812, Oct. 1963.
- [129] E. Ballestar, “An introduction to epigenetics,” *Adv. Exp. Med. Biol.*, vol. 711, no. 3, pp. 1–11, Mar. 2011.
- [130] R. H. Randall and H. N. Maxwell, “An Introduction to Acoustics,” *Am. J. Phys.*, vol. 20, no. 3, pp. 189–190, Mar. 1952.
- [131] B. Kolbrek, “Horn Theory: An Introduction, Part 1.”
- [132] K. Vanmol *et al.*, “Mode-field Matching Down-Tapers on Single-Mode Optical Fibers for Edge Coupling Towards Generic Photonic Integrated Circuit Platforms,” *J. Light. Technol.*, pp. 1–1, May 2020.
- [133] M. A. Richards, J. A. Scheer, and W. A. Holm, *Principles of Modern Radar*

Volume I-Basic Principles. 2010.

- [134] M. J. Wohlgemuth, J. Luo, and C. F. Moss, “Three-dimensional auditory localization in the echolocating bat,” *Curr. Opin. Neurobiol.*, vol. 41, pp. 78–86, Dec. 2016.
- [135] R. Müller *et al.*, “Dynamic Substrate for the Physical Encoding of Sensory Information in Bat Biosonar,” *Phys. Rev. Lett.*, vol. 118, no. 15, p. 158102, Apr. 2017.
- [136] O. Behrend, M. Kössl, and G. Schuller, “Binaural influences on Doppler shift compensation of the horseshoe bat *Rhinolophus rouxi*,” *J. Comp. Physiol. A.*, vol. 185, no. 6, pp. 529–38, Dec. 1999.
- [137] T. Götz, R. Antunes, and S. Heinrich, “Echolocation clicks of free-ranging Chilean dolphins (*Cephalorhynchus eutropia*),” *J. Acoust. Soc. Am.*, vol. 128, no. 2, pp. 563–566, Aug. 2010.
- [138] J. C. J. Nihoul, “Echolocation in Bats and Dolphins,” *J. Mar. Syst.*, vol. 50, no. 3–4, p. 283, Oct. 2004.
- [139] L. Zhao *et al.*, “Ultrasound beam steering with flattened acoustic metamaterial Luneburg lens,” *Appl. Phys. Lett.*, vol. 116, no. 7, p. 071902, Feb. 2020.
- [140] M. J. Wohlgemuth, N. B. Kothari, and C. F. Moss, “Action Enhances Acoustic Cues for 3-D Target Localization by Echolocating Bats,” *PLoS Biol.*, vol. 14, no. 9, p. e1002544, Sep. 2016.
- [141] Q. H. Wang, T. Ivanov, and P. Aarabi, “Acoustic robot navigation using distributed microphone arrays,” *Inf. Fusion*, vol. 5, no. 2, pp. 131–140, Jun. 2004.

- [142] J.-M. Valin, F. Michaud, and J. Rouat, "Robust Localization and Tracking of Simultaneous Moving Sound Sources Using Beamforming and Particle Filtering," *Rob. Auton. Syst.*, vol. 55, no. 3, pp. 216–228, Feb. 2016.
- [143] N. Uchiyama, A. Yamamoto, S. Sano, and S. Takagi, "Sound source tracking and obstacle avoidance for a mobile robot," in *2009 IEEE Conference on Emerging Technologies & Factory Automation*, 2009, no. January 2010, pp. 1–5.
- [144] N. Uchiyama, S. Sano, and A. Yamamoto, "Sound source tracking considering obstacle avoidance for a mobile robot," *Robotica*, vol. 28, no. 7, pp. 1057–1064, Dec. 2010.
- [145] F. Schillebeeckx, F. De Mey, D. Vanderelst, and H. Peremans, "Biomimetic Sonar: Binaural 3D Localization using Artificial Bat Pinnae," *Int. J. Rob. Res.*, vol. 30, no. 8, pp. 975–987, Jul. 2011.
- [146] J. C. Murray, H. R. Erwin, and S. Wermter, "Robotic sound-source localisation architecture using cross-correlation and recurrent neural networks.," *Neural Netw.*, vol. 22, no. 2, pp. 173–89, Mar. 2009.
- [147] S. Lee, Y. Park, and J.-S. Choi, "Estimation of multiple sound source directions using artificial robot ears," *Appl. Acoust.*, vol. 77, pp. 49–58, Mar. 2014.
- [148] G. Lathoud and M. Magimai-Doss, "A Sector-Based, Frequency-Domain Approach to Detection and Localization of Multiple Speakers," in *Proceedings. (ICASSP '05). IEEE International Conference on Acoustics, Speech, and Signal Processing, 2005.*, 2005, vol. 3, pp. 265–268.

- [149] A. D. Horchler, R. E. Reeve, B. Webb, and R. D. Quinn, “Robot phonotaxis in the wild: a biologically inspired approach to outdoor sound localization,” *Adv. Robot.*, vol. 18, no. 8, pp. 801–816, Jan. 2004.
- [150] J. G. Harris, C. J. Pu, and J. C. Principe, “Monaural cue sound localizer,” *Analog Integr. Circuits Signal Process.*, vol. 23, no. 2, pp. 163–172, 2000.
- [151] J. Han, S. Han, and J. Lee, “The Tracking of a Moving Object by a Mobile Robot Following the Object’s Sound,” *J. Intell. Robot. Syst.*, vol. 71, no. 1, pp. 31–42, Jul. 2013.
- [152] J. H. Han and J. M. Lee, “Sound signal following control of a mobile robot with the estimation of the sound source location by a microphone array,” in *2014 11th International Conference on Ubiquitous Robots and Ambient Intelligence (URAI)*, 2014, pp. 262–265.
- [153] A. S. Conceição, A. P. Moreira, and P. J. Costa, “A nonlinear model predictive control strategy for trajectory tracking of a four-wheeled omnidirectional mobile robot,” *Optim. Control Appl. Methods*, vol. 29, no. 5, pp. 335–352, Sep. 2008.
- [154] C. Baumann, C. Rogers, and F. Massen, “Dynamic binaural sound localization based on variations of interaural time delays and system rotations.,” *J. Acoust. Soc. Am.*, vol. 138, no. 2, pp. 635–50, Aug. 2015.
- [155] M. Banitalebi Dehkordi, H. R. Abutalebi, and M. R. Taban, “Sound source localization using compressive sensing-based feature extraction and spatial sparsity,” *Digit. Signal Process.*, vol. 23, no. 4, pp. 1239–1246, Jul. 2013.
- [156] S. Argentieri, P. Danès, and P. Souères, “A survey on sound source

- localization in robotics: From binaural to array processing methods,” *Comput. Speech Lang.*, vol. 34, no. 1, pp. 87–112, Nov. 2015.
- [157] J. M. Carmena and J. C. T. Hallam, “Narrowband target tracking using a biomimetic sonarhead,” *Rob. Auton. Syst.*, vol. 46, no. 4, pp. 247–259, 2004.
- [158] G. Orchard and R. Etienne-Cummings, “Discriminating multiple nearby targets using single-ping ultrasonic scene mapping,” *IEEE Trans. Circuits Syst. I Regul. Pap.*, vol. 57, no. 11, pp. 2915–2924, 2010.
- [159] J. Huang, T. Supaongprapa, I. Terakura, F. Wang, N. Ohnishi, and N. Sugie, “Model-based sound localization system and its application to robot navigation,” *Rob. Auton. Syst.*, 1999.
- [160] N. Gageik, P. Benz, and S. Montenegro, “Obstacle detection and collision avoidance for a UAV with complementary low-cost sensors,” *IEEE Access*, 2015.
- [161] K. Song, Q. Liu, and Q. Wang, “Olfaction and hearing based mobile robot navigation for odor/sound source search,” *Sensors*, vol. 11, no. 2, pp. 2129–2154, 2011.
- [162] Z. Liang, X. Ma, and X. Dai, “Robust tracking of moving sound source using multiple model Kalman filter,” *Appl. Acoust.*, vol. 69, no. 12, pp. 1350–1355, 2008.
- [163] J. M. Carmena and J. C. T. Hallam, “Estimating Doppler shift using bat-inspired cochlear filter bank models: A comparison of methods for echoes from single and multiple reflectors,” *Adaptive Behavior*, vol. 9, no. 3–4, pp. 241–261, 2001.

- [164] D. K. Barton, *Radar Equations for Modern Radar*. Artech House, 2013.
- [165] N. Gageik, T. Müller, and S. Montenegro, “Obstacle Detection and Collision Avoidance Using Ultrasonic Distance Sensors for an Autonomous Quadrocopter,” *Proc. UAVweek Work. Contrib.*, 2012.
- [166] J. Muller, A. V. Ruiz, and I. Wieser, “Safe & sound: A robust collision avoidance layer for aerial robots based on acoustic sensors,” in *2014 IEEE/ION Position, Location and Navigation Symposium - PLANS 2014*, 2014, pp. 1197–1202.
- [167] S. S. Kelkar, L. L. Grigsby, and J. Langsner, “An Extension of Parseval’s Theorem and Its Use in Calculating Transient Energy in the Frequency Domain,” *IEEE Trans. Ind. Electron.*, vol. IE-30, no. 1, pp. 42–45, 1983.
- [168] P. Elliott, “The Biology of Bats,” *Biol. Conserv.*, vol. 96, no. 2, p. 260, Dec. 2000.
- [169] A. Surlykke, K. Ghose, and C. F. Moss, “Acoustic scanning of natural scenes by echolocation in the big brown bat, *Eptesicus fuscus*,” *J. Exp. Biol.*, vol. 212, no. 7, pp. 1011–1020, Apr. 2009.
- [170] J. Mogdans, J. Ostwald, and H. Schnitzler, “The role of pinna movement for the localization of vertical and horizontal wire obstacles in the greater horseshoe bat, *Rhinolopus ferrumequinum*,” *J. Acoust. Soc. Am.*, vol. 84, no. 5, pp. 1676–1679, Nov. 1988.
- [171] W.-J. Lee, B. Falk, C. Chiu, A. Krishnan, J. H. Arbour, and C. F. Moss, “Tongue-driven sonar beam steering by a lingual-echolocating fruit bat,” *PLOS Biol.*, vol. 15, no. 12, p. e2003148, Dec. 2017.

- [172] A. Boonman, S. Bumrungsri, and Y. Yovel, “Nonecholocating fruit bats produce biosonar clicks with their wings.,” *Curr. Biol.*, vol. 24, no. 24, pp. 2962–7, Dec. 2014.